
A Control Strategy for Self-Sustained and Flexible DC Nanogrids

Dem Fachbereich 18

- Elektrotechnik und Informationstechnik –
der Technischen Universität Darmstadt

Zur Erlangung des akademischen Grades eines
Doktor-Ingenieurs (Dr.-Ing)

vorgelegte

Dissertation

von

M.Sc. Thanh Lich Nguyen

Geboren am 30. Januar 1981 in Namdinh – Vietnam

Referent: Prof. Dr.-Ing. Gerd Griepentrog

Korreferent: Prof. Dr.-Ing. Ulrich Konigorski

Tag der Einreichung: 22.01.2019

Tag der mündlichen Prüfung: 03. 07. 2019

D17

Darmstadt 2019

Thanh Lich Nguyen, M. Sc.

A Control Strategy for Self-Sustained and Flexible DC Nanogrids

Darmstadt, Technische Universität Darmstadt,

Year thesis published in TUPrints 2019

Day of the viva voce: 03. July 2019

Published under CC BY-SA 4.0 International

<https://creativecommons.org/licenses/>

Erklärungen laut der Promotionsordnung

§8 Abs. 1 lit. c PromO

Ich versichere hiermit, dass die elektronische Version meiner Dissertation mit der schriftlichen Version übereinstimmt.

§8 Abs. 1 lit. d PromO

Ich versichere hiermit, dass zu einem vorherigen Zeitpunkt noch keine Promotion versucht wurde. In diesem Fall sind nähere Angaben über Zeitpunkt, Hochschule, Dissertationsthema und Ergebnis dieses Versuchs mitzuteilen.

§9 Abs. 1 PromO

Ich versichere hiermit, dass die vorliegende Dissertation selbstständig und nur unter Verwendung der angegebenen Quellen verfasst wurde.

§9 Abs. 2 PromO

Die Arbeit hat bisher noch nicht zu Prüfungszwecken gedient.

Darmstadt, den 17. Juli 2019

(Thanh Lich Nguyen)

Abstract

Microgrids are becoming a potential solution for combining distributed generation units, such as photovoltaic panels, wind turbines and energy storage systems. As a simple and small version of a microgrid, a nanogrid is a power distribution system that is suitable for a single node, such as a small building or a private house. The nanogrid can be flexibly connected to or disconnected from other power entities through a gateway. In most cases, the nanogrid is connected to the utility grid to avoid the power outage and to increase the operational efficiency. However, the current standalone nanogrid model is not suitable because an imbalance between the generated and consumed electrical power might occur.

The main objective of this research work is to develop a self-sustained and flexible control strategy for autonomous direct current (DC) nanogrids in remote and rural areas without the need for a communication system. The proposed control strategy for the nanogrids is based upon a hierarchical control, in which the primary control manages the power balance inside the nanogrids and the secondary control is responsible for removing deviation of the DC bus voltage caused by droop operation. The state of charge (SoC) of the battery and the external DC bus voltage are taken into account in the proposed control strategy in order to avoid the overcharge/deep discharge of the battery as well as the collapse of the external DC bus. The control algorithm also ensures a flexible exchange of power inside a nanogrid as well as among multiple nanogrids without any extra digital communication link. Bidirectional power flow among multiple nanogrids is implemented through a dedicated interconnected bidirectional Dual Active Bridge (DAB) DC/DC converter installed inside each nanogrid to ensure a galvanic isolation among multiple, interconnected nanogrids. The proposed control strategy is validated through both simulations and experiments. Simulation and experimental results are used to validate the operation of the proposed control algorithm and prove the resemblance between theory and experiments.

However, in order to implement the proposed control strategy, a model of the DC nanogrid has to be developed. For that reason, modeling of every single converter in the system should be conducted. The second important contribution of this research is modeling and control for converters independently, including a bidirectional buck converter and a dual active bridge converter. A small-signal model based on the state-space averaging technique for the bidirectional buck converter is developed, in which only the mean value (i.e. “zeroth” harmonic) of the state variables is taken into account. On the other hand, the generalized state-space averaging-based modeling method is used to obtain the state-space representation of the DAB

converter, in which the direct current (DC) component and the fundamental harmonics in the Fourier series expansion of state variables are considered. Transfer functions from control-to-output are determined, which will be used to define two controllers for the current and voltage loops in a cascaded control structure. Simulations and experiments will be used to validate the operation of the proposed method.

As aforementioned, modeling and control for each converter in the DC nanogrid is performed separately. Nevertheless, when these converters are connected to form a complete DC nanogrid, they will affect each other and the stability of the entire system is influenced as well. To overcome this problem, a model of the entire system has to be developed and the system stability has to be analyzed. For this purpose, the small-signal transfer function of a DC nanogrid is synthesized from the small-signal transfer functions of every single converter of the system. Using this transfer function, the system stability is analyzed and the secondary controller is designed. Simulation and experimental results are used to verify a stable operation of the DC nanogrid system.

Zusammenfassung

Microgrids stellen eine Möglichkeit zum Zusammenschluss verteilter Erzeugersysteme, wie z.B. Photovoltaikanlagen, Windenergieanlagen sowie Speicherlösungen, dar. Als ein daraus abgeleitetes Subsystem mit begrenzter geometrischer Ausdehnung gilt das Nanogrid, das für einzelne Netzknoten, wie sie im Bereich von kleineren öffentlichen Gebäuden, oder Privathaushalten anzutreffen sind, zum Einsatz kommt. Über eine Schnittstelle kann das jeweilige Nanogrid flexibel mit lokalen Erzeuger-, oder Verbrauchereinheiten verbunden werden. Für einen verlustminimalen und ausfallsicheren Betrieb arbeiten die Nanogrids überwiegend im Parallelbetrieb zum Verbundnetz. Die bislang vorhandenen Strategien zur Beherrschung des Inselnetzbetriebs sind aufgrund des etwaigen Ungleichgewichts zwischen Erzeugung und Verbrauch jedoch nicht zwangsläufig stabil.

Das Hauptziel der vorliegenden Forschungsarbeit ist die Entwicklung einer Regelungsstrategie für autonome, flexibel erweiterbare DC Nanogridsysteme in abgelegenen, ländlichen Gebieten ohne die Notwendigkeit einer zusätzlichen, parallelen Kommunikationsinfrastruktur. Die vorgeschlagene Regelung basiert auf einem hierarchischen Ansatz, bei dem eine Primärregelung das Leistungsgleichgewicht innerhalb eines Nanogridknotens sicherstellt und eine Sekundärregelung stationäre Abweichungen der internen DC Spannung durch eine Statikaufschaltung ausregelt. Zusätzlich werden der Ladezustand (SoC) der Batterie sowie die externe DC Spannung durch die Regelung berücksichtigt, um ein Überladen/Tiefentladen der Batterie zu vermeiden und einem Systemzusammenbruch entgegenzuwirken. Weiterhin stellt der Regelalgorithmus einen flexiblen Energieaustausch innerhalb eines und zwischen mehreren Nanogrids sicher. Letzteres wird durch den bidirektionalen Betrieb eines DC-DC Wandlers in Form einer Dual Active Bridge (DAB) in jeder Einheit ermöglicht, der zusätzlich für die galvanische Trennung zwischen den Nanogridknoten sorgt. Zur Koordinierung des Energieaustauschs zwischen den Nanogridknoten ist kein zusätzlicher Kommunikationskanal notwendig. Die Validierung des gewählten Regelungsansatzes erfolgt auf Basis von Simulationen und Laborexperimenten.

Zur Auslegung der jeweiligen Reglerparameter wird ein Systemmodell des Nanogrids entworfen. Die Modellierung und Regelung eines Zweiquadranten-Tiefsetzstellers sowie eines DAB Konverters stellt in diesem Zusammenhang den zweiten wichtigen Beitrag der vorliegenden Forschungsarbeit dar. Für den Tiefsetzsteller wird ein Kleinsignalmodell auf Basis des Mittelwertansatzes im Zustandsraum entworfen. Die Zustandsraumdarstellung der DAB erfolgt unter Anwendung des verallgemeinerten Mittelwertmodells, bei dem neben den

Gleichgrößen zusätzlich die infolge der Schaltfrequenz erzeugte Grundschiwingung (erste Oberschiwingung) der Zustandsgrößen berücksichtigt wird. Die daraus ermittelten Übertragungsfunktionen zwischen Stell- und Ausgangsgrößen dienen anschließend der Bestimmung der Reglerparameter der Strom- und Spannungsregelschleifen in einer Kaskadenstruktur. Auch hier werden Simulationen und praktische Experimente zur Validierung durchgeführt.

Wie beschrieben, erfolgt die Modellierung und Regelung der einzelnen Wandlerstufen zunächst isoliert. Die Überlagerung der Einzelübertragungsfunktionen zur Beschreibung des gesamten Nanogrids führt dabei zu Wechselwirkungen, die die Stabilität des Gesamtsystems beeinflussen können. Für die Stabilitätsbetrachtung wird daher die Gesamtübertragungsfunktion herangezogen, die als Kleinsignaldarstellung aus der Summe der Kleinsignaldarstellungen der einzelnen Wandlerstufen hervorgeht. Sie dient der Auslegung der Parameter für die Sekundärregelung. Simulation und praktische Untersuchungen zeigen, dass unter Anwendung dieser Methodik ein stabiler Inselbetrieb des Nanogrids sichergestellt ist.

Acknowledgements

This research work was supported by the Ministry of Education and Training, Vietnam under the 911 Project and carried out at the Institute for Power Electronics and Control of Drives of the Technische Universität Darmstadt. Apart from my personal research activities, the present work was supported directly and indirectly by many people. Therefore, I would like to express my gratitude towards them.

Firstly, I would like to express my deepest gratitude to my supervisor and the head of institute, Prof. Dr.-Ing. Gerd Griepentrog, for his professional guidance and his inspiration during my doctoral study. I would also like to give my sincere appreciation to my co-supervisor, Prof. Dr.-Ing. Ulrich Konigorski at the Institute of Control Systems and Mechatronics, for his valuable advices and interest in my work.

Moreover, I am thankful to my colleagues of the institute for providing me supportive working conditions and a friendly environment. I would like to mention Mr. Markus Holbein, Mr. Danil Drozhzhin, Mr. Tao Liu, Mr. Erik Smailus, Mr. Adeel Jamal, Ms. Silvia Zennia and the technicians Mr. Thomas Maul and Mr. Kevin Poth for their great technical and administrative assistance.

I would like to say special thanks to Mr. Bernhard Hammer and Mr. Rashid Hussain at the Institute of Control Systems and Mechatronics and at the Institute of High Voltage Technology, respectively, for their useful suggestions and comments. I am also grateful to Dr. Quoc Hoan Tran and Mr. Duy Hung Dam at the University of Ulsan for their kind help and valuable research instructions and beneficial comments during this project.

I would like to thank the World University Service (WUS) on behalf of MOET and Hessen State Ministry of Higher Education, Research and the Arts (HMWK) for their kind support, especially at the beginning of my study.

I am very thankful to my flatmates, Mr. Aaron Louis Correya and Mr. Muhammad Umer Akbar for their help and friendship. In addition, I would like to appreciate Dr. -Ing. Quang Vinh Trinh at the institute of Light Technology for helping me to settle in Darmstadt.

Special thanks to Dr.-Ing. Van Trang Phung and my brother, Dr. Lam Nguyen, who supported me through every step of the progress, gave me effective and vital advices and inspired me to go forward in the path of studying and researching. I would like to thank my parents for their unconditional support and encouragement during my Ph.D. period. Finally, I am particularly



thankful to my wife Dr. Loan Pham who has always been by my side and shared this tough study period with exceptional love, especially taking care of my daughter for the last four years.

Table of Contents

Erklärungen laut der Promotionsordnung.....	I
Abstract.....	II
Zusammenfassung.....	IV
Table of Contents	VIII
Table of Figures.....	XI
Tables	XIV
Nomenclatures	XV
1 Introduction	1
1.1 Motivation of the work.....	1
1.2 State of the art.....	2
1.2.1 Architecture of DC micro/nanogrids.....	2
1.2.2 Control of DC micro/nanogrids	3
1.2.3 Modeling and stability analysis of DC micro/nanogrids	6
1.3 Objectives of the work.....	7
1.4 Publications	8
1.5 Thesis outline.....	9
2 Overview of micro/nanogrids: components, technologies and control topologies	10
2.1 Introduction.....	10
2.2 Components of a nanogrid	11
2.2.1 Photovoltaic panel.....	11
2.2.2 Wind turbine.....	15
2.2.3 Energy storage	16
2.3 The roles of power electronics in renewable energy systems.....	17
2.4 Types of nanogrid technology	18
2.4.1 AC micro/nanogrids	18
2.4.2 DC micro/nanogrids.....	19
2.4.3 DC nanogrids versus AC nanogrids.....	20

2.5	Control topologies of nanogrids	23
2.5.1	Droop control.....	23
2.5.2	Centralized control.....	26
2.5.3	Distributed control	27
2.5.4	Decentralized control	28
2.5.5	Summary of control topologies.....	29
2.6	Summary and the selection for the configuration of the nanogrid	30
3	Modeling and control of DC/DC power electronics converters	33
3.1	Introduction.....	33
3.2	Small-signal modeling method based on the state-space averaging technique	34
3.3	Generalized state-space averaging method and Fourier interpolation.....	35
3.4	Modeling and control of a bidirectional buck converter.....	38
3.4.1	Introduction.....	38
3.4.2	Circuit description.....	38
3.4.3	State-space averaged model of the bidirectional buck converter	40
3.4.4	Small-signal model of the bidirectional buck converter.....	41
3.4.5	Closed-loop control of the bidirectional buck converter	43
3.4.6	Simulation and experimental results	46
3.5	Modeling and Control of Dual Active Bridge Converter	49
3.5.1	Introduction.....	49
3.5.2	The conventional DAB converter	50
3.5.3	Generalized model of the DAB converter.....	51
3.5.4	Small-signal model of the DAB converter	56
3.5.5	Closed-loop control of the DAB converter.....	59
3.5.6	Simulation and experimental results	62
3.6	Summary	66
4	A self-sustained and flexible control strategy for DC nanogrids.....	67
4.1	Introduction.....	67
4.2	Proposed control strategy.....	68
4.2.1	Primary control	68

4.2.2	Secondary control	71
4.2.3	The participation factor k_2 based on SoC.....	71
4.2.4	The participation factor k_3 based on the external DC bus voltage	73
4.3	Modelling, control and stability analysis for an DC nanogrid system.....	77
4.4	Simulation and experimental verification.....	83
4.5	Interconnection of multiple DC nanogrids	88
4.5.1	Configuration of interconnected DC nanogrids	88
4.5.2	Case study and simulation results.....	90
4.6	Summary	95
5	Conclusion and outlook	96
5.1	Conclusion.....	96
5.2	Outlook.....	97
6	Appendix.....	98
6.1	Design of dual active bridge converter	98
6.1.1	Power part	98
6.1.2	Measurement circuit.....	104
6.1.3	Gate driver	107
6.2	Design of half-bridge converter	109
6.2.1	Power part	109
6.2.2	Measurement circuits and gate drivers	110
6.3	Schematics and printed circuit boards.....	111
6.3.1	Schematics and printed circuit boards of the DAB converter.....	111
6.3.2	Schematics and PCB layout of the bidirectional buck converter	125
6.4	Photos of the converter prototype	136
	Bibliography.....	139

Table of Figures

Figure 2.1: The simple equivalent circuit of an ideal PV cell	12
Figure 2.2: The equivalent circuit of a practical PV device	13
Figure 2.3: The I - V curve of the practical PV device	13
Figure 2.4: Typical P-V Characteristics of a PV module for changes in solar radiation	14
Figure 2.5: Typical P-V Characteristics of a PV module for changes in PV cell temperature. ..	14
Figure 2.6: Typical power coefficient characteristic of a wind turbine.....	16
Figure 2.7: The simple equivalent circuit model of a battery.....	17
Figure 2.8: Typical configuration of an AC nanogrid.....	19
Figure 2.9: Typical configuration of a DC nanogrid	20
Figure 2.10: A typical control structure with droop control for DC nanogrids	24
Figure 2.11: Thévenin equivalent circuit for a DG.....	24
Figure 2.12: Load regulation characteristic of the droop method	25
Figure 2.13: Droop control for AC systems: (a) P - f droop; (b) Q - V droop.....	25
Figure 2.14: Centralized control topology.....	27
Figure 2.15: Distributed control topology	28
Figure 2.16: Decentralized control topology	29
Figure 2.17: The modular structure of a nanogrid	31
Figure 2.18: A DC microgrid made of interconnected nanogrids	32
Figure 3.1. Flowchart of the small-signal modeling approach based on the state-space averaging technique [125]	35
Figure 3.2: Two periodic signal with the same fundamental period T_s , but different phase shift	37
Figure 3.3: The bidirectional buck converter	39
Figure 3.4: Waveforms of the bidirectional buck converter during one period	39
Figure 3.5: Control scheme for the bidirectional buck converter	44
Figure 3.6: Bode plot of the open-loop transfer function of the current loop.....	45
Figure 3.7: Bode plot of the open-loop transfer function of the voltage loop	46
Figure 3.8: Simulation results of the bidirectional buck converter.....	47

Figure 3.9: System diagram of the bidirectional buck converter.....	48
Figure 3.10: Experimental result of the buck converter for load current step up from 0.96 A to 2.88 A.....	49
Figure 3.11: Experimental result of the buck converter for load current step down from 2.88 A to 0.96 A.....	49
Figure 3.12: Bidirectional dual active bridge converter.....	51
Figure 3.13: Simplified DAB converter referred to the secondary side.....	52
Figure 3.14: Waveforms during one period.....	53
Figure 3.15: Control scheme for DAB converter.....	60
Figure 3.16: Bode plot of the open-loop transfer function of the current loop of the DAB converter	61
Figure 3.17: Bode plot of the open-loop transfer function of the voltage loop of the DAB converter	62
Figure 3.18: Simulation results of DAB converter	63
Figure 3.19: System diagram of the DAB converter.....	64
Figure 3.20: Experimental result of the DAB converter for load current step up from 0.96 A to 2.88 A.....	65
Figure 3.21: Experimental result of the DAB converter for load current step down from 2.88 A to 0.96 A.....	65
Figure 3.22: Switching wave form for load current of 0.96 A.....	66
Figure 4.1: The proposed hierarchical control structure of the nanogrid	68
Figure 4.2: Primary control of nanogrids	69
Figure 4.3: Droop curves of different sources in a nanogrid	70
Figure 4.4: Relationship between power and SoC of battery	72
Figure 4.5: Effect of the participation factor based on SoC on primary control.....	73
Figure 4.6: Effect of the participation factor based on external DC bus voltage on primary control	74
Figure 4.7: Relationship between exchanged power and external DC bus voltage	75
Figure 4.8: Proposed control strategy for the nanogrid	76
Figure 4.9: Equivalent model of the DC nanogrid	77
Figure 4.10: The small-signal model of the entire nanogrid	78

Figure 4.11: The control structure of DC nanogrid with secondary control	80
Figure 4.12: Closed-loop eigenvalues of the NG.....	81
Figure 4.13: The dominant eigenvalues with different load models	81
Figure 4.14: The maximum real parts of eigenvalues of the nanogrid with respect to the different load resistances	82
Figure 4.15: Bode plot of the closed-loop transfer function of the DC nanogrid	82
Figure 4.16: Topology of a DC nanodrid for the experiment	83
Figure 4.17: Experimental setup.....	84
Figure 4.18: Simulation results for the load changes	85
Figure 4.19: Experimental results for load changes.....	86
Figure 4.20: Simulation results for the PV changes	87
Figure 4.21: Experimental results for PV changes	88
Figure 4.22: Simulation model of three interconnected nanogrids	89
Figure 4.23: Simulation results for load changes	91
Figure 4.24: Simulation results for PV source changes.....	94
Figure 6.1: Typical waveforms of the voltage and the magnetic flux.....	99
Figure 6.2: Current transducer LA25-NP.....	105
Figure 6.3: Current sensor and operational amplifier.....	106
Figure 6.4: Voltage transducer LV25-P	107
Figure 6.5: Voltage sensor and operational amplifier.....	107
Figure 6.6: Gate drive circuit.....	108
Figure 6.7: PCB layout of an H-Bridge of the DAB converter.....	111
Figure 6.8: PCB layout of the measurement circuit of the DAB converter	120
Figure 6.9: PCB layout of the buck converter.....	125
Figure 6.10: Photo of the DAB converter (top side)	136
Figure 6.11: Photo of the DAB converter (front side).....	137
Figure 6.12: Photo of the DAB converter (back side)	137
Figure 6.13: Photo of the measurement circuit	138
Figure 6.14: Photo of the bidirectional buck converter	138

Tables

Table 2.1: Comparison between AC and DC micro/nanogrids [84], [88]	22
Table 3.1: Parameters of controller.....	45
Table 3.2: Parameters of bidirectional buck converter	47
Table 3.3: Parameters of controllers	60
Table 3.4: Parameters of DAB converter	62
Table 4.1: Parameters of secondary controller	80
Table 4.2: Parameters of interface converters	84
Table 4.3: Parameters of the microgrid.....	89
Table 6.1: Main parameters of the power MOSFET of the DAB converter	104
Table 6.2: Main parameters of the isolated gate driver	107
Table 6.3: Main parameters of the isolated DC/DC converter	108
Table 6.4: Main parameters of the power MOSFET of the buck converter	110

Nomenclatures

Symbols

A	Area swept by the wind turbine rotor
\mathbf{A}	State matrix
A_e	Effective cross-section area of the core
A_{w1}	Cross-section of the primary wire of the HF transformer
a	Diode ideality constant
\mathbf{B}	Input matrix
B_{\max}	Maximum magnetic flux density
' _b '	Nomenclature corresponding to the bidirectional buck converter
C_{bat}	Capacitance of the battery
C_{bus2}	Capacitance of the external DC bus capacitor
C_f	Capacitance of the LC output filter
C_p	Power coefficient of the wind turbine
C_o	Capacitance of the filter capacitor
C_Σ	Total capacitance of the common DC bus
d, D	Duty cycle
d_{\max}	Maximum value of the phase shift ratio
d_{w1}	Diameter of the primary winding of HF transformer
' _{dab} '	Nomenclature corresponding to the dual active bridge converter
f_s	Switching frequency
$G_b(s)$	Control-to-output transfer function of the bidirectional buck converter
$G_{\text{ci,b}}(s), G_{\text{cv,b}}(s)$	Transfer functions of the current and voltage controllers of the bidirectional buck converter, respectively
$G_{\text{ci,bat}}(s), G_{\text{ci,dab}}(s), G_{\text{ci,pv}}(s)$	Transfer functions of the current controllers of the battery, dual active bridge and PV converters, respectively
$G_{\text{cv,bat}}(s), G_{\text{cv,dab}}(s), G_{\text{cv,pv}}(s)$	Transfer functions of the voltage controllers of the battery, dual active bridge and PV converters, respectively
$G_{\text{c,sec}}(s)$	Transfer function of the secondary control loop
$G_{\text{d,b}}(s)$	Transfer function of the control delay of the bidirectional buck converter

$G_{d,bat}(s), G_{d,dab}(s), G_{d,pv}(s)$	Transfer functions of the control delay of the battery, interconnected (DAB) and PV converter, respectively
$G_{dab}(s)$	Control-to-output transfer function of the dual active bridge converter
$G_{iLd,b}(s)$	Transfer functions from the small signal $\Delta\langle i_L \rangle_0$ to the control small signal Δd of the bidirectional buck converter
$G_{iLd,bat}(s)$	Transfer functions from the small signal $\Delta\langle i_L \rangle_0$ to the control small signal Δd of the battery converter
$G_{iLd,pv}(s)$	Transfer functions from the small signal $\Delta\langle i_L \rangle_0$ to the control small signal Δd of the PV converter
$G_{ifd,dab}(s)$	Transfer functions from the small signal $\Delta\langle i_f \rangle_0$ to the control small signal Δd of the dual active bridge converter
$G_{I,bat}(s)$	Transfer function from the output current i_{bat} to the voltage correction δv
$G_{I,dab}(s)$	Transfer function from the output current i_{dab} to the voltage correction δv
$G_{I,pv}(s)$	Transfer function from the output current i_{pv} to the voltage correction δv
$G_{OLi,b}(s)$	Open-loop transfer functions from i_L to $i_{L,ref}$ of the bidirectional buck converter
$G_{OLi,dab}(s)$	Open-loop transfer functions from i_f to $i_{f,ref}$ of the dual active bridge converter
$G_{OLv,b}(s)$	Open-loop transfer functions from v_o to $v_{o,ref}$ of the bidirectional buck converter
$G_{OLv,dab}(s)$	Open-loop transfer functions from v_o to $v_{o,ref}$ of the dual active bridge converter
$G_{sys}(s)$	Transfer function of the DC nanogrid without the secondary control
$G_{CL,sys}(s)$	Closed-loop transfer function from v_{bus} to $v_{bus,ref}$ of the DC nanogrid with the secondary control
$G_{vd,b}(s)$	Transfer functions from the small signal $\Delta\langle v_o \rangle_0$ to the control small signal Δd of the bidirectional buck converter
$G_{vd,bat}(s)$	Transfer functions from the small signal $\Delta\langle v_o \rangle_0$ to the control small signal Δd of the battery converter
$G_{vd,dab}(s), G_{iRd,dab}(s), G_{ild,dab}(s), G_{vcfd,dab}(s), G_{ifd,dab}(s)$	Transfer functions from the small signal $\Delta\langle v_o \rangle_0$, $\Delta(\Re\{\langle i_t \rangle_1\})$, $\Delta(\Im\{\langle i_t \rangle_1\})$, $\Delta\langle i_{cf} \rangle_0$, and $\Delta\langle i_f \rangle_0$ to the control small signal Δd of the dual active bridge converter, respectively

$G_{vd,pv}(s)$	Transfer functions from the small signal $\Delta\langle v_o \rangle_0$ to the control small signal Δd of the PV converter
I_b	Battery current
I_d	Diode current
I_{pv}	PV current
$I_{pv,cell}$	Magnitude of the ideal current source generated by the incident light
I_0	Saturation current of the PV device
$I_{0,cell}$	Reverse saturation current
I_{L1}	Root mean square value of the primary current of the dual active bridge converter
I_{SN}	Nominal output current in secondary side of the current transducer
I_P	Primary current of the current transducer
i_{Co}	Filter capacitor's current of the bidirectional buck converter
i_f	Filter current of the dual active bridge converter
i_L	Inductor current of the bidirectional buck converter
i_{Lbat}	Inductor current of the battery converter
i_{bat}, I_{bat}	Current of the battery
i_{dab}	Current of the interconnected converter
i_{Ldab}	Output current of the dual active bridge converter
i_{pv}	The current of the PV source
i_R	Load current
i_t	Transformer current
i_o	Output current
\mathbf{I}	Identity matrix
\Im	Imaginary part
J	Current density of the wire
k	Boltzmann constant (1.381×10^{-23} J/K)
k_d	Droop coefficient
$k_{d,bat}, k_{d,dab}, k_{d,pv}$	Droop coefficients of the battery, interconnected and PV converters, respectively
k_i	Participation factor ($i = 1 \div 3$)
K_N	Turns ratio of the current and voltage transducers

$K_{pi,b}, K_{ii,b}$	Gains of the proportional and integral parts of the current controller of the bidirectional buck converter
$K_{pv,b}, K_{iv,b}$	Gains of the proportional and integral parts of the voltage controller of the bidirectional buck converter
$K_{pi,dab}, K_{ii,dab}$	Gains of the proportional and integral parts of the current controller of the dual active bridge converter
$K_{pv,dab}, K_{iv,dab}$	Gains of the proportional and integral parts of the voltage controller of the dual active bridge converter
$K_{p,sec}, K_{i,sec}$	Proportional and integral gains of the secondary controller
L_{ext}	External inductance referred to the primary side of the HF transformer
L_f	Inductance of the LC output filter
L_t	Leakage inductance referred to the output side of the transformer
$L_{t,max}$	Maximum value of the leakage inductance referred to the secondary side of the transformer
L'_t	Total inductance of the dual active bridge converter
$L'_{t,max}$	Maximum total inductance referred to the primary side of the dual active bridge converter
L_σ	Total leakage inductance of the HF transformer referred to the primary side
$L_{1\sigma}, L_{2\sigma}$	Leakage inductances in the input and output sides of the transformer, respectively
L_1, L_2, L_3	Tie-line inductances of nanogrids
m_0, m_1	Coefficients for modification of the participation factor k_2
N	Turn ratio from the primary side to the secondary side of the HF transformer
N_1	Number of turns of the primary side of the HF transformer
$N_{1,min}$	Minimum number of turns of the primary side of the HF transformer
N_2	Number of turns of the secondary side of the HF transformer
N_{ext}	Number of turns of the additional inductor
N_{ind}	Number of turns of the inductor of the buck converter
N_p	Number of parallel PV cells
N_s	Number of series PV cells
n_0, n_1	Coefficients for modification of the participation factor k_3

P	Power
P_{\max}	Maximum power of the DAB converter
P_C	Power to the external DC bus capacitor
P_L	Delivered power to other nanogrids
P_S	Output power of the interconnected converter of a nanogrid
q	Electron charge ($1.602 \times 10^{-19}\text{C}$)
R	Turbine radius
R_{int}	Internal resistance of the battery
R_p	Equivalent parallel resistance of PV cells
R_s	Equivalent series resistance of PV cells
R_f	Resistance of the LC output filter
R_L	Parasitic resistance of the inductor
R_M	Measuring resistance of the current and voltage transducers
R_t	Equivalent resistance of the HF transformer
R'_t	Total resistance of the dual active bridge converter @50kHz
R_o	Load resistance
R_1, R_2, R_3	Tie-line resistances of the nanogrids
R_4, R_5, R_6	Resistances of the operational amplifier
\Re	Real part
s	Laplace variable
$s(t)$	Switching mode of the bidirectional buck converter
$s_1(t), s_2(t)$	Switching mode of the left H-bridge and right H-bridge of the dual active bridge converter, respectively
S_1, S_2	Switches of the bidirectional buck converter
$S_{11} \div S_{14}$	Switches of the left H-bridge of the dual active bridge converter
$S_{21} \div S_{24}$	Switches of the right H-bridge of the dual active bridge converter
SoC_h	High-threshold of the state of charge (SoC)
SoC_l	Low-threshold of the state of charge
$SoC(0)$	Initial SoC
T	Junction temperature of the $p - n$ junction
t_{on}	Time interval when switch S_1 is ON
t_{off}	Time interval when switch S_1 is OFF

T_s	Switching period
V	Voltage
V_{d1}, V_{d2}	Input and output voltages of the dual active bridge converter, respectively
v_{bus}	Internal DC bus voltage
$v_{bus,ref}$	Reference value of the internal DC bus voltage
v_{bus2}	External DC bus voltage
$V_{bus2,h}$	High-threshold of the external DC bus voltage
$V_{bus2,l}$	Low-threshold of the external DC bus voltage
$V_{bus2,ref}$	Rated value of the external DC bus voltage
v_{cf}	Filter voltage of the dual active bridge converter
v_i, V_i	Input voltage of the converter
v_o, V_o	Output voltage of the converter
V_b	Output voltage of the battery
V_{oc}	Open-circuit voltage of the battery
V_t	Thermal voltage of the PV device
V_{ADC}	Output measuring voltage from the current measurement
V_{min}, V_{max}	Minimum and maximum input voltages of the ADC of DSP
V_{offset}	Offset voltage for the current measurement
v_{ref}	Reference voltage of the voltage control loop
V_n	Voltage threshold of the converter
v_p, v_s	Square wave voltages at the primary and secondary terminals of the HF transformer
v	Wind velocity
x	State variable
$x(\tau)$	Periodic signal in one fundamental period
$\langle x \rangle_k$	Coefficient of the k^{th} harmonic
X	State variable vector
y	State variable
Y	Output variable vector
λ	Tip speed ratio for the wind turbine
β	Blade pitch angle of the wind turbine rotor
ρ	Air density (approximately 1.225 kg/m ³)
μ_0	Vacuum permeability
η	Charging/discharging efficiency

ω	Rotational speed of the turbine rotor
ω_s	Angular frequency
ϕ	Phase shift between the two bridges
ϕ_{\max}	Maximum value of the phase shift between the two bridges
Φ	Magnetic flux
Φ_{\max}	Maximum value of the magnetic flux
Δ	Small-signal variable
ΔI_f	Current ripple of the output filter
$\Delta I_{f,\max}$	Maximum current ripple of the output filter
ΔQ	Additional charge
ΔV_o	Peak-to-peak output voltage ripple
δ	Air gap of the ferrite core
δv	Voltage correction

Acronyms

AC	Alternative current
AWG	American Wire Gauge
CAN	Controller Area Network
CSC	Current source converter
DAB	Dual active bridge
DC	Direct current
DG	Distributed generation
DSP	Digital signal processing
EMI	Electromagnetic interference
ESS	Energy storage system
ETD	Economical Transformer Design
EV	Electrical vehicle
FFT	Fast-Fourier Transform
HF	High frequency
IEA	International Energy Agency
IED	Intelligent electronic device
IGBT	Insulated-gate bipolar transistor
LED	Light-emitting diode
MOSFET	Metal–oxide–semiconductor field-effect transistor
MPP	Maximum power point

MPPT	Maximum power point tracking
NG ₁	The first nanogrid
NG ₂	The second nanogrid
NG ₃	The third nanogrid
OES	Open Energy System
PCB	Printed circuit board
PI	Proportional-Integral
PV	Photovoltaic
PWM	Pulse-width modulation
RES	Renewable energy source
RMS	Root mean square
SELV	Safety extra-low voltage
SISO	Single Input Single Output
SoC	State of charge
VSC	Voltage source converter
VPP	Virtual power plant

1 Introduction

1.1 Motivation

Electrical energy is a critical factor for solving many issues, including poverty, lack of education and unsustainable environment [1]. However, supplying electricity to off-grid areas is still limited due to economic issues, accessibility, lack of resources or a scattered population [2]–[4]. According to the latest survey conducted by the International Energy Agency (IEA), around 1.2 billion people living in rural areas of developing countries still do not have access to electricity [5]. For example, in a recent study carried out in six states of India by the Council for Energy, Environment and Water, around 50% of the households have no electricity even though a grid connection is available [6]. Expansion of the utility grid is one option for providing electricity to rural areas [1]. However, it is not a quickly realizable solution in developing countries as expansion of the utility grid demands a very high cost of investment [7], [8]. For this reason, off-grid is considered as a promising solution for providing electricity in such rural areas.

In the past, electricity in off-grid areas was often generated by using generators equipped with combustion engines. Yet, the fossil fuel consumed by the engine is expensive because of the high cost for transportation to remote areas, resulting in a high price of electricity. In addition, engines are unfriendly to the environment as they emit carbon dioxide during operation. An alternative is to use renewable energy sources (RESs) locally, such as solar or wind energy [9], [10]. This solution provides a clean, reliable and renewable electricity. Compared to fossil fuels, RESs have advantages in transmission, transportation, grid extension and environmental protection. For instance, a solar or wind farm can be located close to the consumers, resulting in a shorter transmission distance [11]. However, power generated by RESs is intermittent due to changes in the weather conditions, leading to a mismatch between power generation and consumption [11], [12]. One solution for this problem is to combine several RESs with storages to form a microgrid [13]–[15]. The concept of the microgrid was proposed based on the idea of integrating a number of microsources and loads into one system, which could be explained as a single prosumer according to power system perspective [16].

The concept of nanogrids was introduced in [9], [11], [17] to indicate simple and small scale microgrids. By its definition, a nanogrid is a power distribution system that is suitable for a single node, such as a household or a small building. It can be easily connected to or disconnected from other power entities through a gateway.

In remote and rural areas, where the main electricity grid is not reliable or does not even exist, micro/nanogrids, especially low-cost systems, are the first choice for providing energy. For example, in Africa and India, microgrids were installed for the purpose of rural electrification and economic development [18]. Normally, nanogrids are connected to the utility grid to avoid power outage and increase the operational efficiency [19], [20]. Otherwise, the nanogrids may suffer from an imbalance between the generated and consumed electrical power.

Based on the aforementioned motivation, this research work aims to develop a stable isolated direct current (DC) nanogrid to supply regions that are inaccessible to the utility grid. The application of the proposed DC nanogrid system is intended for geographical islands or rural electrification. The islanded DC nanogrid proposed for these regions are able to provide reliable, flexible and sustainable solutions to the off-grid systems.

1.2 State of the art

1.2.1 Architecture of DC micro/nanogrids

Hardware architectures of DC micro/nanogrids have been proposed based on primary criteria of control flexibility, robustness and reliability [16]. Those criteria are often incompatible with each other. Therefore, tradeoffs have to be considered to choose the most suitable configuration for a given application. From architectural point of view, topologies of micro/nanogrids can be classified into two types, including a radial configuration and a ring configuration [21]. Each of these configurations owns both advantages and disadvantages.

Radial topology is commonly used for DC microgrids, where all sources and loads are connected to a single DC bus. In this topology, energy storage system (ESS) can be directly connected to the common DC bus or through a controllable DC/DC converter. Each architecture has its own benefits and drawbacks depending on the applications and their requirements. Authors in [22] introduces a hybrid system, including a wind generation module, a solar module, a battery bank and an alternating current (AC) load, where the battery bank is directly connected to the common DC bus to achieve high reliability of the system. This topology offers some advantages as it enables simple and low-cost designs as well as low power losses due to the absence of the power electronic converter between the battery and the common DC bus. Although this architecture is robust and reliable, it has some limitations regarding control flexibility as the battery cannot participate in regulating the common DC bus voltage. Besides, the charging

control strategy cannot be applied for this approach, leading to fast charge/discharge action and lifetime reduction of the battery.

To increase the efficient use of the battery, a regulated DC/DC converter is recommended to be used as an interface between the battery and the common DC bus [19], [23], [24]. This approach allows the implementation of an optimal charge/discharge operational mode. Moreover, the use of interface converter can provide a flexible control as it allows the regulation of the common DC bus. In addition, the topology equipped with multiple battery banks are employed to improve the reliability of the system [25].

The same architecture can be extended to multiple DC microgrid systems in order to obtain higher reliability and availability [26], [27]. In such systems, the DC bus of each microgrid might be directly interconnected to form a cluster of the microgrids. In this way, each microgrid is able to absorb power from or inject power to its neighboring microgrids.

The radial topology-based DC microgrid systems have some benefits such as simplicity and ability to share the power between multiple buses. Nevertheless, this architecture is not flexible during fault conditions. For instance, all nodes that are connected to a single bus system could be affected by a single fault [21].

In order to overcome the previous drawbacks of the radial topology, a ring configuration was introduced as an alternative [28]. In this topology, each node and link are connected with others by the use of a ring bus. Intelligent electronic devices (IEDs) are used to control nodes and links with their neighbors. This configuration enhances reliability and redundancy. For example, when a fault occurs in any node, the IED will detect and isolate the faulty node from the system. Then the IED will provide the alternative path to supply the customers since the load connected to the common DC bus can be fed in both directions.

1.2.2 Control of DC micro/nanogrids

The goal of micro/nanogrid control is to optimize power generation and consumption to make the system more efficient. In DC micro/nanogrids, two main issues regarding the control are the voltage regulation and current sharing. In order to attain these objectives, a suitable control architecture is required.

Many researches have been carried out on the control and energy management of a micro/nanogrid. One practical approach for small-sized microgrids is to use a centralized control [29]–[31]. According to the centralized control topology, a central controller collects

and processes all system related information. A high observability and controllability of the whole system can be realized in the centralized method, however, it has some drawbacks that are linked with a single point of failure and the reduced flexibility and expandability [32].

A decentralized control architecture is another well-known approach. This method is commonly realized by the droop control for both AC and DC grids for current sharing [15], [33]–[35]. The droop control-based approach utilizes only the local measurements without the need for any extra communication links that makes the system simple and reliable. Even though the classical droop control has no requirement for the communication network and provides plug-and-play functionality, it has a side effect as the droop control introduces a (small) voltage excursion in the DC grid along with an inefficient current-sharing performance [36]. For these reasons, many studies have been conducted to enhance the performance of the classical droop control at the primary level [25], [37]–[39].

Another decentralized method that can be used for coordinated control is power line signaling [40]. In this approach, the power line signal is utilized as a main communication carrier, and in order to communicate with others, each power unit injects a sinusoidal signal with specific-frequency pattern into the common DC bus. However, distortion of the common DC bus voltage is observed due to the presence of the sinusoidal signals with different frequencies. Besides, this approach is used only for changing the operation modes of the system and therefore it is not appropriate for power sharing.

DC bus signaling is another alternative decentralized approach. The DC bus is used as a communication carrier between the sources in the DC bus signaling method, as presented in [19], [23], [41]. The control strategy allows communication among various sources/storages through local information without requiring any other component, except the interface converters. For optimization of the microgrid operation, a set of various modes are defined as a function of the DC bus voltage levels. According to the value of the DC bus voltage within the corresponding range, the particular operation mode would be selected. Nonetheless, this method requires a pre-definition of different operation modes based on the DC bus voltage levels. If the voltage difference between the adjacent levels is too large, the fluctuation of the DC bus voltage cannot be guaranteed within an acceptable range. By contrast, if this value is too small, it is sensitive to realize the exact operating mode, making the system unreliable.

On the other hand, the authors in [42] proposed a DC bus signaling-based method to obtain autonomous coordinated performance of the system, in which the change in the operational modes is unnecessary. In this scenario, the ESS is employed as a master unit to regulate the DC

bus voltage in correspondence to its state of charge (SoC) while the RESs function as slave units to adjust the generated power according to the DC bus voltage signal. This method ensures current sharing and the control of the DC bus voltage without the selection of the operation modes. However, in case of disconnection or failure of the ESS, the system will not be able to operate.

Another control architecture is a distributed control that is based on both local measurement and neighboring communication [43]. In this topology, there is no central controller and therefore less computational burden. Single point of failure can be avoided when all local controllers communicate with each other through a dedicated digital communication link, improving the reliability of the system. Recently, the distributed control architecture has been extensively investigated for DC microgrid applications [44]–[47]. Authors in [45] developed distributed controllers that can exchange the information of the supplying current with other distributed controllers via CAN communication to determine the total average current supplied by the sources. As a result, the voltage mismatch between converters can be compensated. However, the distributed control also requires a proper communication network like the centralized control.

All of the abovementioned approaches emphasize on ensuring a reliable and robust operation of a single micro/nanogrid. An alternative method is to integrate multiple micro/nanogrids in order to share the electrical power and improve reliability and stability of the whole system [17], [27]. A hierarchical control structure presented in [27] allows a coordinated operation inside a local microgrid to be controlled and power to be shared among multiple microgrids, which can form a microgrid cluster¹. In this topology, the power flow is regulated by changing the voltage levels inside each microgrid, which is considered as a node. Multiple nodes are connected to the same common DC bus and low-bandwidth communication is employed to exchange information among nodes. However, the integration of multiple microgrids sometimes tends to destabilize the system, since microgrids are connected to the same common DC bus.

As presented in [17], the authors propose a nanogrid network based on the concept of Open Energy System (OES). The system allows exchange of power within a local community by using a bidirectional DC/DC converter and a communication line. In each nanogrid, a distributed

¹ In this dissertation the term “microgrid” will be used differently in order to describe a cluster of multiple nanogrids.

network controller based on digital communication is also employed that allows the nanogrid to communicate and exchange power with others. Nevertheless, this approach still relies on the digital communication infrastructure.

Despite lots of effort spent in the field of micro/nanogrids, control of these systems and control of power flow among multiple micro/nanogrids are still an open topic for researchers.

1.2.3 Modeling and stability analysis of DC micro/nanogrids

Modelling of micro/nanogrids is a key step in order to achieve a suitable control. In addition, stability is one of the main concerns of power systems. Consideration of the dynamics and the use of suitable modeling methodologies are important issues for control synthesis and stability analysis of the micro/nanogrids. Depending on the configuration, type and components of the micro/nanogrids, their dynamics might change. Different modeling methodologies can be employed for different applications. A number of approaches for the modeling and control for AC micro/nanogrids were listed in [48], [49]. Although interest in DC nanogrids has been increasing significantly, there are only little research activities pertaining to the modeling of DC micro/nanogrid systems.

The common method for modeling of switching power converters in DC micro/nanogrids is averaging. State-space averaging is the most popular method, which has been applied in many applications since it introduces some advantages, such as simplicity and good performance [50]–[53]. However, there are some constraints that can limit this method. The first constraint is that the switching frequency is required to be much higher than the frequencies of interest. The second one is that the ripple of the state variables must be insignificant [54]. Because of these reasons, this method is not suitable for modeling some converters such as resonant converters and dual active bridge converters. For example, the dual active bridge converters do not satisfy the second condition as transformer current has to be purely AC in order to avoid saturation [55]. In order to cope with this problem, a generalized state-space method is employed [55]–[57]. In this method, more terms in the Fourier series of the state variables are taken into account rather than just the DC component. As a result, the accuracy of the mathematical model is improved. Yet, the generalized state-space method has a disadvantage associated with the high demand of computation due to the complexity of the model. A tradeoff between the accuracy and complexity has to be considered when selecting the number of state-space variables.

Depending on the averaging method, different techniques for modeling and stability analysis, including small and large signal, have been proposed [54]. In some cases, the large-signal averaged models can be used to analyze the stability of the nonlinear system [58]. However, this technique requires a nonlinear tool for studying the system stability, making it less attractive.

On the other hand, small-signal modeling method is also a promising solution for modeling and stability analysis of the DC micro/nanogrids [56], [59]–[61]. By linearizing the system around a certain operating point, a linear model can be obtained. From the linearized model, it is easy to design the controller and analyze the stability of the system. For example, for the case of using a conventional Proportional-Integral (PI) controller, the selection of the controller parameters and the system analysis can be carried out by means of the well-known Bode diagram, Nyquist diagram or Routh-Hurwitz criterion [62].

Small-signal modeling and stability issues of DC microgrid clusters was also presented in [63]. This work develops a small-signal model for DC microgrids in order to design and synthesize control loops, to deal with stability analysis and to study the impact of different parameters of the systems as well as loads. The outcomes of [63] showed that the instability of the system was caused due to the increase in negative resistance of constant power load and line inductance.

Also, small-signal stability analysis of low voltage DC microgrids was introduced in [60]. Three main components of a DC microgrid, including sources, loads and distribution cables are considered and modeled by differential equations. The effects of variation in inductances and resistances of the cable on the system stability were studied. It indicated that any increase in the cable resistance would lead to the increase in the transmission losses. Therefore, a tradeoff between the system stability and transmission losses should be taken into consideration. Based on the same approach, the authors in [64] analyze the system stability under different compensation schemes.

1.3 Objectives of the work

This research work deals with modeling, control and stability analysis of DC nanogrid systems, which is operated in a standalone mode. The main objective is to develop a self-sustained and flexible, decentralized control strategy based on hierarchical control for islanded DC nanogrids without the need for an extra communication network. The flexible DC nanogrid has to be able

to inject/absorb energy to/from other nanogrids, control the power flow and manage the connected energy storage. The architecture of the DC nanogrid is based on the integration of RESs and storage devices. The nanogrid is established to obtain some characteristics, including modularity, self-sustained capability, scalability, simplicity and ease of commission so that it does not require any manual configuration in terms of installation and operation. The proposed control strategy manages the power of the photovoltaic (PV) panel, of the interconnections and of the battery in such a way that renewable energy can be harvested as much as possible. The exchange of power inside a nanogrid and among multiple nanogrids is also regulated based on the SoC of the battery and the variation of the external DC bus voltage in order to prevent the battery from overcharge or deep discharge situations and to avoid the disruption of the external DC bus.

The second objective of the work addresses the modeling of power electronic converters employed in the proposed DC nanogrid. There are two types of power electronic converters being used in the nanogrid: a bidirectional buck converter and a dual active bridge converter. Based on the state-space averaging method, a small-signal model is obtained for the bidirectional buck converter. On the other hand, a full-order small-signal model of the dual active bridge converter is developed based on a generalized state-space averaging method. A cascaded control structure is utilized for both output current and output voltage control loops in order to provide a flexible power exchange inside each nanogrid as well as among multiple nanogrids.

The last objective of the work concerns the modeling and stability analysis of the DC nanogrid. A model of the entire system is derived from the mathematical models of three single converters. Based on this approach, a small-signal transfer function of the DC nanogrid integrated with two buck converters and one dual active bridge converter can be synthesized. The obtained transfer function is eventually used to design the secondary controller and to analyze the stability of the entire system.

1.4 Publications

This thesis is synthesized and developed from some previous publications, which were published in IEEE conferences and IEEE journal. In these publications, the author of this thesis is the first author. The author has proposed approaches for modeling and control for the DC nanogrid, implemented the proposed control strategy by simulations as well as experiments and was mainly responsible for writing this complete thesis. Parts of Chapter 1 are based on [65]–

[67]. Chapter 2 slightly relies on [65], [67]. The main content of Chapter 3 is a combination of both [56] and [66]. Chapter 4 is mainly based on [65]–[67].

1.5 Thesis outline

The structure of this thesis is organized as follows: The motivation and the objectives of the work are described in Chapter 1. In Chapter 2, an overview of micro/nanogrids regarding components, technologies and control topologies is introduced. Afterwards, the appropriate configuration of a nanogrid is chosen for this research work. Chapter 3 is dedicated to the modeling and control of power electronic converters. First, modeling and control of a bidirectional buck converter based on state-space averaging method is presented. Second, the same procedure of modeling and control of a dual active bridge converter is proposed but it is based on generalized stage-space averaging technique. Chapter 4 focuses on the control strategy for self-sustained and flexible DC nanogrids. Modeling, control and stability analysis for an entire system is also mentioned. The effectiveness of the proposed control strategy for a single DC nanogrid is verified by both simulation and experimental results. Finally, simulation results are presented to show the feasibility of interconnection of multiple DC nanogrids.

2 Overview of micro/nanogrids: components, technologies and control topologies

2.1 Introduction

A microgrid is a flexible and independent system which might be operated in either grid-connected [68]–[70] or island modes [42], [71], [72]. The operation modes are defined by a control system according to the objectives of the system. In the grid-connected mode, the microgrids are able to exchange power with the utility, while in the autonomous mode, the microgrids are operated independently without an interconnection with the main grid. However, some microgrids that are capable of operating in both grid-connected and island modes, have been deployed to increase the flexibility of the microgrid systems [73]–[75].

In terms of classification, microgrids can be divided into two main types: AC and DC microgrids [76]. To date, many researches have been carried out and focused on AC microgrids [77]–[81]. Recently, however, the interest in the DC microgrids has been significantly increased as they could offer several benefits regarding efficiency, simplicity, reliability and cost reduction [82], [83]. For instance, in some DC microgrids, DC/AC and AC/DC converters are unnecessary as most of the renewable energy generators are DC sources, such as solar panels or fuel cells [16], [45], [83], [84]. As a result, reduction of power loss can be achieved due to reduction of the power conversion. The use of such DC microgrids is feasible and reliable as their control and management are much simpler than those of the AC microgrids [32]. Besides, the advanced development of new DC power technologies, ongoing standards and initiatives make it possible to develop future DC applications for homes, offices, buildings and other electrical power systems [85].

Microgrids and nanogrids are different in scale. A nanogrid can be seen as a small and technologically simple microgrid, and it is confined to a single home or building [11], [17], while a microgrid can be formed by connecting multiple nanogrids, in case electrical power needs to be shared among multiple houses or buildings. Nanogrids can offer a power structure with a lower cost compared to microgrids and customers can have a flexibility to choose a small or a large system. According to the grid hierarchy, nanogrids and microgrids are the electrical grids corresponding to households/buildings and small communities, respectively. They are able to connect to the utility grid or to other micro/nanogrids.

For the sake of clarity of the nanogrid concept, a definition of nanogrids was introduced in [11]: “A nanogrid is a power distribution system for a single house/small building, with the capability

of connecting or disconnecting from other power entities via a gateway. It consists of local power production powering local loads, with the option of utilizing energy storage and/or a control system”.

In this chapter, a brief overview of nanogrids is introduced. Then the basic issues of components, technologies and control topologies of micro/nanogrids are addressed. The comparison between AC and DC micro/nanogrids is also highlighted. Finally, a suitable topology of a nanogrid selected for this research is presented.

2.2 Components of a nanogrid

In the conventional AC systems, such as hydro power or thermal power stations, power is generated by synchronous generators. The generators are normally operated at a constant speed to generate a 50 or 60 Hz current while the generated reactive and active powers are controlled via the flux-producing current and the angle between rotor and flux linkage, respectively. Nevertheless, in a nanogrid system, the output power of the RESs is uncontrollable due to the intermittent nature of these sources [86]. In this case, the generated power is only dependent on the availability of the primary sources, irrespective of the control of the interfaced converters. Typical examples of these non-dispatchable sources are the solar and wind, which produce an intermittent output power. In order to cope with the fluctuation problem of power, an ESS is required to ensure the generation adequacy of the system. Thus, the nanogrid system is an integration of different distributed generation (DG) sources (e.g., solar and wind), ESSs and a large variety of loads [76], [87], [88]. This approach allows the system to exploit and harvest such energy sources locally. The typical RESs are solar and wind, which will be introduced in this section.

2.2.1 Photovoltaic panel

Photovoltaic (PV) power is one of the most promising renewable energy sources, because such systems are reliable, require low maintenance costs and do not produce pollution, emission or noise. However, solar power systems have high initial costs for material and installation.

PV cells are devices which can be used to convert solar energy into electrical energy by using semiconducting materials based on the photovoltaic effect. A single PV cell is rarely used in an application as it only produces a voltage of around 0.5 V. Therefore, a PV module consisting of a number of PV cells is needed in order to generate higher voltages and currents. Multiple cells

can be connected in series to increase the voltage or in parallel to increase the current [89]. For even higher voltages, a PV panel composed of several PV modules can be employed. Multiple PV panels can also be connected together to form a PV array with a very high range of generated voltage.

A simple equivalent circuit of an ideal PV cell is composed of an ideal current source connected in parallel with a real diode as shown in Figure 2.1.

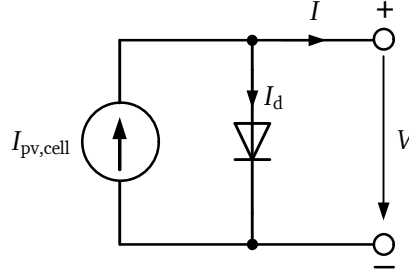


Figure 2.1: The simple equivalent circuit of an ideal PV cell

From Figure 2.1, the output current of the ideal PV cell is given by [90]

$$I = I_{pv,cell} - I_d \quad (2.1)$$

where $I_{pv,cell}$ is the magnitude of the ideal current source generated by the incident light, which is proportional to the solar radiation, I_d is the diode current which is defined by

$$I_d = I_{0,cell} \left[\exp \left(\frac{qV}{akT} \right) - 1 \right] \quad (2.2)$$

where $I_{0,cell}$ is the reverse saturation current (A), V is the output voltage (V), q is the electron charge (1.602×10^{-19} C), k is the Boltzmann constant (1.381×10^{-23} J/K), a is the diode ideality constant and T is the junction temperature of the $p - n$ junction (K).

Substituting (2.2) into (2.1), the mathematical description of the I - V characteristics of the ideal PV cell is as follows

$$I = I_{pv,cell} - I_{0,cell} \left[\exp \left(\frac{qV}{akT} \right) - 1 \right] \quad (2.3)$$

However, a practical PV device consists of a number of PV cells connected in series or in parallel to obtain the required voltage. The equivalent circuit including both series and parallel resistances is depicted in Figure 2.2. The mathematical equation describing the I - V characteristics of the practical PV device is as follows [90]:

$$I = I_{pv} - I_0 \left[\exp \left(\frac{V + R_s I}{a V_t} \right) - 1 \right] - \frac{V + R_s I}{R_p} \quad (2.4)$$

where $I_{pv} = I_{pv,cell} \cdot N_p$ and $I_0 = I_{0,cell} \cdot N_p$ are the PV current and saturation current of the PV device, respectively, N_p is the number of parallel PV cells, R_s and R_p are the equivalent series and parallel resistances, respectively, $V_t = N_s kT/q$ is the thermal voltage of the PV device with N_s being the number of the PV cells wired in series.

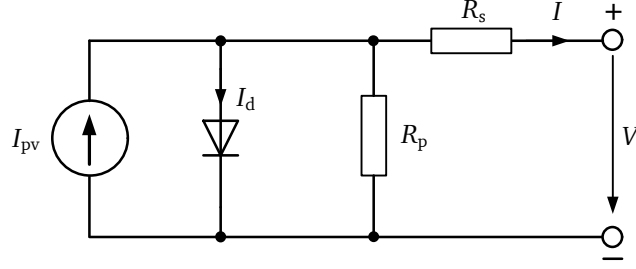


Figure 2.2: The equivalent circuit of a practical PV device

From equation (2.4), the I - V curve can be highlighted as shown in Figure 2.3 where three remarkable points are taken into account: short circuit $(0, I_{sc})$, MPP (V_{mpp}, I_{mpp}) and open circuit $(V_{oc}, 0)$. The practical PV device behaves either as a current source or as a voltage source depending on the operating point. In the current source region, the influence of the parallel resistance R_p is dominant while the series resistance R_s takes effects in the voltage source region [90].

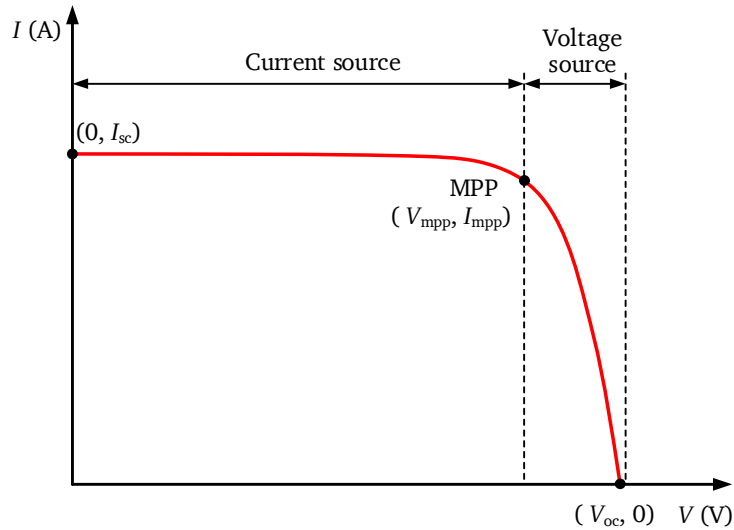


Figure 2.3: The I - V curve of the practical PV device

The I - V characteristics of the PV module depends on the internal parameters (e.g. R_s, R_p) and on the external impacts, such as solar radiation and temperature of PV cells [90]. As a result,

the maximum power point (MPP) of a PV panel changes accordingly to the solar radiation and the temperature of PV cell as well. The P - V characteristics associated with the radiations of 600 W/m^2 and 1000 W/m^2 are given in Figure 2.4. It is observed that an increase in solar radiation leads to a significantly increase in the maximum power. Similarly, the P - V curve for the changes in the temperature of 25°C and 50°C is shown in Figure 2.5. It can be seen that the maximum power decreases considerably as cell temperature increases [89].

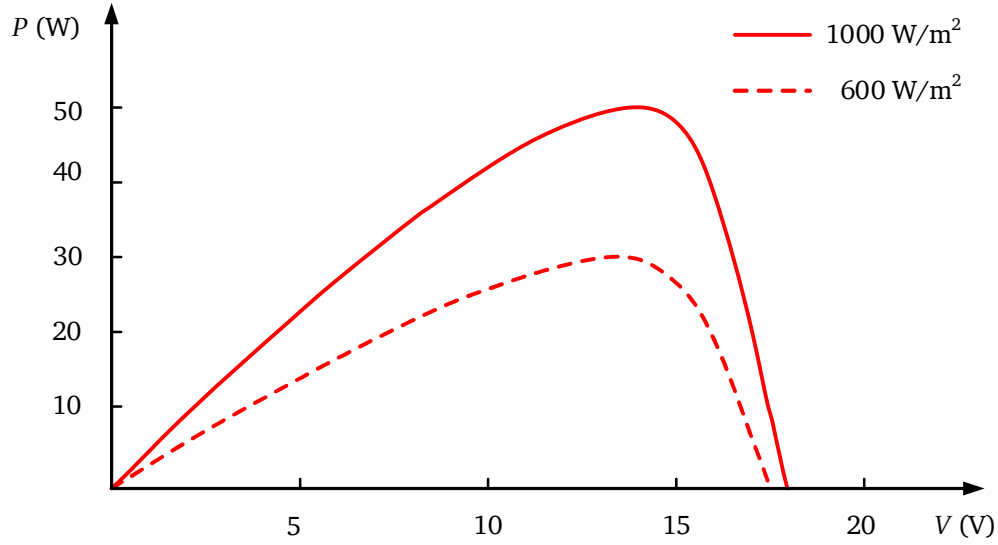


Figure 2.4: Typical P - V Characteristics of a PV module for changes in solar radiation

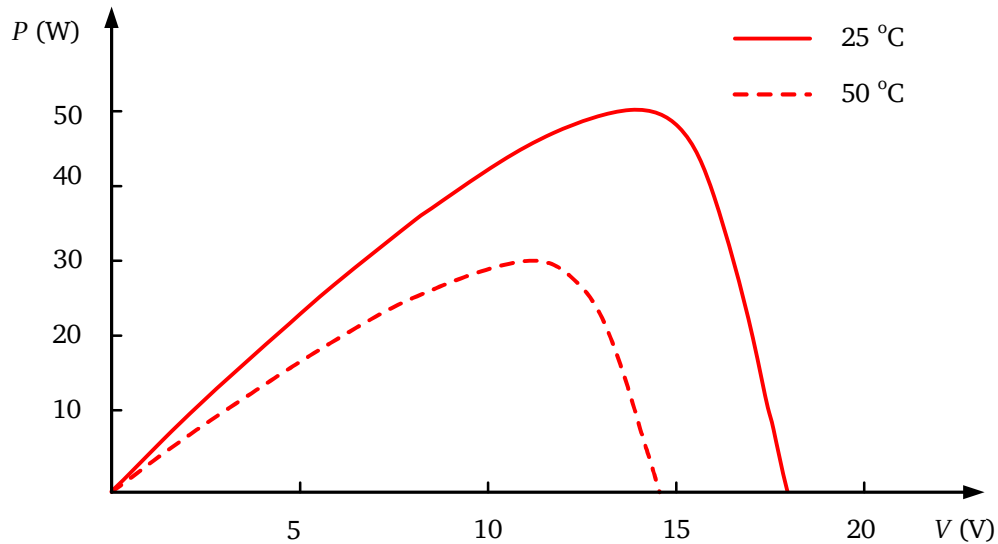


Figure 2.5: Typical P - V Characteristics of a PV module for changes in PV cell temperature.

2.2.2 Wind turbine

Similarly to solar power, wind power is one of the most widely used renewable source of energy. Wind power offers many advantages, including high efficiency, low maintenance and low operational costs. It is also a clean, sustainable and renewable energy source [91]. Wind power based technologies and wind turbines can be installed in both on-shore and off-shore [92] and they can produce high power for small land footprints. Nevertheless, wind power systems have a number of drawbacks such as high initial costs, technology immaturity, noise and visual pollution.

Wind turbine systems are used to convert the air kinetic energy into electrical energy. The air kinetic energy is converted into rotational mechanical energy due to the rotation of the turbine rotor blades. The rotor is connected to the main shaft to spin a generator, which generates electrical energy. The output from the wind turbine depends on the wind speed, which varies over time. The aerodynamic power output from the wind turbine is modeled as follows [93]

$$P = 0.5 \cdot \rho \cdot A \cdot C_p(\lambda, \beta) \cdot v^3 \quad (2.5)$$

where ρ is the air density (approximately 1.225 kg/m^3), A is the area swept by the wind turbine rotor (m^2), v is the wind velocity (m/s), C_p is the power coefficient of the turbine, β is the blade pitch angle of the wind turbine rotor ($^\circ$), λ is the tip speed ratio which is given by

$$\lambda = \frac{\omega \cdot R}{v} \quad (2.6)$$

where ω is the rotational speed of the turbine rotor (rad/s), R is the turbine radius (m). Figure 2.6 shows the relationship between the power coefficient (C_p) and the tip speed ratio (λ) of a wind turbine with the blade pitch angle (β) being equal to zero [91]. It can be observed from Figure 2.6 that the maximum power coefficient C_p can be obtained by adjusting the tip speed ratio. In theory, the maximum value of power coefficient is defined by the Betz's law, by which the maximum theoretical efficiency of a rotor is 59.3% [94]. In reality, however, wind turbine rotors just obtain the maximum values of C_p in the range of 25 – 45% [93]. In order to attain the maximum value of C_p , the wind turbine needs to be operated at a variable speed to maintain the optimal tip speed ratio when the wind speed changes. For instance, if the wind speed increases, the rotational speed of the wind turbine must be increased as well to retain the optimal tip speed ratio.

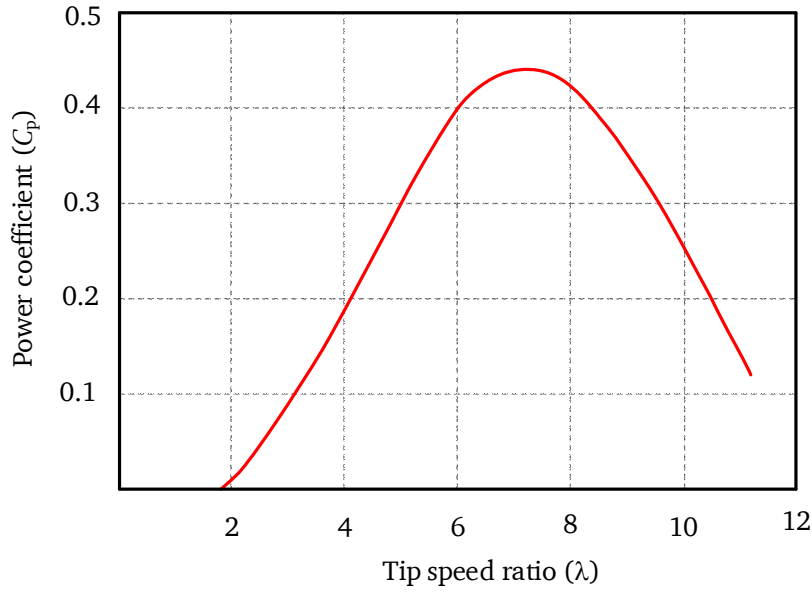


Figure 2.6: Typical power coefficient characteristic of a wind turbine

2.2.3 Energy storage

Micro/nanogrid systems, based on the integration of RESs, generate power in an intermittent characteristic. The ESSs is therefore necessary to be included to smooth out the intermittent phenomenon and to balance supply and demand. In addition, the use of the ESSs can enhance the utilization of the RESs [95]. For example, the ESSs can charge any excess power or discharge stored power under variation of solar radiation or wind speed. The ESSs is indispensable in standalone systems, which are not connected to the main grid, as they can provide a continuous operation of critical loads.

Various forms of energy storage technology are introduced in [96]. The commonly used technologies in micro/nanogrid systems include supercapacitors, flywheel and batteries. The selection of the ESS is according to practical applications of the micro/nanogrids. For instance, a battery is the most suitable for micro/nanogrids due to its capacity and residential location [11]. The lead-acid battery is a typical example of an affordable battery energy storage.

Various models for lead-acid battery have been proposed [97], [98]. In this research, a simple model is presented for simulation purposes. The equivalent circuit model as depicted in Figure 2.7 consists of an ideal voltage source connected in series with an internal resistance [99]. This model is assumed to have the same charging and discharging characteristics. As shown in Figure 2.7, V_b and V_{oc} indicate the output voltage and the open-circuit voltage of the battery, respectively, I_b is the current of the battery, R_{int} is the internal resistance. R_{int} is supposed to

be constant, but in fact, it is slightly changed when the load is connected to the battery or when temperature changes. Therefore, the model is only suitable for applications where the energy of the battery is considered as infinite and where the transient behavior is ignored [98]. The output voltage of the battery can be calculated as follows

$$V_b = V_{oc} - R_{int} \cdot I_b \quad (2.7)$$

During charging time, the voltage (V_b) applied to the terminals of the battery is higher than the open-circuit voltage (V_{oc}) as the sign of the battery current (I_b) is negative. On the other hand, when the battery is discharging, the value of the output voltage is less than that of the open-circuit voltage.

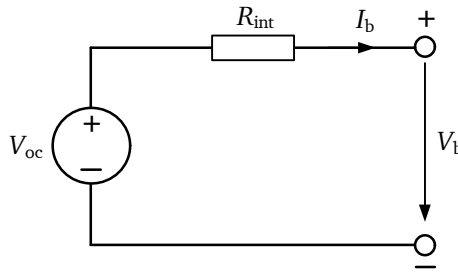


Figure 2.7: The simple equivalent circuit model of a battery

2.3 The role of power electronics in renewable energy systems

Power electronic converters play an important role in renewable energy systems as the control and conversion of electrical energy is a key issue. They are considered as a flexible and controllable power link of the systems which are mandatorily used as an interface between the electrical generation sources and the loads or between the generators/loads and the grid. These converters are commonly used to control the power flow and convert it into suitable form, which can be AC or DC. The converter consists of semiconductor switches such as IGBTs, MOSFETs and diodes, along with passive elements such as inductors, capacitors and resistors and current and voltage sources [100]. The power flow can be unidirectional or bidirectional based on topology and applications.

Overviews on the configurations and control strategies for power electronics in microgrids and in renewable energy systems are introduced in detail in [101] and [102], respectively, but these are out of the scope of this thesis. The applications of power electronic converters for both AC and DC systems are highlighted in the next section.

2.4 Types of nanogrid technology

A suitable type of the micro/nanogrids is mainly selected based on some aspects such as costs for investment, operation and maintenance [82], the use of power converters, the availability of energy sources and their integration [103]. Nanogrids can be identified according to the used voltage and current from which two types of nanogrids can be considered 1) AC and 2) DC [82]. The selection of those systems is still a controversial issue. Each has different advantages and disadvantages in terms of control, protection and power losses [88]. AC systems are thought to be dominant, mainly due to the limitation of technology issues at the time the grid was installed. On the other hand, DC systems were recognized as a natural and simple solution for electric power systems in the past; however, they were not commonly used due to difficulties in voltage level conversion because it was hard to transmit DC power with low voltage for long distance. This section presents both of these technologies, but only focusing on technical issues regarding configurations and architectures implemented in a nanogrid. These configurations are discussed to provide suitable selections for appropriate control strategies and potential applications of DGs in remote and rural areas.

2.4.1 AC micro/nanogrids

A typical configuration of AC nanogrids is illustrated in Figure 2.8 where all DGs and loads are connected to the common AC bus through power electronic interfaces. DC sources such as PV panels and ESSs need a DC/DC conversion stage before being converted to AC by using DC/AC inverters in order to connect to the common AC bus. On the other hand, AC/DC and DC/AC converters are employed to interface the common AC bus with AC sources such as wind turbines. Similarly, two power conversion stages are required to connect the common AC bus to both AC and DC loads as shown in Figure 2.8 [83]. A rectifier and an inverter are needed for supplying the AC loads, while a combination of a rectifier and a DC/DC converter is required to connect the common AC bus to the DC loads. The utility grid can be connected directly to the common AC bus or through a transformer according to the voltage level of the AC bus.

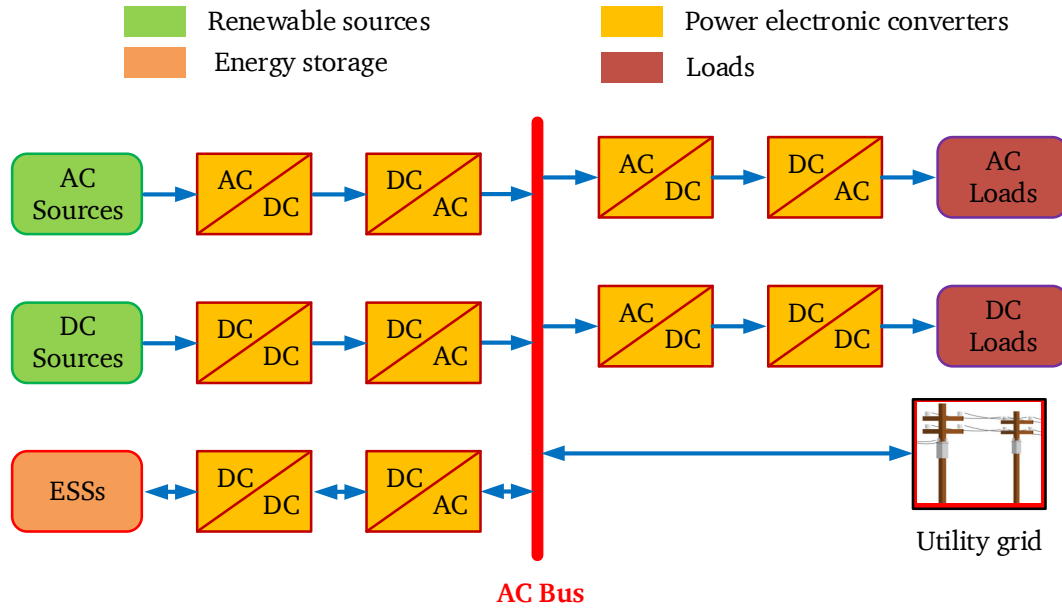


Figure 2.8: Typical configuration of an AC nanogrid

During normal operating conditions, the loads are supplied from the local DGs (e.g., photovoltaic panels, wind turbines and ESSs). If load demand power is higher than the power produced by DGs, power deficit can be compensated by importing from the utility grid. On the contrary, excess power can be exported to the main grid when power consumption is less than power generation. In most cases, the operation of the AC nanogrid system must be adapted with the voltage and frequency standards applied for the conventional distribution systems [84].

2.4.2 DC micro/nanogrids

Figure 2.9 depicts a typical configuration of the DC nanogrids where all DGs and loads are connected to the common DC bus. In the DC nanogrids, a rectifier is needed to connect AC sources to the common DC bus while an inverter is employed for supplying the AC loads [83]. For DC sources and DC loads, a DC/DC converter is equipped to interface with the common DC bus. Differently from AC nanogrids, a bidirectional DC/AC converter is required to connect the common DC bus to the main AC grid. Depending on requirements for converters and applications of the DC nanogrid topologies such as low inrush current, low switching stress, low weight and size, isolated or non-isolated converters might be used [104]. The operation of the DC nanogrids is similar to that of the AC counterparts while the import/export of power to/from the utility grid depends on the imbalance of power inside the DC nanogrids.

Both the AC and DC nanogrids can function either as a power source or as a load. When the power of the nanogrid is in surplus it can be used to feed the utility. Otherwise the nanogrid will absorb power from the utility when its power is insufficient for supplying the loads.

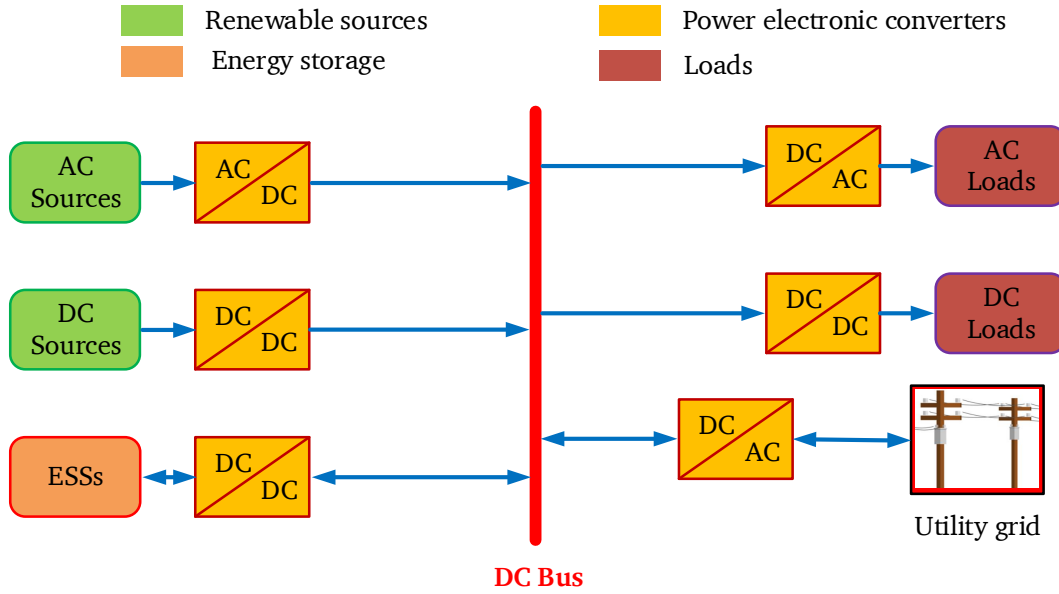


Figure 2.9: Typical configuration of a DC nanogrid

2.4.3 DC nanogrids versus AC nanogrids

There are a number of considerations when comparing the topology of AC and DC nanogrids. The selection of a suitable nanogrid is dependent on its applications. For example, if the nanogrid is in need of being connected to AC-based main grid, then AC nanogrids is the suitable option as it is easier to integrate AC nanogrids with conventional utility grid than the DC ones. By contrast, DC nanogrids are a suitable candidate when they are developed and applied to isolated areas. The DC nanogrids are also cost-effective pertaining installation for offices and data centers where a lot of DC loads are equipped. AC microgrids, on the other hand, are applicable to factories and plants with a variety of AC loads [88]. This section focuses on highlighting the advantages and drawbacks of both DC and AC technologies with respect to integration of RESs, such as solar and wind power.

Based on the historical perspectives, AC nanogrids have been the standard selection for commercial and residential electrical systems as a large number of electrical devices have been manufactured to be suitable for AC systems. Besides, the AC networks have existed for more than one century along with the manufacture dedicated for the AC electrical equipment and

loads [84]. Because of this reason, currently most electrical devices in homes, buildings, companies, factories and retail stores are still AC electric appliances.

On the other hand, the DC nanogrids might offer several advantages in comparison with the AC nanogrids, such as higher efficiency, more natural interface with DGs, more suitable to modern electronic loads and no requirement for synchronization [16]. First, when the efficiency is taken into account as the main factor, the DC nanogrids are advantageous. It can be clearly seen from Figure 2.8 and Figure 2.9 that a number of power electronic converters are reduced for the DC nanogrid system. During each stage of the conversion, some power is lost. Therefore, the reduction of the power conversion stages results in the decrease in power losses.

Second, the DC systems provide an ease of integration of various DC DGs, storage systems and modern electronic loads. Most RESs including PV panels and fuel cells are DC sources. Even for AC renewable sources, such as wind turbines, the double conversion can be avoided by using only one AC/DC converter in order to connect to the DC bus. The similarity can also be seen for ESSs, such as batteries, flywheels and super capacitors as they store and deliver DC power. In addition, many electrical appliances, such as TV sets, chargers for mobiles, computers and light-emitting diode (LED) lights use DC. Furthermore, for AC loads, e.g., air conditioners, refrigerators, washing machines, AC/DC conversion stages are eliminated as only one DC/AC conversion is necessary to interface the DC bus with these loads [83]. Moreover, the use of electrical vehicles (EVs) where the batteries are equipped is the future trend as the number of EVs is predicted to be 30 million by 2025 and exceed 150 million in 2040 according to the survey conducted by IEA in 2016 [5]. Last but not least, there is no need for synchronization as well as there are no issues with reactive power flow in the DC systems. As a result, the systems can provide less complexity, simpler configuration, higher efficiency and higher reliability [76]. Hence, the DC systems introduce a high potential for future applications in homes, buildings, data centers and plug-in electrical vehicles.

However, there are several challenges for DC systems, including the lack of commercially available products, standards, codes and regulations. As aforementioned, most electrical devices, such as power converters, protection devices, connectors are currently manufactured for the AC systems, leading to fewer choices of the electrical equipment when installing any DC systems [83]. In addition, the appliances and devices that are compatible to DC sources are still limited.

Another challenge of the DC systems is the protection problem. For instance, an arc voltage appearing when breaking DC current cannot be extinguished naturally due to no zero-current

crossing. The standard current interruption technique is mainly based on the natural zero crossing of the AC current that is not the case in the DC systems [21]. Recently, protection devices and circuit breakers designed for DC systems are available but they are still more expensive than those installed in AC systems.

The comparison of AC and DC micro/nanogrids is summarized in Table 2.1.

Table 2.1: Comparison between AC and DC micro/nanogrids [84], [88]

Issues	AC micro/nanogrids	DC micro/nanogrids
Control	<ul style="list-style-type: none"> - Active and reactive power control - Voltage and frequency regulation 	<ul style="list-style-type: none"> - Active power control - Voltage regulation
Costs	<ul style="list-style-type: none"> - Higher investment costs - Higher operation costs 	<ul style="list-style-type: none"> - Lower investment costs - Lower operation costs
Transmission	<ul style="list-style-type: none"> - More conductors (three or four lines) leads to high resistance - Have reactance in the line - Have skin effect in AC current flow - Less efficiency due to high transmission losses - Need for compensation 	<ul style="list-style-type: none"> - Less conductors (two lines) leads to low resistance - No reactance in the line - No skin effect in DC current flow - High efficiency due to low transmission losses - No need for compensation
Power Analysis	<ul style="list-style-type: none"> - Require power analysis for reactive power - Require analysis for magnitude and phase of the voltage and current - Complicated analysis due to complex number 	<ul style="list-style-type: none"> - No power analysis for reactive power - Only analysis for magnitude of the voltage and current - Simple analysis due to only real number
Integration	<ul style="list-style-type: none"> - Require synchronization - Less natural with DC DGs, ESSs and modern electronic devices - More conversion stages are used 	<ul style="list-style-type: none"> - No synchronization - More natural with DC DGs, ESSs and modern electronic devices - Less conversion stages are used

Protection	- Short-circuit current interruption is easy due to natural zero current crossing	- Short-circuit current interruption is difficult due to no natural zero current crossing
------------	---	---

For regulation issues, there are no specific standards for regulating the operation of the DC systems at the moment. One problem in control of DC micro/nanogrids is that the integration of multiple DGs and ESSs might cause unexpected current circulation [36]. The current circulation leads to the bus voltage deviation and the instability of the systems. Therefore, the key control issue in a micro/nanogrid system is to coordinate all DGs and ESSs to ensure the current sharing and stability of the DC bus voltage. In other words, the objective of the control in DC micro/nanogrids is to maintain the power balance between generation and consumption of the system. In order to obtain these objectives, a suitable control topology of the system has to be developed. The next section will provide an overview of typical control approaches, including centralized, decentralized and distributed controls.

2.5 Control topologies of nanogrids

As already presented in Section 1.2.2, there are different control topologies proposed for DC nanogrids. In this section, a close look on the most commonly used topologies, including droop control, centralized control, decentralized control and distributed control, is presented. After the consideration of benefits and drawbacks of the control topologies, the most suitable one will be selected for the DC nanogrid.

2.5.1 Droop control

The droop control has been presented as a well-known approach for both AC and DC grids [33]. The droop control method is commonly used in order to obtain coordinated control among distributed units without the need for communication links [76]. The basic idea behind this method is adding a control loop with a droop coefficient so-called virtual resistance on top of the voltage controller of the converter, allowing current sharing among parallel converters. In DC systems, the DC bus voltage is measured at each converter and all converters participate to balance the power between generation and consumption of the system. In contrast to physical resistance, the virtual resistance has no power losses. Moreover, this approach offers a plug-and-play capability that is suitable for modular structures [101]. Also, the droop control

provides active damping to the system since the virtual resistance is connected in series with the output filter of the converter [105]. In addition, the absence of digital communication links makes this method significantly enhanced in flexibility and reliability [106]. The operating principle of the droop control is to linearly decrease the reference voltage of the voltage control loop as the output power increases. By this way, the output power of the converter is inversely proportional to the droop coefficient.

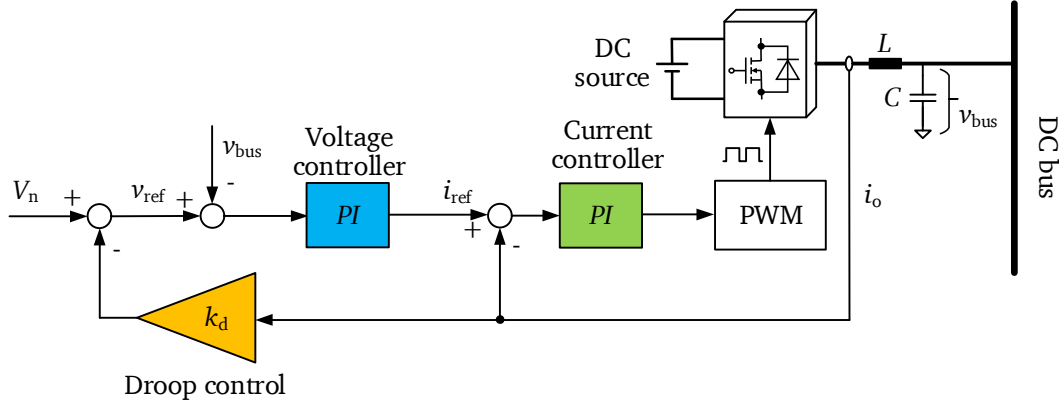


Figure 2.10: A typical control structure with droop control for DC nanogrids

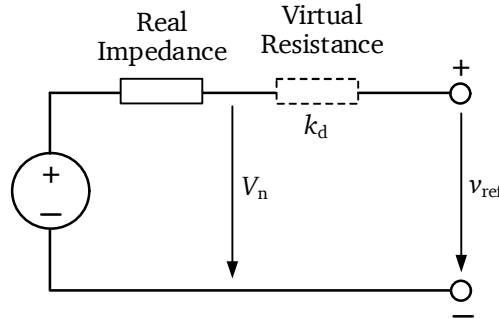


Figure 2.11: Thévenin equivalent circuit for a DG

The typical droop control structure is demonstrated in Figure 2.10, in which the interface converter with droop control can be modeled as a Thévenin equivalent circuit in Figure 2.11 [107]. It shows that the desired current sharing depends on the value of the droop coefficient and the voltage deviation. The reference voltage of the voltage control loop is given by

$$v_{\text{ref}} = V_n - k_d \cdot i_o \quad (2.8)$$

where V_n is the voltage threshold of the converter, i_o is the output current and k_d is the droop coefficient which represents the relationship between the output voltage and current. It can be seen from Figure 2.12 that with higher droop coefficient a better accuracy of current sharing can be achieved, but on the cost of higher voltage deviation [108].

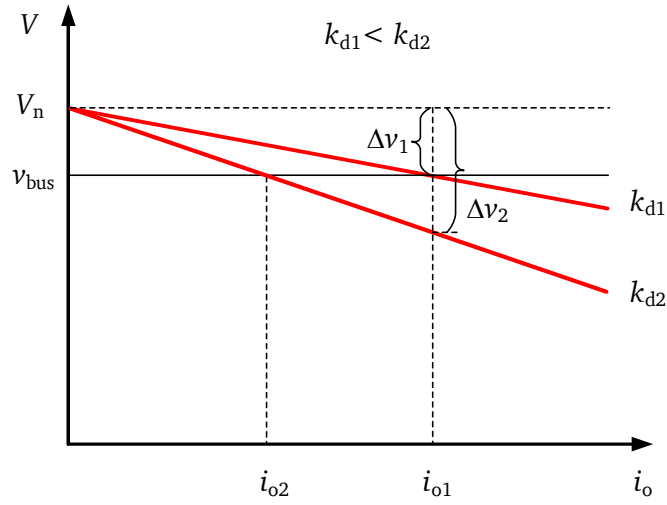


Figure 2.12: Load regulation characteristic of the droop method

In AC systems, another type of droop control is used to regulate the instantaneous sharing of active and reactive power between parallel inverters. Such a type of the droop control is shown in Figure 2.13. In this case, the active power versus frequency droop ($P-f$ droop) is used to share real power, while the reactive power sharing is performed by using the reactive power versus voltage droop ($Q-V$ droop) [109]. Since AC systems are out of the scope of this work, ($P-f$ droop) and ($Q-V$ droop) are not considered here.

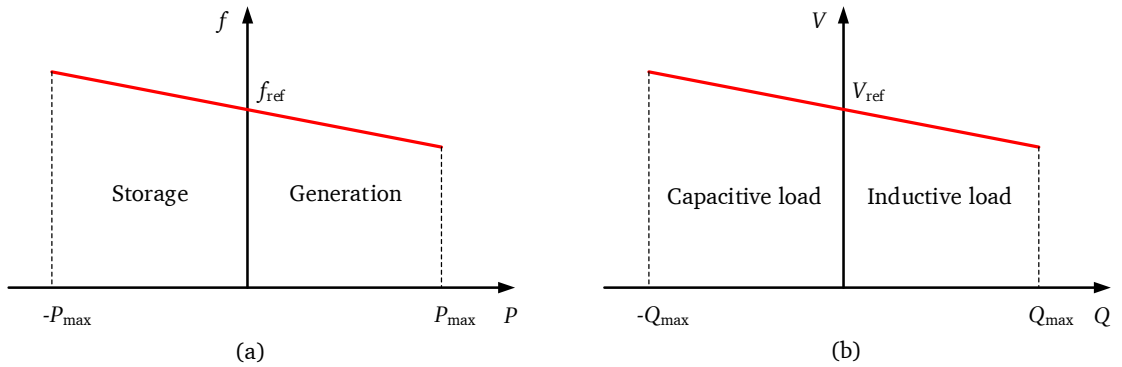


Figure 2.13: Droop control for AC systems: (a) $P-f$ droop; (b) $Q-V$ droop

Although the droop control method offers some benefits, this technique also has several drawbacks that limit its applicability. One of the disadvantages of this method is an inherent trade-off between voltage regulation and current sharing, since the better current sharing results in the higher voltage deviation. In this case, a secondary controller based on centralized or distributed approach needs to be implemented in order to eliminate the voltage deviation of the bus voltage. Another problem with the basic droop method is a poor coordinated performance with renewable energy sources since the maximum power point tracking (MPPT) algorithms needs to be used in order to generate as much power as possible. In this situation,

the selection of operational modes is realized by implementing either a centralized, decentralized or distributed supervisory control. By this way, the supervisory control will decide whether the converter is operated in the droop control mode or in other special control modes, e.g., MPPT for renewable energy sources [110], [111] or regulated charging mode for the battery [25].

Along with the droop control, a suitable control topology need to be implemented to achieve advanced power management. According to the communication point of view, the control topologies can be classified into three types including centralized, decentralized and distributed controls that can be introduced hereafter.

2.5.2 Centralized control

The centralized control consists of a central controller and a digital communication network as highlighted in Figure 2.14. The central controller is responsible for managing and controlling the operation of all local sources based on the collected information. The high-bandwidth communication network is needed to gather information with minimum delay as all execution and control are performed in the central controller.

The centralized control structure offers several advantages, such as high observability, controllability and an ease of implementation [32]. The advanced control functionalities can be easily implemented in the central controller which is aware of each node in the system. In addition, the central controller can effectively manage the power of distributed sources to meet the demand of the load.

One of the main drawbacks of this control topology is associated with a risky single point of failure, which degrades the reliability of the system [76]. If either the central controller or communication link fails, the system will not be able to operate. For applications which require high availability, redundant controllers and communication networks need to be installed in order to minimize the failure issues. However, this solution leads to the increase in investment and installation costs.

Another major disadvantage of the centralized control architecture is the reduction of flexibility and expandability as all information of the distributed units is required to be collected into the central controller. Also, it is unsuitable for large scale systems, which are equipped with various units in different locations, as the central control requires a significantly high computing

capacity. Thus, the centralized control architecture is usually suitable for local and small size microgrid systems [29], [112].

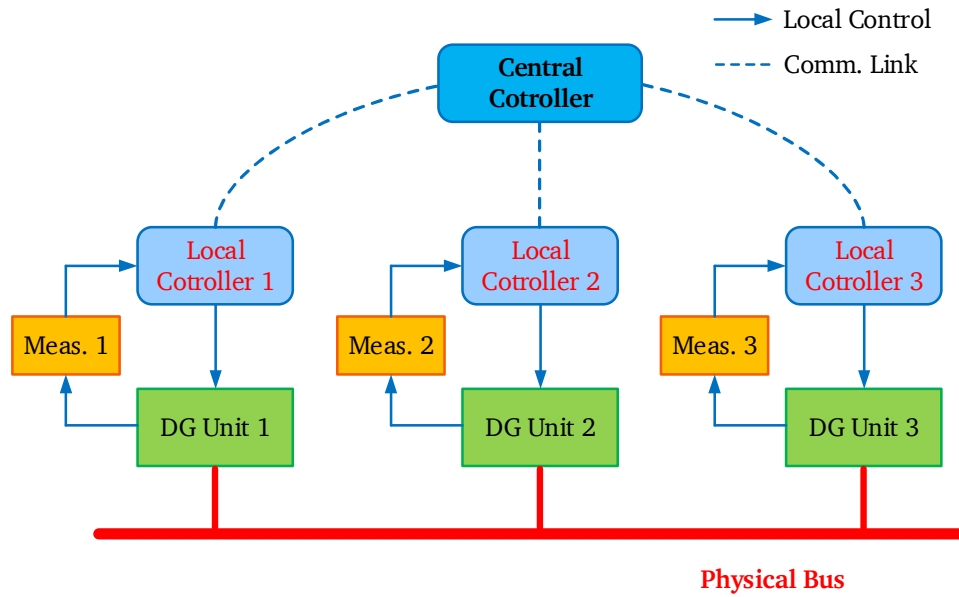


Figure 2.14: Centralized control topology

2.5.3 Distributed control

Beside the centralized control topology, distributed control is another approach, which offers some attractive features such as higher reliability, easier scalability and simpler communication system [46]. Distributed control, as shown in Figure 2.15, does not require a central controller but an external communication network. This topology is based on both local measurement and communication among neighboring units. Each distributed controller can measure and control locally while the operating modes of the units are determined according to the information exchanging among the local controllers. For example in an autonomous nanogrid, the renewable units communicate with the storage unit to decide whether they should operate in the MPPT mode or the droop control mode. If the storage unit is fully charged, the renewable nodes will switch to the droop control mode to balance power between generation and consumption.

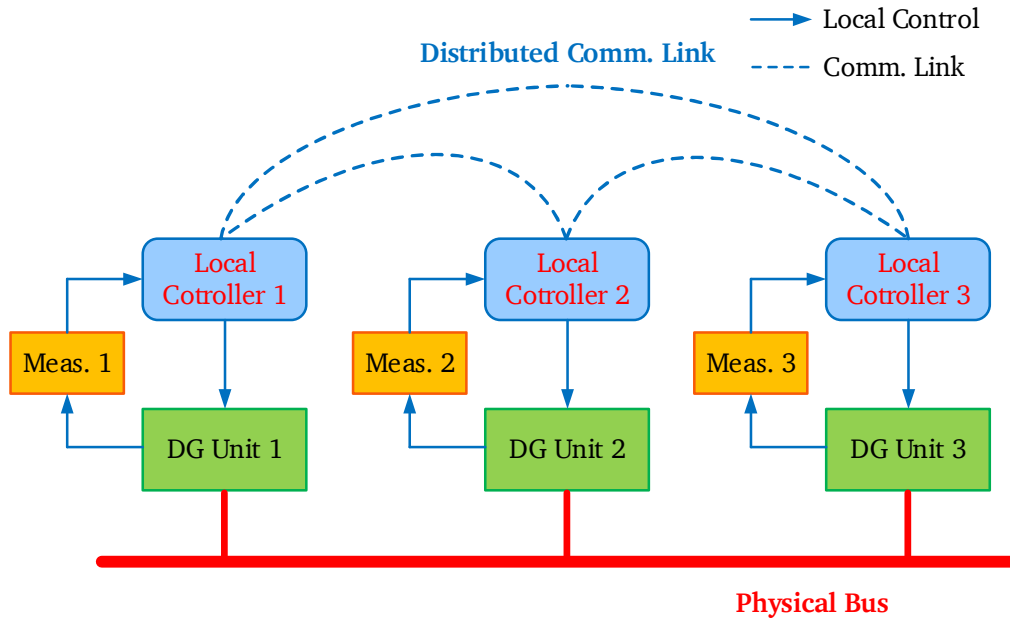


Figure 2.15: Distributed control topology

The distributed control ensures a higher reliability than the centralized control topology because it does not have a central controller and therefore the system is still operational even if a single point of failure occurs. In other words, if there is a failure unit in the distributed system, the other units are still operated properly. In addition, the distributed control approach provides the scalability and modularity, since it allows the autonomous operation of distributed generation sources and loads in different scenarios. However, like the centralized control, the system based on distributed control architecture is still dependent on the communication network [32].

2.5.4 Decentralized control

In contrast to the centralized and distributed control architectures, the coordination strategies based on decentralized control, as shown in Figure 2.16, are implemented exclusively by local controllers with the absence of a central controller and digital communication link. Each distributed unit is controlled by the respective local controller based on only the local information. In other words, each distributed unit is able to operate independently without communication of data with other units. Therefore, this strategy provides plug-and-play capability, allowing a unit can be added to or removed from the system without changes in the control structure. This characteristic significantly enhances the flexibility of the system. Also, the decentralized control architecture can avoid the centralized data acquisition and reduces the complexity of centralized computation. The decentralized control scheme is therefore

simple, fast, modular and reliable. This control strategy is commonly used in both AC and DC systems to regulate the instantaneous power sharing among parallel converters. A typical example of the decentralized control structures is the droop control. It allows power sharing among distributed generation sources without the need for a communication network.

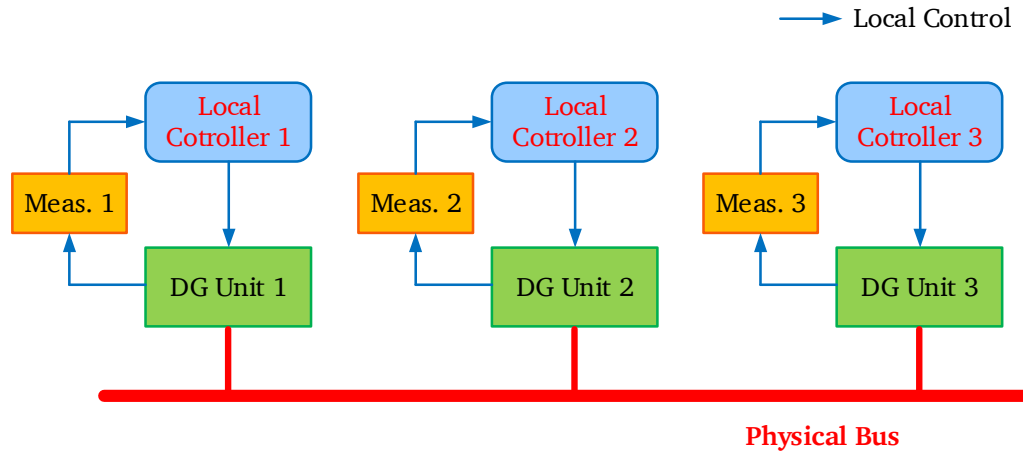


Figure 2.16: Decentralized control topology

Although the decentralized control scheme provides several advantages such as simplicity, reliability, modularity and no need for the communication link, it has limitation of operational performance due to a lack of awareness of the other distributed units. To mitigate the drawbacks of three aforementioned topologies, a hierarchical control topology is often employed as an alternative way to enhance the reliability of the system, to reduce the computational burden on the central controller as well as to remedy the shortcoming of the decentralized control. In this structure, centralized and decentralized control techniques can be combined in such a way that if the centralized controller fails, the system still works with fundamental functions being remained due to decentralized local controllers.

2.5.5 Summary of control topologies

Many studies have been carried out to assess the advantages and disadvantages of the different approaches. The schemes such as virtual power plant (VPP) or other types of aggregations seem to be suitable for centralized control schemes as they provide optimal cooperation of multiple energy sources based on the top-down approach with mutual economic benefits [29]. Other solutions based on modular micro/nanogrids might offer the best solution regarding resiliency, since this approach requires decentralized control to handle power balance between generation and consumption of the micro/nanogrid systems. Most of the microgrids around the world employ centralized control due to the fact that its design is simple for small microgrids [113].

However, there is an increasing interest in use of decentralized control, since it provides a plug-and-play capability and it is more suitable for large scale microgrids [88].

Nowadays, the modern energy systems are becoming more complex and require higher flexibility and reliability. All the functionalities cannot be obtained in a single centralized, decentralized or distributed way [32]. One promising solution for this issue is the use of hierarchical control architecture, which will be proposed and presented in more detail in Chapter 4.

2.6 Summary and the selection for the configuration of the nanogrid

This chapter presented the overview of nanogrids regarding components, technologies and control topologies. Nowadays, electricity of the nanogrids is still more expensive than that of the traditional grid as the investment cost of such systems is high [114]. Therefore, the nanogrid is now suitable for applications in remote and rural areas, where the electricity is unreliable or even not available. For this purpose, this research work proposes a topology which consists of two layers: 1) a nanogrid installed in each individual household; and 2) a DC microgrid, that is an integration of multiple nanogrids via an external DC bus. The nanogrid is designed based upon a modular structure with a set of the following modules [65]:

- 1) Renewable energy sources: PV panels and/or wind turbines.
- 2) Energy storage systems: batteries. A battery can be operated either as a power source or as a load.
- 3) Power loads: electrical household appliances, such as TV sets, laptops, refrigerators and mobile chargers.
- 4) A gateway: a bidirectional connection that is used to interconnect multiple nanogrids to form a microgrid.

As aforementioned, a typical nanogrid is composed of RESs and ESSs. Since RESs have intermittent nature, ESSs are commonly employed as an energy buffer between the sources and the loads to enhance the efficiency of the RESs [13]. ESSs can be connected either directly to the DC bus or through bidirectional DC/DC converters. Since the latter configuration ensures the reliability of system, it is preferred for use in renewable energy systems [27]. In this work, both RESs and ESSs are connected to the common DC bus via DC/DC converters.

For the sake of simplicity, this work deals with a nanogrid equipped with a PV panel, a battery, a DC load and a gateway for interconnection as demonstrated in Figure 2.17. By adding more sources, storage devices and loads, the proposed topology can be expanded. To connect the PV panel and the battery to the common DC bus, a buck DC/DC converter and a bi-directional DC/DC converter are typically used, respectively. The battery functions as a prosumer, which can either generate or consume power. For example, the battery is being charged when the power from the PV is in excess, while by contrast, it feeds the load when power from the PV is inadequate. There are two voltage levels for the two DC buses in the proposed topology, in which the lower level is set to 48 V for the internal DC bus, while 100 V is selected for the level of the external DC bus. Both DC voltages meet the requirement of the safety extra-low voltage (SELV) standard [83]. During the design of the control algorithm, the protection of overcharge and undercharge of the battery needs to be taken into account in order to maintain the battery lifetime.

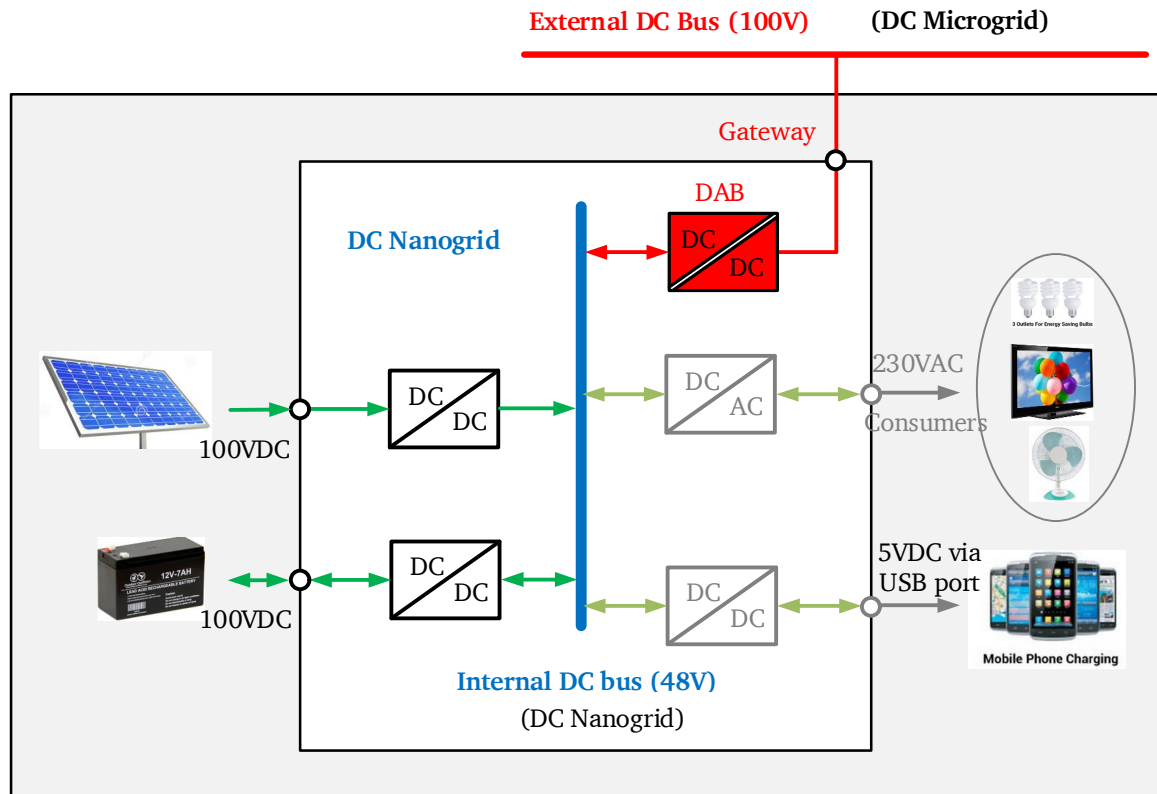


Figure 2.17: The modular structure of a nanogrid

The aim of the interconnection is to provide the reliability and expandability for the system. The integration of multiple DC nanogrids forms a DC microgrid that enables each nanogrid capable of absorbing power from or injecting power to others according to its current power status [27]. The control strategy allows a flexible power exchange among nanogrids through

the nanogrid network, mitigating the impacts of intermittency of generation and consumption of power along with enhancing the system reliability [11].

Figure 2.18 illustrates the proposed topology with multiple nanogrids interconnected through a bidirectional converter to an external DC bus. For this purpose, the dual active bridge topology is employed, as it meets the requirements for a bidirectional power transfer capability and galvanic isolation [56]. More importantly, there is no requirement for a communication link in the proposed topology. Each nanogrid can be plugged in and plugged out during the operation of the microgrid without requiring any manual configuration, leading to a flexible and scalable configuration.

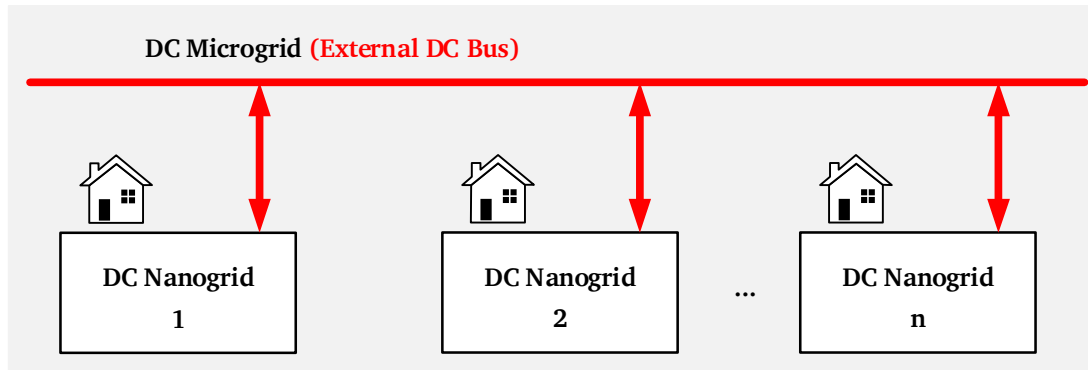


Figure 2.18: A DC microgrid made of interconnected nanogrids

3 Modeling and control of DC/DC power electronics converters

3.1 Introduction

An important step in designing power electronic systems concerns modeling and control of these systems. In addition, computer-based simulations which need mathematical models have recently been extensively used. Once a mathematical model of a system is obtained, analytical and computing tools can be employed for analysis and synthesis purposes. The more complete a mathematical model is, the more accurate corresponding analyses could be. However, it is challenging to attain a precise model of the power electronic systems without losing insights of the real-world applications as the topologies of the systems are composed of continuous-time elements and discrete-time power switches. A balance between the simplicity and the accuracy of the model should be taken into account. A typical approach is that the power switches are assumed to be ideal components, then the power electronic converters are modelled as switching systems [100]. Therefore, some certain inherent physical properties of the systems should be neglected, resulting in a simpler analysis as well as a decrease in the computational load for numerical simulations. If the effects of these ignored properties are negligible, the mathematical model is coincident with the experimental model.

Power stages of switching converters are nonlinear systems as they consist of power switches, which have two operation modes with the numerical values of either “zero” or “one”. In control systems, linear control theory is used for studying the behavior of the switching converters. However, in order to implement this theory, nonlinear power stages of switching converters should be averaged and linearized [57], [115], [116]. Two traditional techniques including state-space averaging [50], [51], [53], [55]–[57] and circuit averaging [117]–[122] are commonly used to model DC/DC converters. The circuit averaging method is suitable for linear circuit models as the average values of voltages and currents are considered. The benefit of this approach is the simplicity of the attained equivalent circuits of the converters and the ease of analysis with the use of common circuit simulators [123]. However, when the dynamic behavior of the switching systems is taken into account, the state-space averaging method is preferred. One of the advantages of this method is to obtain the unified description of all power stages through the utilization of the exact state-space equations of the switching models [56]. Another benefit of this approach is that a small-signal averaged model can always be obtained from the state equations of the original converter [131]. Furthermore, this method is also appropriate for the analysis of nonlinear systems as it allows the examined nonlinear system to be approximated as a linear system.

One of the purposes of this research is to model a complete DC nanogrid system. First, a good model of a single converter needs to be obtained. Next, the entire system can be modeled by synthesizing the single models and this will be presented in Chapter 4. This chapter presents modeling and control of bidirectional buck converters and dual active bridge converters, which are used in the proposed DC nanogrid. The state-space averaging method is utilized for the modeling process and the small-signal approximation is used to obtain a linearized model.

3.2 Small-signal modeling method based on the state-space averaging technique

The modeling method based on the state-space averaging technique is commonly used in power electronic converter systems [50], [51]. The state-space description of dynamical systems is a backbone of the modern control theory. Averaging and small-signal linearization are the main steps in modeling switching converters. The state-space averaging approach is very practical, as it allows the use of the state-space description to derive the small-signal averaged equations of switching converters. This approach is based on analytical averaging of state-space equations, which describe equivalent circuits for different states of the converters. Then the average values of the state variables in each switching cycle are achieved with low frequency approximation. Finally, the small-signal model can be obtained by applying the linearization process [124].

The procedure of the modeling method based on the state-space averaging technique is described in the flowchart as shown in Figure 3.1.

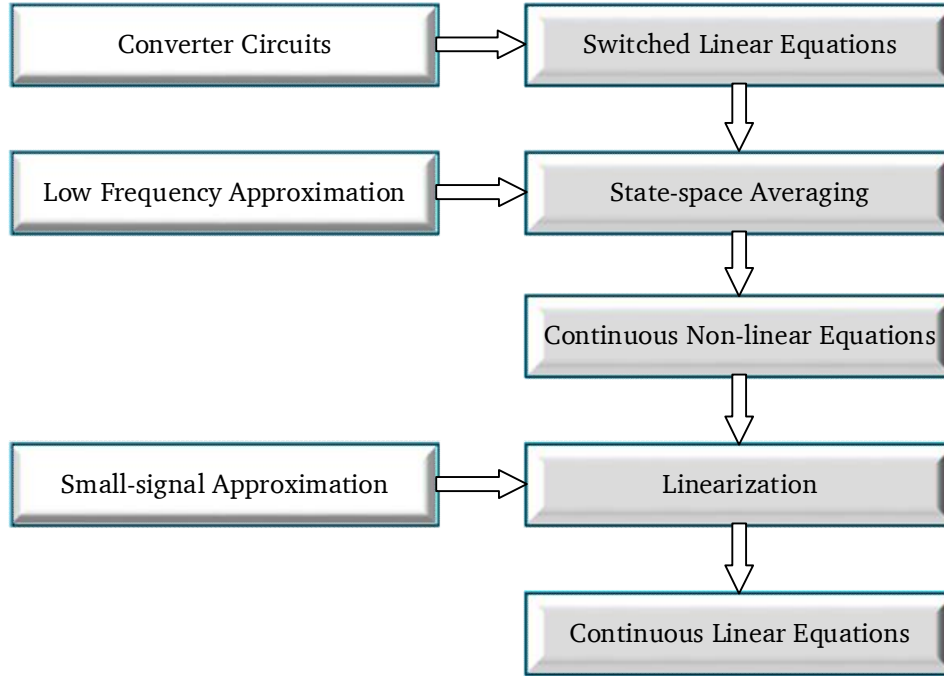


Figure 3.1. Flowchart of the small-signal modeling approach based on the state-space averaging technique [125]

3.3 Generalized state-space averaging method and Fourier interpolation

The state-space averaging method can provide a good model if two conditions are satisfied: 1) the switching frequency is much higher than the frequencies of the variables under consideration; 2) the ripple of the state variables is sufficiently small [54]. However, there are some converters that cannot be modeled with this method. For instance, the dual active bridge (DAB) converter cannot be modelled by applying the state-space averaging method as the AC ripples of the state variables are high and must be taken into account. Therefore, the generalized state-space averaging method is applied as an alternative way for the DAB converters. In this method, the analysis of variables with AC behavior can be considered. As the generalized average modeling method is based upon the Fourier interpolation of time-dependent variables, for convenience, some important properties of the Fourier interpolation will be presented hereafter.

The Fourier series expansion of a periodic signal $x(t)$ is expressed by [55]–[57]:

$$x(t) = \sum_{k=-\infty}^{\infty} \langle x \rangle_k(t) \cdot e^{jk\omega_s t} \quad (3.1)$$

where $\omega_s = 2\pi f_s = 2\pi/T_s$, $\langle x \rangle_k(t)$ are the Fourier coefficients. Since the interval under consideration slides as a function of time, these Fourier coefficients are functions of time. At any time, the coefficient of the k^{th} harmonic is defined as:

$$\begin{aligned}\langle x \rangle_k(t) &= \frac{1}{T_s} \int_{t-T_s}^t x(\tau) \cdot e^{-jk\omega_s\tau} d\tau \\ &= \frac{1}{T_s} \int_{t-T_s}^t x(\tau) \cdot \cos(k\omega_s\tau) d\tau - j \frac{1}{T_s} \int_{t-T_s}^t x(\tau) \cdot \sin(k\omega_s\tau) d\tau\end{aligned}\quad (3.2)$$

In case the ripples of the state variables are small, the conventional state-space average model can be employed where only DC terms ($k = 0$) given in (3.1) and (3.2) are taken into consideration. However, the transformer current in the DAB converter is a pure alternating current, which means that the current ripple is large and the DC term is zero [126]. Therefore, in the present work both DC ($k = 0$) and fundamental terms ($k = \pm 1$) in the Fourier series expansion are taken into account.

From (3.2) coefficients $\langle x \rangle_k$ and $\langle x \rangle_{-k}$ satisfy

$$\Re\{\langle x \rangle_k\} = \Re\{\langle x \rangle_{-k}\}; \quad \Im\{\langle x \rangle_k\} = -\Im\{\langle x \rangle_{-k}\} \quad (3.3)$$

where the nomenclatures "ℜ" and "ℑ" denote the real and the imaginary parts of the complex coefficients, respectively.

From (3.1), the derivative of $x(t)$ with respect to t is written:

$$\frac{dx(t)}{dt} = \sum_{k=-\infty}^{\infty} \left(\frac{d}{dt} \langle x \rangle_k(t) + jk\omega_s \langle x \rangle_k(t) \right) \cdot e^{jk\omega_s t} \quad (3.4)$$

From (3.4), derivative of the k^{th} coefficient for variable $x(t)$ is given as follows:

$$\frac{d}{dt} \langle x \rangle_k(t) = \left\langle \frac{d}{dt} x \right\rangle_k(t) - jk\omega_s \langle x \rangle_k(t) \quad (3.5)$$

The proof of (3.5) can be obtained directly by using the Fourier representation (3.1). The k^{th} coefficient of the product of two variables x and y is

$$\langle xy \rangle_k = \sum_{i=-\infty}^{\infty} \langle x \rangle_{k-i} \langle y \rangle_i \quad (3.6)$$

By taking into account only the DC and the first harmonics, the product of zeroth coefficient terms given in (3.6) is approximated by

$$\langle xy \rangle_0 = \langle x \rangle_0 \langle y \rangle_0 + \langle x \rangle_1 \langle y \rangle_{-1} + \langle x \rangle_{-1} \langle y \rangle_1 \quad (3.7)$$

According to (3.2) and (3.3), the coefficients corresponding to $k = 1$ and $k = -1$ are complex conjugates, and if only harmonics up to the 1st order are taken into account, the fundamental coefficient terms are given by

$$\langle x \rangle_1 = \Re\{\langle x \rangle_1\} + j \cdot \Im\{\langle x \rangle_1\} \quad (3.8)$$

$$\langle x \rangle_{-1} = \Re\{\langle x \rangle_{-1}\} + j \cdot \Im\{\langle x \rangle_{-1}\} = \Re\{\langle x \rangle_1\} - j \cdot \Im\{\langle x \rangle_1\} \quad (3.9)$$

$$\langle y \rangle_1 = \Re\{\langle y \rangle_1\} + j \cdot \Im\{\langle y \rangle_1\} \quad (3.10)$$

$$\langle y \rangle_{-1} = \Re\{\langle y \rangle_{-1}\} + j \cdot \Im\{\langle y \rangle_{-1}\} = \Re\{\langle y \rangle_1\} - j \cdot \Im\{\langle y \rangle_1\} \quad (3.11)$$

From (3.7)-(3.11), the product of the zeroth coefficient term is given by

$$\langle xy \rangle_0 = \langle x \rangle_0 \langle y \rangle_0 + 2(\Re\{\langle x \rangle_1\} \Re\{\langle y \rangle_1\} + \Im\{\langle x \rangle_1\} \Im\{\langle y \rangle_1\}) \quad (3.12)$$

Similarly, the 1st coefficient terms are approximated by

$$\Re\{\langle xy \rangle_1\} = \langle x \rangle_0 \cdot \Re\{\langle y \rangle_1\} + \Re\{\langle x \rangle_1\} \cdot \langle y \rangle_0 \quad (3.13)$$

$$\Im\{\langle xy \rangle_1\} = \langle x \rangle_0 \cdot \Im\{\langle y \rangle_1\} + \Im\{\langle x \rangle_1\} \cdot \langle y \rangle_0 \quad (3.14)$$

The Fourier coefficients can be determined theoretically. In the following section, the DC and the 1st coefficient of a well-known signal will be described as an example.

Figure 3.2 shows two periodic square-wave signals with fundamental period of T_s and two possible values of $+1$ and -1 . It is realized that $x_1(t)$ is the special case of $x_2(t)$ corresponding to $d = 0$. Hence, the calculation of the Fourier coefficients will be conducted for the signal $x_2(t)$.

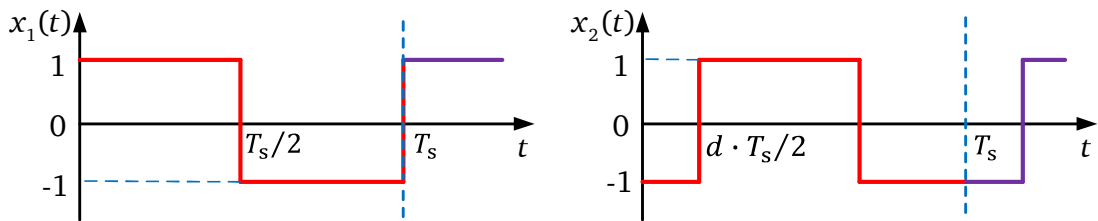


Figure 3.2: Two periodic signal with the same fundamental period T_s , but different phase shift. Because $x_2(t)$ is symmetric regarding t , the DC component is zero:

$$\langle x_2 \rangle_0(t) = 0 \quad (3.15)$$

From Figure 3.2, the 1st coefficient of $x_2(t)$ is calculated as follows:

$$\begin{aligned}
 \langle x_2 \rangle_1 &= \frac{1}{T_s} \int_0^{T_s} x(t) \cdot e^{-j\omega_s t} dt \\
 &= \frac{1}{T_s} \left[\int_0^{dT_s/2} (-1) \cdot e^{-j\omega_s t} dt + \int_{dT_s/2}^{T_s(d+1)/2} 1 \cdot e^{-j\omega_s t} dt + \int_{T_s(d+1)/2}^{T_s} (-1) \cdot e^{-j\omega_s t} dt \right] \quad (3.16) \\
 &= -\frac{2\sin(\pi d)}{\pi} - j \frac{2\cos(\pi d)}{\pi}
 \end{aligned}$$

Therefore

$$\Re\{\langle x_2 \rangle_1\} = -\frac{2\sin(d\pi)}{\pi}; \quad \Im\{\langle x_2 \rangle_1\} = -\frac{2\cos(d\pi)}{\pi} \quad (3.17)$$

With $d = 0$, the corresponding coefficients of $x_1(t)$ are

$$\langle x_1 \rangle_0 = 0; \quad \Re\{\langle x_1 \rangle_1\} = 0; \quad \Im\{\langle x_1 \rangle_1\} = -\frac{2}{\pi} \quad (3.18)$$

3.4 Modeling and control of a bidirectional buck converter

3.4.1 Introduction

As aforementioned, the topology of the DC nanogrid consists of a buck converter for the PV source, a bidirectional buck converter for charging and discharging the battery and a DAB converter for the purpose of interconnection. For convenience, the bidirectional buck topology is employed for both the PV source and the battery in this work. In order to design controllers for the bidirectional buck converter, the small-signal transfer functions need to be derived and will be presented hereafter.

3.4.2 Circuit description

The topology of a bidirectional buck converter is shown in Figure 3.4. It consists of two switches S_1 and S_2 , an inductor L , a parasitic resistor R_L of the inductor and a filter capacitor C_o . A passive DC load is represented by a resistor R_o . Each switch is composed of a power MOSFET and a freewheeling diode. With this topology, the switches are bidirectional for the current, allowing energy flow in both directions from left to right and vice versa. The switch S_1 and S_2 must never

be closed at the same time in order to avoid short circuit on the input voltage which would cause a shoot-through current spike and can result in power MOSFET failure [127]. In order to prevent power MOSFET from cross conduction, a delay between the turn-off of one MOSFET and the turn-on of the other must be added. The switches are controlled by a pulse-width modulation (PWM) generator from a digital signal processing unit (DSP) from which they are turned on and turned off at the switching frequency f_s . The duty ratio D for the switches is defined as follows

$$D = \frac{V_o}{V_i} = \frac{t_{on}}{t_{on} + t_{off}} = \frac{t_{on}}{T_s} \quad (3.19)$$

where t_{on} is the time interval when switch S_1 is ON, t_{off} is the time interval when switch S_1 is OFF, $T_s = 1/f_s$ is the switching period, V_i and V_o are the input and output voltages, respectively. In most cases, the input voltage V_i often fluctuates over a certain range while the output voltage V_o needs to be maintained at the reference value. By regulating the duty ratio D , the amount of energy exchanged between the input and output sides can be controlled.

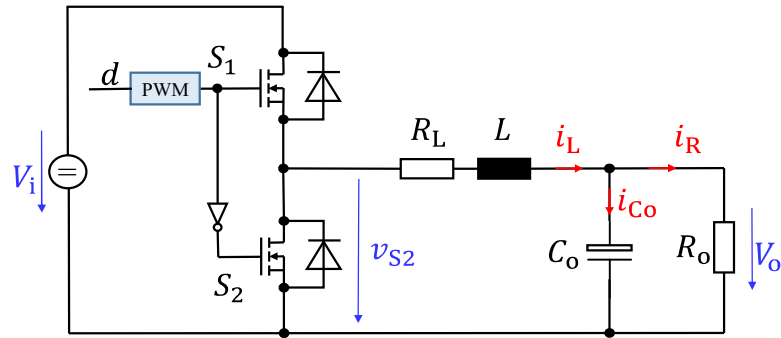


Figure 3.3: The bidirectional buck converter

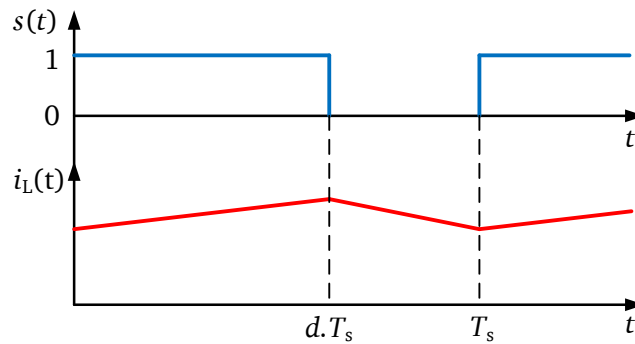


Figure 3.4: Waveforms of the bidirectional buck converter during one period

3.4.3 State-space averaged model of the bidirectional buck converter

In this section, a small-signal model for a buck converter is developed based on the state-space averaging method. For simplicity, only the zeroth harmonics of the output voltage v_o and the inductor current i_L as state variables are considered in this work since they are DC in the steady state [66].

As shown in the Figure 3.4 the voltage v_{S2} has two states: 1) $+V_i$ when switches S_1 is ON and S_2 is OFF; and 2) 0 when switches S_1 is OFF and S_2 is ON. Therefore,

$$v_{S2}(t) = s(t)v_i(t)$$

$$\text{with } s(t) = \begin{cases} 1, & 0 \leq t < d \cdot T_s \\ 0, & d \cdot T_s \leq t < T_s \end{cases} \quad (3.20)$$

where T_s is the switching period, d is the duty cycle, and $v_i(t)$ is the input voltage with taking into account the perturbation, $\langle v_i \rangle_0 = V_i$ with $\langle x \rangle_k$ corresponding to the coefficient of the k^{th} harmonic of the signal $x(t)$. The dynamics of the converter are achieved by applying Kirchhoff's law:

$$i_L(t) = i_{C_o}(t) + i_R(t) = C_o \frac{dv_o(t)}{dt} + \frac{v_o(t)}{R_o} \quad (3.21)$$

or

$$\frac{dv_o(t)}{dt} = -\frac{v_o(t)}{R_o C_o} + \frac{1}{C_o} i_L(t) \quad (3.22)$$

$$s(t)v_i(t) = R_L i_L(t) + L \frac{di_L(t)}{dt} + v_o(t) \quad (3.23)$$

or

$$\frac{di_L(t)}{dt} = -\frac{1}{L} v_o(t) - \frac{R_L}{L} i_L(t) + \frac{s(t)v_i(t)}{L} \quad (3.24)$$

The state-space model of the bidirectional buck converter is represented by equation (3.22) and equation (3.24), respectively, as the switched model in which the binary valued nature of the switch position function $s(t)$ is the set of $\{0,1\}$. By taking the determination of the zeroth coefficient term for both sides of (3.22) and (3.24), the state-space equations of the bidirectional buck converter can be deduced as

$$\frac{d\langle v_o \rangle_0}{dt} = -\frac{1}{R_o C_o} \langle v_o \rangle_0 + \frac{1}{C_o} \langle i_L \rangle_0 \quad (3.25)$$

$$\frac{d\langle i_L \rangle_0}{dt} = -\frac{1}{L}\langle v_o \rangle_0 - \frac{R_L}{L}\langle i_f \rangle_0 + \frac{1}{L}\langle sv_i \rangle_0 \quad (3.26)$$

According to (3.12), $\langle sv_i \rangle_0$ can be given as follows

$$\langle sv_i \rangle_0 = \langle s \rangle_0 \langle v_i \rangle_0 + 2(\Re\{\langle s \rangle_1\}\Re\{\langle v_i \rangle_1\} + \Im\{\langle s \rangle_1\}\Im\{\langle v_i \rangle_1\}) \quad (3.27)$$

Substituting $\langle sv_i \rangle_0$ from (3.27) into (3.26) yields

$$\frac{d\langle i_L \rangle_0}{dt} = -\frac{1}{L}\langle v_o \rangle_0 - \frac{R_L}{L}\langle i_f \rangle_0 + \frac{1}{L}(\langle s \rangle_0 \langle v_i \rangle_0 + 2(\Re\{\langle s \rangle_1\}\Re\{\langle v_i \rangle_1\} + \Im\{\langle s \rangle_1\}\Im\{\langle v_i \rangle_1\})) \quad (3.28)$$

For simplicity, the first harmonics of $s(t)$ are neglected, then (3.28) is equivalent to:

$$\frac{d\langle i_L \rangle_0}{dt} = -\frac{1}{L}\langle v_o \rangle_0 - \frac{R_L}{L}\langle i_f \rangle_0 + \frac{1}{L}\langle s \rangle_0 \langle v_i \rangle_0 \quad (3.29)$$

From Figure 3.4, the zeroth component of $s(t)$ can be determined as follows

$$\langle s \rangle_0 = \frac{1}{T_s} \int_0^{T_s} s(t) dt = \frac{1}{T_s} \left(\int_0^{dT_s} s(t) dt + \int_{dT_s}^{T_s} s(t) dt \right) = d \quad (3.30)$$

Substituting $\langle s \rangle_0$ from (3.30) into (3.29), the following equation is achieved:

$$\frac{d\langle i_L \rangle_0}{dt} = -\frac{1}{L}\langle v_o \rangle_0 - \frac{R_L}{L}\langle i_f \rangle_0 + \frac{1}{L}d\langle v_i \rangle_0 \quad (3.31)$$

From (3.25) and (3.31), the state-space model of the bidirectional buck converter in a matrix form is given by

$$\frac{d}{dt} \begin{bmatrix} \langle v_o \rangle_0 \\ \langle i_L \rangle_0 \end{bmatrix} = \begin{bmatrix} -\frac{1}{R_o C_o} & \frac{1}{C_o} \\ -\frac{1}{L} & -\frac{R_L}{L} \end{bmatrix} \begin{bmatrix} \langle v_o \rangle_0 \\ \langle i_L \rangle_0 \end{bmatrix} + \begin{bmatrix} 0 \\ \frac{d}{L} \end{bmatrix} [\langle v_i \rangle_0] \quad (3.32)$$

3.4.4 Small-signal model of the bidirectional buck converter

The small-signal model of the bidirectional buck converter can be obtained by linearizing (3.32) around a steady state operating point. The control signal and the state variables are defined as follows:

$$d = D + \Delta d \quad (3.33)$$

$$\langle v_o \rangle_0 = \langle V_o \rangle_0 + \Delta \langle v_o \rangle_0 \quad (3.34)$$

$$\langle i_L \rangle_0 = \langle I_L \rangle_0 + \Delta \langle i_L \rangle_0 \quad (3.35)$$

$$\langle v_i \rangle_0 = \langle V_i \rangle_0 + \Delta \langle v_i \rangle_0 \quad (3.36)$$

where steady state variables are represented by capital characters, large-signal state variables by lower case characters and small-signal variables by Δ . If the input voltage is constant and the multiplication of two small variables is negligible, $\Delta \langle v_i \rangle_0 \approx 0$ and $\Delta \langle v_o \rangle_0 \cdot \Delta d \approx 0$. Steady state values of $\langle v_o \rangle_0$ and $\langle i_L \rangle_0$ can be found from (3.32) by solving

$$\frac{d}{dt} \begin{bmatrix} \langle v_o \rangle_0 \\ \langle i_L \rangle_0 \end{bmatrix} = 0 \quad (3.37)$$

Substituting (3.33)–(3.37) into (3.32) results in the small-signal model of the bidirectional buck converter given in (3.38), which can be used to obtain the control-to-output transfer functions of the bidirectional buck converter.

$$\frac{d}{dt} \begin{bmatrix} \Delta \langle v_o \rangle_0 \\ \Delta \langle i_L \rangle_0 \end{bmatrix} = \begin{bmatrix} -\frac{1}{R_o C_o} & \frac{1}{C_o} \\ -\frac{1}{L} & -\frac{R_L}{L} \end{bmatrix} \begin{bmatrix} \Delta \langle v_o \rangle_0 \\ \Delta \langle i_L \rangle_0 \end{bmatrix} + \begin{bmatrix} 0 \\ \frac{\langle V_i \rangle_0}{L} \end{bmatrix} \Delta d \quad (3.38)$$

The small-signal control to output transfer function given in (3.38) is represented in the matrix form as follows

$$\begin{cases} \frac{d}{dt} X = \mathbf{A} \cdot X + \mathbf{B} \cdot \Delta d \\ Y = \mathbf{I} \cdot X \end{cases} \quad (3.39)$$

where

$$X = [\Delta \langle v_o \rangle_0, \Delta \langle i_L \rangle_0]^T \quad (3.40)$$

$$\mathbf{A} = \begin{bmatrix} -\frac{1}{R_o C_o} & \frac{1}{C_o} \\ -\frac{1}{L} & -\frac{R_L}{L} \end{bmatrix} \quad (3.41)$$

$$\mathbf{B} = \begin{bmatrix} 0 \\ \frac{\langle V_i \rangle_0}{L} \end{bmatrix} \quad (3.42)$$

$$\mathbf{I} = \begin{bmatrix} 1 & 0 \\ 0 & 1 \end{bmatrix} \quad (3.43)$$

3.4.5 Closed-loop control of the bidirectional buck converter

3.4.5.1 Control scheme for the bidirectional buck converter

According to the state-space representation (3.39), the control-to-output transfer functions are given by

$$\mathbf{G}_b = [G_{vd,b}, G_{iLd,b}]^T = (s \cdot \mathbf{I} - \mathbf{A})^{-1} \mathbf{B} \quad (3.44)$$

where the nomenclature ‘_b’ denotes the bidirectional buck converter, $G_{vd,b}$ and $G_{iLd,b}$ are the transfer functions from the small signal $\Delta \langle v_o \rangle_0$ and $\Delta \langle i_L \rangle_0$ to the control small signal Δd , respectively. From these functions, $G_{vd,b}$ represents the relationship between a change of the duty cycle Δd and the output voltage while $G_{iLd,b}$ represents the relationship between Δd and the inductor current i_L . Assuming that the input voltage is constant, then $\langle V_i \rangle_0 = V_i$. The transfer functions of the bidirectional converter are given by

$$G_{vd,b} = \frac{V_i}{LC_o s^2 + \left(R_L C_o + \frac{L}{R_o}\right)s + \frac{R_L}{R_o} + 1} \quad (3.45)$$

$$G_{iLd,b} = \frac{V_i \left(C_o s + \frac{1}{R_o}\right)}{LC_o s^2 + \left(R_L C_o + \frac{L}{R_o}\right)s + \frac{R_L}{R_o} + 1} \quad (3.46)$$

The cascaded control structure with two control loops for the bidirectional buck converter is shown in Figure 3.5, where the power stage of the converter is represented by the obtained small-signal transfer functions. The inductor current i_L is regulated by the inner loop while the outer loop controls the output voltage v_o . For cascaded control structures, the closed-loop bandwidth of the inner control loop needs to be adequately higher than that of the outer control loop [128]. In Figure 3.5, the control delay is approximated by a first-order lag element $G_{d,b}(s)$ with the time constant $T_d = 2 \cdot T_s$.

$$G_{d,b}(s) = \frac{1}{1 + T_d \cdot s} \quad (3.47)$$

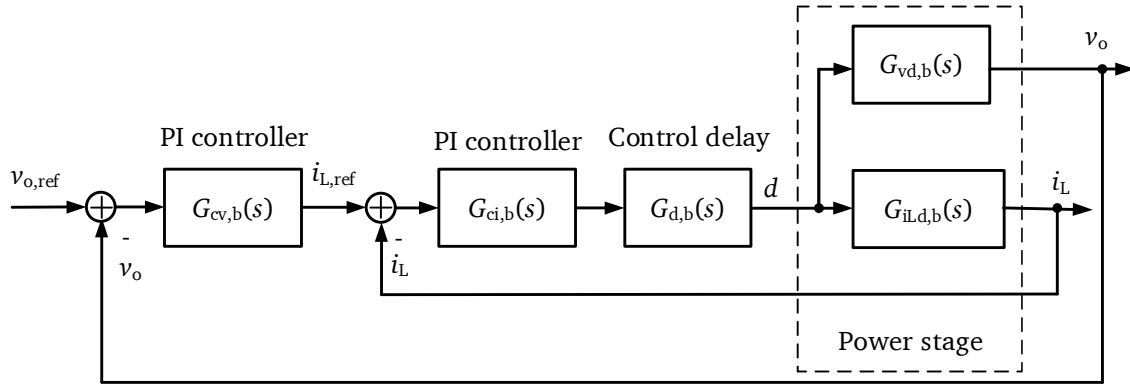


Figure 3.5: Control scheme for the bidirectional buck converter

The controller design of the bidirectional buck converter is based on the obtained small-signal transfer functions. Conventional PI controllers can be used for both the current and voltage control loops as they are simple and robust. The transfer functions of the PI controllers for the current and the voltage loops are given by (3.48) and (3.49), respectively.

$$G_{ci,b}(s) = K_{pi,b} + \frac{K_{ii,b}}{s} \quad (3.48)$$

$$G_{cv,b}(s) = K_{pv,b} + \frac{K_{iv,b}}{s} \quad (3.49)$$

where $K_{pi,b}$, $K_{ii,b}$ are the gains of the proportional and integral parts of the current controller, while $K_{pv,b}$, $K_{iv,b}$ correspond to the voltage controller. From the control structure of the bidirectional buck converter, as shown in Figure 3.5, the open-loop transfer functions $G_{OLi,b}(s)$ from i_L to $i_{L,ref}$ and $G_{OLv,b}(s)$ from v_o to $v_{o,ref}$ are given by

$$G_{OLi,b}(s) = G_{ci,b}(s)G_{d,b}(s)G_{iLd,b}(s) \quad (3.50)$$

$$G_{OLv,b}(s) = \frac{G_{cv,b}(s)G_{ci,b}(s)G_{d,b}(s)G_{vd,b}(s)}{1 + G_{ci,b}(s)G_{d,b}(s)G_{iLd,b}(s)} \quad (3.51)$$

The parameters of PI controllers are tuned by using the SISO (Single Input Single Output) tool in MATLAB along with the procedure presented in [125]. These parameters are selected to ensure appropriate bandwidths, phases and gain margins, in which gain and phase margins will be at least 6 dB and at least 60° away from 180° , respectively [129]. The inner current loop needs to be tuned first without closing the voltage loop as the inner loop is much faster than the outer loop. This way, appropriate parameters of the current controller can be chosen by examining the step response of the loop. Afterwards, the same procedure is examined by closing the voltage loop in order to achieve the PI parameters for the outer loop. The obtained values

for the proportional and integral gains, which are used in both simulations and experiments, are summarized in Table 3.1.

Table 3.1: Parameters of controller

Voltage controller	Current controller
$K_{pv,b} = 1.2 \text{ (A/V)}$	$K_{pi,b} = 0.008 \text{ (1/A)}$
$K_{iv,b} = 150 \text{ (A/Vs)}$	$K_{ii,b} = 25 \text{ (1/As)}$

3.4.5.2 Bode plots of the open-loop transfer functions

Figure 3.6 and Figure 3.7 show the Bode diagrams of the open-loop transfer functions of the current and the voltage control loops, respectively. The gain and phase margins of the open loop transfer function of the current control loop are infinite and 71 degrees, respectively, as illustrated in Figure 3.6. For the open-loop transfer function of the voltage control loop, the phase and gain margins are 86 degrees and 26 dB at frequency of 2.2 kHz, respectively. It is observed that the bandwidths of the inner current loop and the outer voltage loop are 1240 Hz and 190 Hz, respectively. Therefore, it meets the requirement that the bandwidth of the inner current loop is significant higher than that of outer voltage loop.

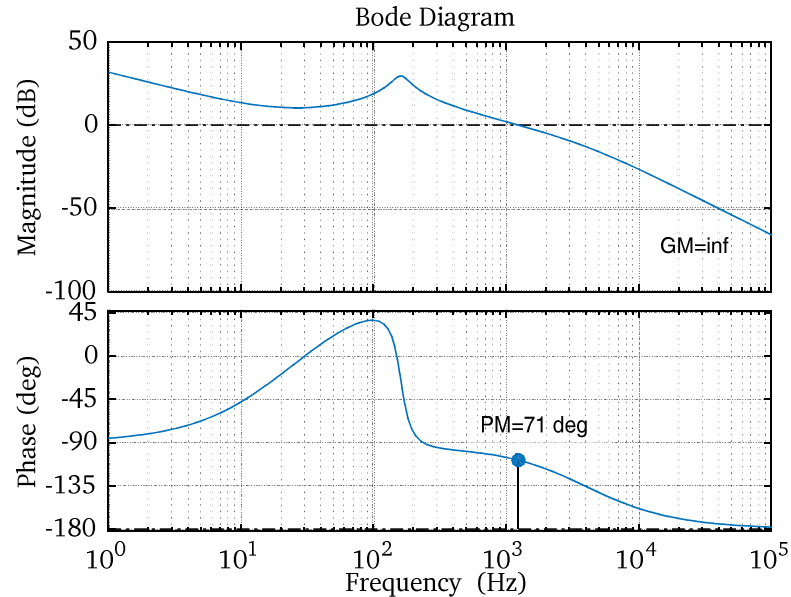


Figure 3.6: Bode plot of the open-loop transfer function of the current loop

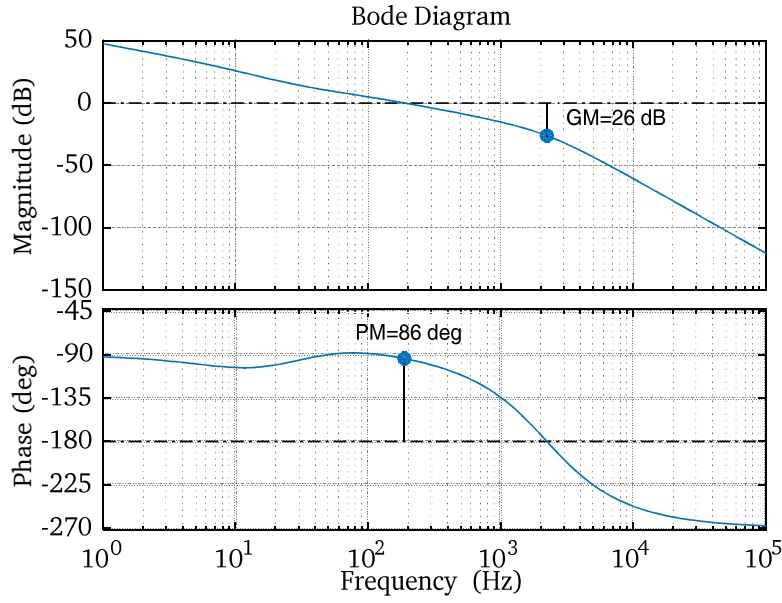


Figure 3.7: Bode plot of the open-loop transfer function of the voltage loop

3.4.6 Simulation and experimental results

Simulation and experimental models were built to verify the operation of the proposed method. The parameters of the bidirectional buck converter are summarized in Table 3.2. The simulation results that correspond to step changes in the resistive loads are shown in Figure 3.8. It can be observed in Figure 3.8 that the output voltage v_o remains stable around the reference value of 48 V with a small overshoot and a small undershoot, which are approximately 1 V equivalent to 2% of the reference value, with respect to the changes in the load. The settling time is around 15 ms. At $t = 0.07$ s the load is suddenly increased, leading to a decrease in the output voltage v_o and an increase in the inductor current i_L . By contrast, the load is decreased at $t = 0.11$ s resulting in an overshoot of the output voltage v_o and a drop of the inductor current i_L .

Figure 3.9 depicts the schematic of the bidirectional buck converter built in the laboratory. A TMS320F28335 DSP is employed to execute the control algorithm and generate PWM signals at a switching frequency of 50 kHz. The input and output DC voltages are measured by the measurement circuit equipped with two voltage transducers LEM LV-25P while two current transducers LEM LA-25-NP are used to measure the input and the inductor currents.

Table 3.2: Parameters of bidirectional buck converter

Parameter	Symbol	Value	Unit
Input voltage	V_i	100	V
Output voltage	V_o	48	V
Power	P	300	W
Inductance @50kHz	L	1000	μH
Resistance @50kHz	R_L	180	$\text{m}\Omega$
Power semi. devices	S_1 and S_2	IRFP260MPBF	MOSFET
Switching frequency	f_s	50	kHz
Output capacitor	C_o	20	μF
DC link capacitor	C_{DC}	1000	μF

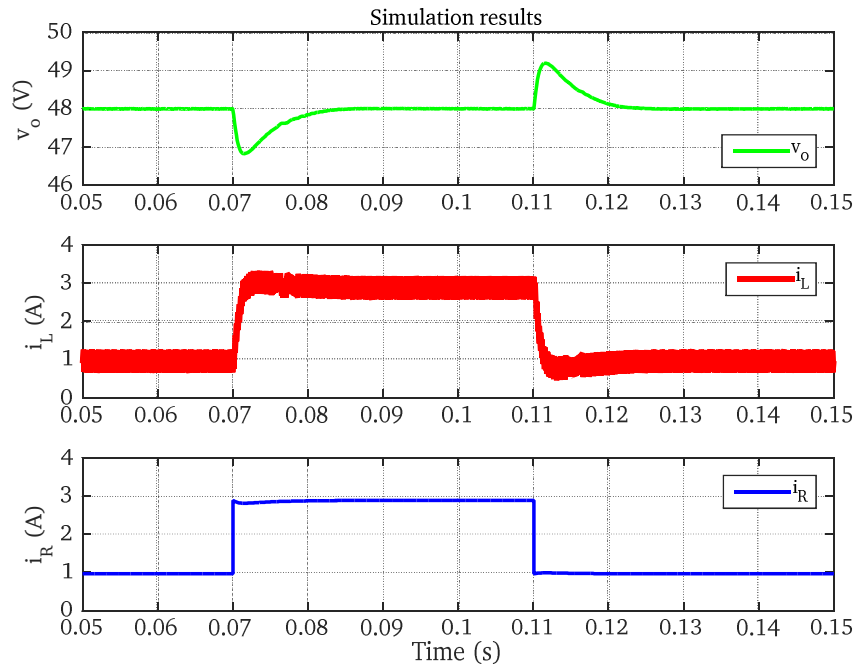


Figure 3.8: Simulation results of the bidirectional buck converter

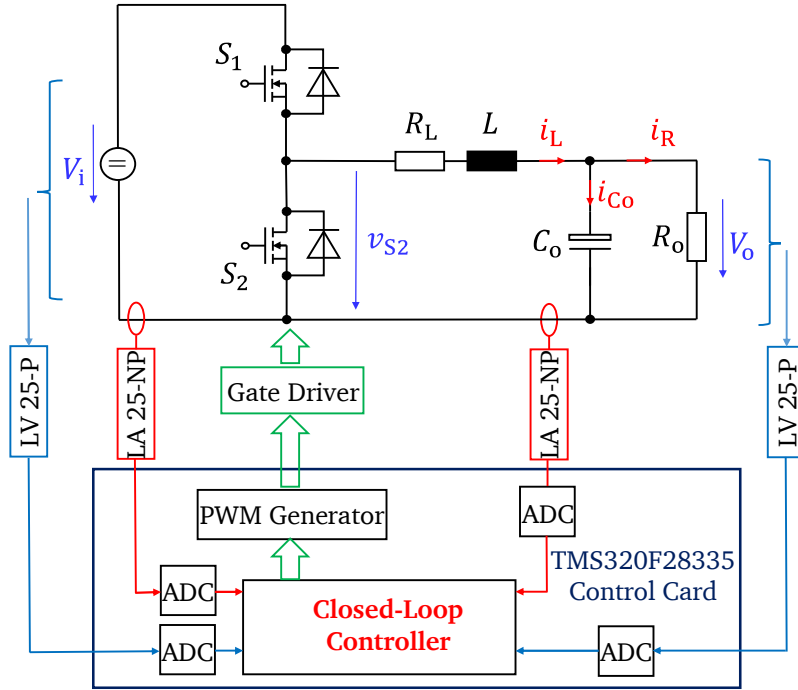


Figure 3.9: System diagram of the bidirectional buck converter

Experimental results are illustrated in Figure 3.10 and Figure 3.11. Figure 3.10 shows the responses of the output voltage v_o , the inductor current i_L and the load current i_R corresponding to an increase in the resistive load. On the contrary, the experimental results depicted in Figure 3.11 show that the decrease in the load leads to an overshoot of the voltage and a decrease in the inductor current as well. It is observed that the undershoot and overshoot of the voltage are around 1 V or 2% of the reference value and the settling time is almost 15 ms in both cases. From Figure 3.8 and Figure 3.10 - Figure 3.11, it is confirmed that experimental results concur with those attained in the simulation model, verifying the validity of the simulation results.

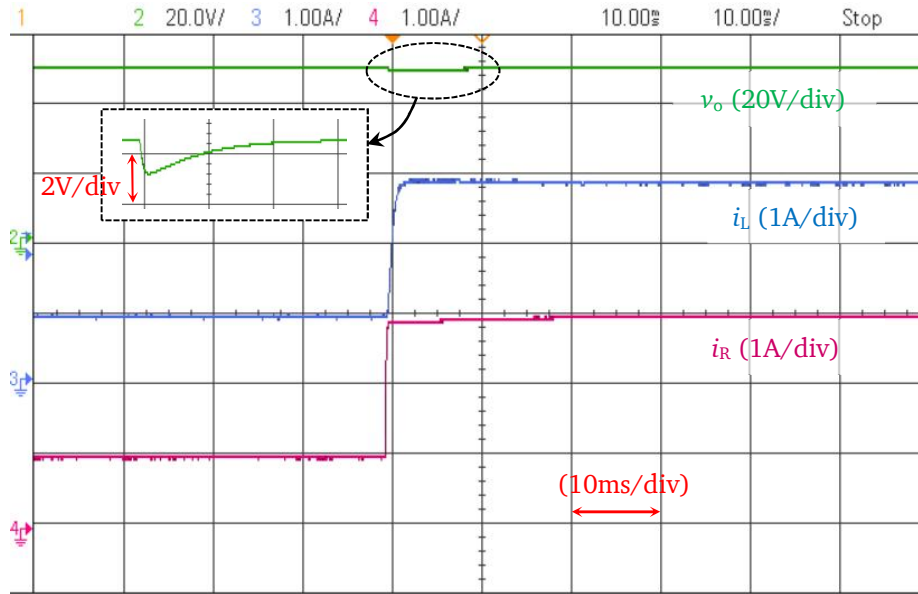


Figure 3.10: Experimental result of the buck converter for load current step up from 0.96 A to 2.88 A

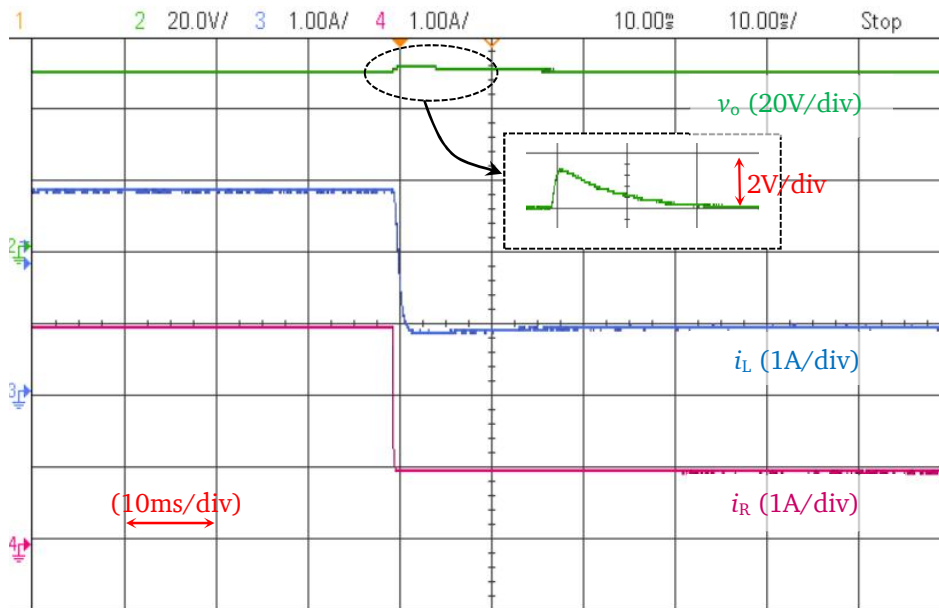


Figure 3.11: Experimental result of the buck converter for load current step down from 2.88 A to 0.96 A

3.5 Modeling and Control of Dual Active Bridge Converter

3.5.1 Introduction

As shown in Figure 2.17, the interconnected converter portrayed in the red box is required to provide a galvanic isolation and bidirectional power transfer capability. For these requirements, the DAB converter is a suitable candidate. This chapter focusses on the modeling and control of

the interface converter where a DAB converter is adapted. Both the output current and output voltage of the DAB converter are controlled in a cascaded two-control-loop structure to ensure a flexible exchange of power inside a nanogrid and among different nanogrids.

Many researches have been carried out for modeling of the DAB converter. The authors in [55] and [130] present the full-order modeling and dynamic analysis of a phase-shift DAB converter in both continuous-time domain and discrete-time domain, respectively. The leakage inductance current of the high-frequency (HF) transformer is considered as a state variable in both approaches. These two methods model the DAB converter in such a way that a single closed loop control structure is designed for the output voltage. Since more variables are considered, the attained full-order models ensure higher accuracy as compared to reduced-order models introduced in [131].

Apart from the single voltage control loop, a cascaded control structure has been developed for the DAB converter, as presented in [132], in which an inner current control loop is inserted within an outer voltage cascade. Typically, the current control loop is responsible for controlling the current in the windings of the HF transformer. An alternative solution as presented in [133] proposes the function of the current control loop to regulate the output current which is fed to the output voltage. This approach is based on modeling of the DAB converter in the discrete-time domain and is developed to be implemented on a digital signal processing unit (DSP).

Based on a generalized averaging method mentioned in [55], this work presents a full-order continuous-time state-space model of a DAB converter which offers a modification in the topology of the DAB in a manner that an LC filter is added before the output DC link for meeting the electromagnetic interference (EMI) requirement. The generalized state-space averaging technique has an advantage associated to achieve more accurate models [126], as it considers more terms in Fourier series of the high frequency transformer currents as state variables [115], [134]. Moreover, rather than using a single voltage control loop as proposed in previous work, a cascaded control structure is developed for the output current and the output voltage in this research.

3.5.2 The conventional DAB converter

The bidirectional isolated DAB converter was first introduced in early 1990s [135] as a candidate for high power density and high power DC/DC converter. Figure 3.12 shows the circuit diagram of a conventional DAB converter. It is composed of two H-bridges, two DC

capacitors and a HF transformer. The HF transformer functions to provide galvanic isolation between the two voltage levels. Besides, using the HF transformer along with high-frequency switching devices results in the reduction of the weight and volume of passive magnetic devices [126]. The DAB converter has a symmetrical configuration where each H-bridge consists of four switching devices along with anti-parallel freewheeling diodes.

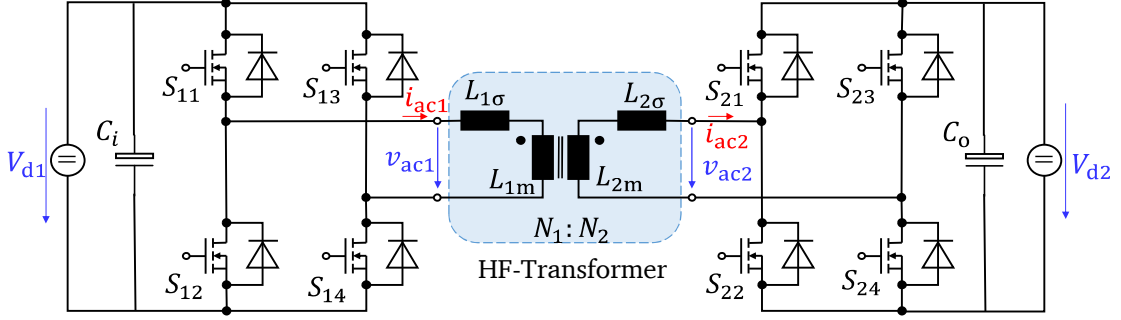


Figure 3.12: Bidirectional dual active bridge converter

Three methods are commonly applied to control the DAB converter: 1) the control of phase shift ϕ between the two bridges; 2) the duty ratios of switching devices and 3) the switching frequency [55], [133]. The phase-shift control method is employed in this work, as it is simple and effective. In the phase-shift modulation technique, the power flow is controlled by changing the phase shift between two square wave voltages generated by the two H-bridges while the duty cycle is kept constant at 50%. The sign of the phase shift determines the direction of power flow. Power transferred from the leading bridge to the lagging bridge is given as follows

$$P = \frac{V_{d1}V_{d2}}{2Nf_sL_t}d(1-d) \quad (3.52)$$

where V_{d1} and V_{d2} are the input and output voltages, respectively, f_s is the switching frequency, $d = \phi/\pi$ is the phase shift ratio with ϕ being the phase shift, $N = N_1/N_2$ is the turn ratio from the primary side to the secondary side of the HF transformer, $L_t = L_{1\sigma}/N^2 + L_{2\sigma}$ is the leakage inductance referred to the secondary side where $L_{1\sigma}$ and $L_{2\sigma}$ are the leakage inductances in the primary and secondary sides, respectively.

3.5.3 Generalized model of the DAB converter

A simplified DAB referred to the secondary side is depicted in Figure 3.13. Note that Figure 3.13 slightly differs from Figure 3.12 where $V_i = V_{d1}/N$ is the input voltage referred to the secondary side, and $V_o = V_{d2}$ is the output voltage. The two bridges generate square wave voltages v_p and v_s at the terminals of the HF transformer with amplitudes equal to the DC

voltages V_i and V_o , respectively. L_t is the equivalent inductance and R_t is the equivalent resistance of the HF transformer, whereas, R_o is the load resistance. In comparison to the conventional DAB as shown in Figure 3.12, the DAB portrayed in Figure 3.13 has an LC output filter described by three components: an inductor L_f , a DC resistance R_f of the inductor and a capacitor C_f in order to meet the EMI requirement. The calculation of the parameters of the LC filter can be referred to the Appendix 6.2.1.2.

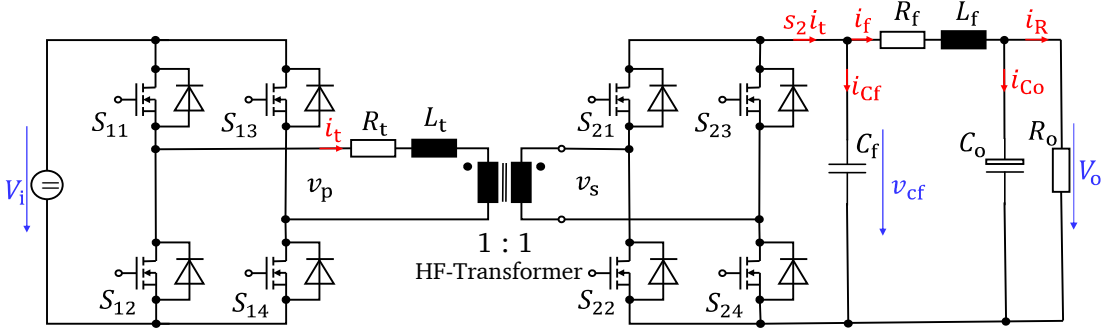


Figure 3.13: Simplified DAB converter referred to the secondary side

According to the phase shift modulation technique, the switching mode $s_1(t)$ of the left H-bridge, $s_2(t)$ of the right H-bridge and the transformer current for one period are illustrated in Figure 3.14 [55]. Assuming the transformers magnetizing current is neglected and the switching devices are ideal and have no voltage drop, the following waveforms are derived.

Only two states are possible for the voltage v_p at the transformer input side: 1) $+V_i$ when switches S_{11} and S_{14} are ON; and 2) $-V_i$ when switches S_{12} and S_{13} are ON [55]. Therefore,

$$v_p(t) = s_1(t)v_i(t)$$

$$\text{with } s_1(t) = \begin{cases} 1, & 0 \leq t < \frac{T_s}{2} \\ -1, & \frac{T_s}{2} \leq t < T_s \end{cases} \quad (3.53)$$

where $T_s = 1/f_s$, $v_i(t)$ is the input voltage with taking into account the perturbation, $\langle v_i \rangle_0 = V_i$.

Correspondingly, the terminal voltage at the secondary side is given as

$$v_s(t) = s_2(t)v_{cf}(t)$$

$$\text{with } s_2(t) = \begin{cases} 1, & \frac{d \cdot T_s}{2} \leq t < \frac{T_s}{2} + \frac{d \cdot T_s}{2} \\ -1, & \text{otherwise} \end{cases} \quad (3.54)$$

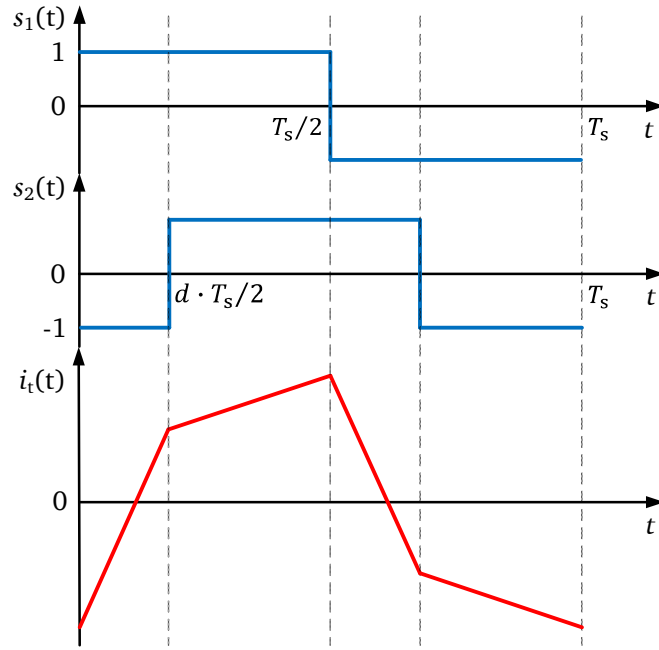


Figure 3.14: Waveforms during one period

The output voltage v_o , the filter voltage v_{cf} , the transformer current i_t and the filter current i_f are considered as state variables to model the DAB converter. By applying the Kirchhoff's law, the mathematical description of the DAB can be achieved as follows.

For $v_o(t)$:

$$i_f(t) = i_{Co}(t) + i_R(t) = C_o \frac{dv_o(t)}{dt} + \frac{v_o(t)}{R_o} \quad (3.55)$$

or

$$\frac{dv_o(t)}{dt} = -\frac{v_o(t)}{R_o C_o} + \frac{i_f(t)}{C_o} \quad (3.56)$$

For $i_t(t)$:

$$s_1(t)v_i(t) - s_2(t)v_{cf}(t) = R_t i_t(t) + L_t \frac{di_t(t)}{dt} \quad (3.57)$$

or

$$\frac{di_t(t)}{dt} = -\frac{R_t}{L_t} i_t(t) + \frac{s_1(t)v_i(t)}{L_t} - \frac{s_2(t)v_{cf}(t)}{L_t} \quad (3.58)$$

For $v_{cf}(t)$:

$$s_2(t)i_t(t) = i_f(t) + i_{cf}(t) = i_f(t) + C_f \frac{dv_{cf}(t)}{dt} \quad (3.59)$$

or

$$\frac{dv_{cf}(t)}{dt} = \frac{s_2(t)i_t(t)}{C_f} - \frac{i_f(t)}{C_f} \quad (3.60)$$

For $i_f(t)$:

$$v_{cf}(t) = R_f i_f(t) + L_f \frac{di_f(t)}{dt} + v_o(t) \quad (3.61)$$

or

$$\frac{di_f(t)}{dt} = -\frac{v_o(t)}{L_f} - \frac{R_f}{L_f} i_f(t) + \frac{v_{cf}(t)}{L_f} \quad (3.62)$$

The transformer current i_t is purely AC. By contrast, only DC components of the three state variables: the output voltage v_o , the filter voltage v_{cf} and the output current i_f , are considered, as they are DC in the steady state. If more terms in the Fourier series are used, a more accurate model could be obtained, but that would render a more complex model, influencing the controller design [126]. For simplicity, only the 1st harmonic of i_t is taken into account in this work. By determining the DC and the 1st harmonic according to (3.5) and (3.12)-(3.14), the state-space differential equations of the DAB are given as follows

$$\frac{d\langle v_o \rangle_0}{dt} = -\frac{1}{R_o C_o} \langle v_o \rangle_0 + \frac{1}{C_o} \langle i_f \rangle_0 \quad (3.63)$$

$$\begin{aligned} \frac{d(\Re\{\langle i_t \rangle_1\})}{dt} = & -\frac{R_t}{L_t} \Re\{\langle i_t \rangle_1\} + \omega_s \Im\{\langle i_t \rangle_1\} + \frac{1}{L_t} (\langle s_1 \rangle_0 \Re\{\langle v_i \rangle_1\} + \Re\{\langle s_1 \rangle_1\} \langle v_i \rangle_0) \\ & - \frac{1}{L_t} (\langle s_2 \rangle_0 \Re\{\langle v_{cf} \rangle_1\} + \Re\{\langle s_2 \rangle_1\} \langle v_{cf} \rangle_0) \end{aligned} \quad (3.64)$$

$$\begin{aligned} \frac{d(\Im\{\langle i_t \rangle_1\})}{dt} = & -\frac{R_t}{L_t} \Im\{\langle i_t \rangle_1\} - \omega_s \Re\{\langle i_t \rangle_1\} + \frac{1}{L_t} (\langle s_1 \rangle_0 \Im\{\langle v_i \rangle_1\} + \Im\{\langle s_1 \rangle_1\} \langle v_i \rangle_0) \\ & - \frac{1}{L_t} (\langle s_2 \rangle_0 \Im\{\langle v_{cf} \rangle_1\} + \Im\{\langle s_2 \rangle_1\} \langle v_{cf} \rangle_0) \end{aligned} \quad (3.65)$$

$$\frac{d\langle v_{cf} \rangle_0}{dt} = \frac{1}{C_f} \langle s_2 \rangle_0 \langle i_t \rangle_0 + \frac{2}{C_f} \Re\{\langle s_2 \rangle_1\} \Re\{\langle i_t \rangle_1\} + \frac{2}{C_f} \Im\{\langle s_2 \rangle_1\} \Im\{\langle i_t \rangle_1\} - \frac{1}{C_f} \langle i_f \rangle_0 \quad (3.66)$$

$$\frac{d\langle i_f \rangle_0}{dt} = -\frac{1}{L_f} \langle v_o \rangle_0 - \frac{R_f}{L_f} \langle i_f \rangle_0 + \frac{1}{L_f} \langle v_{cf} \rangle_0 \quad (3.67)$$

Equation (3.63)-(3.67) can be rewritten in a matrix equation as follows:

$$\begin{aligned}
\frac{d}{dt} \begin{bmatrix} \langle v_o \rangle_0 \\ \Re\{\langle i_t \rangle_1\} \\ \Im\{\langle i_t \rangle_1\} \\ \langle v_{cf} \rangle_0 \\ \langle i_f \rangle_0 \end{bmatrix} &= \begin{bmatrix} -\frac{1}{R_o C_o} & 0 & 0 & 0 & \frac{1}{C_o} \\ 0 & -\frac{R_t}{L_t} & \omega_s & -\frac{\Re\{\langle s_2 \rangle_1\}}{L_t} & 0 \\ 0 & -\omega_s & -\frac{R_t}{L_t} & -\frac{\Im\{\langle s_2 \rangle_1\}}{L_t} & 0 \\ 0 & \frac{2 \cdot \Re\{\langle s_2 \rangle_1\}}{C_f} & \frac{2 \cdot \Im\{\langle s_2 \rangle_1\}}{C_f} & 0 & -\frac{1}{C_f} \\ -\frac{1}{L_f} & 0 & 0 & \frac{1}{L_f} & -\frac{R_f}{L_f} \end{bmatrix} \times \begin{bmatrix} \langle v_o \rangle_0 \\ \Re\{\langle i_t \rangle_1\} \\ \Im\{\langle i_t \rangle_1\} \\ \langle v_{cf} \rangle_0 \\ \langle i_f \rangle_0 \end{bmatrix} \\
&+ \begin{bmatrix} 0 \\ \frac{\Re\{\langle s_1 \rangle_1\}}{L_t} \\ \frac{\Im\{\langle s_1 \rangle_1\}}{L_t} \\ 0 \\ 0 \end{bmatrix} [\langle v_i \rangle_0] \quad (3.68)
\end{aligned}$$

The DC and the 1st harmonic of $s_1(t)$ and $s_2(t)$ were already calculated in (3.15), (3.17), (3.18). For convenience, they are restated as follows

$$\langle s_1 \rangle_0 = 0; \Re\{\langle s_1 \rangle_1\} = 0; \Im\{\langle s_1 \rangle_1\} = -\frac{2}{\pi} \quad (3.69)$$

$$\langle s_2 \rangle_0 = 0; \Re\{\langle s_2 \rangle_1\} = -\frac{2\sin(d\pi)}{\pi}; \Im\{\langle s_2 \rangle_1\} = -\frac{2\cos(d\pi)}{\pi} \quad (3.70)$$

Substituting (3.69) and (3.70) into (3.68), the state-space model of the DAB converter in the matrix form is expressed as (3.71).

$$\begin{aligned}
\frac{d}{dt} \begin{bmatrix} \langle v_o \rangle_0 \\ \Re\{\langle i_t \rangle_1\} \\ \Im\{\langle i_t \rangle_1\} \\ \langle v_{cf} \rangle_0 \\ \langle i_f \rangle_0 \end{bmatrix} &= \begin{bmatrix} -\frac{1}{R_o C_o} & 0 & 0 & 0 & \frac{1}{C_o} \\ 0 & -\frac{R_t}{L_t} & \omega_s & \frac{2\sin(d\pi)}{\pi L_t} & 0 \\ 0 & -\omega_s & -\frac{R_t}{L_t} & \frac{2\cos(d\pi)}{\pi L_t} & 0 \\ 0 & -\frac{4\sin(d\pi)}{\pi C_f} & -\frac{4\cos(d\pi)}{\pi C_f} & 0 & -\frac{1}{C_f} \\ -\frac{1}{L_f} & 0 & 0 & \frac{1}{L_f} & -\frac{R_f}{L_f} \end{bmatrix} \times \begin{bmatrix} \langle v_o \rangle_0 \\ \Re\{\langle i_t \rangle_1\} \\ \Im\{\langle i_t \rangle_1\} \\ \langle v_{cf} \rangle_0 \\ \langle i_f \rangle_0 \end{bmatrix} \\
&+ \begin{bmatrix} 0 \\ 0 \\ 2 \\ 0 \\ 0 \end{bmatrix} \left[\frac{1}{\pi L_t} \right] [\langle v_i \rangle_0] \quad (3.71)
\end{aligned}$$

3.5.4 Small-signal model of the DAB converter

To design controllers and analyze the stability for the DAB converter, the small-signal control-to-output transfer functions have to be defined. The state-space representation of the DAB converter given in (3.71) allows determining the small-signal control-to-output transfer functions that illustrate the dynamic responses of the converter from a small deviation of the system to the control signal. The control signal is the phase-shift ratio d as the phase-shift modulation technique is applied. The input voltage is assumed to be constant. The deviation of the state variables and the control signal are defined as

$$d = D + \Delta d \quad (3.72)$$

$$\langle v_o \rangle_0 = \langle V_o \rangle_0 + \Delta \langle v_o \rangle_0 \quad (3.73)$$

$$\Re\{\langle i_t \rangle_1\} = \Re\{\langle I_t \rangle_1\} + \Delta(\Re\{\langle i_t \rangle_1\}) \quad (3.74)$$

$$\Im\{\langle i_t \rangle_1\} = \Im\{\langle I_t \rangle_1\} + \Delta(\Im\{\langle i_t \rangle_1\}) \quad (3.75)$$

$$\langle v_{cf} \rangle_0 = \langle V_{cf} \rangle_0 + \Delta \langle v_{cf} \rangle_0 \quad (3.76)$$

$$\langle i_f \rangle_0 = \langle I_f \rangle_0 + \Delta \langle i_f \rangle_0 \quad (3.77)$$

where large-signal state variables are represented by lower characters, steady state variables by capital characters and small-signal state variables by Δ . Note that (3.71) includes

multiplications of control input and state variables. The following multiplication is derived as an example as described in (3.78) [56]. Other terms can be achieved in the same way.

$$\begin{aligned}
 \sin(d\pi) \langle v_{cf} \rangle_0 &= \sin[(D + \Delta d)\pi] \cdot (\langle V_{cf} \rangle_0 + \Delta \langle v_{cf} \rangle_0) \\
 &= (\sin(D\pi) \cdot \cos(\Delta d\pi) + \cos(D\pi) \cdot \sin(\Delta d\pi)) \cdot (\langle V_{cf} \rangle_0 + \Delta \langle v_{cf} \rangle_0) \\
 &\approx \sin(D\pi) \cdot \langle V_{cf} \rangle_0 + \sin(D\pi) \cdot \Delta \langle v_{cf} \rangle_0 + \cos(D\pi) \cdot \Delta d\pi \cdot \langle V_{cf} \rangle_0
 \end{aligned} \tag{3.78}$$

It should be mentioned that the approximation (3.78) is based on the assumption that for small value of any variable x we have $\sin x \approx x$, $\cos x \approx 1$ and the multiplication of two small variables is ignored.

Steady state values of $\langle v_o \rangle_0$, $(\Re\{\langle i_t \rangle_1\})$, $(\Im\{\langle i_t \rangle_1\})$, $\langle v_{cf} \rangle_0$, $\langle i_f \rangle_0$ can be found from (3.71) by solving

$$\frac{d}{dt} \begin{bmatrix} \langle v_o \rangle_0 \\ \Re\{\langle i_t \rangle_1\} \\ \Im\{\langle i_t \rangle_1\} \\ \langle v_{cf} \rangle_0 \\ \langle i_f \rangle_0 \end{bmatrix} = 0 \tag{3.79}$$

Substituting (3.72)–(3.79) into (3.71), the small-signal model of the DAB converter is given in (3.80), which can be used to obtain the control-to-output transfer functions of the DAB converter.

$$\begin{aligned}
\frac{d}{dt} \begin{bmatrix} \Delta \langle v_o \rangle_0 \\ \Delta(\Re\{\langle i_t \rangle_1\}) \\ \Delta(\Im\{\langle i_t \rangle_1\}) \\ \Delta \langle v_{cf} \rangle_0 \\ \Delta \langle i_f \rangle_0 \end{bmatrix} &= \begin{bmatrix} -\frac{1}{R_o C_o} & 0 & 0 & 0 & \frac{1}{C_o} \\ 0 & -\frac{R_t}{L_t} & \omega_s & \frac{2\sin(D\pi)}{\pi L_t} & 0 \\ 0 & -\omega_s & -\frac{R_t}{L_t} & \frac{2\cos(D\pi)}{\pi L_t} & 0 \\ 0 & -\frac{4\sin(D\pi)}{\pi C_f} & -\frac{4\cos(D\pi)}{\pi C_f} & 0 & -\frac{1}{C_f} \\ -\frac{1}{L_f} & 0 & 0 & \frac{1}{L_f} & -\frac{R_f}{L_f} \end{bmatrix} \\
&\times \begin{bmatrix} \Delta \langle v_o \rangle_0 \\ \Delta(\Re\{\langle i_t \rangle_1\}) \\ \Delta(\Im\{\langle i_t \rangle_1\}) \\ \Delta \langle v_{cf} \rangle_0 \\ \Delta \langle i_f \rangle_0 \end{bmatrix} + \begin{bmatrix} 0 \\ \frac{2\cos(D\pi)\langle V_{cf} \rangle_0}{L_t} \\ -\frac{2\sin(D\pi)\langle V_{cf} \rangle_0}{L_t} \\ \frac{4}{C_f} [\Im\{\langle i_t \rangle_1\} \sin(D\pi) - \Re\{\langle i_t \rangle_1\} \cos(D\pi)] \\ 0 \end{bmatrix} \Delta d
\end{aligned} \quad (3.80)$$

Denoting $X = [\Delta \langle v_o \rangle_0, \Delta(\Re\{\langle i_t \rangle_1\}), \Delta(\Im\{\langle i_t \rangle_1\}), \Delta \langle v_{cf} \rangle_0, \Delta \langle i_f \rangle_0]^T$ as the state variable vector and $Y = \mathbf{I} \cdot X$ as the output variables where \mathbf{I} represents the 5×5 identity matrix, the small-signal state-space representation of the DAB converter is

$$\begin{cases} \frac{d}{dt} X = \mathbf{A} \cdot X + \mathbf{B} \cdot \Delta d \\ Y = \mathbf{I} \cdot X \end{cases} \quad (3.81)$$

where

$$\mathbf{A} = \begin{bmatrix} -\frac{1}{R_o C_o} & 0 & 0 & 0 & \frac{1}{C_o} \\ 0 & -\frac{R_t}{L_t} & \omega_s & \frac{2\sin(D\pi)}{\pi L_t} & 0 \\ 0 & -\omega_s & -\frac{R_t}{L_t} & \frac{2\cos(D\pi)}{\pi L_t} & 0 \\ 0 & -\frac{4\sin(D\pi)}{\pi C_f} & -\frac{4\cos(D\pi)}{\pi C_f} & 0 & -\frac{1}{C_f} \\ -\frac{1}{L_f} & 0 & 0 & \frac{1}{L_f} & -\frac{R_f}{L_f} \end{bmatrix} \quad (3.82)$$

$$\mathbf{B} = \begin{bmatrix} 0 \\ \frac{2\cos(D\pi)\langle V_{cf} \rangle_0}{L_t} \\ -\frac{2\sin(D\pi)\langle V_{cf} \rangle_0}{L_t} \\ \frac{4}{C_f} [\Im\{\langle i_t \rangle_1\} \sin(D\pi) - \Re\{\langle i_t \rangle_1\} \cos(D\pi)] \\ 0 \end{bmatrix} \quad (3.83)$$

In order to complement the state-space equation (3.81), the calculation of $\Re\{\langle i_t \rangle_1\}$ and $\Im\{\langle i_t \rangle_1\}$ is of critical importance. For the determination of the real part $\Re\{\langle i_t \rangle_1\}$ and the imaginary part $\Im\{\langle i_t \rangle_1\}$ of the first harmonic, the DAB converter is run at a steady state with a predefined value of $d = D$ and after obtaining the leakage current i_t , the Fast-Fourier Transform (FFT) is applied.

3.5.5 Closed-loop control of the DAB converter

3.5.5.1 Control scheme for the DAB converter

Based on the state-space representation (3.81), the control-to-output transfer functions are defined by (3.84).

$$\mathbf{G}_{\text{dab}} = [G_{v_d, \text{dab}}, G_{i_{Rd}, \text{dab}}, G_{i_{ld}, \text{dab}}, G_{v_{cf}, \text{dab}}, G_{i_{fd}, \text{dab}}]^T = (s \cdot \mathbf{I} - \mathbf{A})^{-1} \mathbf{B} \quad (3.84)$$

where the DAB converter is represented by the nomenclature ‘dab’. $G_{v_d, \text{dab}}$, $G_{i_{Rd}, \text{dab}}$, $G_{i_{ld}, \text{dab}}$, $G_{v_{cf}, \text{dab}}$, and $G_{i_{fd}, \text{dab}}$ are the transfer functions of the small signals $\Delta\langle v_o \rangle_0$, $\Delta(\Re\{\langle i_t \rangle_1\})$, $\Delta(\Im\{\langle i_t \rangle_1\})$, $\Delta\langle i_{cf} \rangle_0$, and $\Delta\langle i_f \rangle_0$ depending on the small signal Δd , respectively. According to these transfer functions, the relationship between the change of the phase shift ratio Δd and the output voltage is represented by $G_{v_d, \text{dab}}$, while $G_{i_{fd}, \text{dab}}$ denotes the dependence of the current i_f , flowing into the filter, on Δd .

The cascaded control structure consisting of two control loops for the DAB converter is illustrated in Figure 3.15. The inner loop enables the control of the output current i_f and is superimposed by the outer loop which controls the output voltage v_o . Similar to the bidirectional buck converter, the control delay is represented by a first-order lag element $G_{d, \text{dab}}(s)$ with the time constant $T_d = 2 \cdot T_s$.

$$G_{d, \text{dab}}(s) = \frac{1}{1 + T_d \cdot s} \quad (3.85)$$

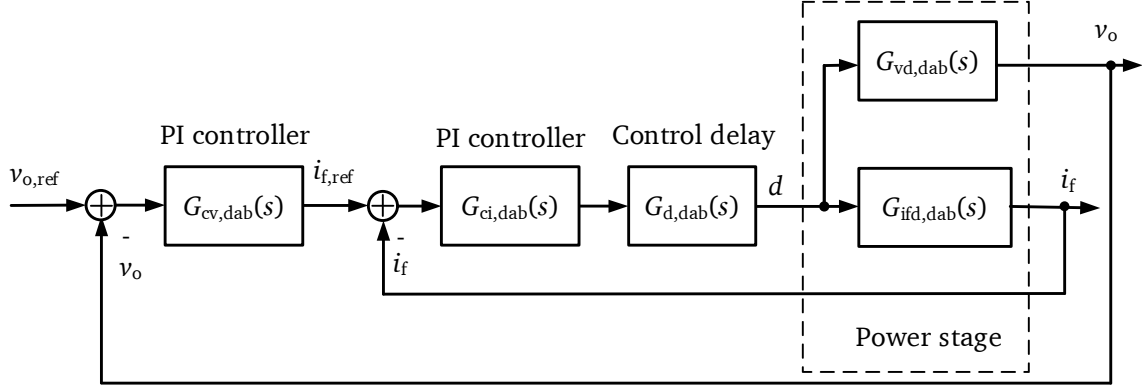


Figure 3.15. Control scheme for DAB converter

The transfer functions of the PI controllers for the current and the voltage loops are represented by (3.86) and (3.87), respectively.

$$G_{ci,dab}(s) = K_{pi,dab} + \frac{K_{ii,dab}}{s} \quad (3.86)$$

$$G_{cv,dab}(s) = K_{pv,dab} + \frac{K_{iv,dab}}{s} \quad (3.87)$$

where $K_{pi,dab}$, $K_{ii,dab}$ are the proportional and integral gains of the current controller while $K_{pv,dab}$, $K_{iv,dab}$ are related to the voltage controller.

The open-loop transfer functions $G_{OLi,dab}(s)$ from i_f to $i_{f,ref}$ and $G_{OLv,dab}(s)$ from v_o to $v_{o,ref}$ are given as:

$$G_{OLi,dab}(s) = G_{ci,dab}(s)G_{d,dab}(s)G_{ifd,dab}(s) \quad (3.88)$$

$$G_{OLv,dab}(s) = \frac{G_{cv,dab}(s)G_{ci,dab}(s)G_{d,dab}(s)G_{vd,dab}(s)}{1 + G_{ci,dab}(s)G_{d,dab}(s)G_{ifd,dab}(s)} \quad (3.89)$$

The SISO tool in MATLAB together with the procedure introduced in [125] is used for tuning the parameters of the PI controllers in the inner and the outer loops. The attained values of the gains of the proportional and integral parts are employed in both simulations and experiments and are listed in Table 3.3.

Table 3.3: Parameters of controllers

Voltage controller	Current controller
$K_{pv,dab} = 1.2 \text{ (A/V)}$	$K_{pi,dab} = 0.001 \text{ (1/A)}$
$K_{iv,dab} = 140 \text{ (A/Vs)}$	$K_{ii,dab} = 100 \text{ (1/As)}$

3.5.5.2 Bode plots of the open-loop transfer functions

Figure 3.16 and Figure 3.17 depicts the Bode diagrams of the open-loop transfer functions of the current and the voltage control loops, respectively. The gain crossover frequencies of the current loop is observed to be 100 Hz and that of the voltage loop 70 Hz. Due to the resonance point at the cut-off frequency of the output filter, the bandwidth of the two control loops are quite low. One possible solution for increasing the bandwidth is to increase the proportional gain of the PI controller. Nevertheless, increasing the proportional gain leads to decreases of both the gain margin and phase margin that might result in the destabilization of the current control loop. Alternative solution for the elimination of the resonance frequency is to provide a damping network at the output side of the converter as presented in [136].

It is observed that the open-loop transfer function of the current control loop has the gain margin of 15.2 dB corresponding to the frequency of 7.8 kHz and the phase margin of 88 degrees at the crossover frequency of 100 Hz, respectively. Similarly, the phase margin of the open-loop transfer function of the voltage control loop is 50 degrees at the crossover frequency of 70 Hz and the gain margin is 35 dB at 700 Hz as shown in Figure 3.17. The results show that the bandwidth of the outer control loop is lower than that of the inner control loop.

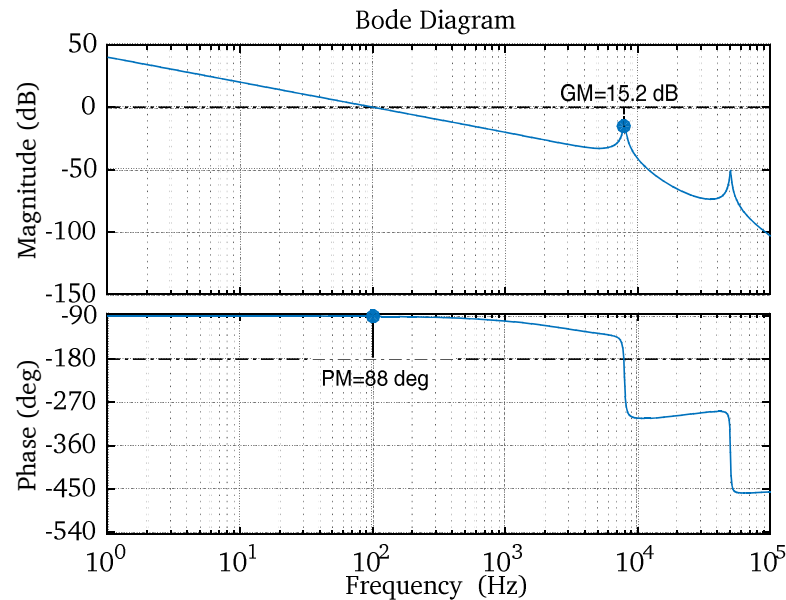


Figure 3.16: Bode plot of the open-loop transfer function of the current loop of the DAB converter

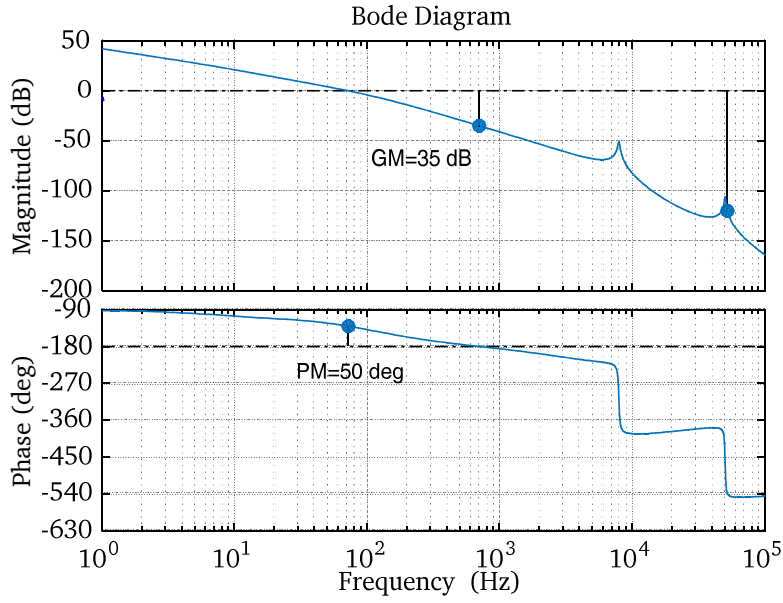


Figure 3.17: Bode plot of the open-loop transfer function of the voltage loop of the DAB converter

3.5.6 Simulation and experimental results

The operation of the proposed method is validated by the results from simulation and experimental models. The parameters of the DAB model are listed in Table 3.4.

Table 3.4: Parameters of DAB converter

Parameter	Symbol	Value	Unit
Input voltage	V_{d1}	100	V
Output voltage	V_{d2}	48	V
Power	P	400	W
Transformer ratio	$N_1 : N_2$	16:8	
Total inductance @50kHz	L'_t	60	μH
Total resistance @50kHz	R'_t	110	$\text{m}\Omega$
Power semi. devices	$S_{11} - S_{24}$	IRFP260MPBF	MOSFET
Switching frequency	f_s	50	kHz
Output capacitor	C_o	2200	μF
Filter capacitor	C_f	40	μF
Filter inductor	L_f	10	μH
Filter resistor	R_f	16	$\text{m}\Omega$

Figure 3.18 shows the simulation results associated to step changes in resistive loads. It can be seen that the output voltage v_o is kept stable around the nominal value of 48 V with only a slight overshoot and undershoot with respect to the fluctuations in the load. The load is raised at $t = 0.07$ s causing a decline in the output voltage v_o and a rise in the output current i_f . The undershoot of the voltage is approximately 1 V equivalent to 2% of the reference value. The settling time is around 20 ms that depends on the magnitude of the load variations and the output capacitance. An analogous phenomenon is visible at $t = 0.11$ s when the load is reduced abruptly.

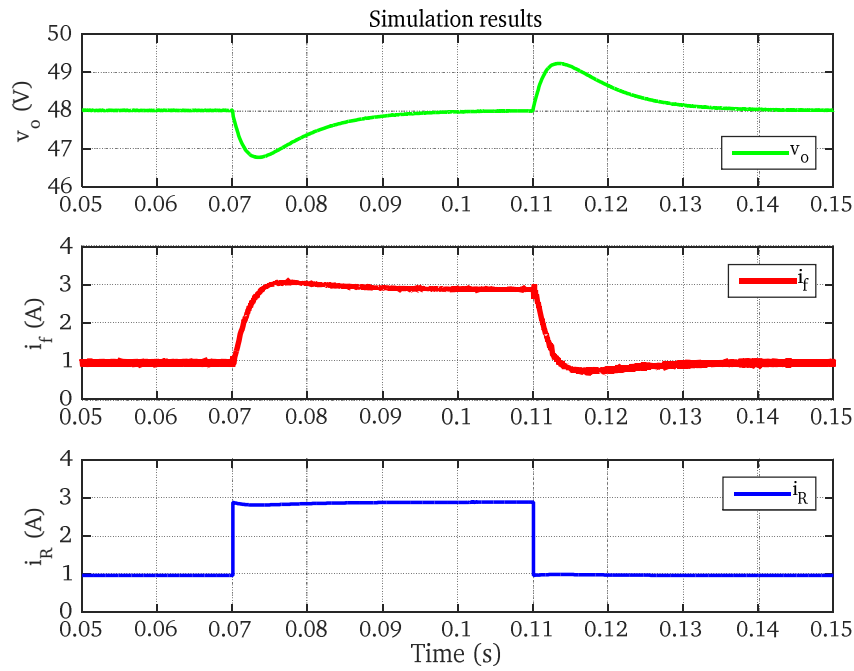


Figure 3.18: Simulation results of DAB converter

The schematic of the DAB converter built in the laboratory is depicted in Figure 3.19. For the execution of control algorithm and the generation of gate signals at a switching frequency of 50 kHz, the TMS320F28335 DSP is used. In this converter, an additional inductor is connected in series with the primary winding of the HF transformer to make sure that the converter can transfer the maximum power of 400 W corresponding to the total inductance, referred to the primary side, of 60 μ H. The calculation of the leakage inductance and the additional inductance can be found in Appendix 6.1.1.

As shown in Figure 3.19, two voltage transducers LEM LV-25P are employed to measure the input and output DC voltages. Similarly, the input and output currents are measured by two current transducers LEM LA-25-NP. The output filter, whose parameters can be referred in Appendix 6.1.1.3, is used in order to suppress conducted EMI.

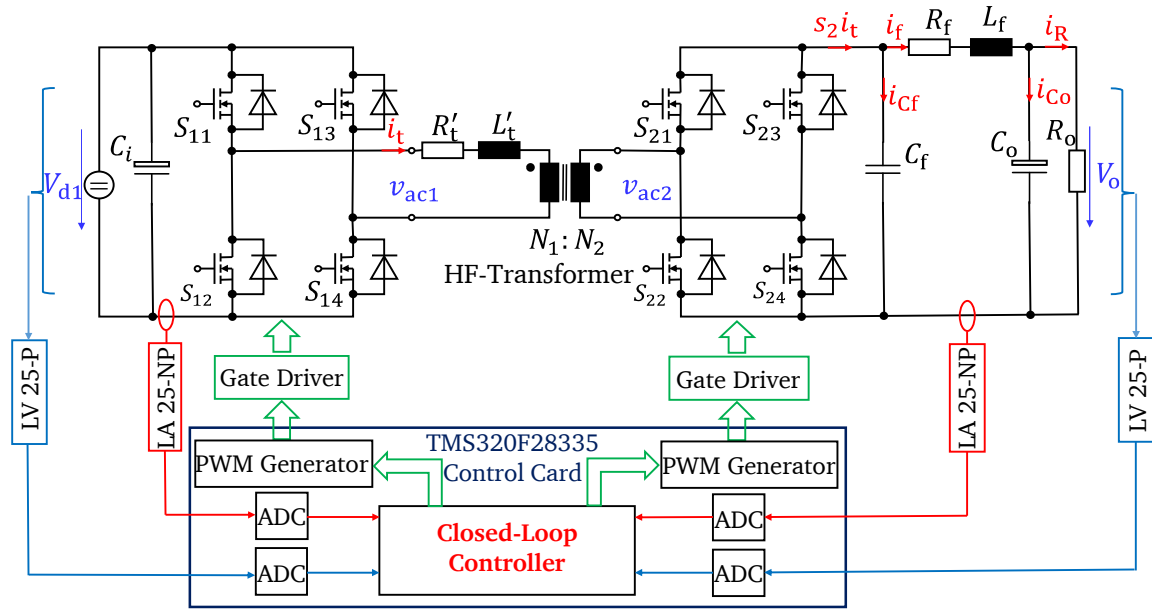


Figure 3.19: System diagram of the DAB converter

Figure 3.20 - Figure 3.22 show the experimental results. The responses of the output voltage v_o , the output current i_f and the load current i_R are demonstrated in Figure 3.20 corresponding to the step up of the resistive load. As observed, the experimental results coincide with simulation results, since the undershoot of the voltage is also around 1 V or 2% of the reference value as well as the settling time is approximately 20 ms. Figure 3.21 illustrates the experimental results regarding the decrease in the resistive load. When comparing Figure 3.18 and Figure 3.21, a similarity between the simulation and experimental results in regards to the step down of the load can be observed. The terminal voltages of the HF transformer and the current flowing in the primary winding are shown in Figure 3.22.

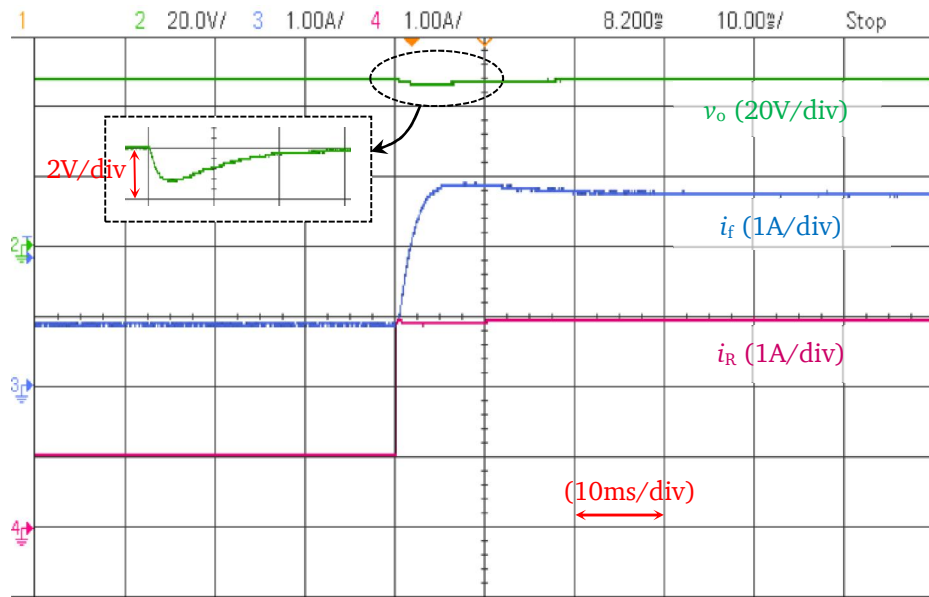


Figure 3.20: Experimental result of the DAB converter for load current step up from 0.96 A to 2.88 A

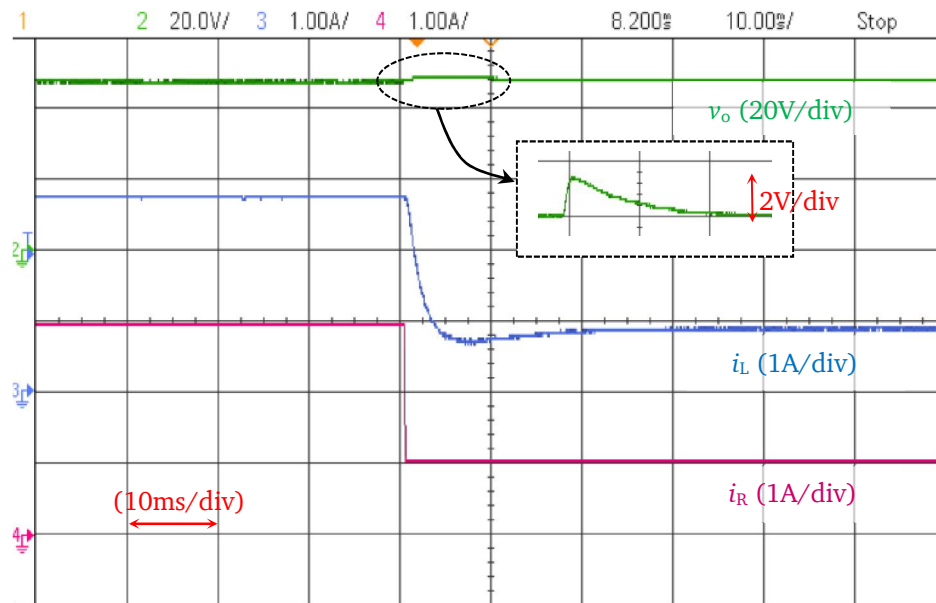


Figure 3.21: Experimental result of the DAB converter for load current step down from 2.88 A to 0.96 A

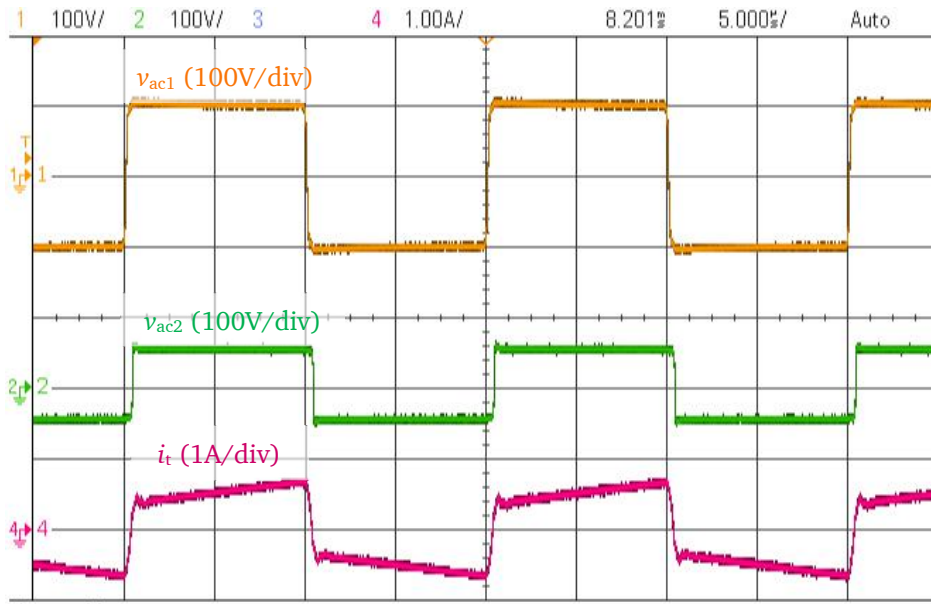


Figure 3.22: Switching wave form for load current of 0.96 A

3.6 Summary

In this chapter, the small-signal modeling method based on state-space averaging technique was used in modeling the bidirectional buck converter and the generalized state-space averaging technique was employed for the DAB converter. For the bidirectional buck converter, only the DC components of the DC state variables are considered while both the DC component of the DC state variables and the fundamental harmonic of the AC state variables are taken into account for the DAB converter. Control-to-output transfer functions were derived from the state-space representation to design a cascaded control structure composed of the output current and the output voltage control loops. The effectiveness of the developed model was verified by both simulations and experiments. The attained results depict good transient responses of the output current as well as the output voltage under the changes in the resistive loads. The next chapter considers the application of the developed control techniques to manage the exchange of electrical power among multiple nanogrids working in the autonomous mode.

4 A self-sustained and flexible control strategy for DC nanogrids

4.1 Introduction

As already mentioned in Chapter 2, a nanogrid is a power distribution system which is analogous to a microgrid but smaller in scale. Like microgrids, nanogrids have a capability of operating in isolated or grid connected mode hence, making them an appropriate solution for population living in rural or remote areas. To avoid power outage and increase the operational efficiency, nanogrids are commonly connected to the utility grid [19], [20]. However, to ensure the reliable operation of nanogrids in remote or isolated areas where main grid does not exist, different methods have been developed to prevent the imbalance between consumed and generated electrical power.

In this thesis, a self-sustained and flexible control for nanogrids is developed. Based on the Open Energy System, the nanogrids can be operated in either independent or interconnected mode without the need for a dedicated communication network. Each nanogrid can exchange power with its counterparts through an external DC bus by using a bidirectional dual active bridge DC/DC converter, resulting in galvanic isolation between the external DC bus and the internal structure. This architecture allows integration of multiple nanogrids and sharing of electrical energy among them with high reliability, flexibility and safety by the virtue of redundancy. If one DC nanogrid is not able to fulfill its load demand, other interconnecting DC nanogrids can support through an external DC bus voltage to ensure a continuous operation of critical loads. Furthermore, the proposed control strategy manages the power of the PV panel, the interconnections and the battery in such a way that renewable energy can be harvested to the maximum since the voltage threshold of the primary control loop of the PV unit is set at the highest value. Additionally, the control algorithm ensures a self-configuration capability of the nanogrid allowing the nanogrid to operate properly even if one or two power units are disconnected. The power exchange in a nanogrid and within the integrated nanogrid architecture is also regulated based on the SoC of the battery in order to prevent extreme charging situations and to avoid the disruption of the external DC bus [65], [67].

4.2 Proposed control strategy

The configuration of the DC nanogrid system and the interconnection of multiple DC nanogrids are shown in Figure 2.17 and Figure 2.18, respectively. This chapter presents the hierarchical control structure, as shown in Figure 4.1, which is used to regulate power in a nanogrid and within nanogrids to provide the system with the capability of self-sustaining itself. The control strategy is also aimed to coordinate among different sources of power supplies and to optimize the power flow between power generation sources and loads. To achieve this coordination and optimization, a control algorithm is implemented with two levels: a primary control and a secondary control. It is necessary to mention again that in order to prevent overcharging or deep discharging of the battery and to prevent the excess and breakdown of voltage through the external DC bus within a defined threshold, the control strategy is implemented according to the SoC of the battery and the levels of the external DC bus voltage.

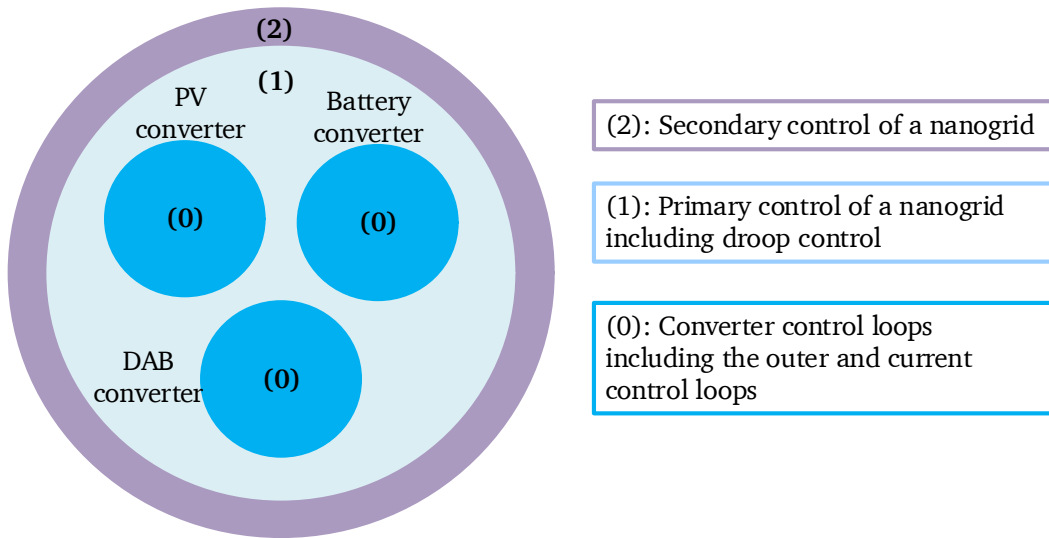


Figure 4.1: The proposed hierarchical control structure of the nanogrid

4.2.1 Primary control

The primary control as shown in Figure 4.2 consists of converter control loops (one converter control loop per converter) and the droop control. This control level is responsible for regulating the internal DC bus voltage of the nanogrid by adjusting the current injection into the nanogrid. Therefore, it is appropriate for nanogrids equipped with a decentralized control architecture that allows sharing power among different DC sources without establishing any communication link between them.

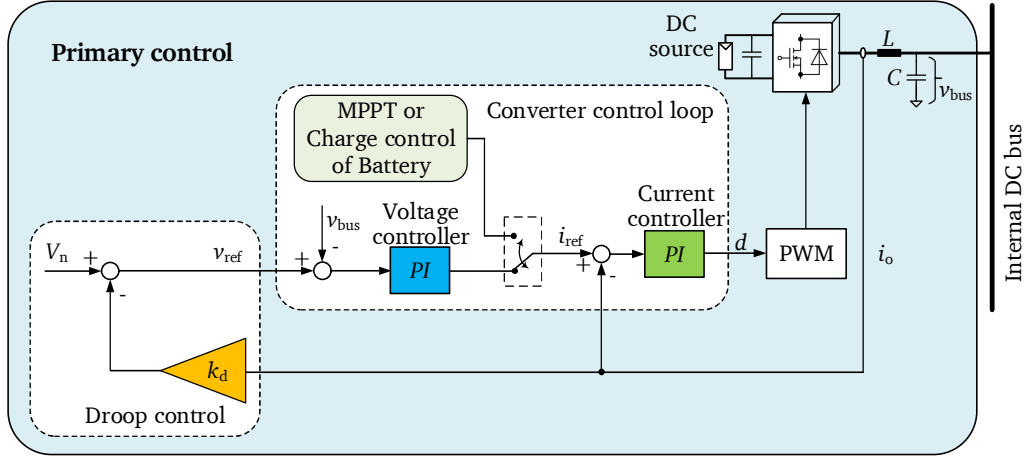


Figure 4.2: Primary control of nanogrids

Typically, a converter control loop consists of an outer converter control loop and an inner converter control loop. The outer converter control loop may be implemented as a voltage control, an MPPT algorithm for the PV system or a charge control strategy of the battery, based on the requirements of the system, while the inner converter control loop is a current control, as shown in Figure 4.2. The outer converter control loop is responsible for setting the reference current while the function of the current control loop is to regulate the output current to track the reference value. Note that the power interfaces between the power sources and the nanogrid can work either as current source converters (CSCs) or voltage source converters (VSCs) [33], [137]. RESs working in an MPPT mode and batteries operating in a charging mode are typical examples of CSCs as they extract constant power regardless of the condition where the RESs unit operates as a constant power source and batteries behave as a constant power load in the nanogrid system. These units can be defined as controllable current sources that set the reference current for the inner current loop. At least one of the converters must regulate the internal bus voltage by controlling the current injection into the internal DC bus according to the feedback signal of the bus voltage to stabilize the internal DC bus voltage of the nanogrid system.

To extract maximum power from RESs, the maximum power point tracking algorithm is employed. However, it is not always applicable in isolated systems, where the nanogrid is not connected to the main grid, an overcharge situation of the battery might occur due to a surplus of renewable energy [25]. In such a case, the droop control is employed in order to limit power surplus. By using the droop control, power can be shared among sources through interface converters in relation to their rated power [32]. As demonstrated in Figure 4.2, the droop control loop superimposes the converter control loops to regulate the reference voltage of each interface converter, thereby allowing current sharing among different sources inside a nanogrid.

The plug-and-play capability is therefore ensured by the droop control algorithm [76]. As shown in Figure 4.3, the droop curves are defined at respective voltage ranges. According to Figure 4.3, the PV has the highest priority to inject power into the loads since its reference voltage is set at the highest threshold [41]. The reference voltage of the voltage control loop is defined as

$$v_{\text{ref},i} = V_{n,i} - k_{d,i} \cdot i_{o,i} \quad (4.1)$$

where $V_{n,i}$ is the voltage threshold, $i_{o,i}$ is the output current and $k_{d,i}$ is the droop coefficient of the converter $\#i$ ($i = 1, 2, 3$), respectively. The typical design principle is to choose the largest droop coefficient while limiting the internal DC voltage deviation at the maximum load condition on the basis of which the droop coefficient is selected [32]. Hence, the droop coefficient of each converter is given as follows

$$k_{d,i} = \frac{\Delta v_{\text{max}}}{i_{o,i,\text{max}}} \quad (4.2)$$

where $i_{o,i,\text{max}}$ is the maximum output current of the corresponding source $\#i$, Δv_{max} is the maximum value of the DC voltage deviation. The maximum value of the internal DC bus voltage deviation is set to 5% of the nominal voltage of 48 V as it is the accepted global value for all converters.

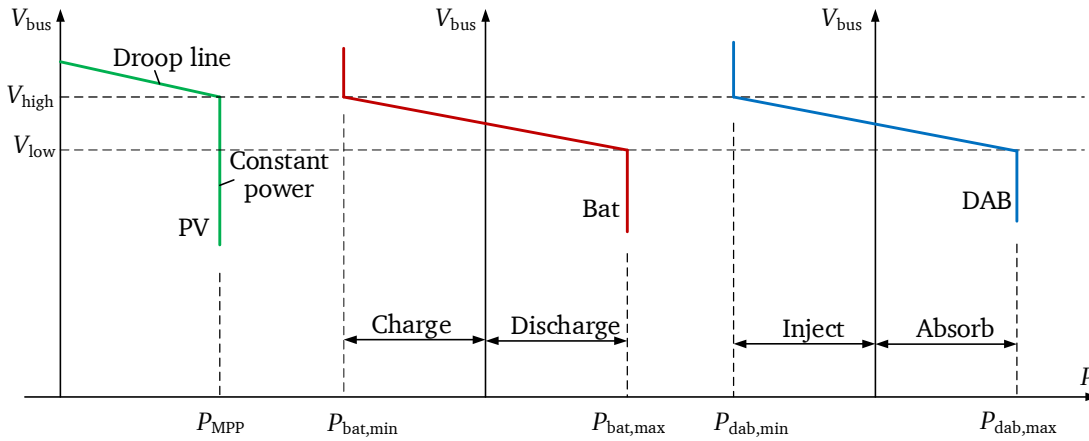


Figure 4.3: Droop curves of different sources in a nanogrid

In a standard situation where it is required to maximize energy yield, the PV is operated in the MPPT mode. If the power harvested from the PV is beyond what is needed to fulfill the load demand, the system will redirect any surplus power to charge the battery or to inject into the external DC network. If the battery is fully charged and the external DC bus voltage reaches the maximum voltage threshold, the PV will be switched into the droop mode to restrict power generation. When power from the PV cannot fulfill the local load demands, the battery starts discharging and the DAB converter extracts power from the interconnection. Under overload

conditions, a load shedding operation is scheduled to prevent the system from collapsing. The load shedding strategy can be found in [42], [138] and is out of scope in this work.

4.2.2 Secondary control

The droop control method ensures a flexible current sharing, but it has a major drawback as it introduces a voltage deviation on the internal DC bus voltage due to the imbalance between the production and consumption of power. To overcome this side effect, the centralized voltage secondary control is employed to stabilize the DC bus voltage. The secondary control eliminates the voltage deviation by adding an appropriate voltage δv , which is passed through a participation factor k_i ($i = 1, 2, 3$), and then $k_i \cdot \delta v$ is added to the reference voltage in the primary control. As the droop lines are shifted in accordance with the value of δv , (see Figure 4.3), the reference voltage of each local converter can be described as

$$v_{\text{ref},i} = V_{n,i} - k_{d,i} \cdot i_{o,i} + k_i \cdot \delta v \quad (4.3)$$

A proportional-integral (PI) controller is generally used for the secondary control due to its simplicity and effectiveness. The secondary control works in a centralized way for a standalone nanogrid operation. Nevertheless, when multiple nanogrids are connected to form a microgrid, it operates in a decentralized manner in order to share power among the interconnected nanogrids.

4.2.3 The participation factor k_2 based on SoC

The control algorithm employs the SoC of the battery to adjust a participation factor k_2 that is used to regulate the reference voltage for the voltage control loop, as shown in Figure 4.5. The relationship between the battery power and the SoC is depicted in Figure 4.4. The value of factor k_2 is dependent on the SoC and charging modes of the battery. Factor k_2 remains at unity when the SoC is higher than the low-threshold SoC (SoC_l) in the discharging mode or smaller than the high-threshold SoC (SoC_h) in the charging mode. In case the SoC is out of the range of $[SoC_l, SoC_h]$, to limit the power exchange between the battery and the DC link, the participation factor k_2 is progressively declined. Factor k_2 is defined by

$$\begin{cases} k_2 = 1 - m_1(\text{SoC} - \text{SoC}_h) & \text{if } (\text{SoC} > \text{SoC}_h) \text{ and } (i_{L,\text{bat}} < 0) \\ k_2 = 1 - m_0(\text{SoC}_l - \text{SoC}) & \text{if } (\text{SoC} < \text{SoC}_l) \text{ and } (i_{L,\text{bat}} > 0) \\ k_2 = 1 & \text{otherwise} \end{cases} \quad (4.4)$$

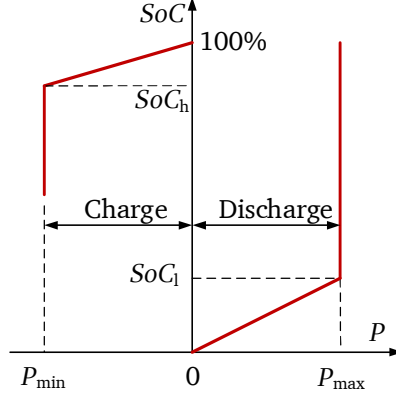


Figure 4.4: Relationship between power and SoC of battery

where the coefficients m_1 and m_0 are defined by

$$m_1 = \frac{1}{100\% - \text{SoC}_h} \quad (4.5)$$

$$m_0 = \frac{1}{\text{SoC}_l} \quad (4.6)$$

and $i_{L,\text{bat}}$ is the inductor current of the interface converter between the battery and the internal DC bus.

There are several methods to estimate the SoC as summarized in [139]. In this work, the Coulomb counting method is implemented, from which the SoC is estimated by the following equation:

$$\text{SoC}(t) = \text{SoC}(t=0) - \frac{\eta}{C_{\text{bat}}} \int_0^t I_{\text{bat}}(\tau) d\tau \quad (4.7)$$

where $\text{SoC}(0)$ is the initial SoC, η is the charging/discharging efficiency, I_{bat} is the battery current, C_{bat} is the nominal or rated capacity. Figure 4.5 shows the determination of the participation factor k_2 according to the SoC.

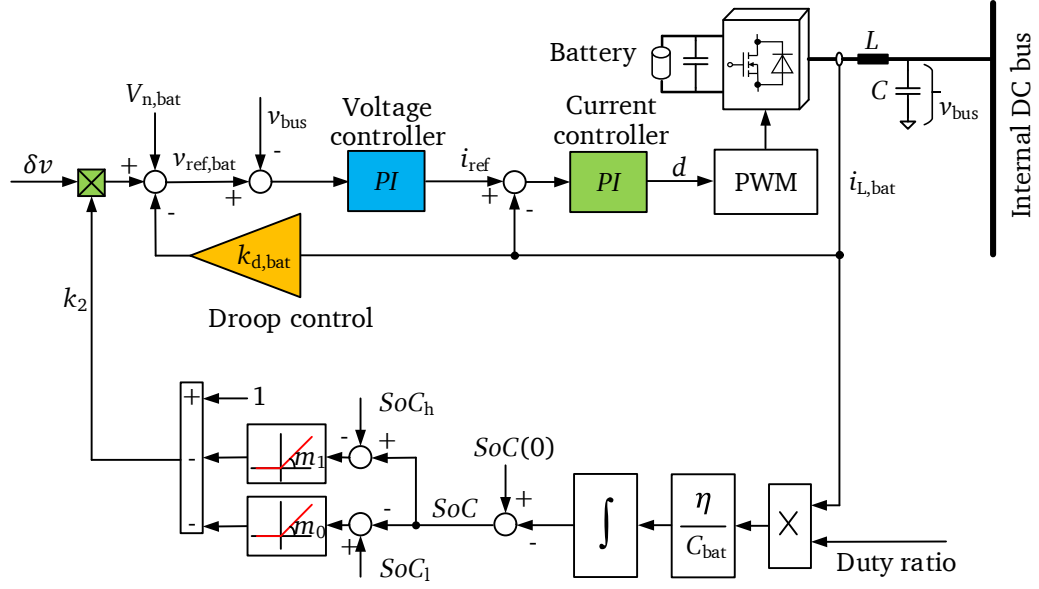


Figure 4.5: Effect of the participation factor based on SoC on primary control

4.2.4 The participation factor k_3 based on the external DC bus voltage

In the control algorithm, which is developed in this research, k_3 is a participation factor that is used to adjust the reference voltage of the primary control loop. Before the determination of k_3 is presented, the role of the external DC bus voltage is introduced as follows.

Assuming that the power produced by the nanogrid is more than the required power for internal consumption, the surplus power can be utilized to support other nanogrids. From Figure 4.6 the charging power of the external DC bus capacitor is given as:

$$P_C = P_S - P_L \quad (4.8)$$

or
$$C_{bus2} \frac{dv_{bus2}}{dt} \cdot v_{bus2} = P_S - P_L \quad (4.9)$$

where P_S is the output power of the interconnected converter of a nanogrid, P_L is the delivered power to other nanogrids, P_C is the power to the external DC bus capacitor.

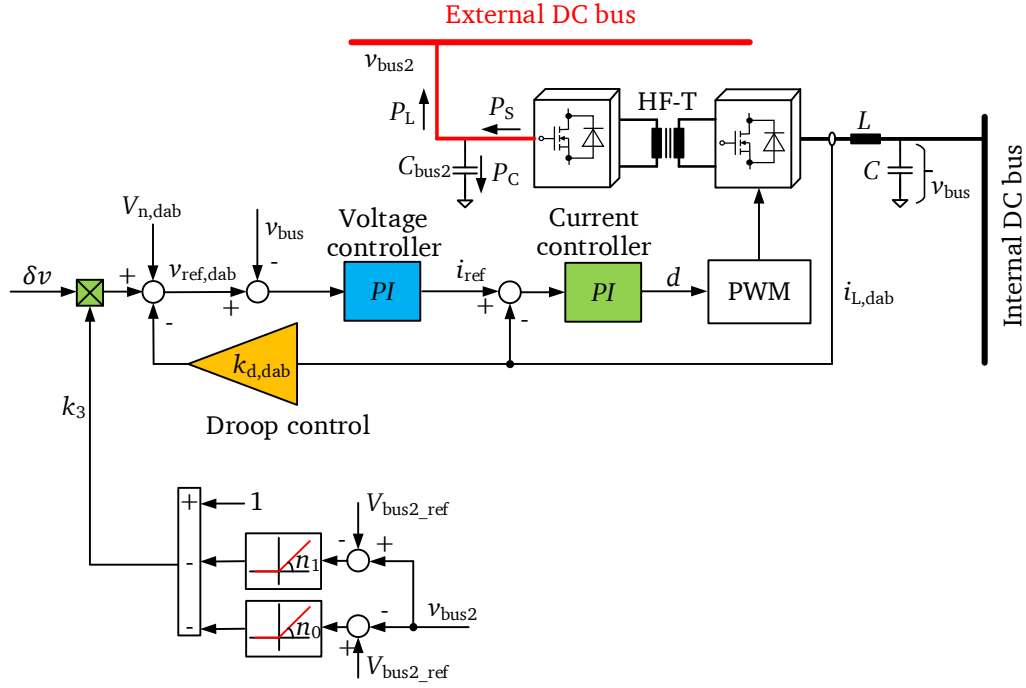


Figure 4.6: Effect of the participation factor based on external DC bus voltage on primary control

From (4.9) it can be inferred that an external DC bus voltage close to the rated level indicates a power balance among nanogrids. A rise or a drop of the external DC bus voltage corresponds to a surplus or deficit of power, respectively. Therefore, in order to regulate power injected into or absorbed from other nanogrids, the external DC bus voltage (v_{bus2}) can be used as an intervention. The dependence of the exchanged power on the external DC bus voltage level is shown in Figure 4.7.

In Figure 4.7, the left and the right regions portray the function of the nanogrid as a power source and as a power load, respectively. While the nanogrid is working as a source, factor k_3 is set to unity as long as the external DC bus voltage is lower than the rated value V_{bus2_ref} ; otherwise, it is gradually reduced to limit the power that the nanogrid is injecting to the interconnecting network. On the other hand, when the nanogrid works as a load, factor k_3 is set to unity if the external DC bus voltage is higher than the nominal value V_{bus2_ref} . Otherwise, it is gradually ramped down to reduce the power that is absorbed from other nanogrids. The participation factor k_3 can be defined as follows

$$\begin{cases} k_3 = 1 - n_1(V_{bus2} - V_{bus2_ref}) & \text{if } (V_{bus2} > V_{bus2_ref}) \text{ and } (i_{L,dab} < 0) \\ k_3 = 1 - n_0(V_{bus2_ref} - V_{bus2}) & \text{if } (V_{bus2} < V_{bus2_ref}) \text{ and } (i_{L,dab} > 0) \\ k_3 = 1 & \text{otherwise} \end{cases} \quad (4.10)$$

The coefficients n_1 and n_0 are given by

$$n_1 = \frac{1}{V_{\text{bus2_h}} - V_{\text{bus2_ref}}} \quad (4.11)$$

$$n_0 = \frac{1}{V_{\text{bus2_ref}} - V_{\text{bus2_l}}} \quad (4.12)$$

where $V_{\text{bus2_h}}$ and $V_{\text{bus2_l}}$ are the high and low thresholds of the external DC bus voltage, respectively, $i_{L,\text{dab}}$ is the output current of the DAB converter.

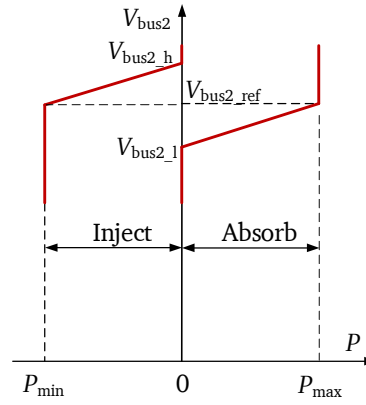


Figure 4.7: Relationship between exchanged power and external DC bus voltage

Figure 4.8 shows the proposed control strategy of autonomous nanogrids. The proposed implementation of the coordinated control is based on hierarchical control levels. Each level has its own functions to perform based on the hierarchy in which the higher control level sends command to the lower control level. The primary and secondary control loops were already mentioned in section 4.2.1 and 4.2.2.

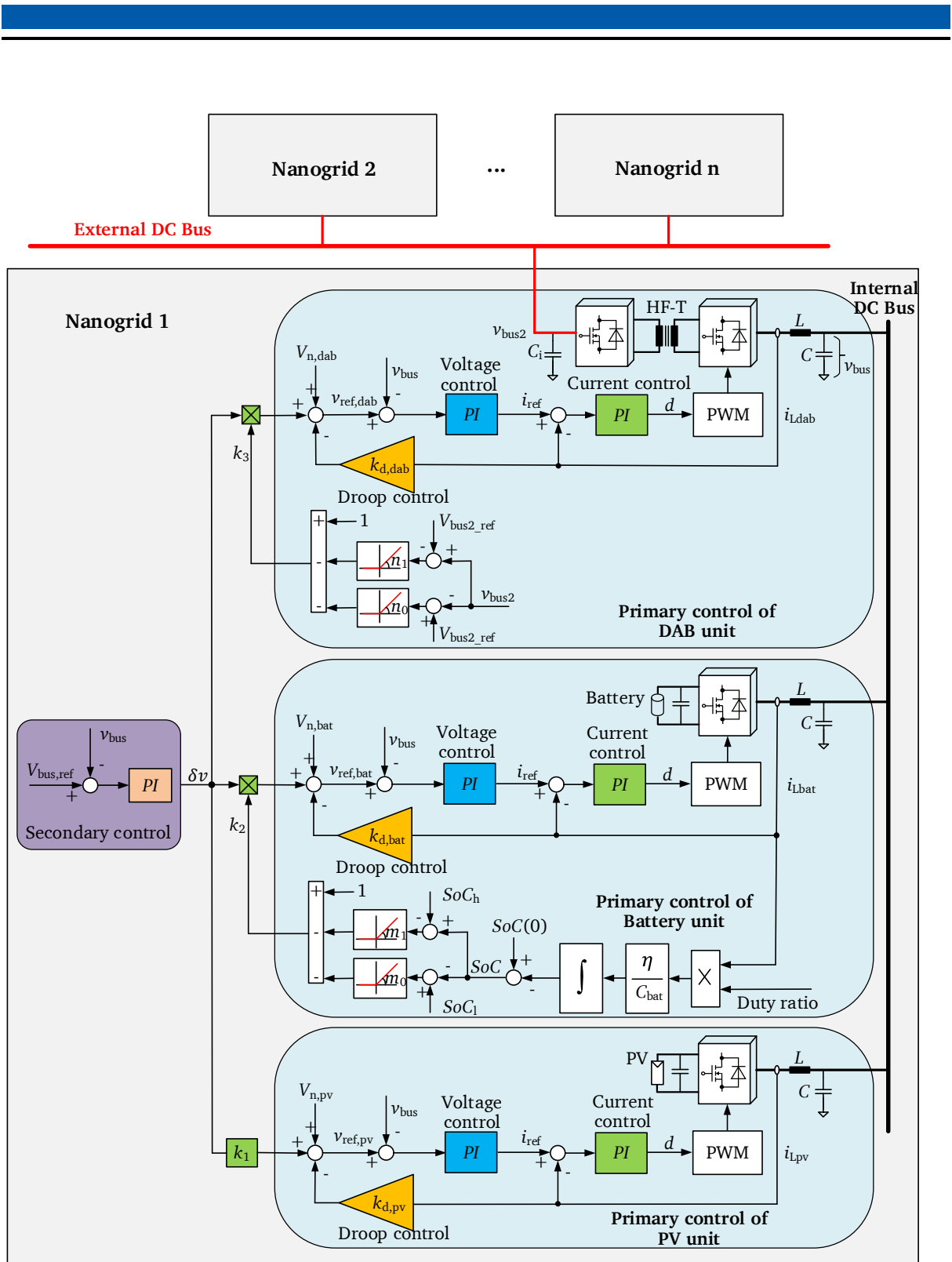


Figure 4.8: Proposed control strategy for the nanogrid

4.3 Modelling, control and stability analysis for an DC nanogrid system

Modelling of DC nanogrids plays an important role to design a suitable control. A number of approaches for modeling and control for AC micro/nanogrids were listed in [48], [49]. Although there has been a significant increase in the interest in DC nanogrids, only few research activities have been carried out regarding modeling of a whole DC nanogrid system. Some researches have been carried out for modeling and controlling of a single converter [56], [140], where the method adapted is often based on the small-signal analysis [63]. However, a modeling method to synthesize a transfer function of a DC nanogrid system consisting of multiple converters is not yet available. The aim of this research is to model a complete DC nanogrid system. First, a mathematical model of a single converter needs to be derived. Subsequently, a model of the entire system can be obtained. This research develops a methodology to achieve a small-signal transfer function of a DC nanogrid integrated with one dual-active bridge converter and two buck converters. The transfer function is eventually utilized to design a secondary controller and to analyze the stability of the entire system.

As already presented in Chapter 3, each converter in the DC nanogrid is modeled and controlled individually. However, when these converters are integrated, they will interact with each other and impact the stability of the entire system. To deal with this issue, a model of the entire system needs to be developed and an appropriate secondary controller has to be designed.

In order to keep the voltage stable for the DC nanogrid system, at least one of the converters that is connected to the internal DC bus must stabilize the internal DC bus voltage. The converter performs this action by adjusting the current injection into the internal DC bus according to the feedback signal of the actual DC bus voltage. Hence, each source is modeled as a controllable current source that feeds the current into the internal DC bus as shown in Figure 4.9.

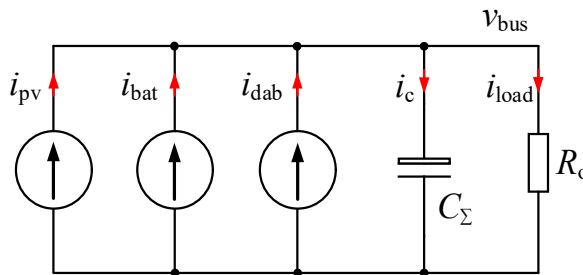


Figure 4.9: Equivalent model of the DC nanogrid

As mentioned earlier in section 4.2.1, in order to allow current sharing among multiple sources inside a DC nanogrid, the droop control is required. Therefore, it is essential to take into

consideration the droop control in modeling of each converter. According to the transfer functions achieved from (3.46) and (3.84), a small-signal model of the DC nanogrid composed of three sources is derived as shown in Figure 4.10

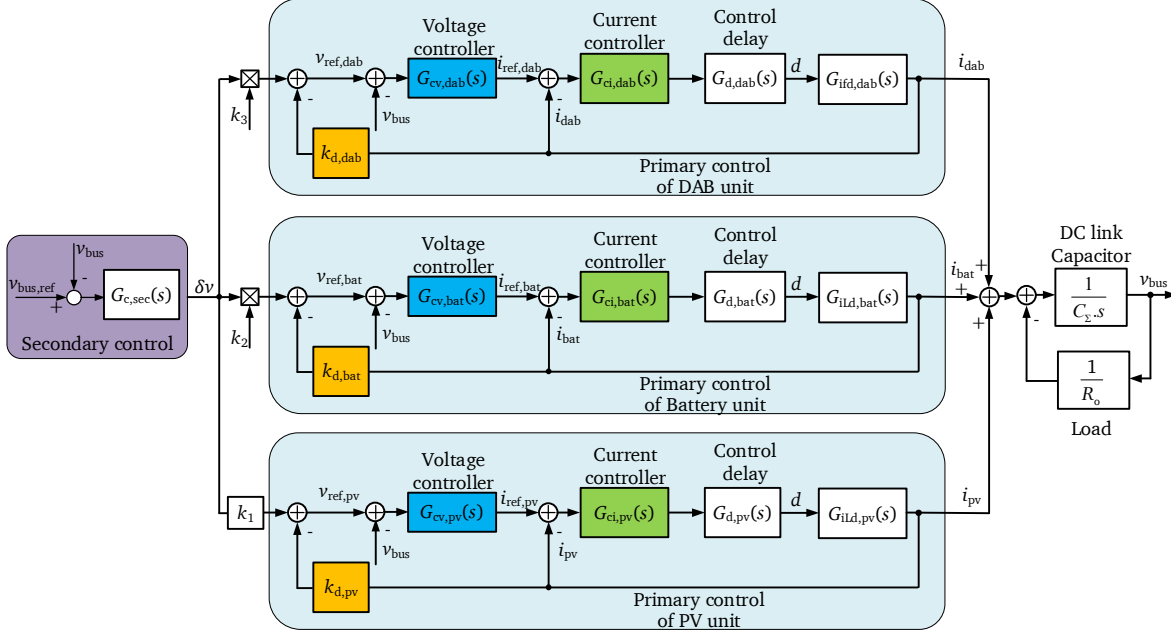


Figure 4.10: The small-signal model of the entire nanogrid

For simplicity, the control structure of the PV converter is studied to develop the correlation between the output current i_{pv} and the voltage correction δv . The same procedure is also applied for the battery and the interconnected converters.

From Figure 4.10, the following equations are derived

$$(i_{ref,pv}(s) - i_{pv}(s)) G_{ci,pv}(s) G_{d,pv}(s) G_{ild,pv}(s) = i_{pv}(s) \quad (4.13)$$

$$(v_{ref,pv}(s) - v_{bus}(s)) G_{cv,pv}(s) = i_{ref,pv}(s) \quad (4.14)$$

$$(k_1 \delta v(s) - k_{d,pv} i_{pv}(s)) = v_{ref,pv}(s) \quad (4.15)$$

Substituting (4.14) and (4.15) into (4.13) results in

$$i_{pv}(s) = (k_1 \delta v(s) - v_{bus}(s)) G_{I,pv}(s) \quad (4.16)$$

where

$$G_{I,pv}(s) = \frac{G_{cv,pv}(s) G_{ci,pv}(s) G_{d,pv}(s) G_{ild,pv}(s)}{1 + G_{ci,pv}(s) G_{d,pv}(s) G_{ild,pv}(s) (1 + k_{d,pv} G_{cv,pv}(s))} \quad (4.17)$$

In the same manner, the correlation between the output current and the voltage correction δv corresponding to the battery and the interconnected converters are specified in (4.18) and (4.19), respectively.

$$i_{\text{bat}}(s) = (k_2 \delta v(s) - v_{\text{bus}}(s)) G_{\text{I,bat}}(s) \quad (4.18)$$

$$i_{\text{dab}}(s) = (k_3 \delta v(s) - v_{\text{bus}}(s)) G_{\text{I,bat}}(s) \quad (4.19)$$

where

$$G_{\text{I,bat}}(s) = \frac{G_{\text{cv,bat}}(s) G_{\text{ci,bat}}(s) G_{\text{d,bat}}(s) G_{\text{iLd,bat}}(s)}{1 + G_{\text{ci,bat}}(s) G_{\text{d,bat}}(s) G_{\text{iLd,bat}}(s) (1 + k_{\text{d,bat}} G_{\text{cv,bat}}(s))} \quad (4.20)$$

$$G_{\text{I,dab}}(s) = \frac{G_{\text{cv,dab}}(s) G_{\text{ci,dab}}(s) G_{\text{d,dab}}(s) G_{\text{ifd,dab}}(s)}{1 + G_{\text{ci,dab}}(s) G_{\text{d,dab}}(s) G_{\text{ifd,dab}}(s) (1 + k_{\text{d,dab}} G_{\text{cv,dab}}(s))} \quad (4.21)$$

Additionally, as presented in Figure 4.10, the coupling equation of the nanogrid system is

$$v_{\text{bus}}(s) = \frac{R_o}{1 + C_\Sigma R_o s} (i_{\text{pv}}(s) + i_{\text{bat}}(s) + i_{\text{dab}}(s)) \quad (4.22)$$

where C_Σ is the total capacitance of the internal DC bus.

From (4.18)-(4.22), the transfer function of the nanogrid without the secondary control is deduced as

$$G_{\text{sys}}(s) = \frac{v_{\text{bus}}(s)}{\delta v(s)} = \frac{k_1 G_{\text{I,pv}}(s) + k_2 G_{\text{I,bat}}(s) + k_3 G_{\text{I,dab}}(s)}{G_{\text{I,pv}}(s) + G_{\text{I,bat}}(s) + G_{\text{I,dab}}(s) + \frac{1 + C_\Sigma R_o s}{R_o}} \quad (4.23)$$

where $G_{\text{sys}}(s)$ is the transfer function demonstrating the dynamic behavior of the DC bus voltage with respect to small variation of the voltage correction. Figure 4.11 illustrates the control structure of the DC nanogrid with the secondary control. A PI controller with a transfer function as given by (4.24) is implemented for the secondary control loop as it is easy to implement and reasonably robust.

$$G_{\text{c,sec}}(s) = K_{\text{p,sec}} + \frac{K_{\text{i,sec}}}{s} \quad (4.24)$$

From Figure 4.11, the closed-loop transfer function $G_{\text{CL,sys}}(s)$ from v_{bus} to $v_{\text{bus,ref}}$ is given by

$$G_{\text{CL,sys}}(s) = \frac{v_{\text{bus}}(s)}{v_{\text{bus,ref}}(s)} = \frac{G_{\text{c,sec}}(s) G_{\text{sys}}(s)}{1 + G_{\text{c,sec}}(s) G_{\text{sys}}(s)} \quad (4.25)$$

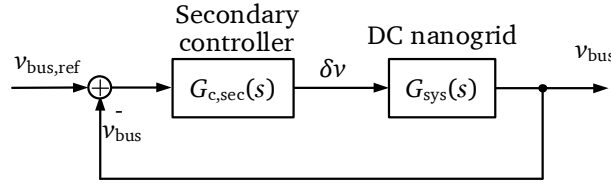


Figure 4.11: The control structure of DC nanogrid with secondary control

In this research, the design of the PI controller is based on a linear model for the nominal load. By using the SISO tool in MATLAB along with the procedure introduced in [125], the parameters of the PI controller are tuned again. The secondary control loop has to be tuned to ensure that the bandwidth of the secondary loop is much slower than that of the primary loop. The obtained values of the proportional and integral gains are summarized in Table 4.1.

Table 4.1: Parameters of secondary controller

Proportional gain	Integral gain
$K_{p,sec} = 0.01$	$K_{i,sec} = 60 \text{ (1/s)}$

With the designed controller, the closed loop needs to be stable within the whole range of all possible loads. To analyze the robustness of the closed loop, the change in the load resistance within the range of $[5 \Omega, 500 \Omega]$ is examined to verify whether the closed loop is robust against the load changes or not. Figure 4.12 and Figure 4.13 demonstrate the corresponding closed-loop eigenvalues and the dominant ones for the resistive load range of $[5 \Omega, 500 \Omega]$, respectively. As shown in Figure 4.12, with the obtained control parameters, all roots of the characteristic polynomials of $G_{CL,sys}(s)$ with different load resistances are located on the left half of the s -plane, ensuring stability of the system.

The performance of the controller is evaluated under different operating points within a wide range of changes in the loads. As visible from Figure 4.13, the dominant eigenvalues shift in the direction of the imaginary axis of the s -plane according to the increase in load resistances. Additionally, it is evident from Figure 4.14 that the maximum real part of eigenvalues of the nanogrid moves towards but never reaches to zero when the load resistance increases.

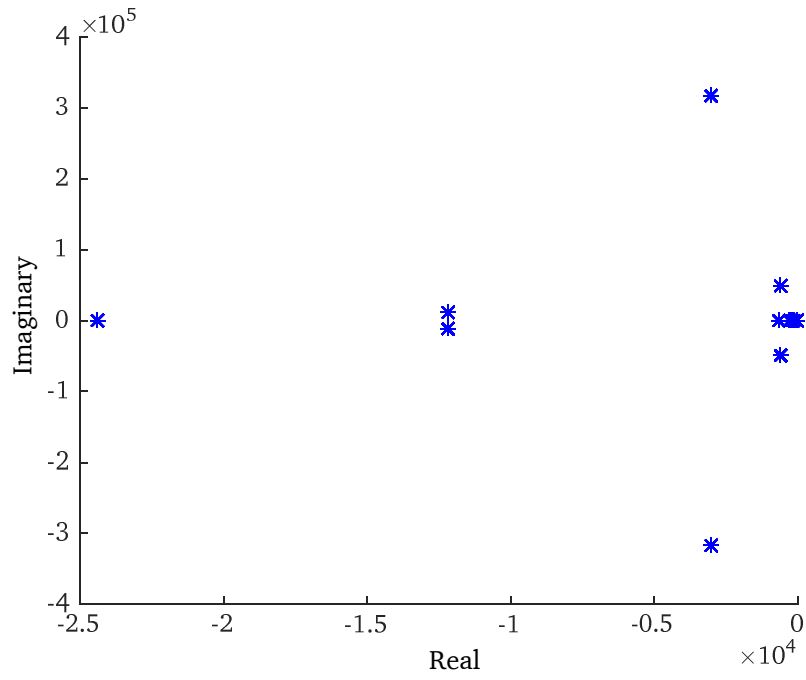


Figure 4.12. Closed-loop eigenvalues of the NG

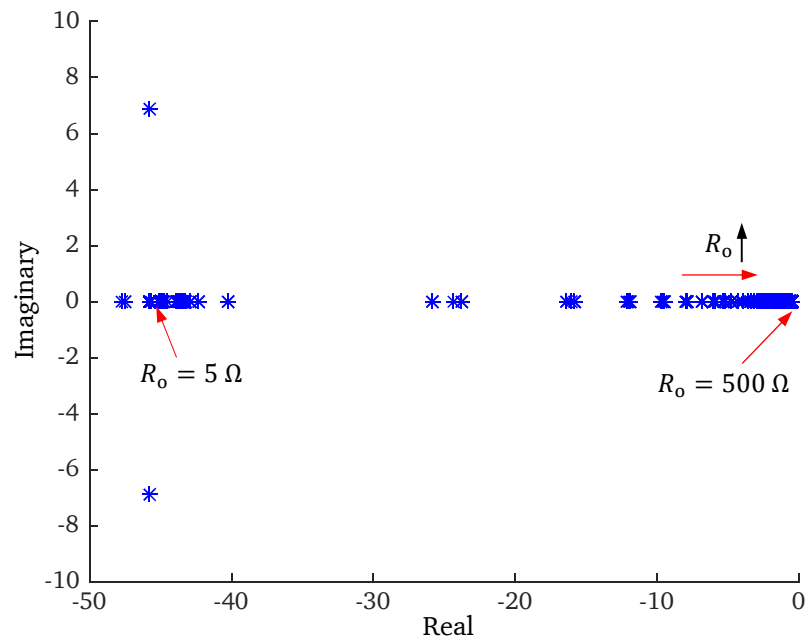


Figure 4.13: The dominant eigenvalues with different load models

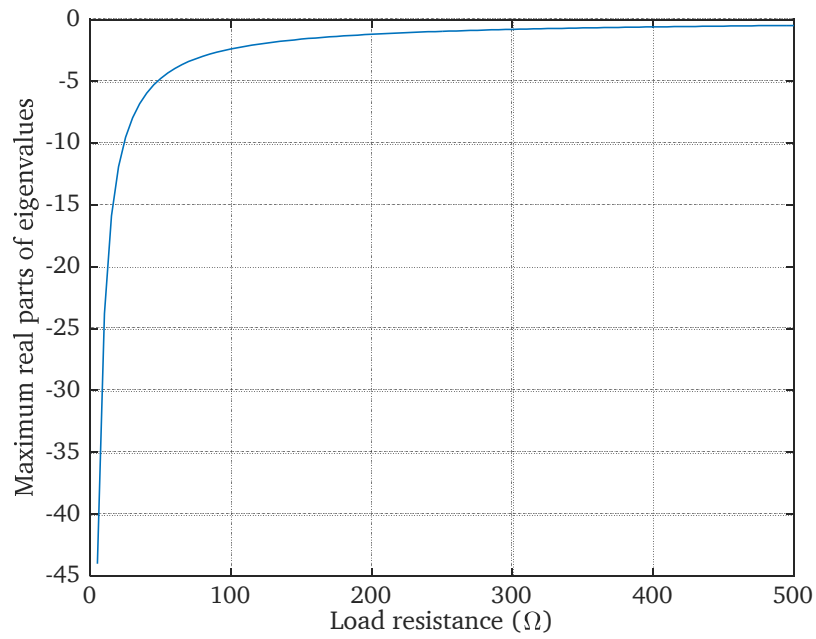


Figure 4.14: The maximum real parts of eigenvalues of the nanogrid with respect to the different load resistances

Figure 4.15 displays the Bode plot of the closed-loop transfer function of the DC nanogrid system. The observed bandwidth of the secondary control loop is around 10 Hz which is lower than 70 Hz of the primary control loop defined by the DAB converter.

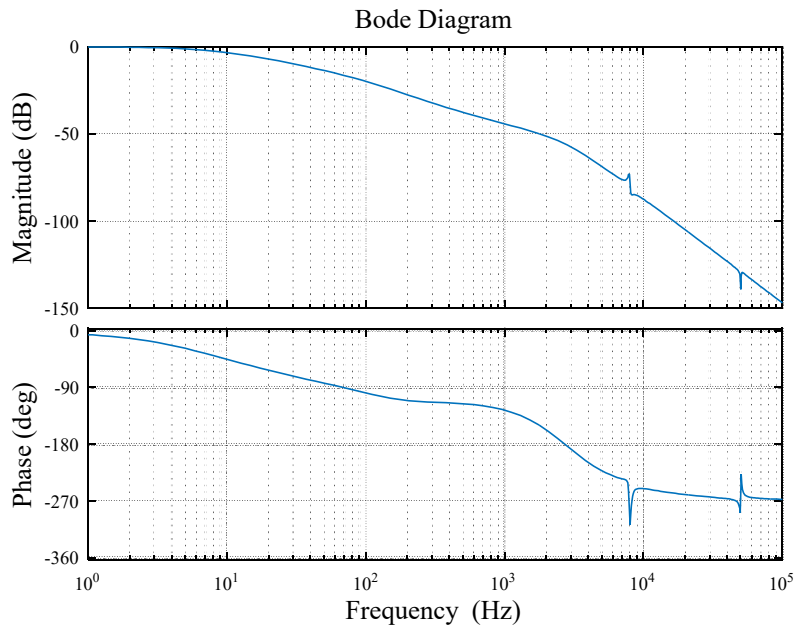


Figure 4.15: Bode plot of the closed-loop transfer function of the DC nanogrid

4.4 Simulation and experimental verification

Simulation and experimental results of a nanogrid are used to verify the proposed control strategy. The topology of a nanogrid being used for simulations and experiments is shown in Figure 4.16. The nanogrid comprises two buck converters, a DAB converter, three DC power supplies and a load bank. In addition, two bidirectional power supplies are used in order to mimic a battery as well as the interconnection of the nanogrid with other nanogrids. By doing this, the interoperability is established when the nanogrid is connected to the bidirectional power supply which functions as the second nanogrid. A bank of four parallel resistors with resistances of 100 Ω , 50 Ω , 25 Ω , 12.5 Ω were used as a passive resistive load. The bank resistors provide $2^4 = 16$ different levels of power load with a resolution of 23.04 W. The main parameters of the system are given in Table 4.2. The picture of the experimental model is illustrated in Figure 4.17

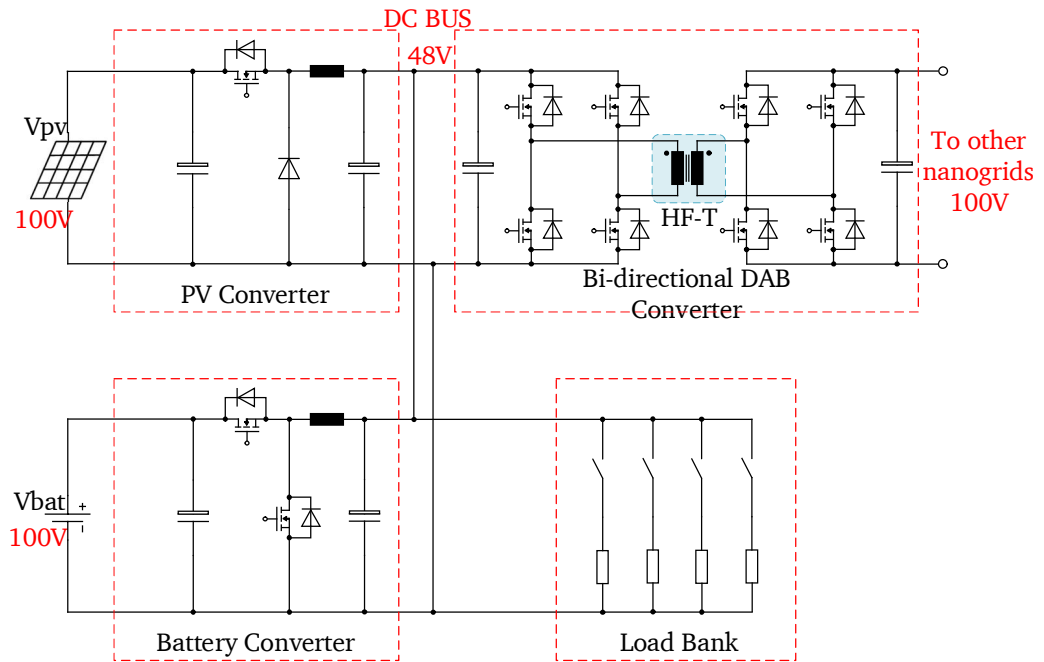


Figure 4.16: Topology of a DC nanodrid for the experiment

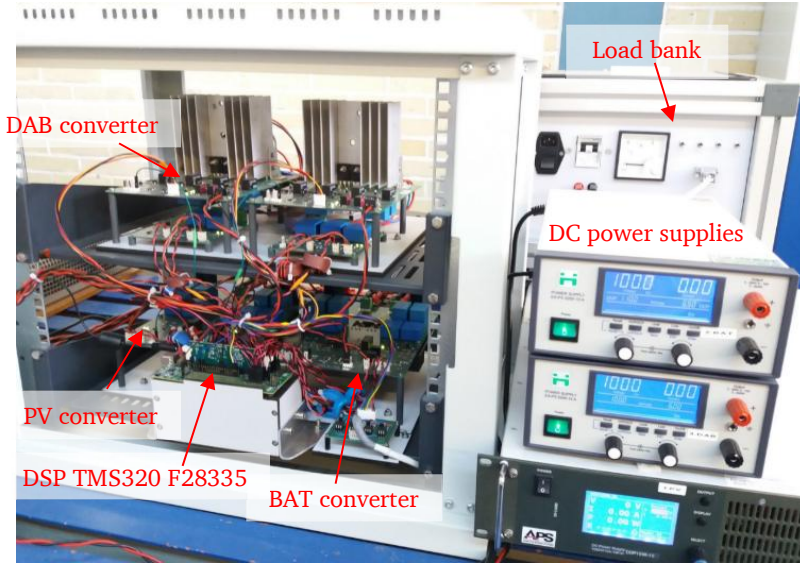


Figure 4.17: Experimental setup

Table 4.2: Parameters of interface converters

Converter	Parameter	Symbol	Value	Unit
PV Interfaced Converter	Rated power	P_{\max}	300	W
	Input voltage	V_{in}	100	V
	Output voltage	V_{out}	48	V
	Droop coefficient	$k_{\text{d,pv}}$	0.5	V/A
Battery Interfaced Converter	Rated power	P_{\max}	300	W
	Input voltage	V_{in}	100	V
	Output voltage	V_{out}	48	V
	Droop coefficient	$k_{\text{d,bat}}$	0.5	V/A
Interconnection Converter	Rated power	P_{\max}	400	W
	Input voltage	V_{in}	100	V
	Output voltage	V_{out}	48	V
	Droop coefficient	$k_{\text{d,dab}}$	0.5	V/A

In this system, the highest priority to supply the load is taken by the PV. Any surplus or deficiency of power is compensated by the battery or by interconnection. For simplicity, the PV panel is assumed to be operating in the MPPT mode to supply a constant power of 200 W as the load varies. As aforementioned, to verify the assumption that the system is stable and robust

with the designed controller, three critical loads are examined to observe the transition between the corresponding nonlinear models for both simulations and experiments. Figure 4.18 and Figure 4.19 demonstrate the simulation and experimental results, respectively, relating to the changes in the loads for the DC nanogrid while the solar power remains constant.

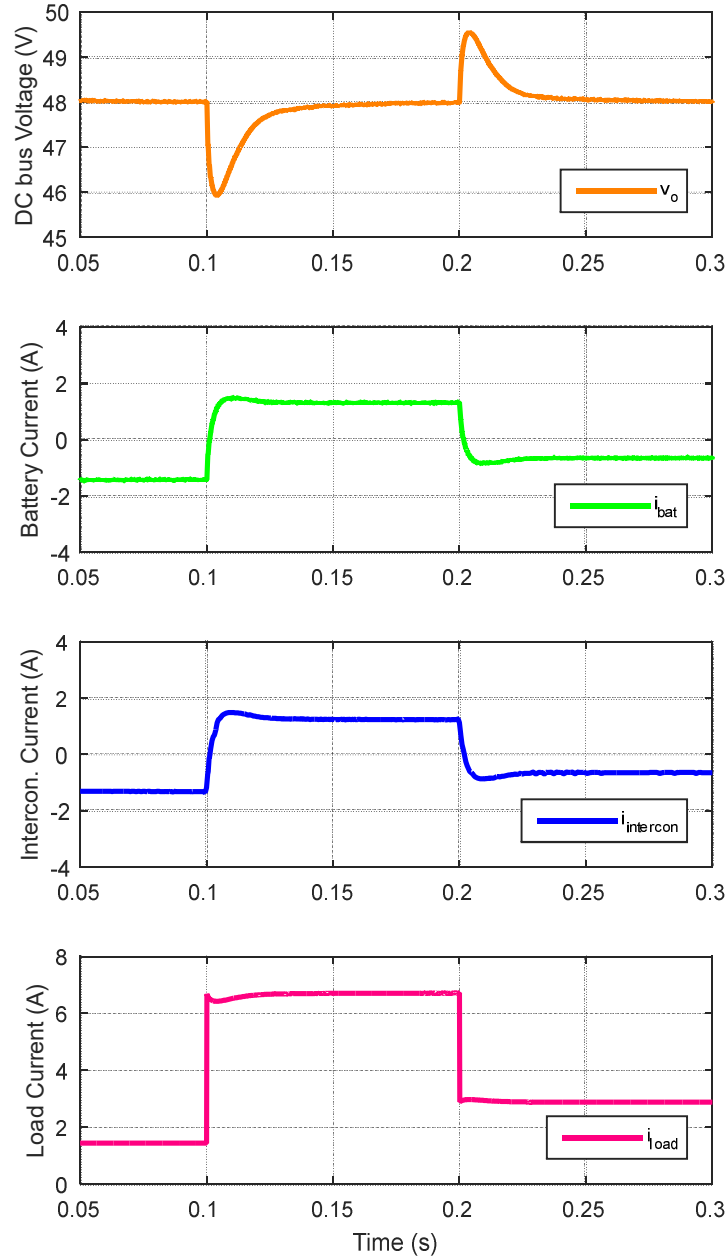


Figure 4.18: Simulation results for load changes

To begin with, the power of the load is set to 70 W. Under this condition, the PV is capable of providing the power to the load, and the excess power is utilized to charge the battery or to inject into the external DC bus. From 0.1 s to 0.2 s time interval, the load power is increased to 323 W, which surpasses the capability of PV to handle the load. Consequently, power is

absorbed from the battery and the external DC bus in order to stabilize the power in the internal DC bus. After 0.2 s, the load power is dropped to 138 W. The PV source is again capable of meeting the load demand that results in a lower rate of charging and injecting power.

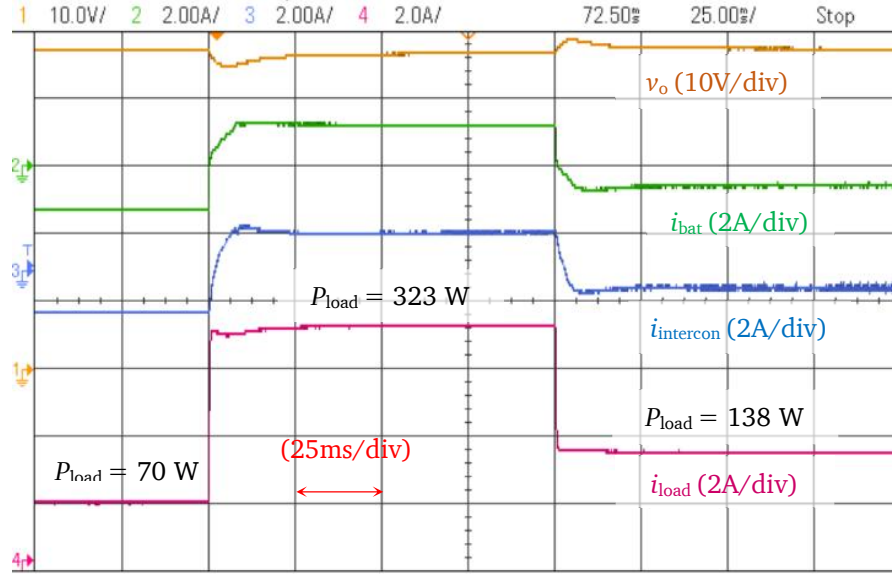


Figure 4.19: Experimental results for load changes

For the second scenario, the fluctuation phenomenon of the renewable power source is emulated by changing the MPP of the PV source. Figure 4.20 and Figure 4.21 illustrate the simulation and experimental results, respectively, with respect to the effects of the changes on the DC bus voltage, the battery and the output currents of the DAB. To demonstrate the impact of the changes in PV power, the load power is kept constant at 138 W during this scenario. During the first interval, the power supplied by the PV is 100 W, which is less than what is required by the load. In this case, the battery discharges and the DAB converter absorbs power from the external DC bus to compensate the power deficiency. In the second interval, the MPP of PV panel is increased to 200 W, which is greater than the load demand. The excessive power can be used to charge the battery and transfer it to outer nanogrids. In the last interval, the MPP of PV panel is reduced to 50 W. Consequently, more power is supplied to the load by the battery and external DC nanogrid.

It is evident from Figure 4.18 - Figure 4.21 that the DC bus voltage of the DC nanogrid is maintained around $v_{bus,ref} = 48$ V through the secondary control. With respect to the changes in the load, a minor undershoot and overshoot of 2 V, or 4% of the nominal voltage is observed. The settling time depends on the extent of the load changes and capacitance rating of the DC bus capacitor. It is clearly visible that the experimental results coincide with those acquired from simulations.

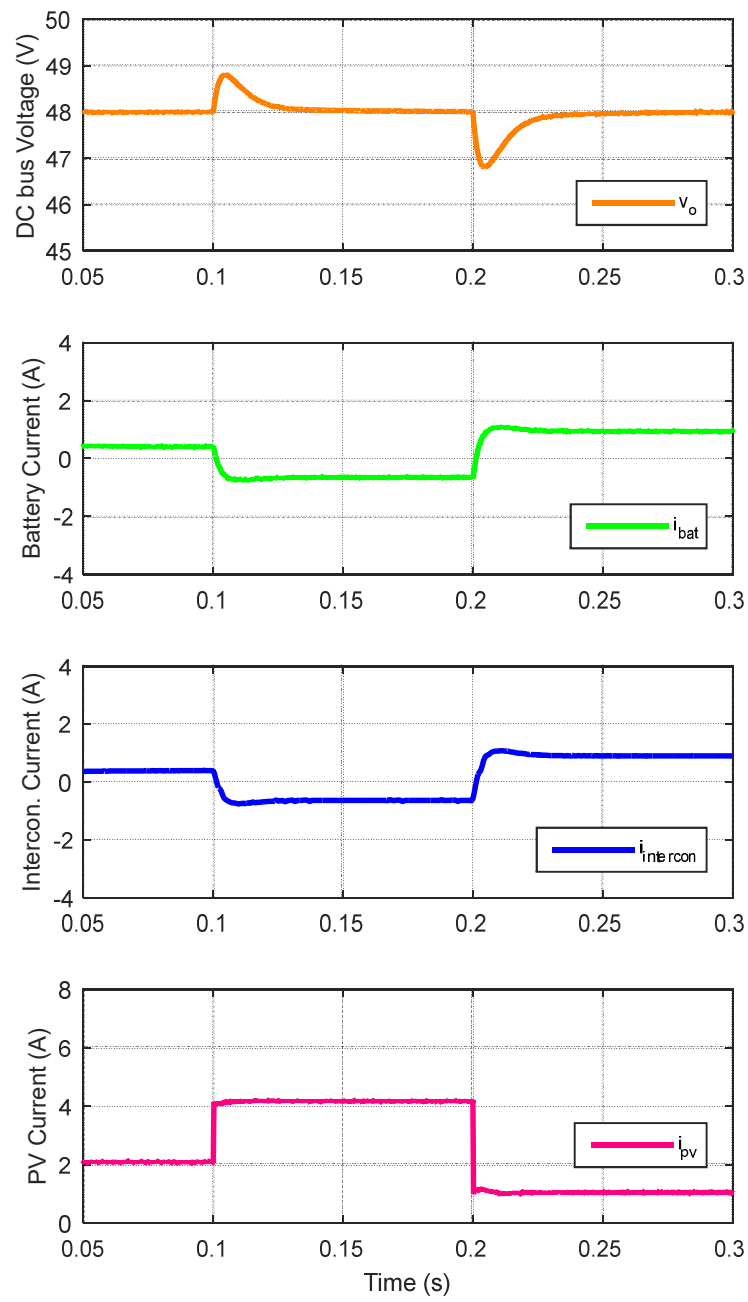


Figure 4.20: Simulation results for PV changes

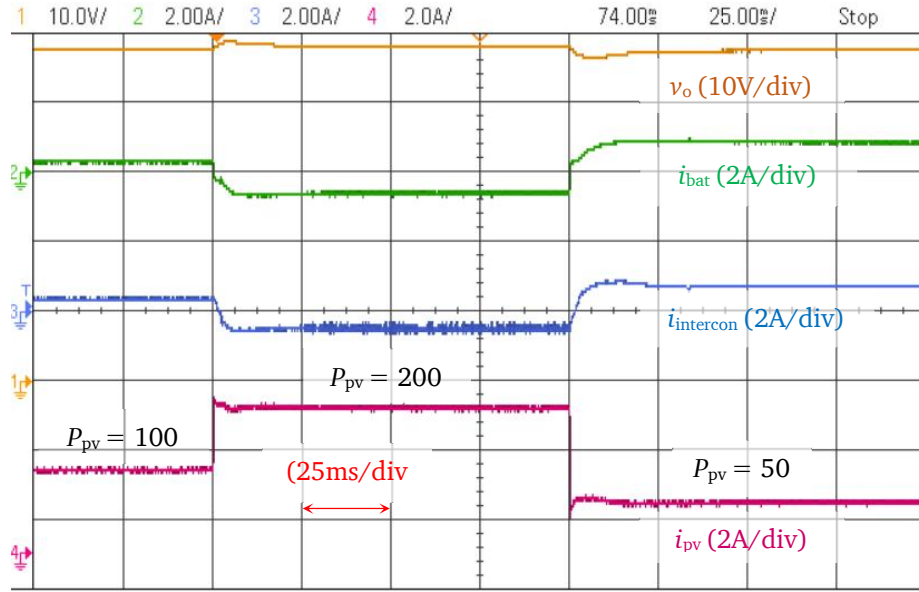


Figure 4.21: Experimental results for PV changes

4.5 Interconnection of multiple DC nanogrids

4.5.1 Configuration of interconnected DC nanogrids

As mentioned before, the proposed control strategy was applied for a single nanogrid that was verified by demonstrations of both simulation and experimental results. In this section, the feasibility of the proposed control strategy implemented by interconnecting multiple nanogrids is tested. Simulation results of a microgrid system that consists of three interconnected nanogrids validate the effectiveness of the proposed strategy. According to Figure 4.22, each nanogrid unit is interconnected with the other units through resistive-inductive lines which are employed to study the impact of the line impedances on the stability of the microgrid system [67]. The reference voltage of the internal DC bus and the nominal voltage of the external DC bus are set at 48 V and 100 V, respectively. All converters that are parts of nanogrids are operated at switching frequency of 50 kHz. The line impedances with respect to their length are selected according to [23], where the line resistance and inductance are 0.1 Ω /km and 0.1 mH/km, respectively. The parameters of the microgrid made of three interconnected nanogrids are summarized in Table 4.3. In this model, each nanogrid can work as either a load or a source as it can consume or distribute power. The SimPowerSystem toolbox and S-function block in MATLAB Simulink were used to build the simulation model.

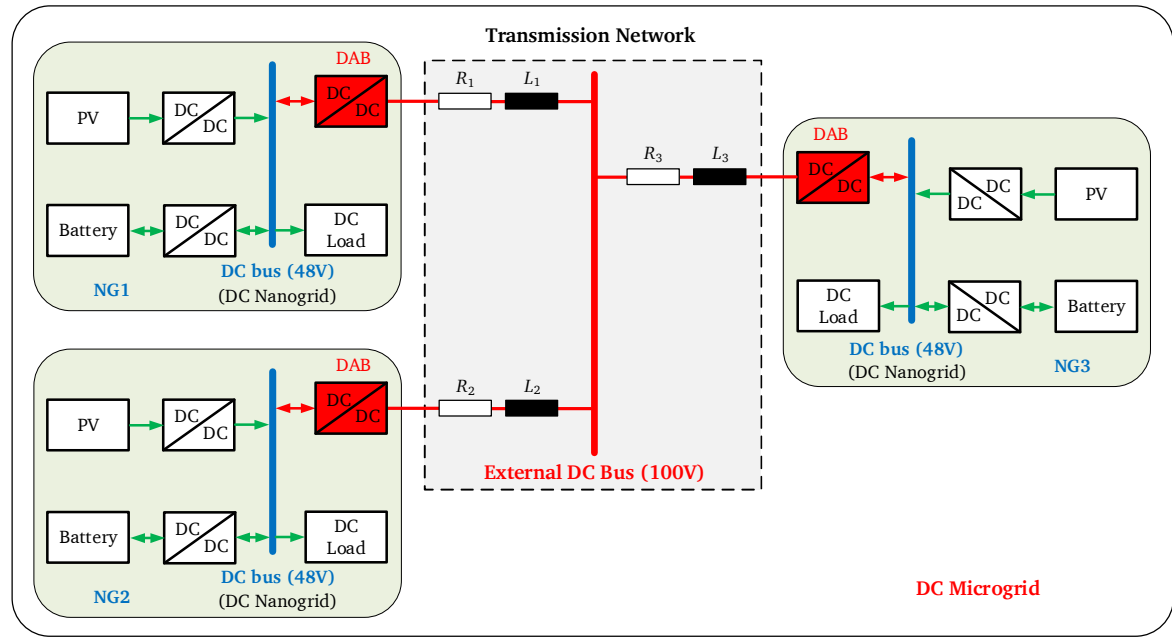


Figure 4.22: Simulation model of three interconnected nanogrids

Table 4.3: Parameters of the microgrid

Parameter	Symbol	Value	Unit
Nominal internal DC bus voltage	V_{bus_ref}	48	V
Nominal external DC bus voltage	V_{bus2_ref}	100	V
High-threshold of the external DC bus voltage	V_{bus2_h}	110	V
Low-threshold of the external DC bus voltage	V_{bus2_l}	90	V
High-threshold SoC	SoC_h	90	%
Low-threshold SoC	SoC_l	30	%
Tie-line inductance of NG ₁	L_1	100	μH
Tie-line resistance of NG ₁	R_1	100	m
Tie-line inductance of NG ₂	L_2	10	μH
Tie-line resistance of NG ₂	R_2	10	m
Tie-line inductance of NG ₃	L_3	100	μH
Tie-line resistance of NG ₃	R_3	100	m
Switching frequency	f_s	50	kHz

4.5.2 Case study and simulation results

As aforementioned, the PV takes the first priority to supply the load according the proposed control strategy. The battery or the interconnection compensates any excess or deficit of power. Two simulation scenarios are considered to investigate the operation of three nanogrids. The first scenario is related to the changes in the load inside each nanogrid while the second one is associated with the variations in the MPP of the PV source.

4.5.2.1 Scenario 1 – Load changes for the nanogrids

Figure 4.23 shows the simulation results for the changes in the loads for three nanogrids while the solar power remains constant. The load change events are highlighted by the dotted lines *Ev. 1 – Ev. 6*. For consideration, the constant power of the PV panel associated with the first nanogrid (NG₁), the second nanogrid (NG₂) and the third nanogrid (NG₃) is set at 200 W, 100 W and 50 W, respectively. In this scenario, NG₁ always feeds power to the external DC bus while NG₃ always consumes power from the external DC bus. Meanwhile, NG₂ can operate as either a power source or a power load as it can inject power to or absorb power from the external DC bus, respectively.

At the beginning, the loads of the NG₁, NG₂ and NG₃ are set at 46 W, 23 W and 230 W, respectively. Under this condition, the excessive renewable power of NG₁ and NG₂ is utilized to charge their batteries and to feed into the external DC bus. Meanwhile, the NG₃ consumes power from the external DC bus to maintain the power balance inside its internal DC bus. The power flow is reflected by the current flow as illustrated in Figure 4.23 (b). The operations of the microgrid in the next intervals corresponding to different events are summarized as follows:

Event 1 (Ev.1): By increasing the load power of NG₁ to 138 W, the charging and the injecting power is reduced, as the PV source still meets the load demand, leading to the diminishing of the charging and injecting current, blue in Figure 4.23 (c) and blue in Figure 4.23 (b), respectively.

Event 2 (Ev.2): As the load power of NG₂ is increased to 253 W which is greater than the generated power, the battery of NG₂ discharges and NG₂ itself absorbs power from the external DC bus as it is shown in the red line in Figure 4.23 (b).

Event 3 (Ev.3): The load power of NG₃ is reduced to 69 W that is still slightly greater than the PV power. The green line in Figure 4.23 (b) describes that NG₃ still consumes power from outside but with a smaller value.

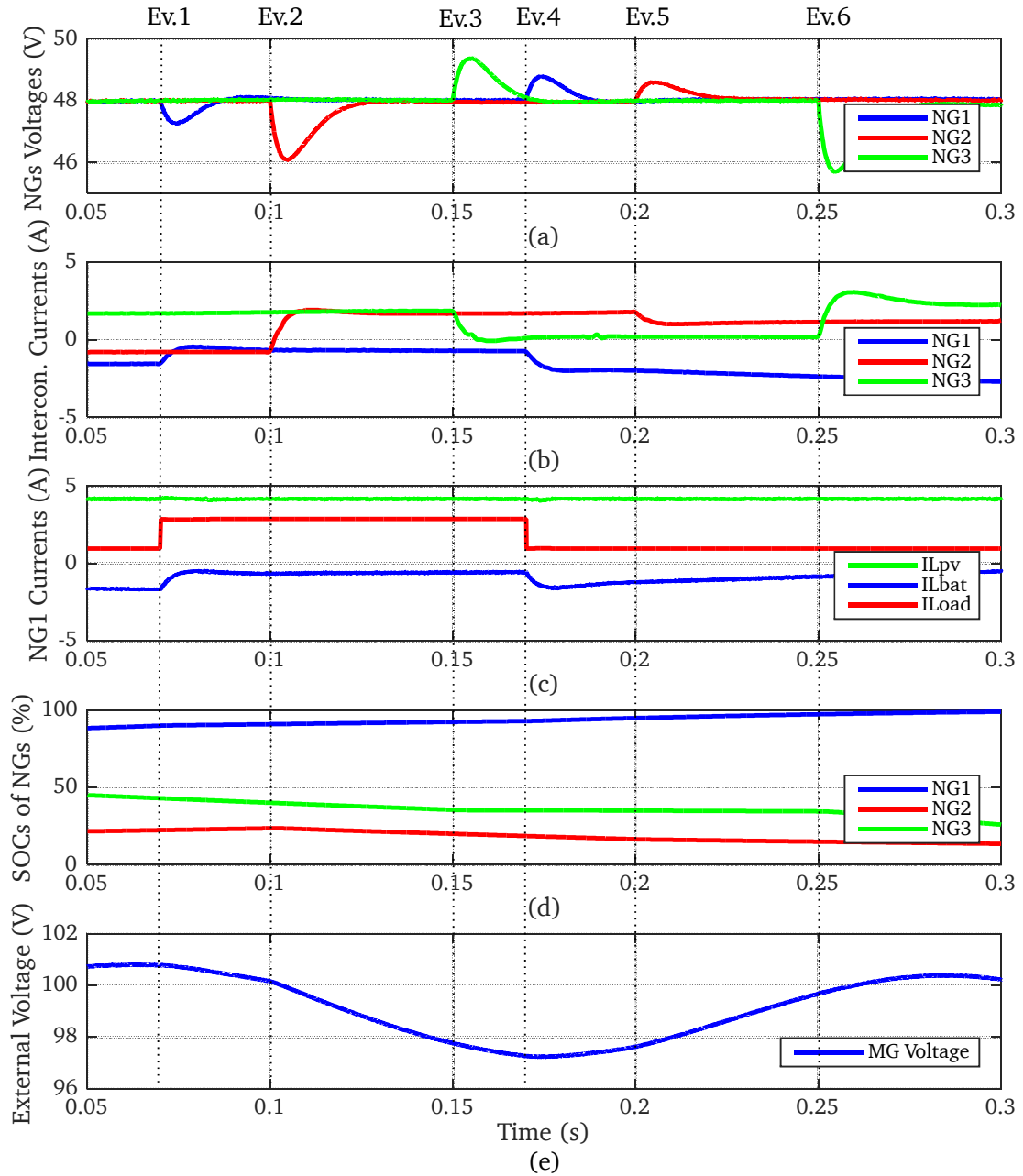


Figure 4.23: Simulation results for load changes

Event 4 (Ev.4): The load power of NG₁ is decreased to 46 W again while the generated power from the PV remains unchanged at 200 W, which means that the surplus power is used to charge the battery and to inject into the interconnected DC bus. Nevertheless, as is observed in Figure

4.23 (c), the charging power is gradually decreased by the reduction of the participation factor k_2 in order to protect the battery from overcharging because the SoC of the battery reaches above the high-threshold of 90% as shown in Figure 4.23 (d). Meanwhile, the remaining excess power of NG₁ is utilized to inject into the external DC bus with a larger value as shown in the blue line in Figure 4.23 (b).

Event 5 (Ev.5): By decreasing the load power of NG₂ to 184 W but still larger than the renewable energy, while NG₂ continue to absorb power from the external DC bus but at a lower rate. This is demonstrated by the decrease in the current, which is in red line in Figure 4.23 (b).

Event 6 (Ev.6): The power consumed by the load of NG₃ is much higher than power generated by the renewable source as the load power of NG₃ is increased to the new value of 346 W. As a result, the battery discharges more power and NG₃ absorbs higher power from the external DC bus, as illustrated in the green line in Figure 4.23 (b), to maintain the power balance inside NG₃.

As is observed in Figure 4.23 (a), the internal DC bus voltages of three nanogrids remains stable at 48 V. It is evident that changing the load of each nanogrid does not have any influence on the internal DC bus voltage of other nanogrids. This guarantees system stability not only within a nanogrid but also within a microgrid. Figure 4.23 (e) depicts the fluctuations of the external DC bus voltage during the interconnecting operation. It is apparent that the external DC bus voltage does not exceed beyond the range of [90 V - 110 V].

4.5.2.2 Scenario 2 – PV power changes for three nanogrids

In this scenario, the operations of three nanogrids are demonstrated in Figure 4.24 in which the PV generation is varied while the load power is kept constant. To observe the influence of the external DC bus voltage on the exchanged power among nanogrids as well as the interaction inside the nanogrids, the loads of NG₁, NG₂ and NG₃ are set at 23 W, 138 W and 46 W, respectively. In this case, power generation is significantly higher than power consumption.

To begin with, the renewable power of NG₁, NG₂ and NG₃ is set at 50 W, 180 W and 100 W, respectively. Since the generated power is greater than the consumed power, the excess power is used to charge the batteries and to feed into the external DC bus voltage. As illustrated in Figure 4.24 (e), the external DC bus voltage almost reaches the high-threshold of 100 V and therefore, by decreasing the participation factor k_3 , injection of power is limited.

Event 1 (Ev.1): The renewable power of NG₁ is increased to 100 W. It is observed from the blue line in Figure 4.24 (c) that most of excess power is used to charge the battery, while injection of power into the external DC bus is insignificant, as illustrated by the blue line in Figure 4.24 (b), since the external DC bus voltage has almost reached the high-threshold. This protects the external DC bus from overvoltage.

Event 2 (Ev.2): The generated power from the PV is reduced to 100 W which is inadequate for load demand. To compensate the power deficiency, the battery discharges to feed the load and NG₂ absorbs power from the interconnected DC bus as shown in the red line in Figure 4.24 (b).

Event 3 (Ev.3): As the PV power of NG₃ is increased to 200 W, major portion of the excess power is utilized for battery charging. Similar to the first event, only a small portion of power is injected to the external DC as shown in the green line in Figure 4.24 (b).

Event 4 (Ev.4): The PV power of NG₁ is gradually increased to 200 W, which results in a rise of battery charging and injected power. It is observed from the blue line in Figure 4.24 (b) that just a minor amount of power is fed to the external DC bus, which approaches its high-threshold. As a result, a major portion of the surplus power of NG₁ is used to charge the battery as depicted in the blue line in Figure 4.24 (c).

Event 5 (Ev.5): The behavior depicted in the red line in Figure 4.24 (b) shows the rise in power consumption of the external DC bus as the power of NG₂ is reduced to 50 W.

Event 6 (Ev.6): In this scenario, the battery-charging power and injected power are insignificant and reaching zero as the PV power of NG₃ is decreased to 50 W, meaning that the generated power and the consumed power are almost equal. The SoC of the NG₁ almost approaches 100% as is observed in the blue line in Figure 4.24 (d), meaning that there is no need for charging the battery. During this condition, PV converter of the NG₁ switches to the droop mode to limit power generation, as shown in the green line in Figure 4.24 (c), since the battery of NG₁ is almost fully charged and the external DC bus voltage is almost at the high-threshold.

Figure 4.24 (a) depicts the fact that the internal DC bus voltage of each nanogrid is kept stable around the reference value of 48 V. Moreover, there is no effect due to changes in the PV power of the other nanogrids. In this scenario, two of the three nanogrids tend to inject power into the external DC bus, increasing the external bus voltage. Nonetheless, the external DC bus voltage stays within the predefined range, which is achieved by the modification of the

participation factor k_3 . This ensures that overvoltage does not occur as demonstrated in Figure 4.24 (e).

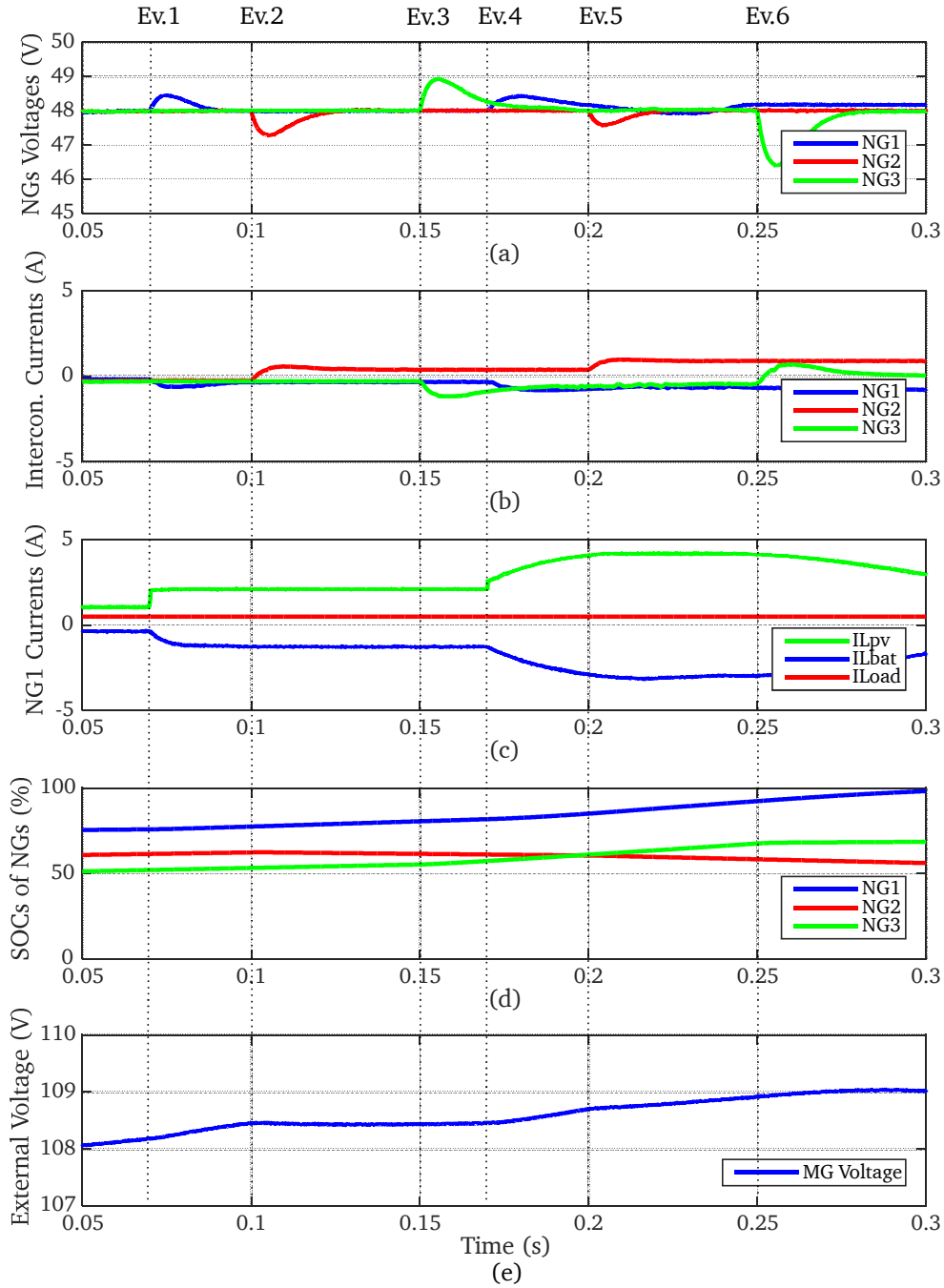


Figure 4.24: Simulation results for PV source changes

As can be observed, due to the control of the dual active bridge converter installed inside each nanogrid, the internal DC bus voltage remains stable regardless of changes in the external DC bus. This decouples the internal and the external DC bus. Consequently, the parameters of the nanogrid such as tie-line impedances has no effect on the stability of the nanogrid. Those

parameters just have an impact on the voltage drop of the external DC bus voltage. However, the external DC bus voltage is regulated to be in the predefined range of [90V, 110V] according to the adjustment of the participation factor k_3 . In addition, as illustrated in Figure 4.23 and Figure 4.24, variation of the external DC bus does not affect the stability of individual nanogrids when multiple nanogrids are integrated.

4.6 Summary

This chapter presents the self-sustained and flexible control strategy based on a hierarchical architecture for nanogrids. In addition, the procedure for development of the small-signal model of the entire nanogrid is introduced. From the obtained small-signal model, the appropriate secondary controller is designed and then the stability of the nanogrid is analyzed. The effectiveness of the proposed control strategy is verified by simulation and experimental results which prove that electric power can be exchanged among multiple nanogrids without using any communication links. The results demonstrate good transient response and stability of the internal DC bus voltage along with the battery and interconnected currents. Despite changes in the loads and PV source, the stability of the nanogrid is still maintained. The proposed control algorithm also has the ability to maintain the state of charge of the battery in each nanogrid by avoiding an overcharge or a deep discharge when there is an excess or deficit of power generated from renewable source. As illustrated by the simulation results of multiple nanogrids, even with variation in the external DC bus voltage, every internal DC bus voltage remains stable. The integration of multiple nanogrids has no impact on the stability of individual nanogrids due to the power flow control of the interconnected bidirectional DAB converter. Additionally, the control strategy manages power in the nanogrids in an effective manner as the nanogrids extract the PV power to the maximum extent. The modular structure enhances the flexibility and reliability of the nanogrid network as it allows each nanogrid to operate autonomously or in connection to other nanogrids. More importantly, the control algorithm provides the plug-and-play capability of one or several power units, enabling the nanogrids to self-sustain themselves. Moreover, while the external DC bus voltage exists as a floating voltage according to the amount of power absorbed from or injected into the external DC bus, this algorithm ensures the stability of the nanogrid by regulating the internal DC bus voltage around the nominal value.

5 Conclusion and outlook

5.1 Conclusion

The main objective of the present work is the development of self-sustained and flexible control strategy for a DC nanogrid, which is supposed to be applied in off-grid areas. It is also focused on modeling and system stability analysis of the DC nanogrid system.

The first step concerned the mathematical representation of each single converter inside a DC nanogrid, including two bidirectional buck converters and a dual-active bridge converter. By means of the state-space averaging technique, a small-signal model of the buck converters was derived. In the case of the dual-active bridge, the generalized state-space averaging based modelling method was used. The state-space representation of the converters allowed the determination of the control-to-output transfer functions, which were then employed for the design of current and voltage controllers in the cascaded control structure. Simulation and experimental results regarding the operation of the converters proved the precision and effectiveness of the modelling methods.

New ideas presented in this work are related to the self-sustained capability of the DC nanogrid whether it operates in an autonomous mode or an interconnected mode without any need for an extra communication system. The safety of the DC nanogrid was improved due to two reasons. First, the SoC of the battery was taken into account in the control algorithm in order to protect the battery from overcharging and deep discharging situations. Second, the external DC bus voltage was under consideration with the purpose of avoiding the collapse of this bus when multiple DC nanogrids are working in the interconnected mode. Moreover, the control topology was designed based on the decentralized approach, making the system flexible and scalable. Simulations and experiments proved that electric power from different sources inside a DC nanogrid was flexibly exchanged while the renewable energy was managed in such a way that it was harvested as much as possible. The control algorithm also provided a plug-and-play capability for one or several power entities. The reliability of the system was also enhanced due to the interconnection capability of multiple DC nanogrids and no need for a digital communication system.

In the next step, a small-signal model of the entire DC nanogrid system was developed and system stability analysis was performed. The small-signal transfer function of the complete DC nanogrid was synthesized from the small-signal transfer functions of three single converters. Based on the obtained transfer function, the secondary controller was designed and the system

stability analysis was conducted. Results obtained from both simulations and experiments showed that the secondary controller eliminated the voltage deviation caused by the droop control operation and ensured the stability of the whole system. More importantly, the proposed control strategy allowed the interconnection of multiple DC nanogrids to form a DC microgrid, in which the stability of a single interconnected DC nanogrid was not influenced by other nanogrid systems.

5.2 Outlook

This work presents a self-sustained and flexible control strategy for a DC nanogrid based on a hierarchical control approach. In order to verify the proposed control strategy, the coordinated operations of a nanogrid as well as multiple nanogrids are introduced through typical test cases such as the changes in the load and the changes in the PV source. However, further research is needed to complete the operation of the micro/nanogrid and to demonstrate the operation of the nanogrid in fault modes such as overload, short circuit or blackout.

First, possible faults and a well-functioning protection scheme of the system should be taken into account in order to ensure reliable operation of a nanogrid. In addition, different protection devices and grounding methods should be employed in DC nanogrids.

Second, a possible solution to avoid overload situation of nanogrids is to utilize load shedding strategy for interruptible loads. In order to achieve this goal, the demand side control needs to be implemented and different preset internal DC bus voltage levels should be used for respective load cutting. Depending on preset voltage levels, the priorities should be assigned to critical loads in order to ensure the uninterrupted operation of nanogrids with these loads.

It is also interesting for future work to develop an algorithm to provide a black start capability after blackouts of the system. Power outages can occur when power consumption is much higher than power generation for a given period, especially for micro/nanogrids working in an island mode. Therefore, future studies should take into consideration the possible black start capability of micro/nanogrids for restoration.

6 Appendix

This section presents the design of main components as well as the schematics and printed circuit boards for the nanogrid system including the DAB and buck converters.

6.1 Design of dual active bridge converter

Figure 3.19 shows the schematic of the DAB converter that consists of power, control, measurement and gate driver circuits. The power part contains two H-bridges, a HF transformer, an additional inductor, an output filter and DC link capacitors. The core element of the control part is a TMS320F28335 DSP that is responsible for executing the control algorithm and generating PWM signals to the gate driver. The measurement circuit comprises two voltage transducers and two current transducers to measure the input and output voltages and currents, respectively. The design of these parts will be presented hereafter.

6.1.1 Power part

The definitions of some components have already been mentioned in section 3.5, and therefore they are not repeated in this section. The design procedure of the HF transformer, the additional inductor, the output filter and power MOSFETs of the DAB converter are introduced in this section.

6.1.1.1 HF transformer

In DAB converter topologies, a HF transformer is used to transfer electric power. The size of the HF transformer depends on the transferred power and the switching frequency. The first step of designing the HF transformer is to select a suitable ferrite core. Afterwards, the numbers of primary and secondary turns are calculated.

As shown in Figure 6.1, the voltage V_{d1} produces a magnetizing current I_M which is proportional to the magnetic flux Φ . According to Faraday's law of induction, the relationship between the voltage and the magnetic flux is expressed as

$$V_{d1} = N_1 \cdot \frac{d\Phi}{dt} \quad (6.1)$$

or

$$V_{d1} = N_1 \cdot \frac{\Phi_{\max} - (-\Phi_{\max})}{T_s/2} = 4 \cdot N_1 \cdot \Phi_{\max} \cdot f_s \quad (6.2)$$

where N_1 is the number of the primary turns of the HF transformer, Φ_{\max} is the maximum value of the magnetic flux. In addition, the maximum magnetic flux is equal to:

$$\Phi_{\max} = B_{\max} \cdot A_e \quad (6.3)$$

where B_{\max} is the maximum magnetic flux density and A_e is the effective cross-section area of the core.

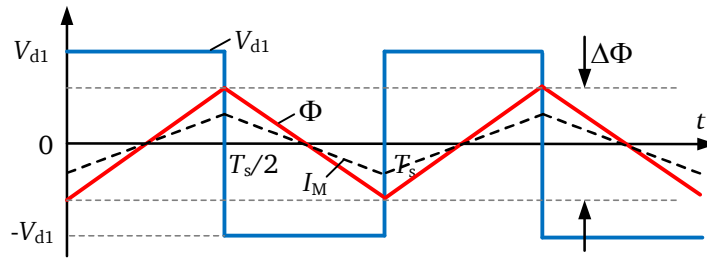


Figure 6.1: Typical waveforms of the voltage and the magnetic flux

From (6.2) and (6.3), the number of the primary turns is given by

$$N_1 = \frac{V_{d1}}{4 \cdot B_{\max} \cdot A_e \cdot f_s} \quad (6.4)$$

A magnetic core without an air gap is employed to minimize the magnetizing current. In this work, an Economical Transformer Design (ETD) 49/25/16 with N87 is selected for the magnetic core. Accordingly, the effective core cross section area is $A_e = 211 \text{ mm}^2$ [141]. The number of the primary turns is calculated to ensure that the flux density does not exceed $B_{\max} = 0.2 \text{ T}$ in order to achieve low core losses and to avoid magnetic saturation. Therefore, the minimum number of the primary turns is

$$N_{1,\min} = \frac{100 \text{ V}}{4 \cdot 0.2 \text{ T} \cdot 211 \text{ mm}^2 \cdot 50 \text{ kHz}} = 11.9 \text{ turns} \quad (6.5)$$

In this work, the selected number of the primary turns is $N_1 = 16$ turns to ensure a high filling factor of the core. As a result, the number of the secondary turns is given by

$$N_2 = \frac{N_1}{N} = \frac{16 \text{ turns}}{2} = 8 \text{ turns} \quad (6.6)$$

The next step is to choose the diameter of the wire based on the root mean square (RMS) value of the current. The diameter of the primary winding is determined as follows

$$d_{w1} = \sqrt{\frac{4I_{L1}}{J \cdot \pi}} \quad (6.7)$$

where I_{L1} is the RMS value of the primary current and J is the current density inside the wire. The RMS value of the primary current can be given as follows

$$I_{L1} = \sqrt{\frac{2}{T_s} \int_0^{T_s/2} i_t^2 dt} \quad (6.8)$$

This RMS value of the primary current is calculated for the maximum power according to the phase shift ratio $d = 0.5$. Hence, (6.8) is rewritten as

$$I_{L1} = \frac{1}{8f_s L} \sqrt{V_{d1}^2 + V_{d2}^{'2}} = \frac{1}{8 \cdot 50 \text{ kHz} \cdot 60 \text{ } \mu\text{H}} \sqrt{(100 \text{ V})^2 + (2 \cdot 48 \text{ V})^2} = 5.77 \text{ A} \quad (6.9)$$

According to the thermal design, the current density of 6 A/mm^2 is given for Litz wire [142]. Therefore, the diameter of the primary winding is calculated as

$$d_{w1} = \sqrt{\frac{4 \cdot 5.77 \text{ A}}{6 \text{ A/mm}^2 \cdot \pi}} = 1.11 \text{ mm} \quad (6.10)$$

The cross-section area of the primary wire A_{w1} is given by

$$A_{w1} = \frac{I_{L1}}{J} = \frac{5.77 \text{ A}}{6 \text{ A/mm}^2} = 0.96 \text{ mm}^2 \quad (6.11)$$

Similarly, the diameter and cross-section area of the secondary wire are calculated as 1.57 mm and 1.92 mm^2 , respectively. Litz wire that consists of $245 \text{ strands} \times 0.1 \text{ mm}$ is selected for both the primary and secondary windings as its copper area and diameter are 1.93 mm^2 and 2.2 mm, respectively.

Using the E5061B network analyzer in the laboratory, the leakage inductance of the primary side $L_{1\sigma}$ and secondary side $L_{2\sigma}$ are measured to be $2.18 \text{ } \mu\text{H}$ and $0.52 \text{ } \mu\text{H}$, respectively. Therefore, the total leakage inductance of the HF transformer referred to the primary side is

$$L_{\sigma} = L_{1\sigma} + N^2 \cdot L_{2\sigma} = 4.26 \text{ } \mu\text{H} \quad (6.12)$$

6.1.1.2 Additional inductor

The coupling inductance is the sum of the leakage inductance of the HF transformer and the additional inductance which can be connected in series to the primary side or the secondary side of the HF transformer. According to (3.52), the coupling inductance referred to the secondary side is calculated as follows

$$L_{t,\max} = \frac{V_{d1}V_{d2}}{2Nf_sP_{\max}} d_{\max}(1 - d_{\max}) \quad (6.13)$$

where $P_{\max} = 400 \text{ W}$ is the maximum power of the converter, d_{\max} is the maximum phase shift ratio between the primary and secondary sides. Power is transferred from the leading bridge to the lagging bridge according to the phase shift ϕ , which is varied from 0 to $\pi/2$ to minimize the reactive current of the HF transformer. The maximum power can be obtained at a phase shift $\phi_{\max} = \pi/2$. Therefore, the maximum phase shift ratio can be obtained by

$$d_{\max} = \frac{\phi_{\max}}{\pi} = 0.5 \quad (6.14)$$

With the given values in Table 3.4, the coupling inductance referred to the secondary side is

$$L_{t,\max} = \frac{100 \text{ V} \cdot 48 \text{ V}}{2 \cdot 2 \cdot 50 \text{ kHz} \cdot 400 \text{ W}} \cdot 0.5(1 - 0.5) = 15 \text{ } \mu\text{H} \quad (6.15)$$

The coupling inductance referred to the primary side is given by

$$L'_{t,\max} = N^2 \cdot L_{t,\max} = 2^2 \cdot 15 \text{ } \mu\text{H} = 60 \text{ } \mu\text{H} \quad (6.16)$$

In addition, the coupling inductance referred to the primary side, which consists of the external inductance L_{ext} , the leakage inductances $L_{1\sigma}$ and $L_{2\sigma}$ of the HF transformer, is obtained by

$$L'_{t,\max} = L_{\text{ext}} + L_{1\sigma} + N^2 \cdot L_{2\sigma} \quad (6.17)$$

The total leakage inductance of the HF transformer referred to the primary side is $L_{\sigma} = L_{1\sigma} + N^2 \cdot L_{2\sigma} = 4.26 \text{ } \mu\text{H}$. Then the external inductance referred to the primary side is deduced as

$$L_{\text{ext}} = L'_{t,\max} - L_{\sigma} = 55.74 \text{ } \mu\text{H} \quad (6.18)$$

The next step is to choose a suitable core for the inductor. The inductor needs a required volume for the air gap to store energy which is given by

$$W = \frac{1}{2} L_{\text{ext}} \hat{i}_{1t}^2 \quad (6.19)$$

where \hat{I}_{1t} is the peak primary current of the HF transformer. On the other hand, the energy stored in the inductor can be given as follows

$$W \approx \frac{1}{2} \frac{B^2 \cdot A_e \cdot \delta}{\mu_0} \quad (6.20)$$

where δ is the air gap and $\mu_0 = 4\pi \cdot 10^{-7}$ H/m is the vacuum permeability. The effective cross-section area of the core can be chosen so that the magnetic flux density is not over its maximum value B_{\max} . Therefore, from (6.19) and (6.20), the effective cross-section area of the core can be expressed as

$$A_e \geq \frac{L_{\text{ext}} \hat{I}_{1t}^2 \cdot \mu_0}{B_{\max}^2 \cdot \delta} \quad (6.21)$$

The peak primary current of the HF transformer can be given by

$$\hat{I}_{1t} = \frac{1}{4f_s L'_t} \left[V_{d1} + \left(\frac{2\phi}{\pi} - 1 \right) V'_{d2} \right] \quad (6.22)$$

where V'_{d2} is the output voltage referred to the primary side of the HF transformer. The maximum value of the peak primary current can be achieved at the phase shift $\phi = \pi/2$. Therefore, the maximum peak primary current of the HF transformer can be given as follows

$$\hat{I}_{1t,\max} = \frac{V_{d1}}{4f_s L'_t} = \frac{100 \text{ V}}{4 \cdot 50 \text{ kHz} \cdot 60 \text{ } \mu\text{H}} \approx 8.33 \text{ A} \quad (6.23)$$

For the given values, the effective cross-section area of the core can be calculated as

$$A_e \geq \frac{L_{\text{ext}} \hat{I}_{1t}^2 \cdot \mu_0}{B_{\max}^2 \cdot \delta} = \frac{55.74 \text{ } \mu\text{H} \cdot (8.33 \text{ A})^2 \cdot 1.2566 \cdot 10^{-6} \frac{\text{H}}{\text{m}}}{(0.2 \text{ T})^2 \cdot 1 \text{ mm}} \approx 122 \text{ mm}^2 \quad (6.24)$$

According to the datasheet of ferrite cores, ETD 39/20/13 is selected for the additional inductor with the effective cross-section area of the core $A_e = 125 \text{ mm}^2$ [143]. Litz wire is used for the winding of the additional inductor for the capability of conducting a high frequency current and for minimizing the skin effect. The number of turns of the additional inductor is calculated as

$$N_{\text{ext}} = \sqrt{\frac{L_{\text{ext}}}{A_L}} \quad (6.25)$$

where A_L is inductance factor of the ferrite core. Material N87 is chosen for the ferrite core with the air gap of 1 mm and the inductance factor of 196 nH [143], the required number of turns of the additional inductor is given as follows

$$N_{\text{ext}} = \sqrt{\frac{55.74 \mu\text{H}}{196 \text{ nH}}} \approx 17 \text{ turns} \quad (6.26)$$

Litz wire with 245 strands \times 0.1 mm is chosen for the inductor wire as the inductor and the primary winding of the transformer have the same current.

6.1.1.3 Output filter

The filter inductance L_f is determined based on the maximum current ripple $\Delta I_{f,\text{max}}$ which is given by [136]

$$\Delta I_f = \left(\frac{V_{d1}}{N} - V_{d2} \right) \frac{d_{\text{max}}}{f_s L_f} \leq 40\% \frac{P_{\text{max}}}{V_{d2}} \quad (6.27)$$

Therefore, the required inductance of L_f is calculated as follows

$$L_f \geq \left(\frac{V_{d1}}{N} - V_{d2} \right) \frac{d_{\text{max}} \cdot V_{d2}}{40\% f_s \cdot P_{\text{max}}} = \left(\frac{100 \text{ V}}{2} - 48 \text{ V} \right) \frac{0.5 \cdot 48 \text{ V}}{40\% \cdot 50 \text{ kHz} \cdot 400 \text{ W}} \approx 6 \mu\text{H} \quad (6.28)$$

For the given values in Table 3.4, the inductance of L_f from (6.28) is calculated to be at least 6 μH . In this work, the inductance of the filter inductor is chosen as $L_f = 10 \mu\text{H}$ with a parasitic resistance $R_f = 16 \text{ m}\Omega$.

According to [142], the capacitance of the output filter is calculated based on the peak-to-peak voltage ripple as follows

$$\Delta V_o = \frac{\Delta Q}{C_f} = \frac{1}{C_f} \cdot \frac{1}{2} \cdot \frac{\Delta I_f}{2} \cdot \frac{1}{2f_s} \quad (6.29)$$

where ΔQ is an additional charge, ΔV_o is the voltage ripple. Substituting ΔI_f from (6.27) into (6.29) yields

$$\Delta V_o = \frac{1}{8f_s^2 C_f} \left(\frac{V_{d1}}{N} - V_{d2} \right) \frac{d_{\text{max}}}{L_f} \quad (6.30)$$

Therefore, the capacitance can be given as follows

$$C_f = \frac{1}{8f_s^2 \Delta V_o} \left(\frac{V_{d1}}{N} - V_{d2} \right) \frac{d_{\max}}{L_f} \approx 10 \mu\text{F} \quad (6.31)$$

The voltage ripple ΔV_o is chosen to be less than 1% of the output voltage of 48 V. From (6.31), with the given values, the capacitance is calculated to be bigger than 10 μF . In this work, film capacitors are selected for the output filter as the losses generated in these capacitors are insignificant and their parasitic inductance is very low [136]. Four films are chosen and are connected in parallel with the total value $C_f = 40 \mu\text{F}$.

6.1.1.4 Power MOSFETs

Power losses on the power switches and thermal design are not considered in this work. For simplicity, the power switches are selected to meet the overvoltage and overcurrent requirement. In this case, IRFP260MPBF is employed for power MOSFETs for both high and low sides with the main parameters being listed in Table 6.1.

Table 6.1: Main parameters of the power MOSFET of the DAB converter

Name	Switch No.	Drain-to-source breakdown voltage $V_{DS,BR}$ (V)	Continuous drain current I_D (A)	Gate-to-source voltage V_{GS} (V)	Drain-to-source On-resistance $R_{DS,on}$ (Ω)
IRFP260MPBF	8	200	50	± 20	0.04

6.1.2 Measurement circuit

In this work, the Hall Effect transducers LV25-P and LA25-NP from LEM manufacturer are used to measure the voltage and current, respectively. They provide some advantages such as an excellent accuracy, a very good linearity, a wide frequency bandwidth and a high immunity to external interference.

6.1.2.1 Current measurement

The LA25-NP, whose figure representation is shown in Figure 6.2, is a Hall Effect transducer which can be used to measure AC or DC signals up to 25 A. It provides a galvanic isolation between the primary and secondary sides. The power supply for this transducer is normally ± 15 V.

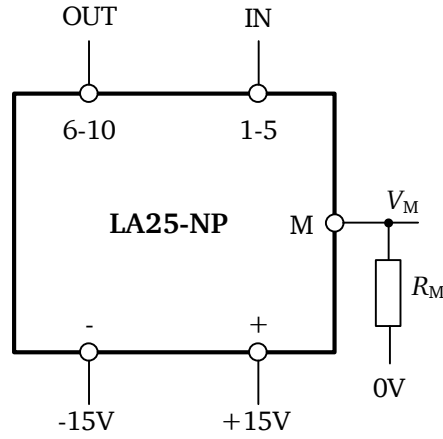


Figure 6.2: Current transducer LA25-NP

The output of the current transducer is a current which is measured at terminal “M”. In this work, 8 A is selected for the nominal primary current. According to the datasheet of LA25-NP, the nominal output current in secondary side is $I_{SN} = 24 \text{ mA}$ and the turns ratio is $K_N = 3: 1000$. In order to make the current signal suitable for input of ADC, it is converted into a voltage signal by using a measuring resistance R_M as shown in Figure 6.2. The measuring voltage V_M depends on the primary current I_P , the turns ratio K_N and the measuring resistance R_M . Because the input voltage of the ADC of DSP varies from $V_{\min} = 0 \text{ V}$ to $V_{\max} = 3 \text{ V}$, the measuring resistance can be calculated as follows

$$R_M = \frac{V_{\max}}{I_{SN}} = \frac{3 \text{ V}}{24 \text{ mA}} = 125 \Omega \quad (6.32)$$

For the design in this work, the selected value of R_M is 120Ω . The measuring voltage V_M is proportional to the primary current and the turns ratio as follows

$$V_M = R_M \cdot I_P \cdot K_N \quad (6.33)$$

Since the DAB converter can deliver power in both directions, the current could be negative or positive depending on the direction of delivered power. As the input voltage of the ADC is in the range of $[0 \text{ V}, 3 \text{ V}]$, the measuring voltage from the current sensor need to be shifted from $-3 \text{ V} \div 3 \text{ V}$ to $0 \text{ V} \div 6 \text{ V}$ and then it is amplified by a gain of 0.5. To meet this requirement, an offset voltage is added and an amplifier is used as shown in Figure 6.3.

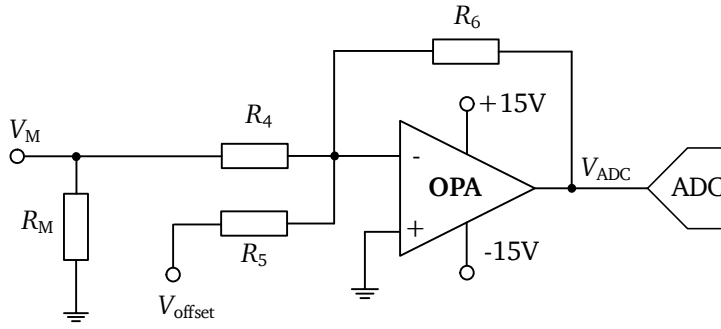


Figure 6.3: Current sensor and operational amplifier

As shown in Figure 6.3, the circuit contains a closed-loop inverting amplifier, which uses negative feedback to control the overall gain of the amplifier. The output measuring voltage is given as

$$V_{ADC} = -\left(\frac{R_6}{R_4} V_M + \frac{R_6}{R_5} V_{offset}\right) \quad (6.34)$$

In this work, the resistances are chosen as $R_4 = R_5 = 2R_6$. Therefore, (6.34) can be deduced as follows

$$V_{ADC} = -\frac{1}{2}(V_M + V_{offset}) \quad (6.35)$$

All values of the components can be found in section 6.3.

6.1.2.2 Voltage measurement

As illustrated in Figure 6.4, LV25-P is a Hall Effect transducer, which is capable of measuring AC and DC voltages up to 500 V while ensuring a galvanic separation between the primary and secondary sides. This sensor is powered with a power supply between ± 12 V and ± 15 V.

For voltage measurement, a resistance R_{in} is connected in series with the “+HT” terminal to produce a current which is proportional to the measured voltage. This resistance is chosen to ensure that the primary nominal current is around 10 mA. The output of the LV25-P transducer is also a current out of terminal “M” with the nominal value of 25 mA. Similar to the current measurement circuit, the output voltage needs to be produced from the output current by using a measuring resistance $R_M = 120 \Omega$ as shown in Figure 6.4. The output voltage is also a product of the primary current, the turns ratio and the measuring resistance.

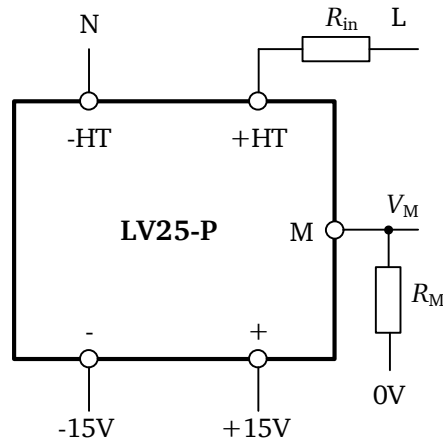


Figure 6.4: Voltage transducer LV25-P

An operational amplifier with a unity gain is also used to provide a buffer for the output voltage connected to the ADC as demonstrated in Figure 6.5.

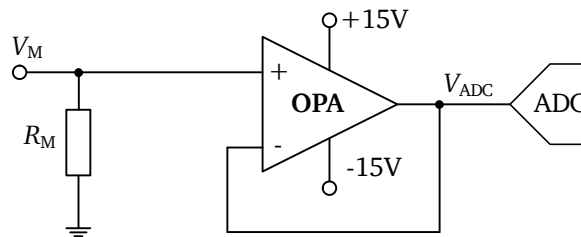


Figure 6.5: Voltage sensor and operational amplifier

6.1.3 Gate driver

The function of a gate driver is to generate high driving current to the gate terminal of a power MOSFET. It also functions as an interface to provide a galvanic isolation between the control and the power sides. Some other requirements of a gate driver are the abilities to protect the power MOSFET from short circuit and over voltage. In this work, gate drive 1ED020I12-B2 is selected, whose main technical information is given in Table 6.2, as it satisfies the aforementioned requirements.

Table 6.2: Main parameters of the isolated gate driver

Name	Power supply input side (V)	Positive power supply output side (V)	Negative power supply output side (V)	Logic input voltage (V)	Gate drive current (A)
1ED020I12-B2	4.5 ÷ 5	13 ÷ 20	-12 ÷ 0	-0.3 ÷ 5.5	2

The isolation is applied for not only the signal but also the power supplied to the chip. Therefore, the isolated 2W gate drive DC/DC converters named MGJ2D241505SC are used in this work. The main parameters of the isolated DC/DC converter are given in Table 6.3.

Table 6.3: Main parameters of the isolated DC/DC converter

Name	Input voltage (V)	Output voltage 1 (V)	Output voltage 2 (V)	Output current 1 (mA)	Output current 2 (mA)	Efficiency (%)
MGJ2D241505SC	24	15	-5	80	40	80.5

The diagram of the isolated gate driver with the isolated DC/DC power supply is shown in Figure 6.6. The TXB0104 device is used to match the logic voltage levels. With this translator device, the PWM voltage level of 3.3 V from DSP can be converted to the voltage level of 5 V at the output side.

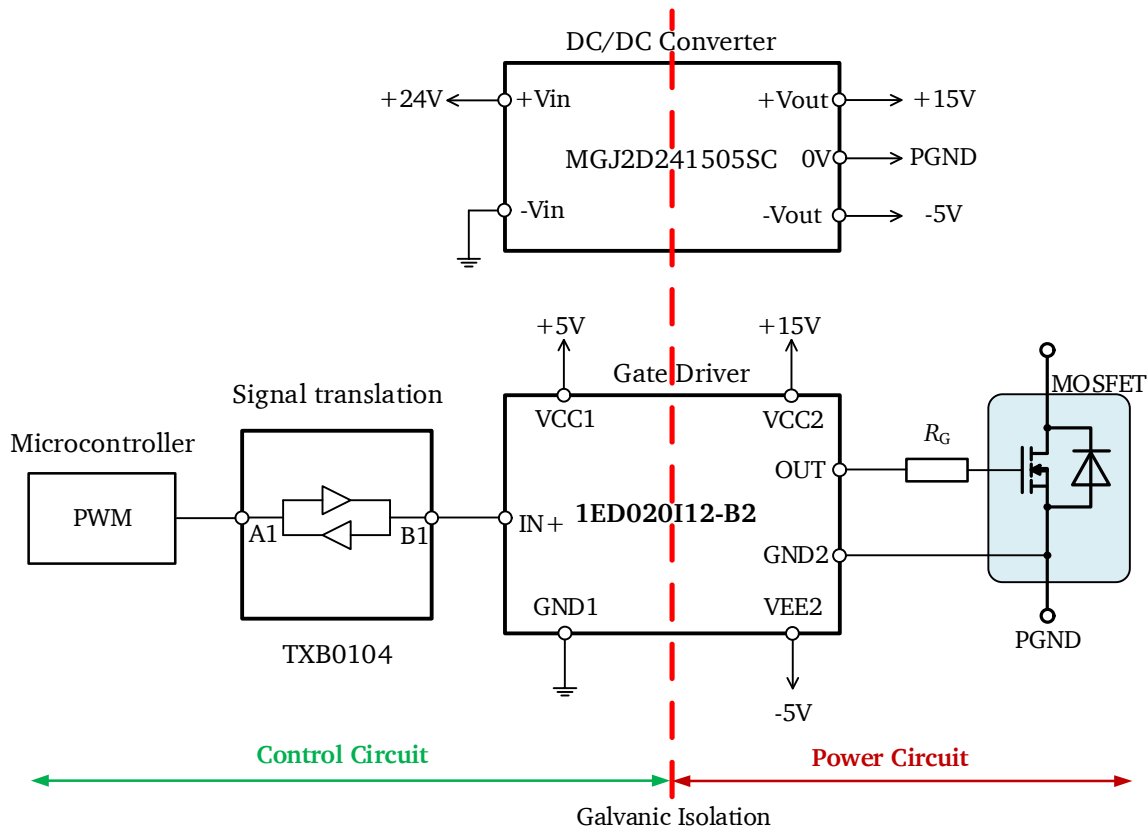


Figure 6.6: Gate drive circuit

6.2 Design of half-bridge converter

Figure 3.9 demonstrates the schematic of the bidirectional buck DC/DC converter that comprises power, control, measurement and gate driver circuits. The power circuit consists of two power MOSFET, an inductor and a DC link capacitor. Similar to the DAB converter, the control part of the buck converter uses the same DSP to generate the PWM signals. In addition, LV25-P and LA25-NP transducers are employed for voltage and current measurements, respectively.

6.2.1 Power part

This section presents the design of the inductor, the output capacitor and the selection of the power MOSFETs for the bidirectional buck converter.

6.2.1.1 Inductor

The inductance is computed according to the ripple of the inductor current and the switching frequency as follows [144].

$$L = \frac{D(V_i - V_o)}{f_s \Delta I_L} \quad (6.36)$$

where ΔI_L is the ripple of the inductor current. In this work, a maximum current ripple of 10% of the load current is considered for design. Therefore, the inductance of the inductor L is calculated as

$$L = \frac{0.48 \cdot (100 \text{ V} - 48 \text{ V})}{50 \text{ kHz} \cdot 10\% \cdot 6 \text{ A}} = 832 \text{ } \mu\text{H} \quad (6.37)$$

In experiment, the selected inductance is 1000 μH . The ferrite core ETD 49/25/16 with an air gap of 1 mm and material N87 is utilized for the inductor design. According to the datasheet of the ETD core, the inductance factor A_L is 314 nH [141]. Thus, the required number of turns of the inductor is calculated as follows

$$N_{\text{ind}} = \sqrt{\frac{1000 \text{ } \mu\text{H}}{314 \text{ nH}}} \approx 56 \text{ turns} \quad (6.38)$$

For convenience, Litz wire with 245 strands \times 0.1 mm is selected for wiring the inductor.

6.2.1.2 Output capacitor

The value of the capacitance of the output capacitor C_o is determined according to the ripple of the output voltage ΔV_o . Typically, the voltage ripple is specified to be less than 1% of the output voltage. Therefore, the capacitance is calculated as follows [142].

$$C_o = \frac{(1 - D) \cdot V_o}{8f_s^2 \cdot L \cdot \Delta V_o} = \frac{(1 - 0.48)}{8 \cdot (50 \text{ kHz})^2 \cdot 0.1 \text{ mH} \cdot 1\%} = 2.6 \mu\text{F} \quad (6.39)$$

In order to achieved the aforementioned requirement, the selected capacitance needs to be higher than 2.6 μF . In this work, a film capacitor with capacitance of 20 μF is used to obtain a smaller voltage ripple. A DC link capacitor with the capacitance of 1000 μF is also added in the output side of the buck converter in order to maintain a stable output voltage.

6.2.1.3 Power MOSFETs

For simplicity, similar to the DAB converter, the power MOSFETs of the bidirectional buck converter are chosen to ensure that the selected voltage and current are higher than the peak values of the voltage and current of the designed converter. Power MOSFETs IRFP4227PbF are used for the bidirectional buck converter with the main parameters being summarized in the Table 6.4.

Table 6.4: Main parameters of the power MOSFET of the buck converter

Name	Switch No.	Drain-to-source breakdown voltage $V_{DS,BR}$ (V)	Continuous drain current I_D (A)	Gate-to-source voltage V_{GS} (V)	Drain-to-source On-resistance $R_{DS,on}$ (Ω)
IRFP4227PbF	2	200	65	± 30	0.021

6.2.2 Measurement circuits and gate drivers

The measurement circuits for voltages and currents as well as the gate drivers for the power MOSFET are designed similarly to those of the DAB converter. Therefore, the procedure for the design of those circuitries is not presented here.

6.3 Schematics and printed circuit boards

The schematics and the printed circuit boards (PCB) of the DAB and buck converters are designed based on the Altium Designer. The main parts of the converters are presented hereafter.

6.3.1 Schematics and printed circuit boards of the DAB converter

This section presents the printed circuit board (PCB) layout and schematics of DAB converter.

6.3.1.1 Schematics and PCB layout for power module and gate drivers

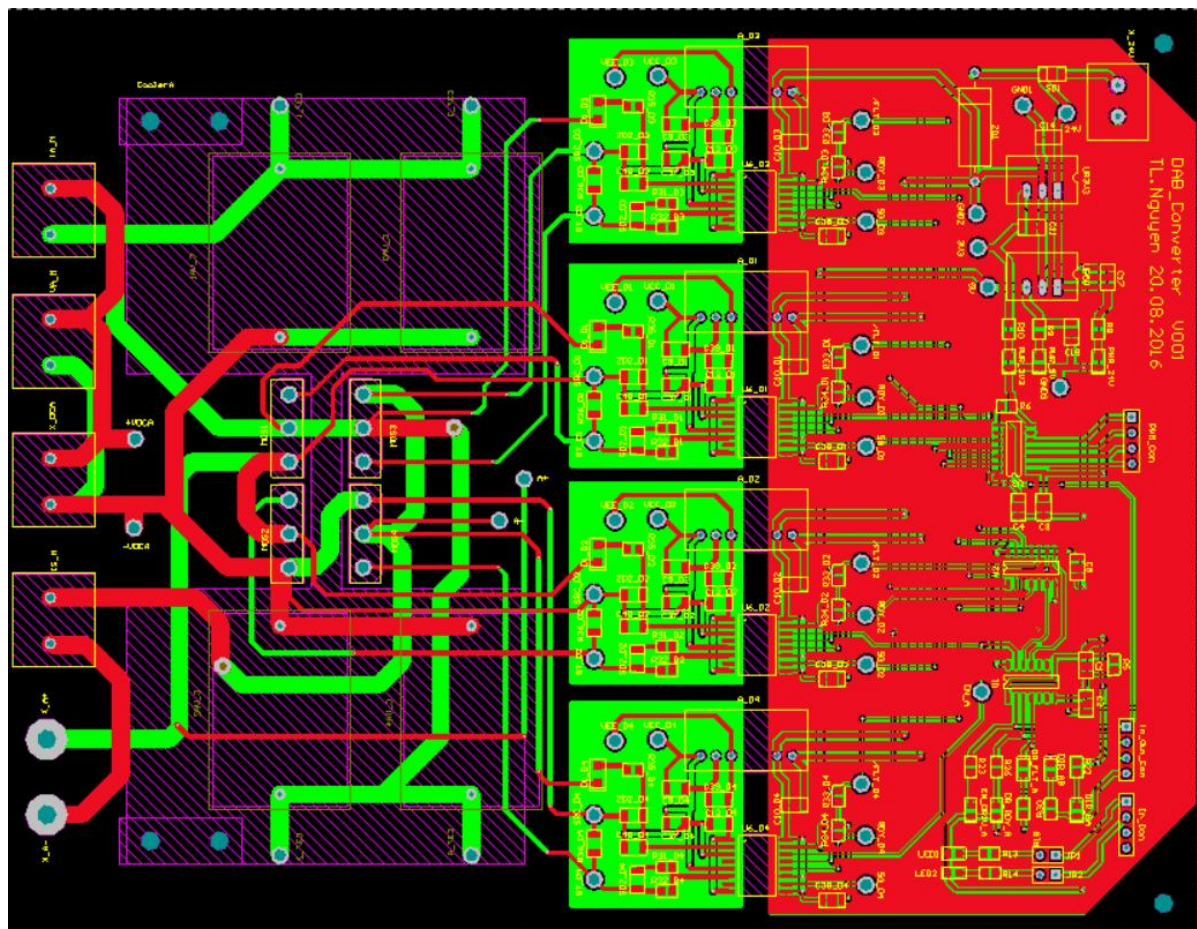
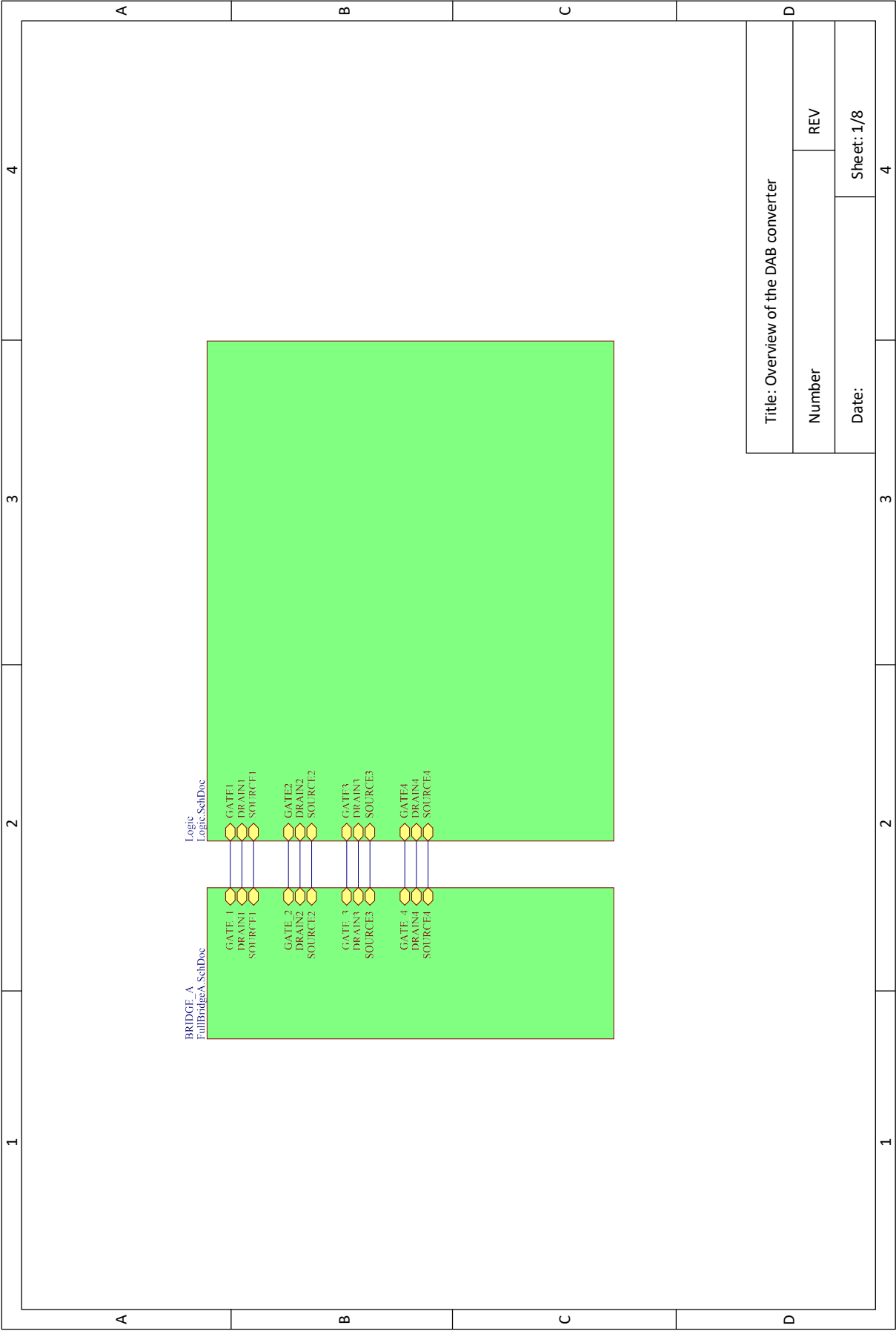
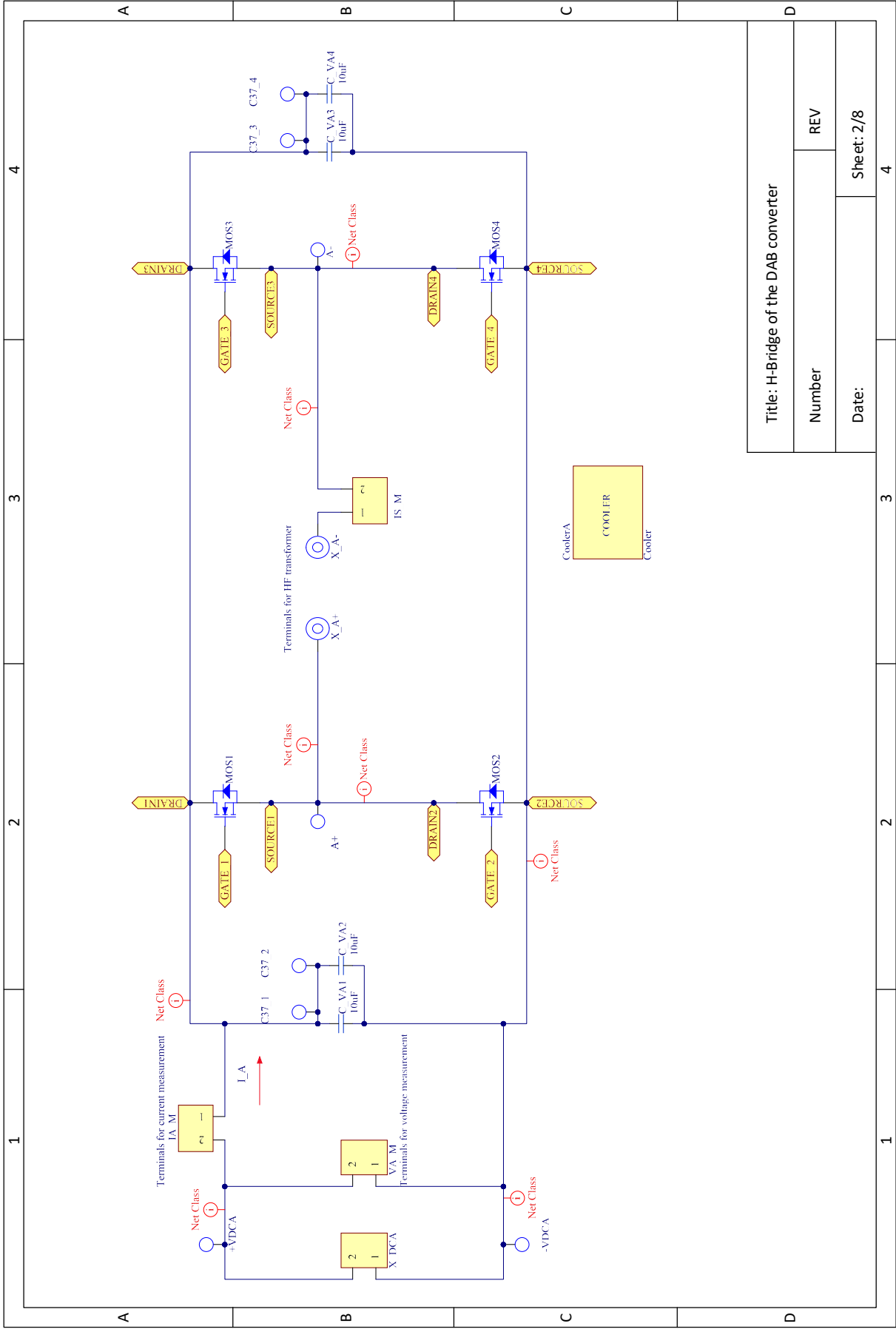
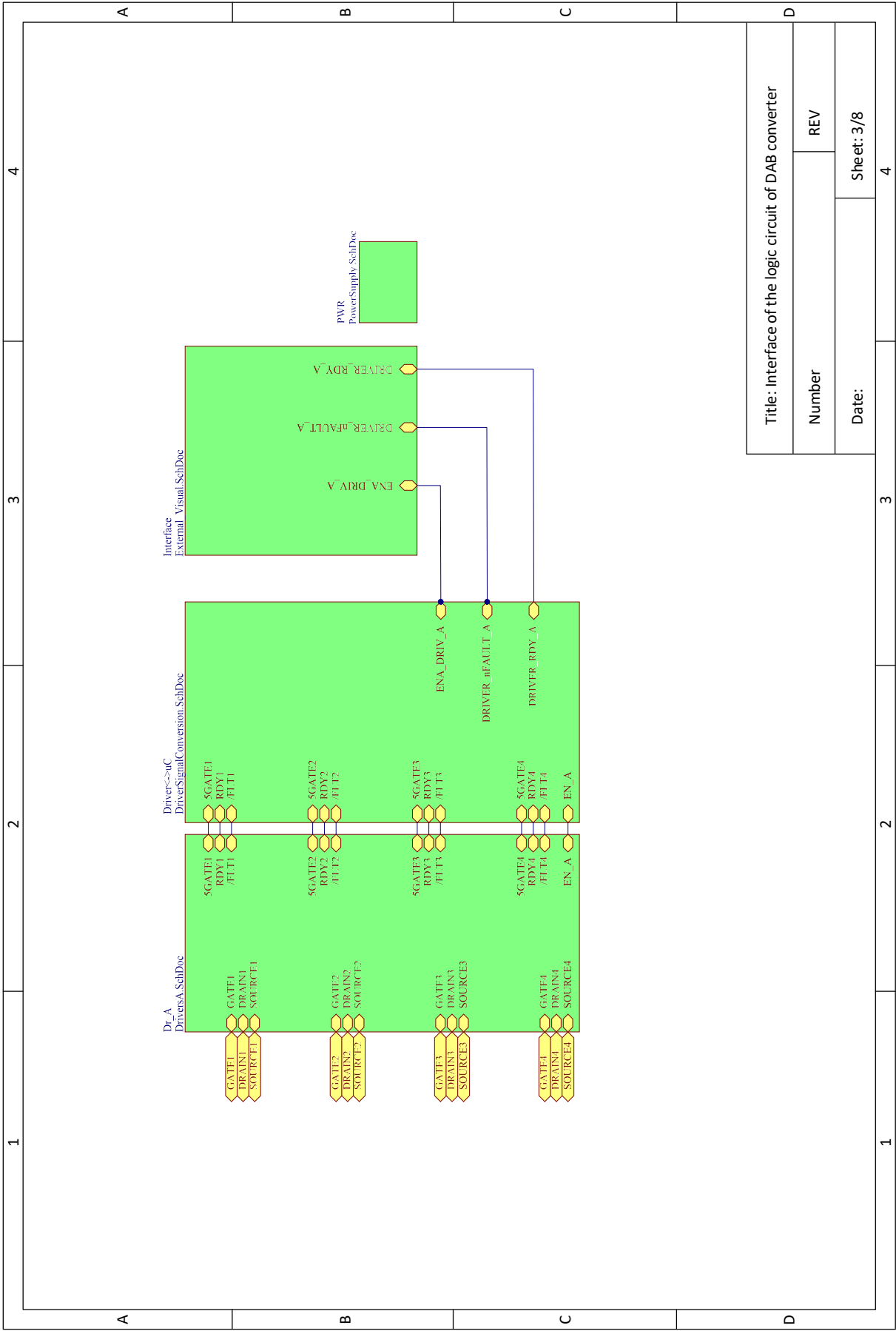
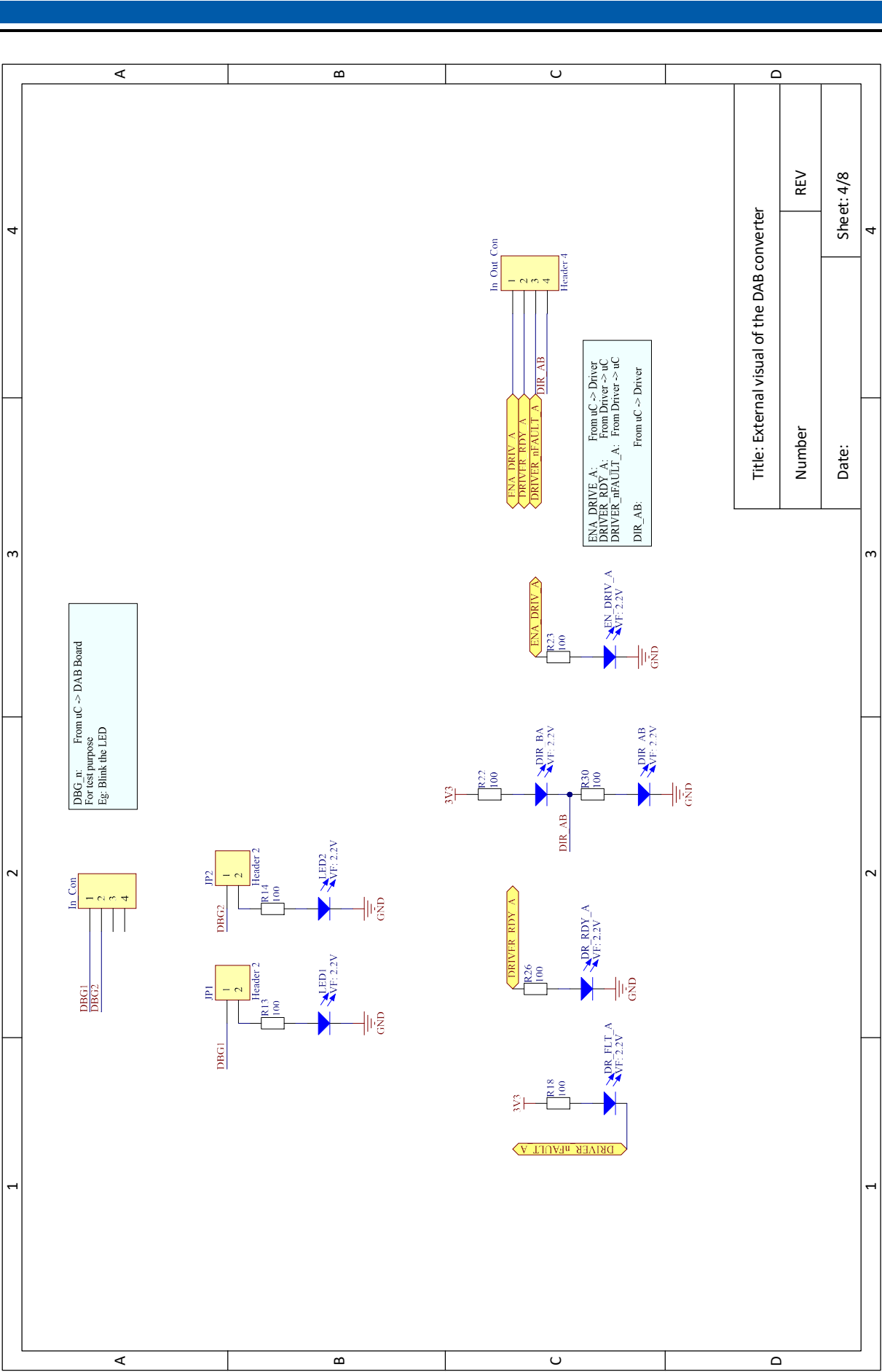


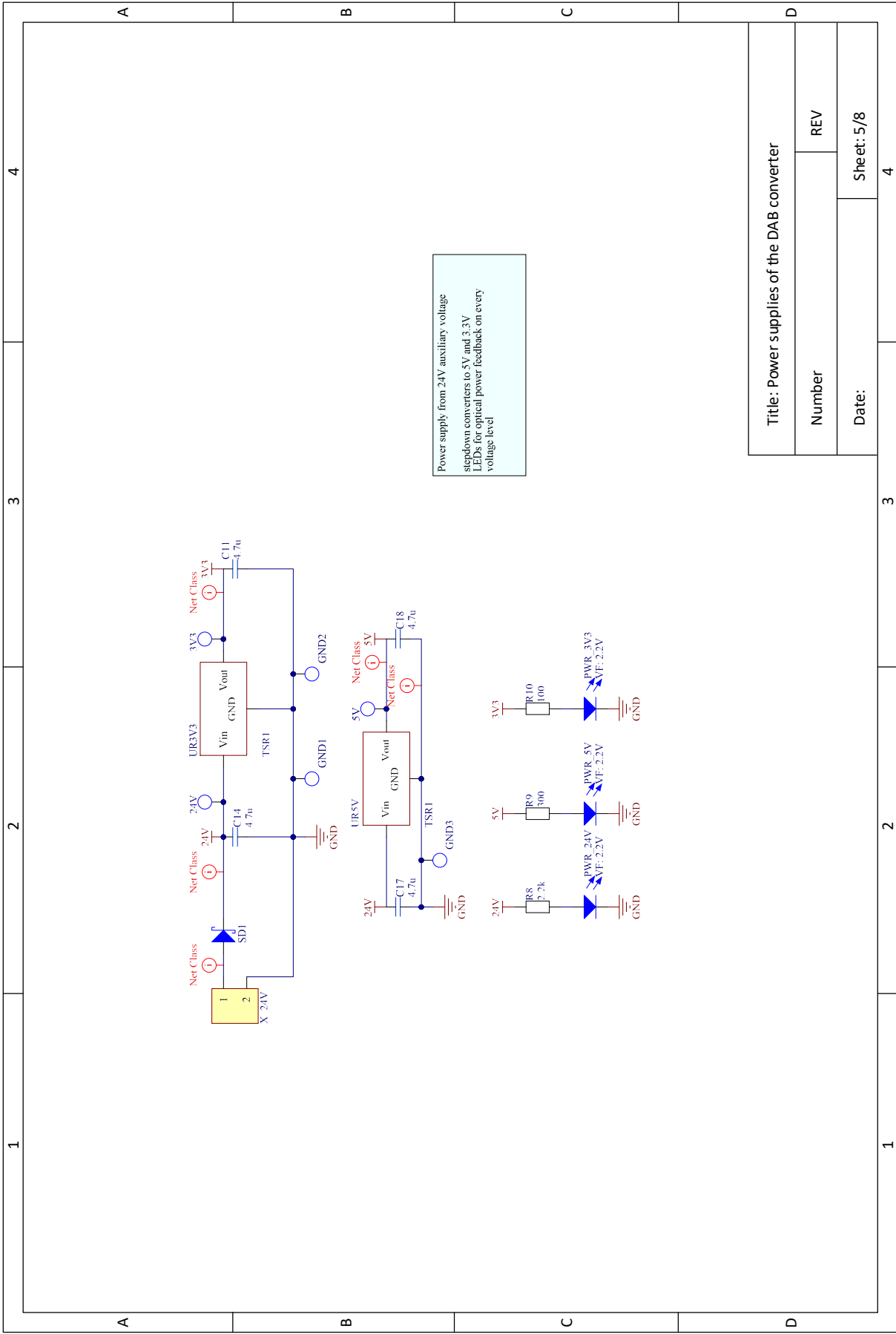
Figure 6.7: PCB layout of an H-Bridge of the DAB converter

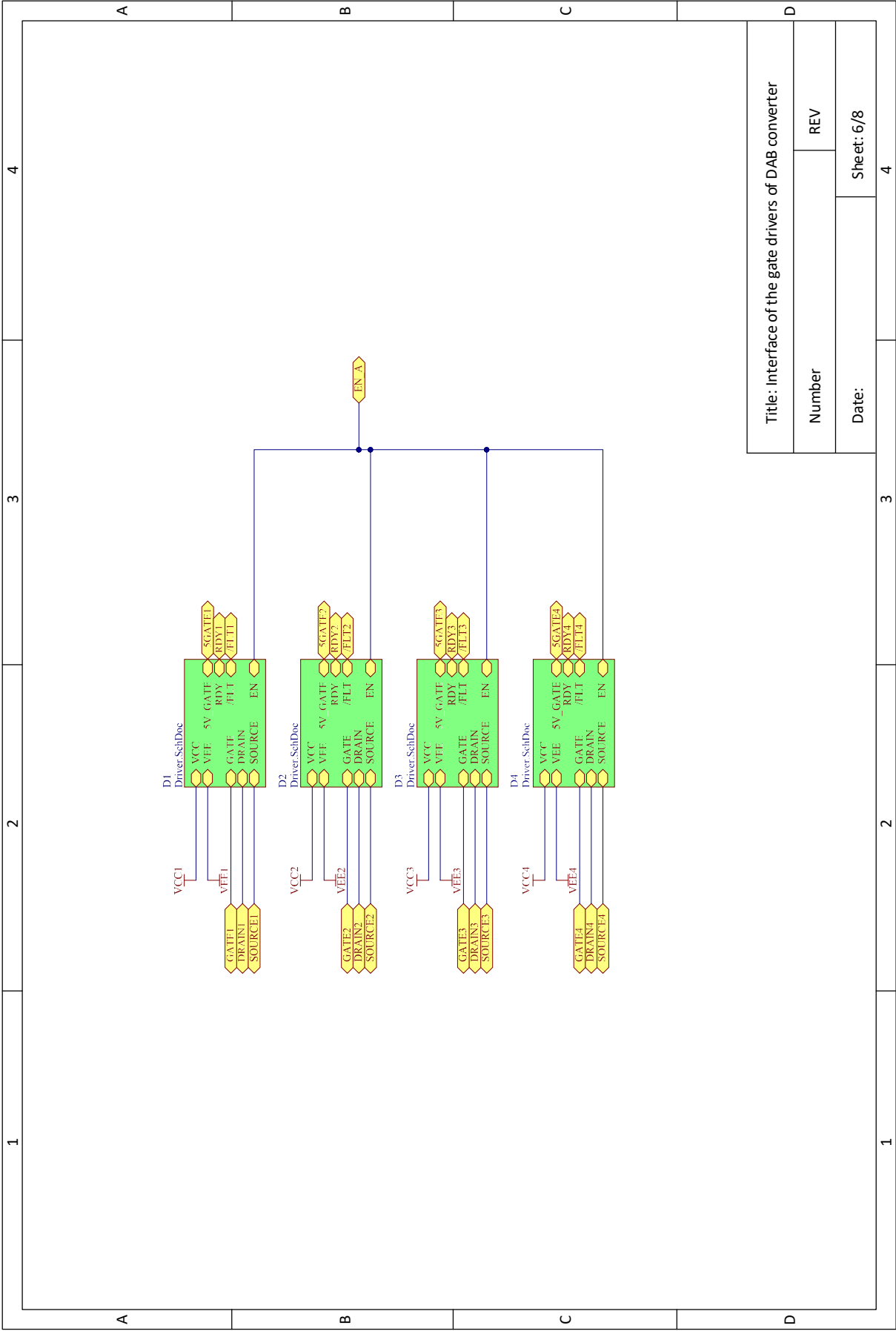


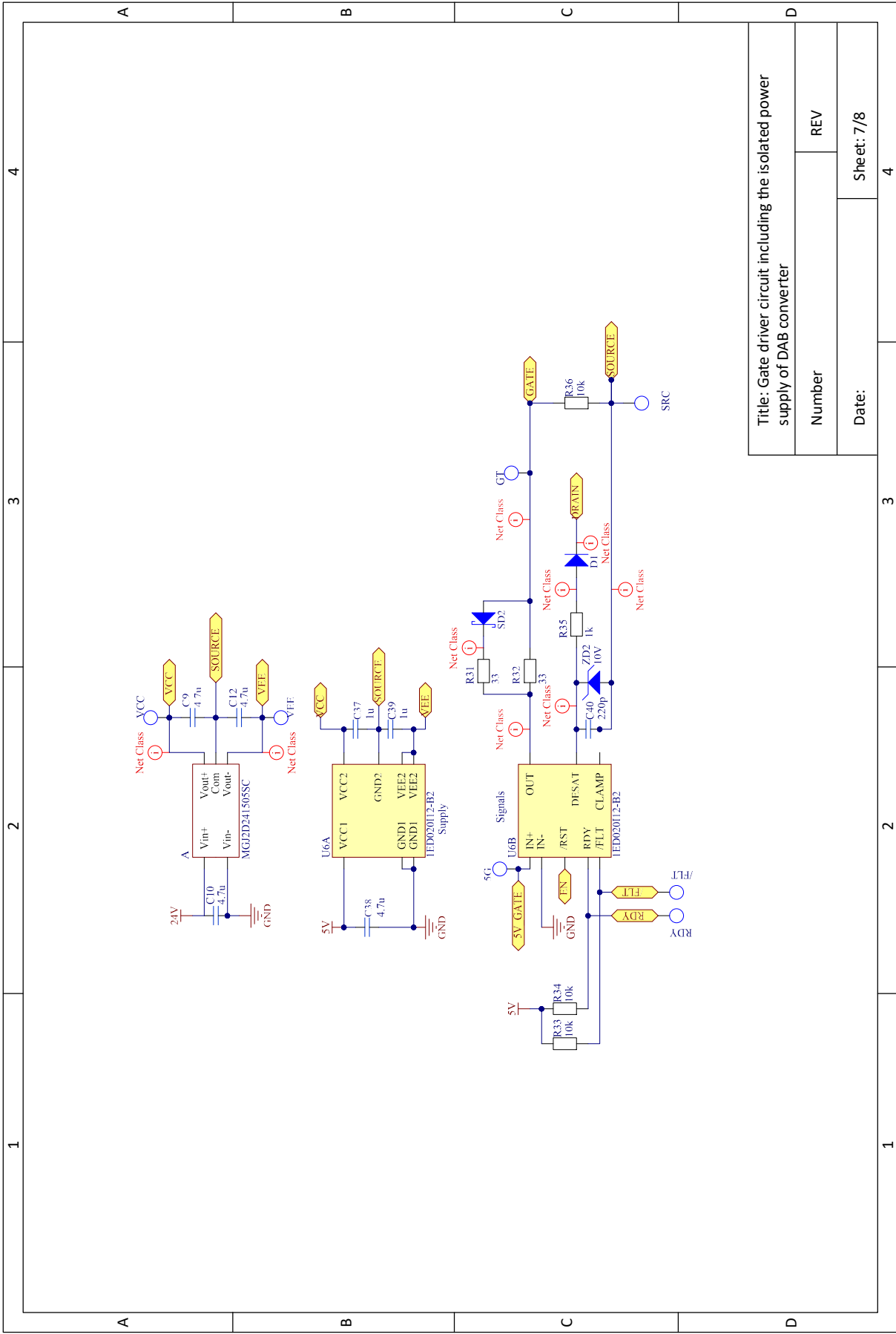




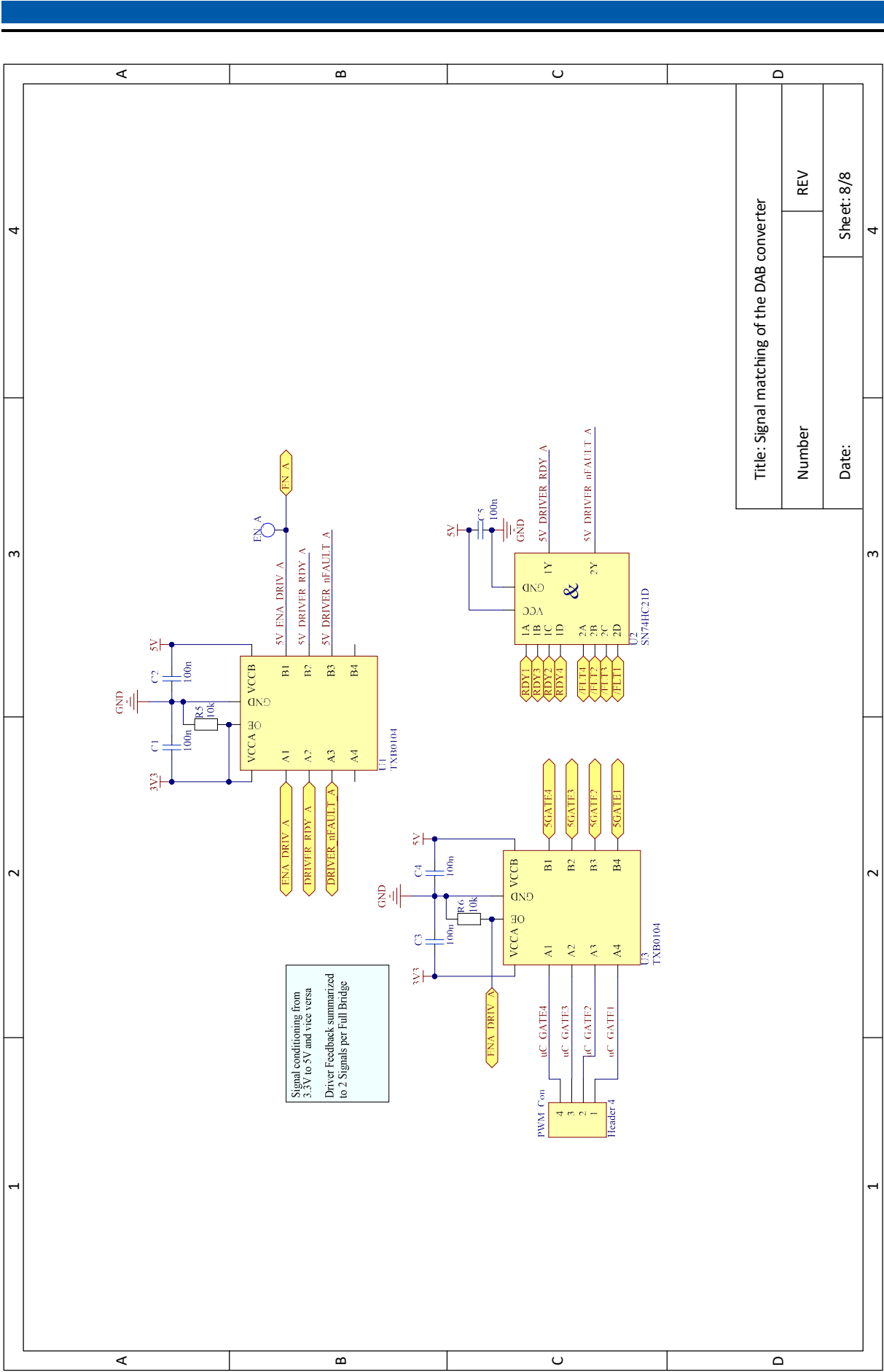








Title: Gate driver circuit including the isolated power supply of DAB converter	
Number	REV
Date:	Sheet: 7/8

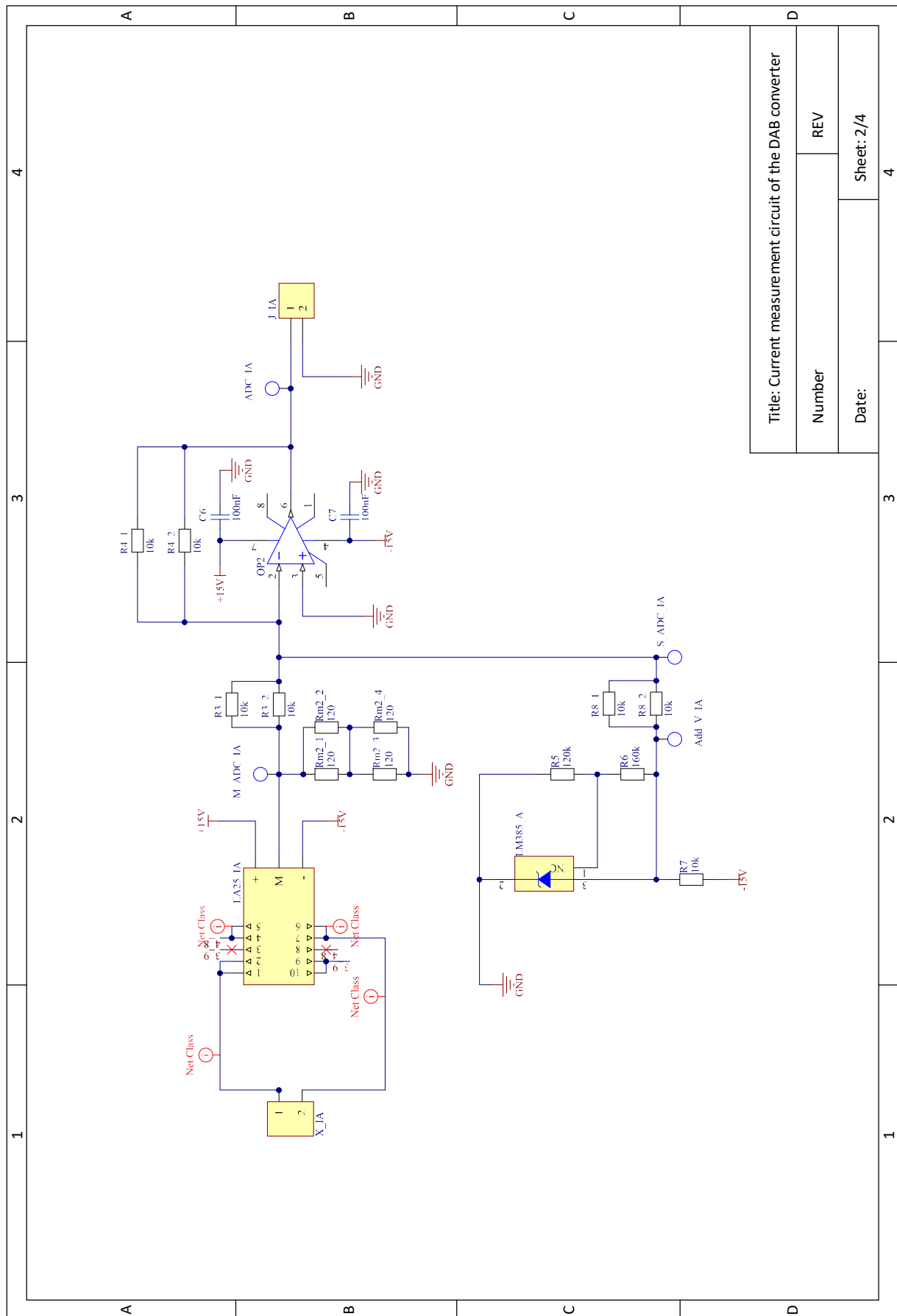


Title: Signal matching of the DAB converter	
Number	REV
Date:	Sheet: 8/8

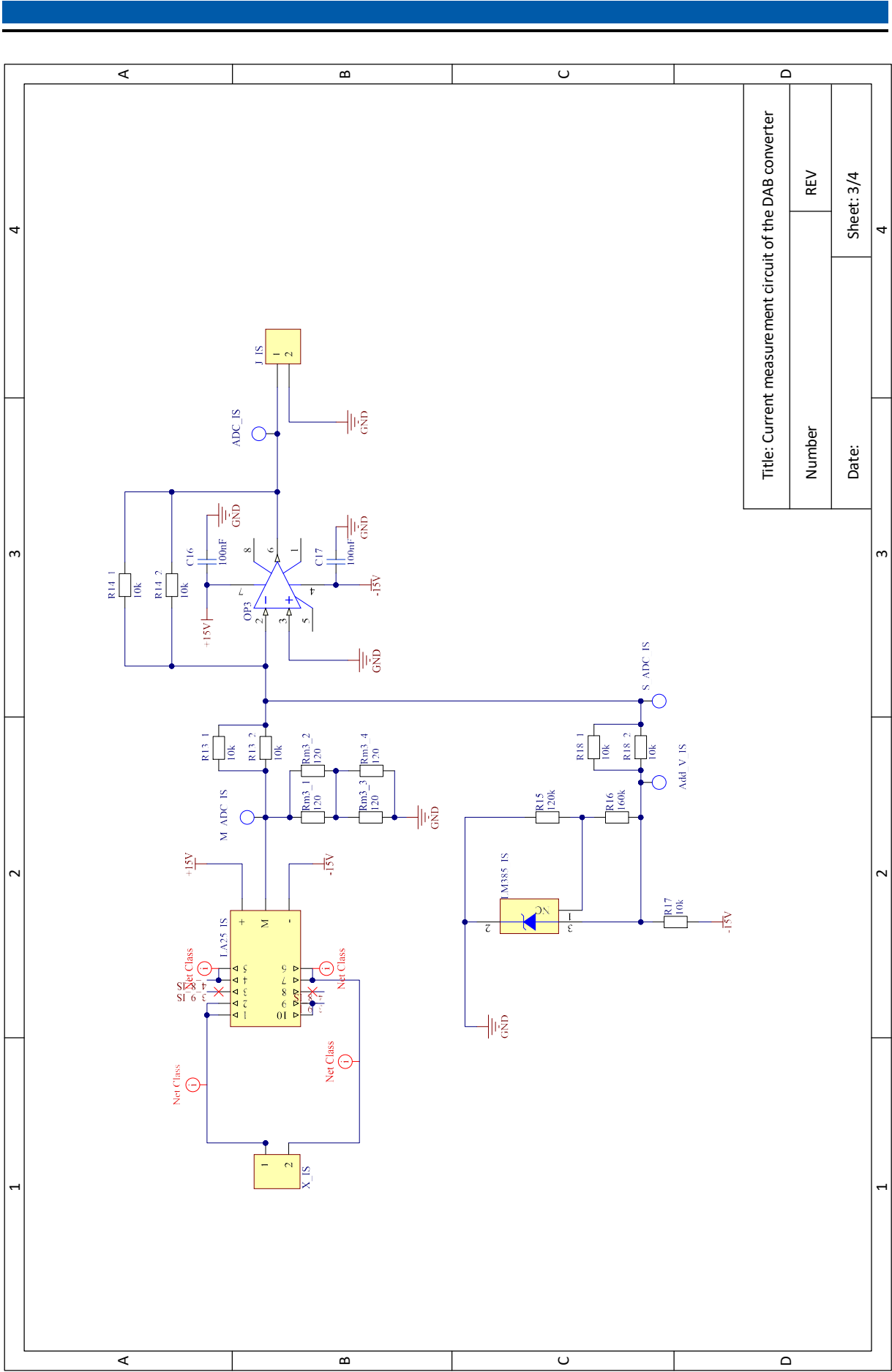
6.3 Schematics and printed circuit boards



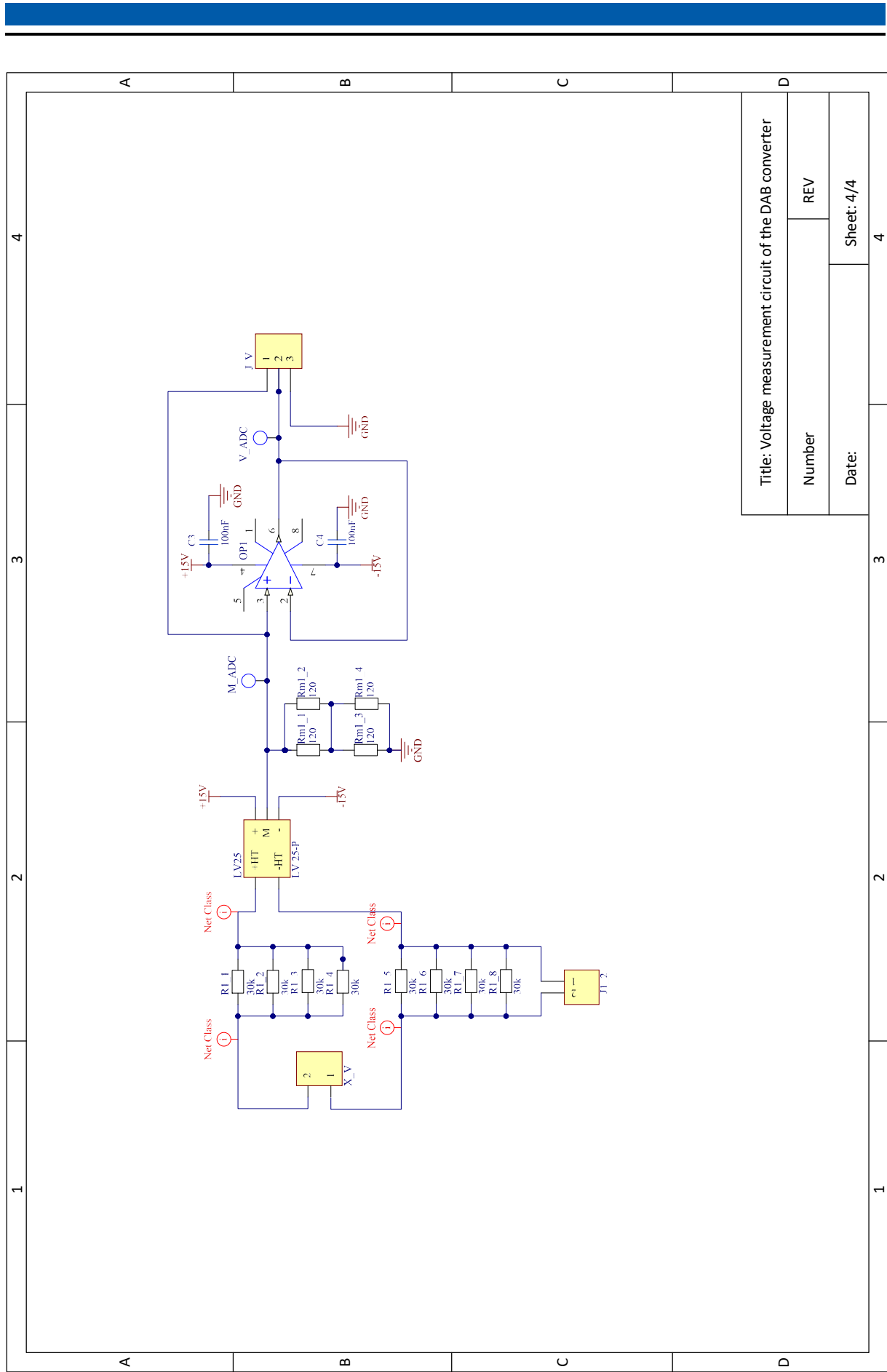
Figure 6.8: PCB layout of the measurement circuit of the DAB converter



Title: Current measurement circuit of the DAB converter	
Number	REV
Date:	Sheet: 2/4



Title: Current measurement circuit of the DAB converter			
Number		REV	
Date:		Sheet: 3/4	



6.3.2 Schematics and PCB layout of the bidirectional buck converter

This section shows the PCB layout and schematics of bidirectional buck converter.

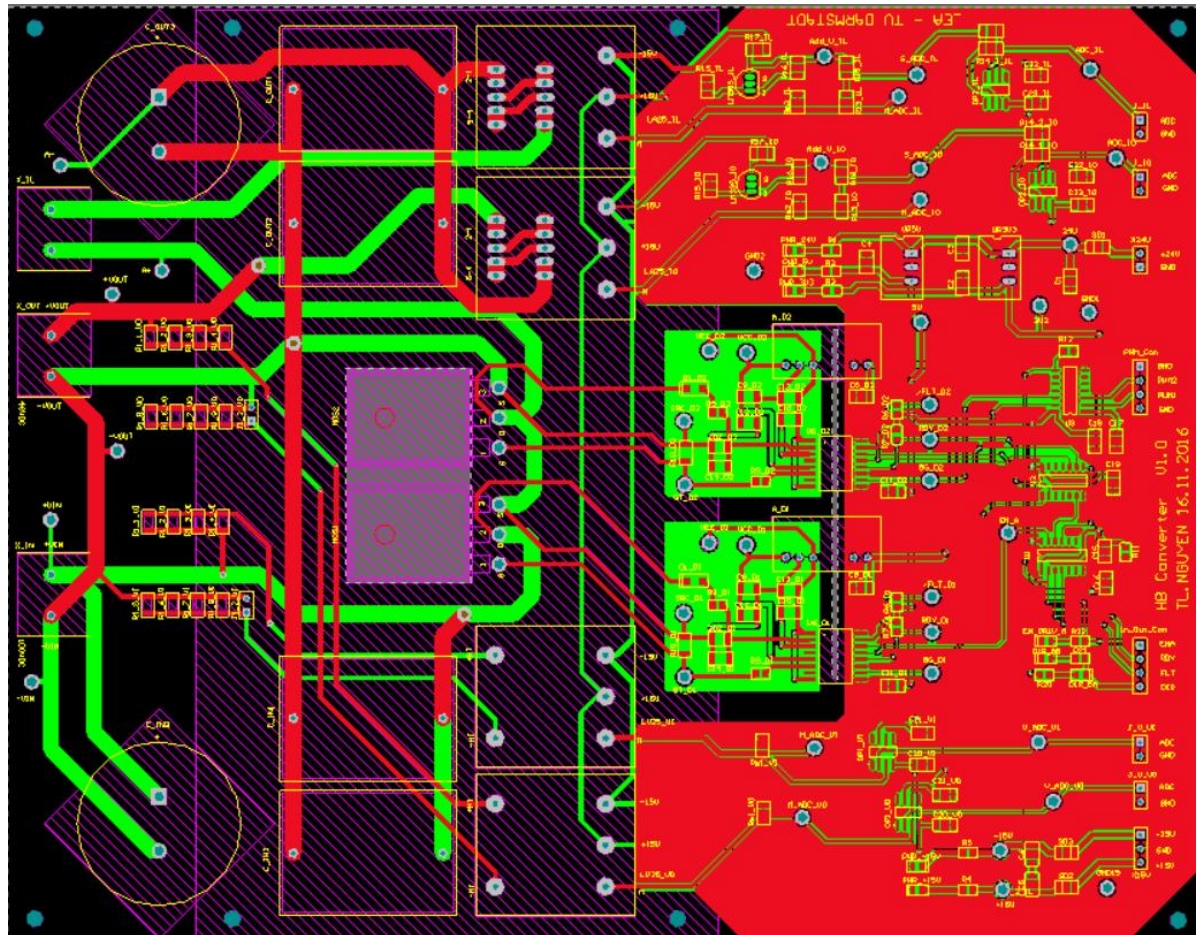
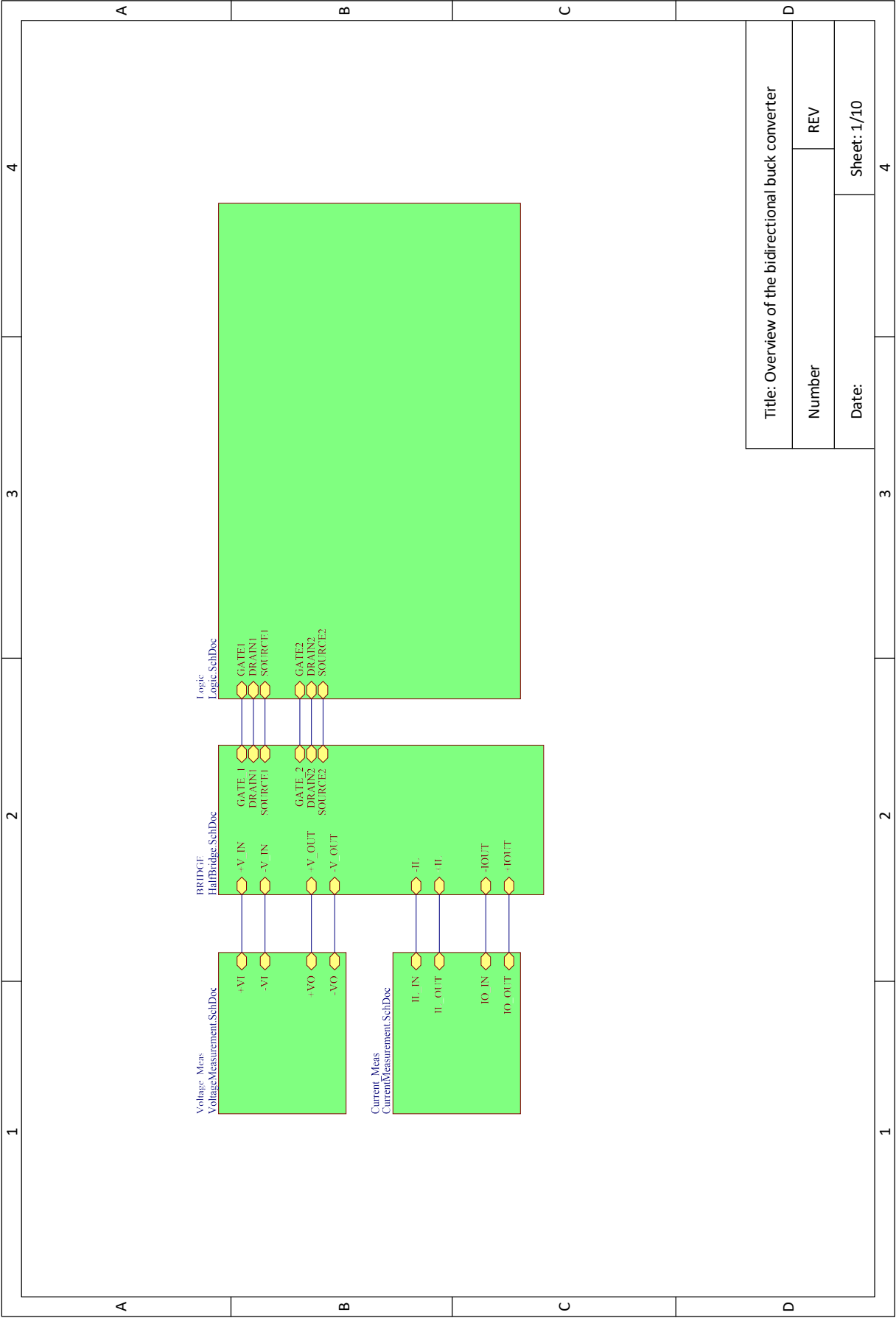
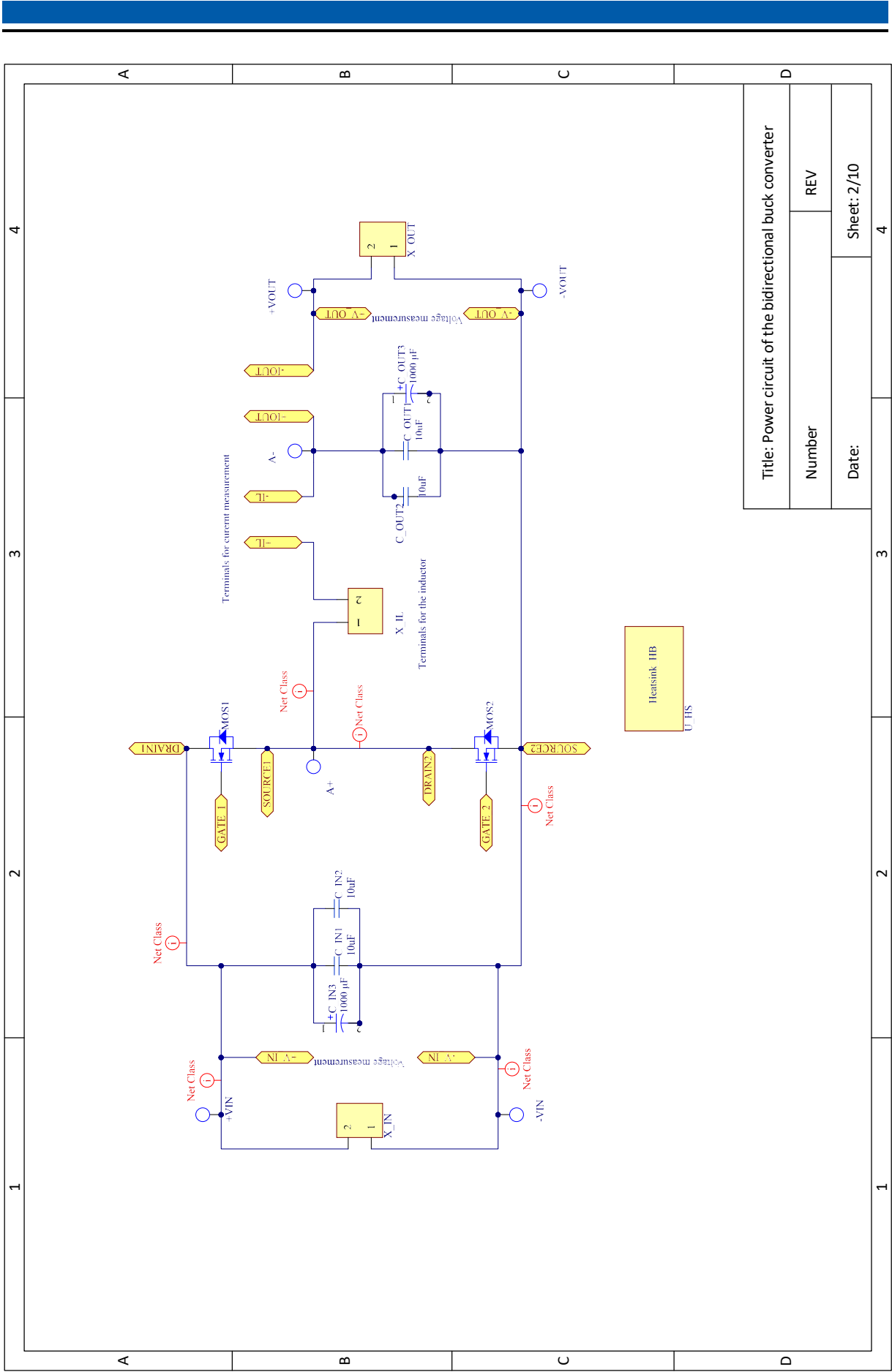
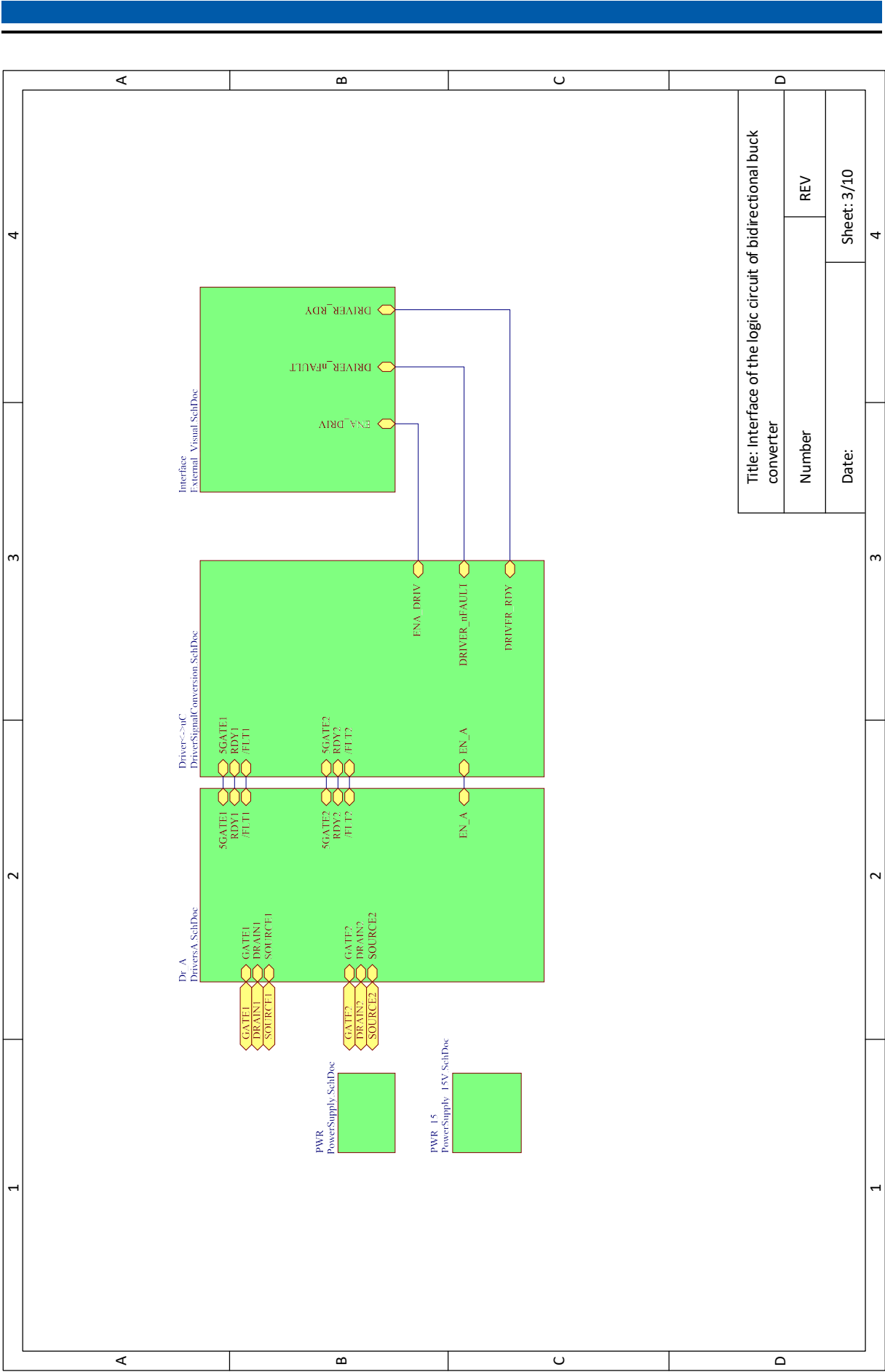
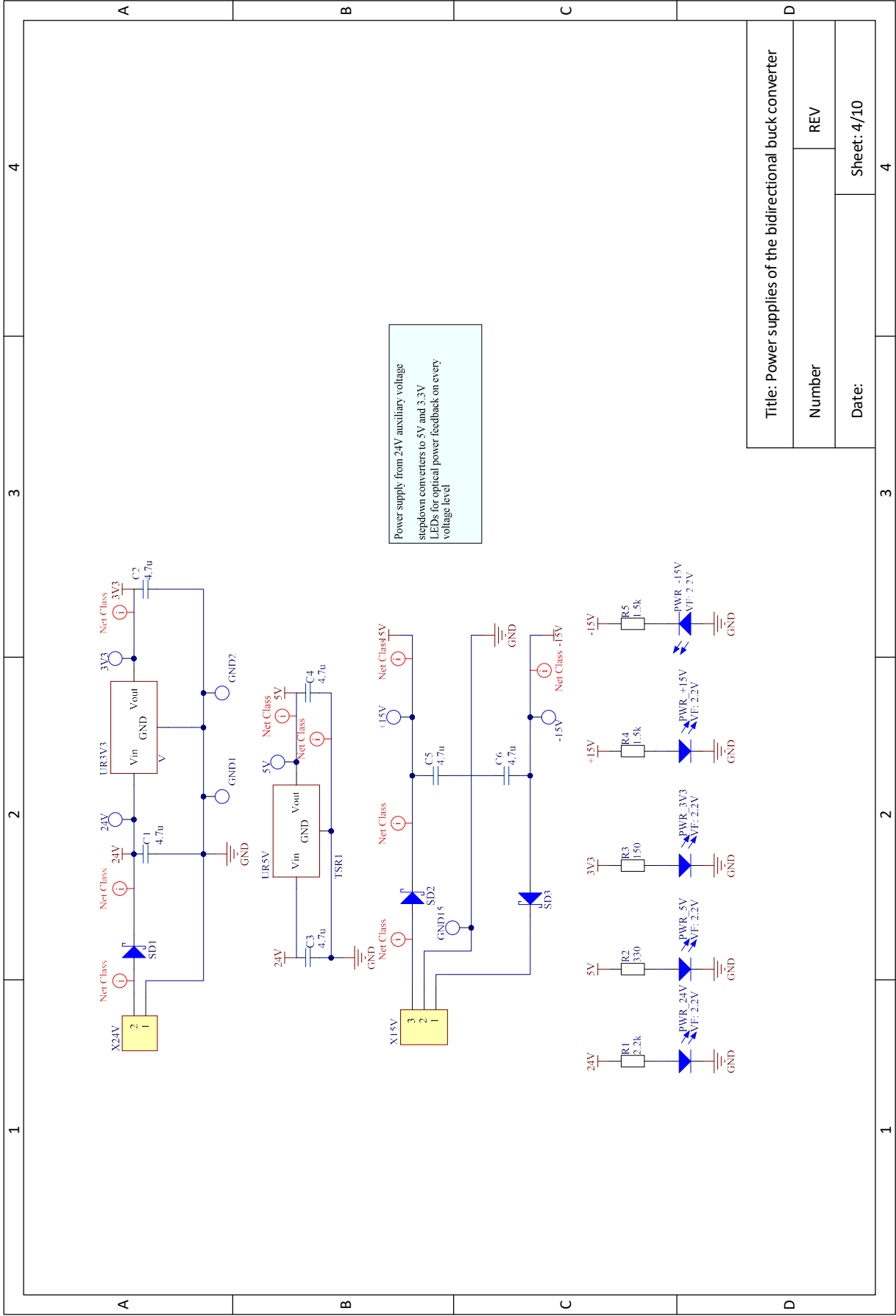


Figure 6.9: PCB layout of the buck converter

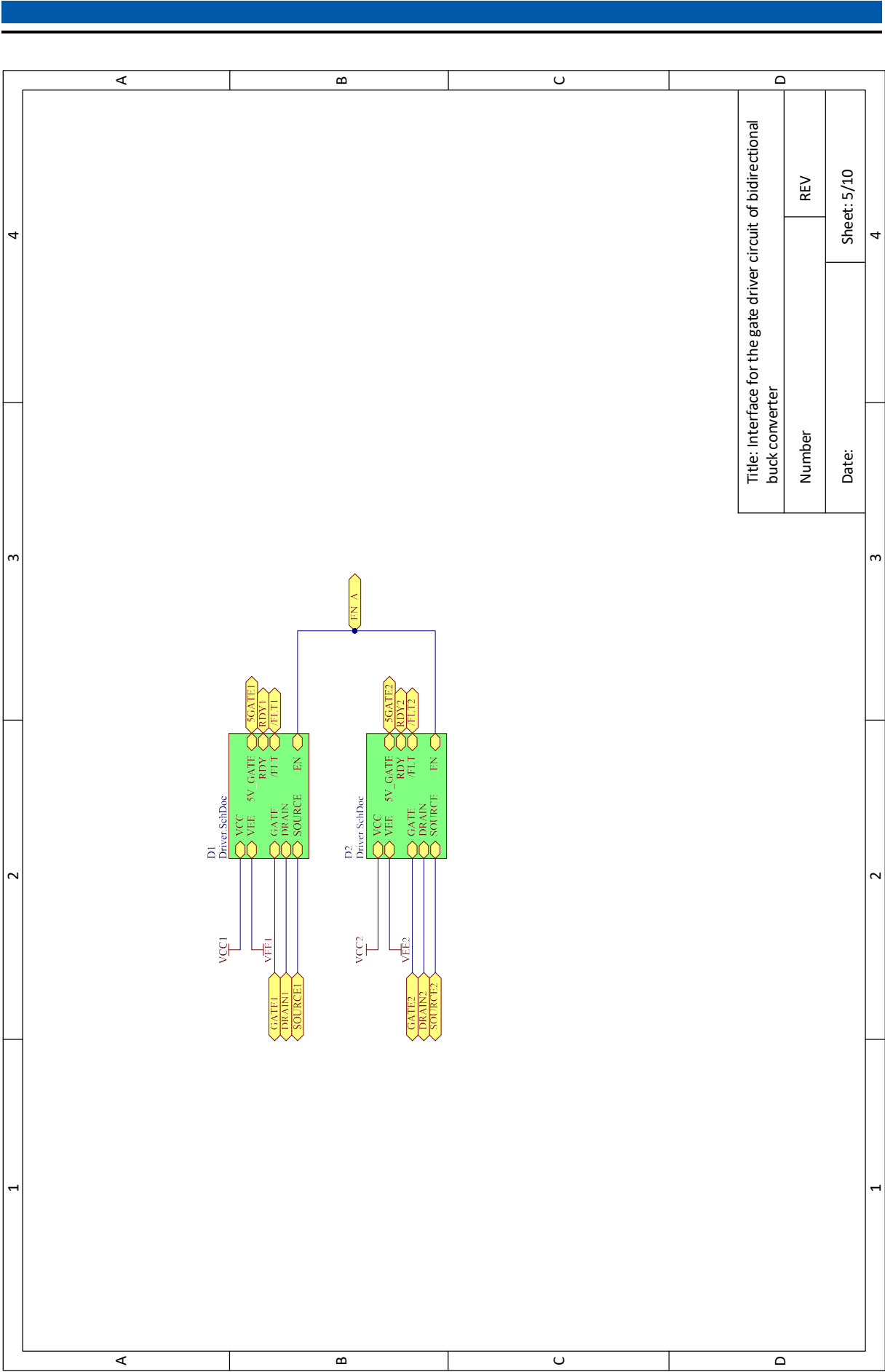


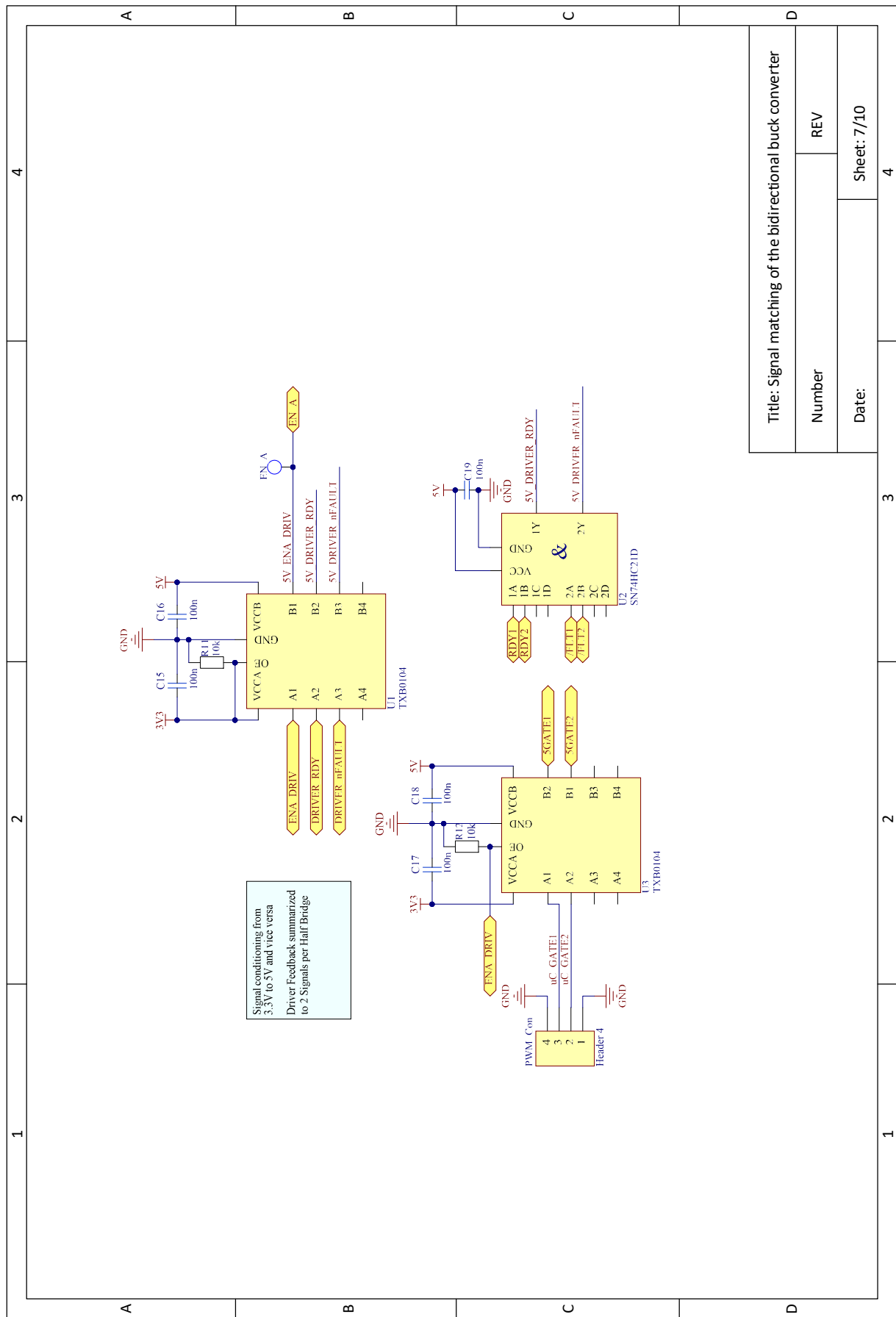


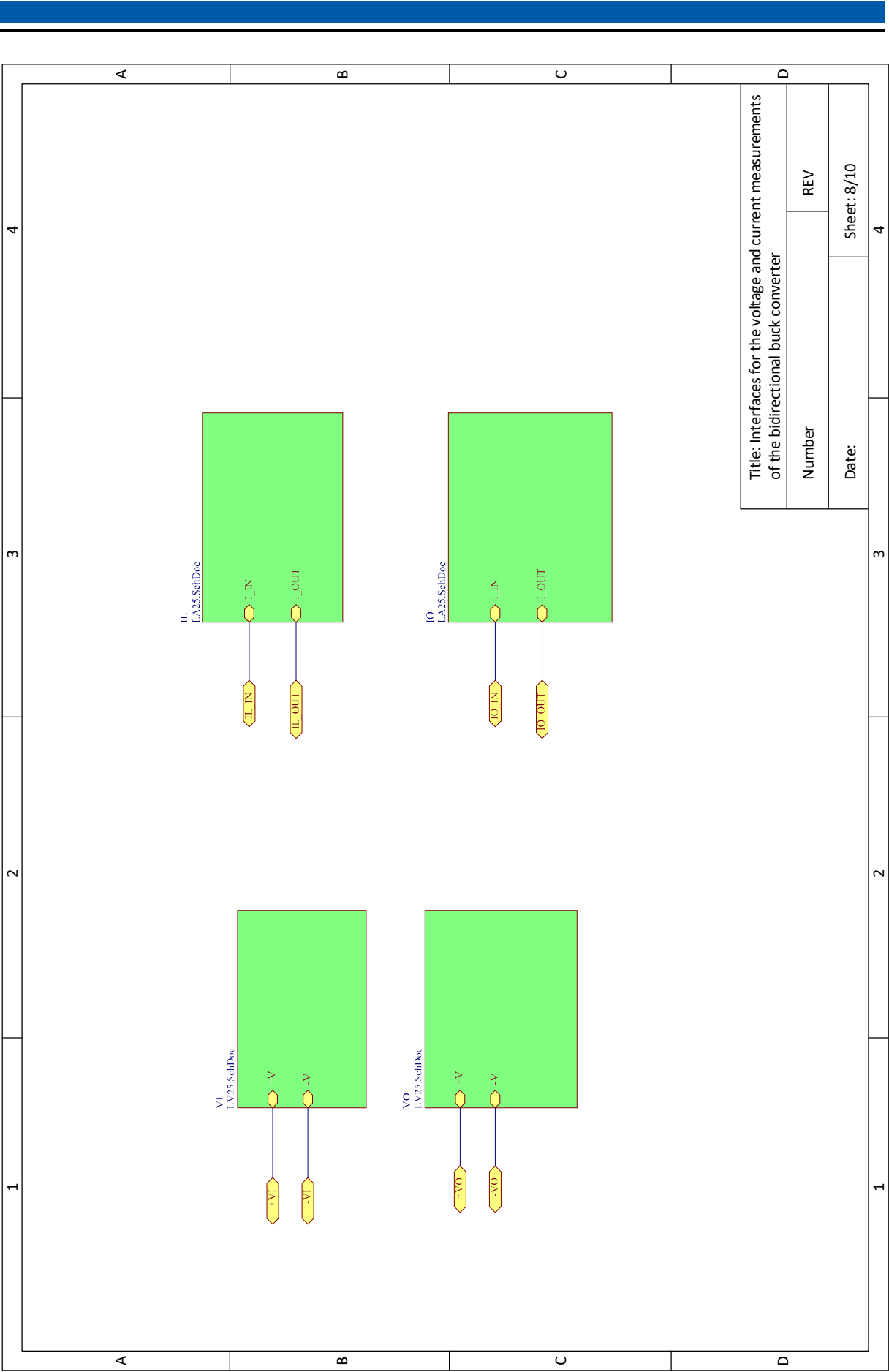


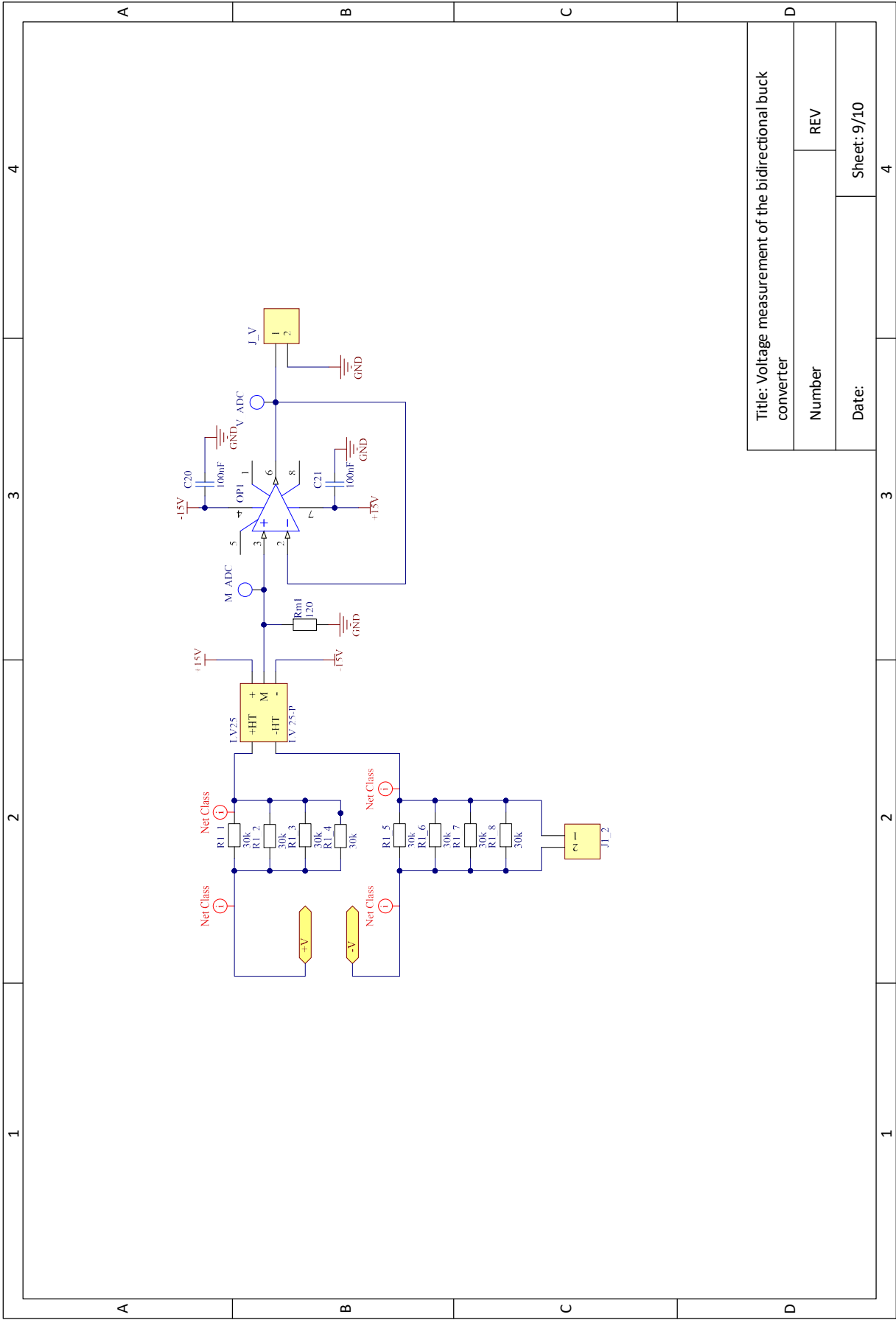


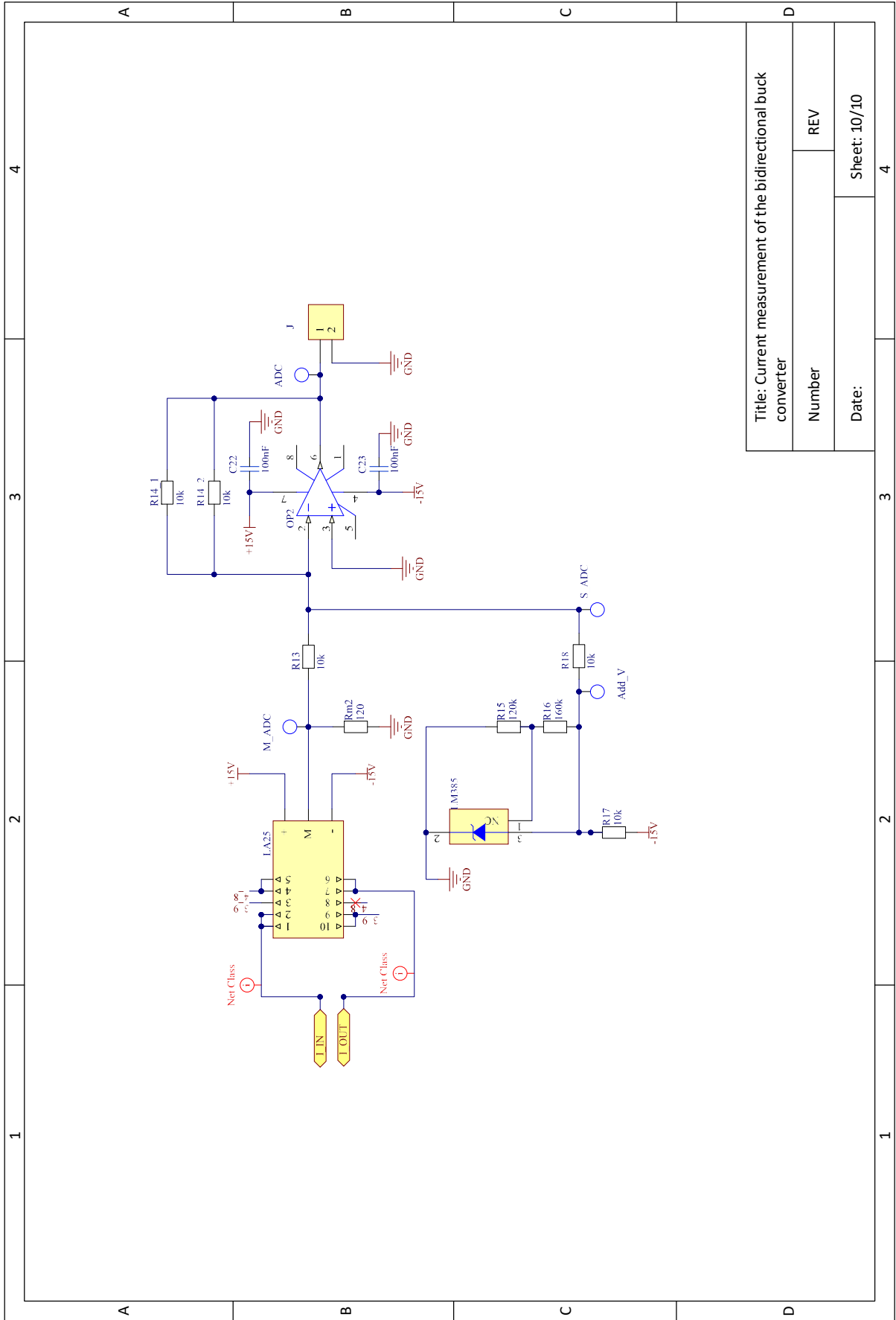
Title: Power supplies of the bidirectional buck converter		
Number	REV	
Date:	Sheet: 4/10	











Title: Current measurement of the bidirectional buck converter

Number REV

Date: Sheet: 10/10

6.4 Photos of the converter prototype

This section shows photos of components of the DC nanogrid including the DAB converter, the measurement circuit and the bidirectional buck converter.

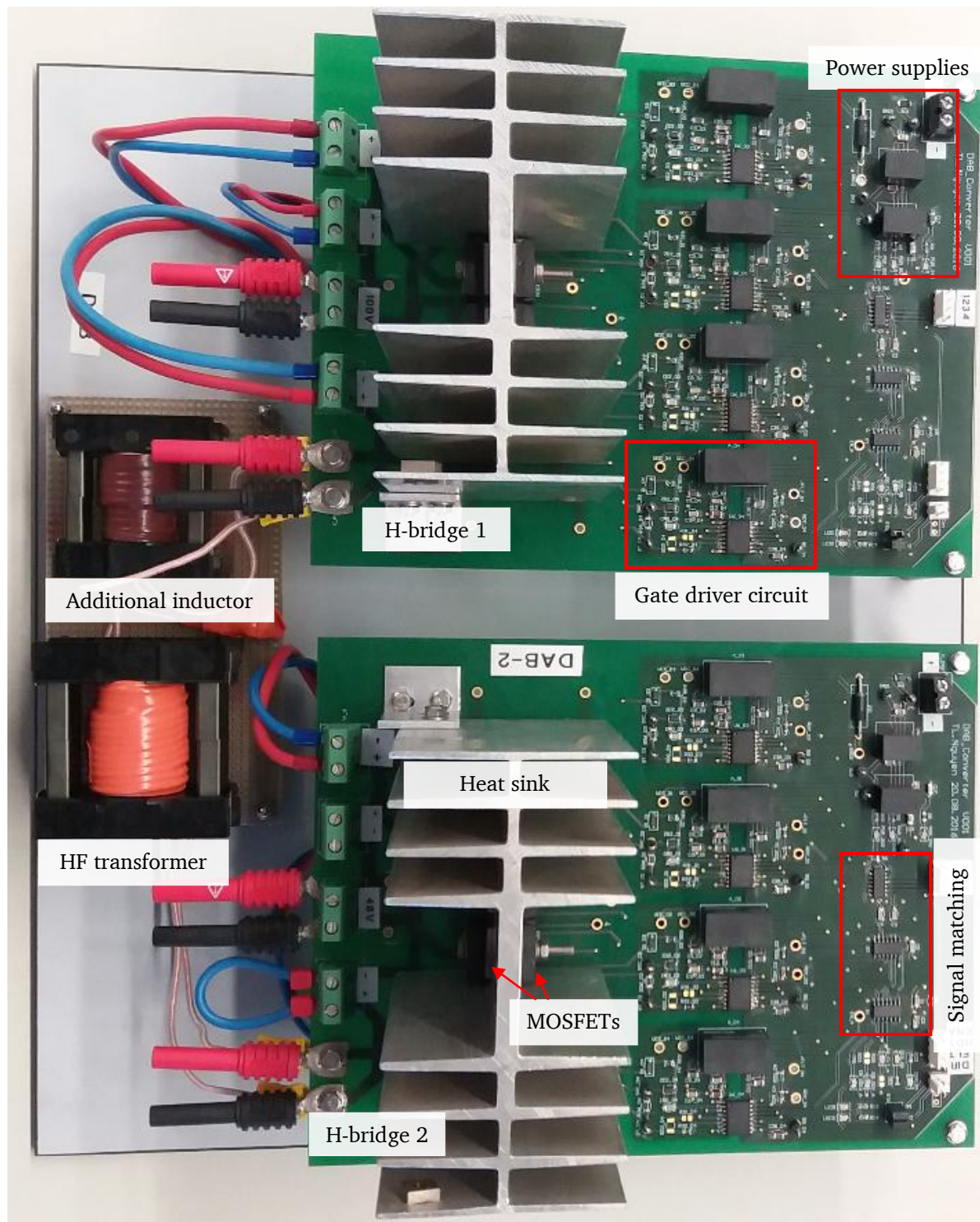


Figure 6.10: Photo of the DAB converter (top side)

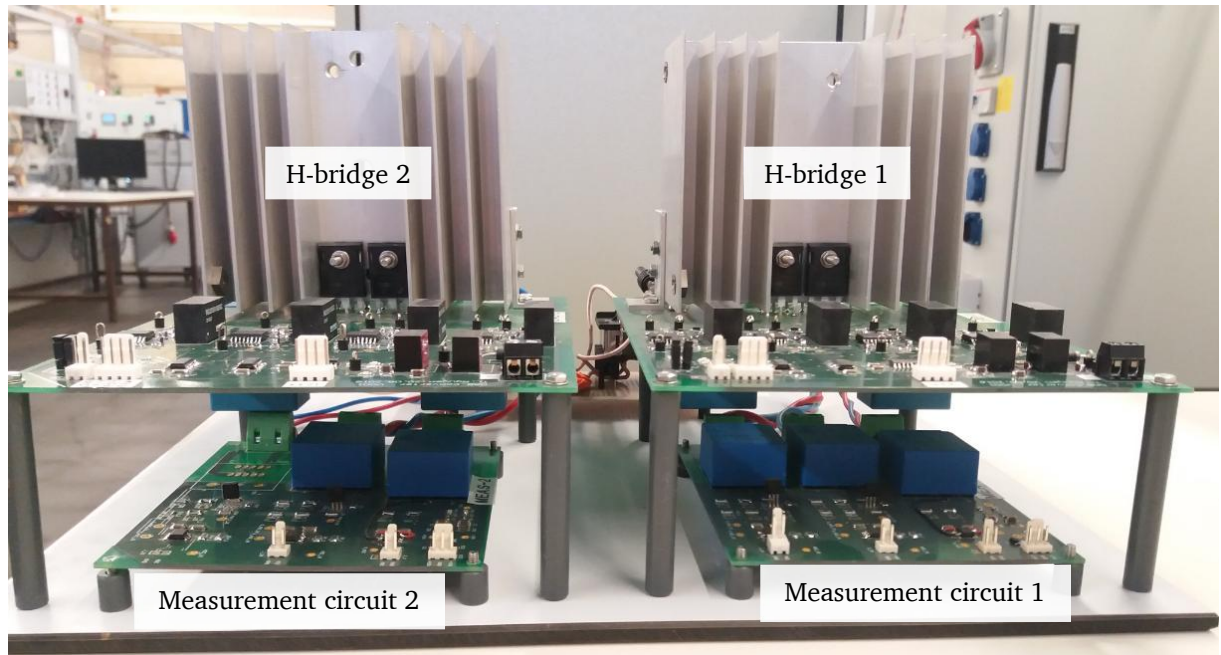


Figure 6.11: Photo of the DAB converter (front side)

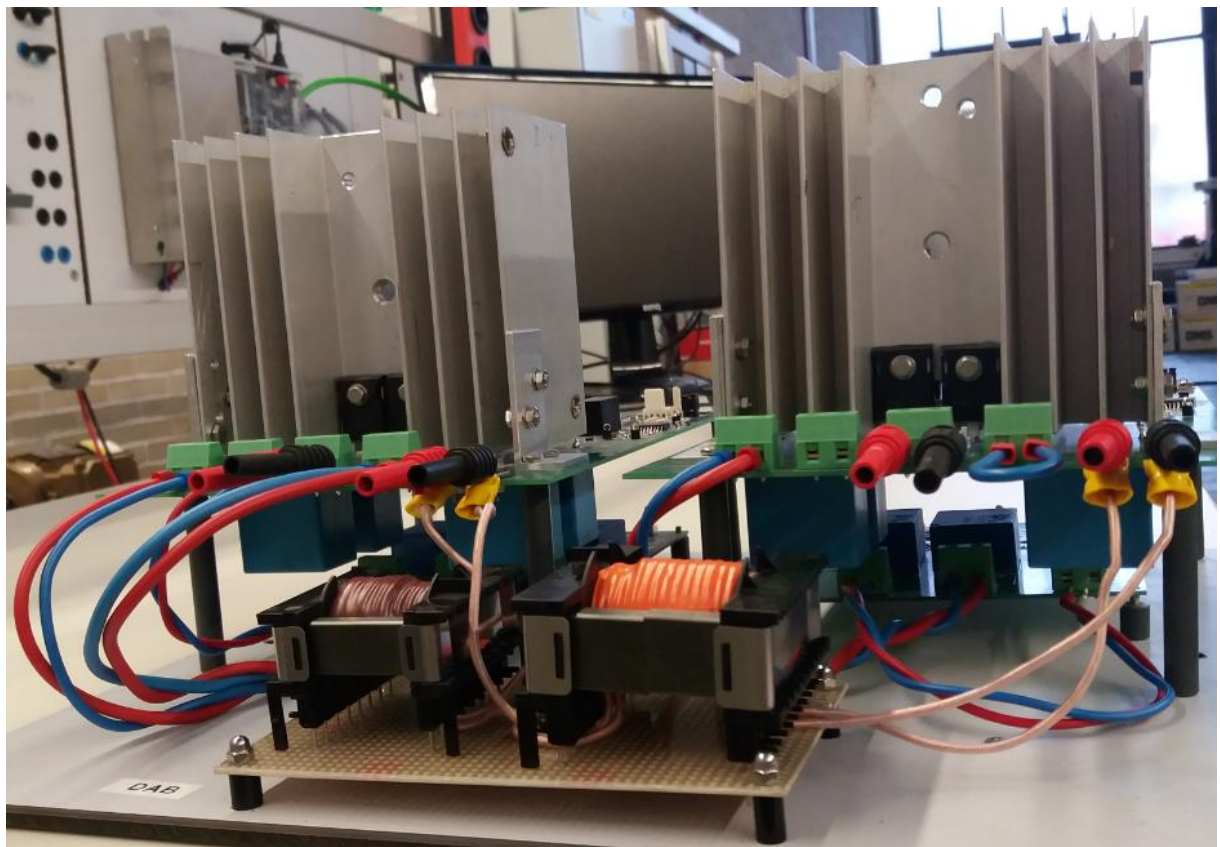


Figure 6.12: Photo of the DAB converter (back side)

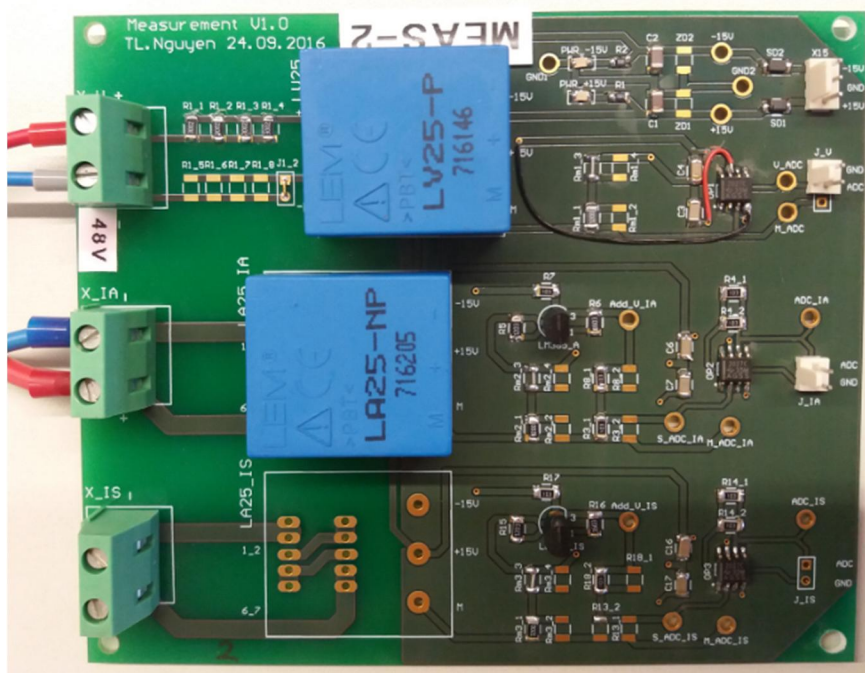


Figure 6.13: Photo of the measurement circuit

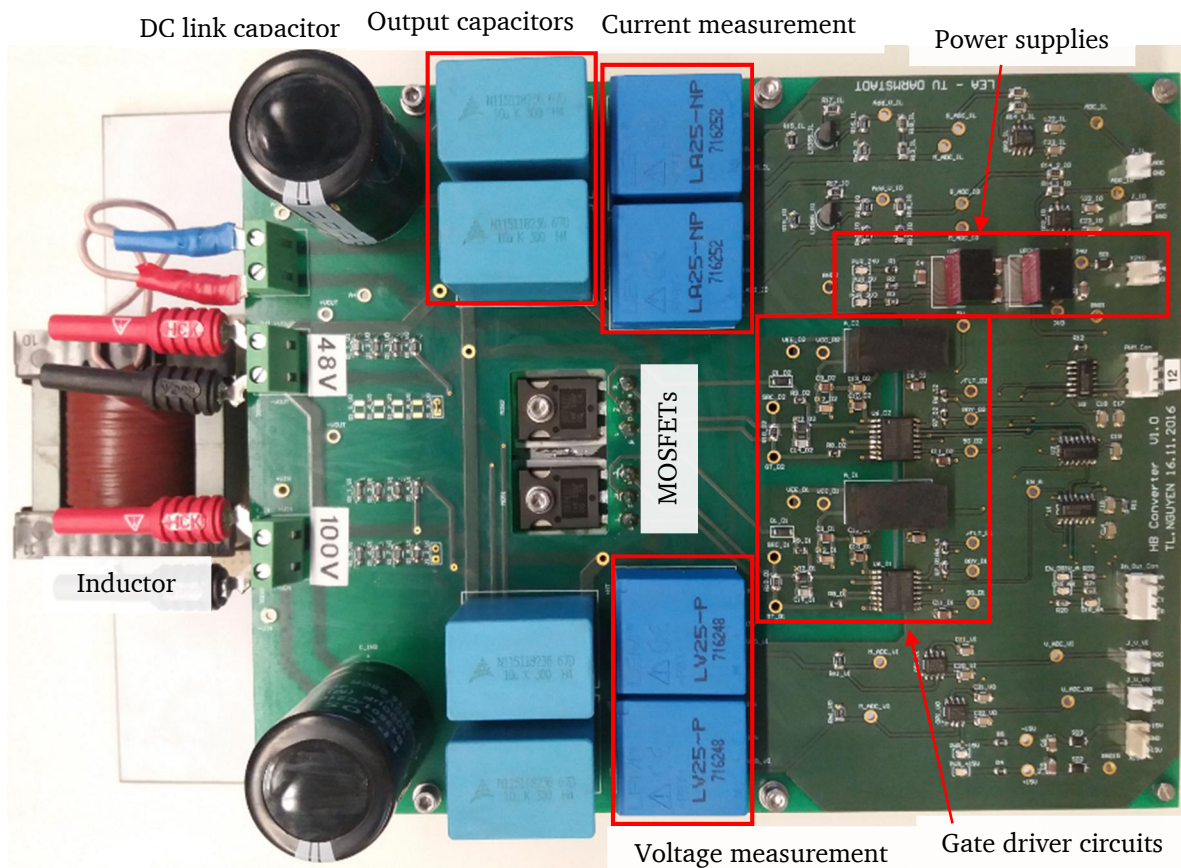


Figure 6.14: Photo of the bidirectional buck converter

Bibliography

- [1] T. W. Bank, "Toward a sustainable energy future for all : directions for the World Bank Group's energy sector," The World Bank, 79597, Jul. 2013.
- [2] M. Arriaga, C. A. Cañizares, and M. Kazerani, "Northern Lights: Access to Electricity in Canada's Northern and Remote Communities," *IEEE Power Energy Mag.*, vol. 12, no. 4, pp. 50–59, Jul. 2014.
- [3] R. Paleta, A. Pina, and C. A. S. Silva, "Polygeneration Energy Container: Designing and Testing Energy Services for Remote Developing Communities," *IEEE Trans. Sustain. Energy*, vol. 5, no. 4, pp. 1348–1355, Oct. 2014.
- [4] M. Nasir, H. A. Khan, A. Hussain, L. Mateen, and N. A. Zaffar, "Solar PV Based Scalable DC Microgrid for Rural Electrification in Developing Regions," *IEEE Trans. Sustain. Energy*, vol. PP, no. 99, pp. 1–1, 2017.
- [5] "World Energy Outlook 2016-Executive Summary," *Int. Energy Agency*, vol. 1, 2016.
- [6] A. Jhunjhunwala, A. Lolla, and P. Kaur, "Solar-dc Microgrid for Indian Homes: A Transforming Power Scenario," *IEEE Electrification Mag.*, vol. 4, no. 2, pp. 10–19, Jun. 2016.
- [7] J. Thornburg, T. S. Ustun, and B. Krogh, "Smart microgrid operation simulator for management and electrification planning," in *2016 IEEE PES PowerAfrica*, 2016, pp. 1–5.
- [8] M. Nasir, S. Iqbal, and H. A. Khan, "Optimal Planning and Design of Low-Voltage Low-Power Solar DC Microgrids," *IEEE Trans. Power Syst.*, vol. PP, no. 99, pp. 1–1, 2017.
- [9] B. Nordman and K. Christensen, "Local power distribution with nanogrids," in *2013 International Green Computing Conference Proceedings*, 2013, pp. 1–8.
- [10] B. Nordman and K. Christensen, "DC Local Power Distribution with microgrids and nanogrids," in *2015 IEEE First International Conference on DC Microgrids (ICDCM)*, 2015, pp. 199–204.
- [11] D. Burmester, R. Rayudu, W. Seah, and D. Akinyele, "A review of nanogrid topologies and technologies," *Renew. Sustain. Energy Rev.*, vol. 67, pp. 760–775, Jan. 2017.
- [12] A. Etxeberria, I. Vechiu, H. Camblong, J. M. Vinassa, and H. Camblong, "Hybrid Energy Storage Systems for renewable Energy Sources Integration in microgrids: A review," in *IPEC, 2010 Conference Proceedings*, 2010, pp. 532–537.

-
-
- [13] M. H. Nehrir *et al.*, “A Review of Hybrid Renewable/Alternative Energy Systems for Electric Power Generation: Configurations, Control, and Applications,” *IEEE Trans. Sustain. Energy*, vol. 2, no. 4, pp. 392–403, Oct. 2011.
- [14] B. S. Borowy and Z. M. Salameh, “Methodology for optimally sizing the combination of a battery bank and PV array in a wind/PV hybrid system,” *IEEE Trans. Energy Convers.*, vol. 11, no. 2, pp. 367–375, Jun. 1996.
- [15] R. H. Lasseter, “MicroGrids,” in *2002 IEEE Power Engineering Society Winter Meeting. Conference Proceedings (Cat. No.02CH37309)*, 2002, vol. 1, pp. 305–308 vol.1.
- [16] T. Dragičević, X. Lu, J. C. Vasquez, and J. M. Guerrero, “DC Microgrids #x2014;Part II: A Review of Power Architectures, Applications, and Standardization Issues,” *IEEE Trans. Power Electron.*, vol. 31, no. 5, pp. 3528–3549, May 2016.
- [17] A. Werth, N. Kitamura, and K. Tanaka, “Conceptual Study for Open Energy Systems: Distributed Energy Network Using Interconnected DC Nanogrids,” *IEEE Trans. Smart Grid*, vol. 6, no. 4, pp. 1621–1630, Jul. 2015.
- [18] “Microgrid Benefits: Eight Ways a Microgrid Will Improve Your Operation,” *Microgrid Knowledge*, 21-Aug-2017. .
- [19] K. Sun, L. Zhang, Y. Xing, and J. M. Guerrero, “A Distributed Control Strategy Based on DC Bus Signaling for Modular Photovoltaic Generation Systems With Battery Energy Storage,” *IEEE Trans. Power Electron.*, vol. 26, no. 10, pp. 3032–3045, Oct. 2011.
- [20] S. K. Kim, J. H. Jeon, C. H. Cho, J. B. Ahn, and S. H. Kwon, “Dynamic Modeling and Control of a Grid-Connected Hybrid Generation System With Versatile Power Transfer,” *IEEE Trans. Ind. Electron.*, vol. 55, no. 4, pp. 1677–1688, Apr. 2008.
- [21] D. Kumar, F. Zare, and A. Ghosh, “DC Microgrid Technology: System Architectures, AC Grid Interfaces, Grounding Schemes, Power Quality, Communication Networks, Applications, and Standardizations Aspects,” *IEEE Access*, vol. 5, pp. 12230–12256, 2017.
- [22] F. Valenciaga and P. F. Puleston, “Supervisor control for a stand-alone hybrid generation system using wind and photovoltaic energy,” *IEEE Trans. Energy Convers.*, vol. 20, no. 2, pp. 398–405, Jun. 2005.
- [23] J. Schonbergerschonberger, R. Duke, and S. D. Round, “DC-Bus Signaling: A Distributed Control Strategy for a Hybrid Renewable Nanogrid,” *IEEE Trans. Ind. Electron.*, vol. 53, no. 5, pp. 1453–1460, Oct. 2006.
-

-
- [24] H. Mahmood, D. Michaelson, and J. Jiang, "Control strategy for a standalone PV/battery hybrid system," in *IECON 2012 - 38th Annual Conference on IEEE Industrial Electronics Society*, 2012, pp. 3412–3418.
- [25] T. Dragičević, J. M. Guerrero, J. C. Vasquez, and D. Škrlec, "Supervisory Control of an Adaptive-Droop Regulated DC Microgrid With Battery Management Capability," *IEEE Trans. Power Electron.*, vol. 29, no. 2, pp. 695–706, Feb. 2014.
- [26] T. Dragicevic, J. C. Vasquez, J. M. Guerrero, and D. Škrlec, "Advanced LVDC Electrical Power Architectures and Microgrids: A step toward a new generation of power distribution networks," *IEEE Electrification Mag.*, vol. 2, no. 1, pp. 54–65, Mar. 2014.
- [27] Q. Shafiee, T. Dragicevic, J. C. Vasquez, and J. M. Guerrero, "Hierarchical control for multiple DC-microgrids clusters," in *2014 11th International Multi-Conference on Systems, Signals Devices (SSD)*, 2014, pp. 1–6.
- [28] J. D. Park, J. Candelaria, L. Ma, and K. Dunn, "DC Ring-Bus Microgrid Fault Protection and Identification of Fault Location," *IEEE Trans. Power Deliv.*, vol. 28, no. 4, pp. 2574–2584, Oct. 2013.
- [29] A. G. Tsikalakis and N. D. Hatziargyriou, "Centralized Control for Optimizing Microgrids Operation," *IEEE Trans. Energy Convers.*, vol. 23, no. 1, pp. 241–248, Mar. 2008.
- [30] M. Saleh, Y. Esa, and A. Mohamed, "Centralized control for DC microgrid using finite state machine," in *2017 IEEE Power Energy Society Innovative Smart Grid Technologies Conference (ISGT)*, 2017, pp. 1–5.
- [31] H. K. M. Paredes, J. P. Bonaldo, and J. A. Pomilio, "Centralized Control Center Implementation for Synergistic Operation of Distributed Multifunctional Single-Phase Grid-Tie Inverters in a Microgrid," *IEEE Trans. Ind. Electron.*, pp. 1–1, 2018.
- [32] L. Meng *et al.*, "Review on Control of DC Microgrids and Multiple Microgrid Clusters," *IEEE J. Emerg. Sel. Top. Power Electron.*, vol. 5, no. 3, pp. 928–948, Sep. 2017.
- [33] J. M. Guerrero, J. C. Vasquez, J. Matas, L. G. de Vicuna, and M. Castilla, "Hierarchical Control of Droop-Controlled AC and DC Microgrids #x2014;A General Approach Toward Standardization," *IEEE Trans. Ind. Electron.*, vol. 58, no. 1, pp. 158–172, Jan. 2011.
- [34] A. Elrayyah, F. Cingoz, and Y. Sozer, "Smart Loads Management Using Droop-Based Control in Integrated Microgrid Systems," *IEEE J. Emerg. Sel. Top. Power Electron.*, vol. 5, no. 3, pp. 1142–1153, Sep. 2017.
-

-
-
- [35] J. W. Simpson-Porco, F. Dörfler, and F. Bullo, "Synchronization and power sharing for droop-controlled inverters in islanded microgrids," *Automatica*, vol. 49, no. 9, pp. 2603–2611, Sep. 2013.
- [36] S. Augustine, M. K. Mishra, and N. Lakshminarasamma, "Adaptive Droop Control Strategy for Load Sharing and Circulating Current Minimization in Low-Voltage Standalone DC Microgrid," *IEEE Trans. Sustain. Energy*, vol. 6, no. 1, pp. 132–141, Jan. 2015.
- [37] N. L. Diaz, T. Dragičević, J. C. Vasquez, and J. M. Guerrero, "Intelligent Distributed Generation and Storage Units for DC Microgrids #x2014;A New Concept on Cooperative Control Without Communications Beyond Droop Control," *IEEE Trans. Smart Grid*, vol. 5, no. 5, pp. 2476–2485, Sep. 2014.
- [38] H. H. Huang, C. Y. Hsieh, J. Y. Liao, and K. H. Chen, "Adaptive Droop Resistance Technique for Adaptive Voltage Positioning in Boost DC #x2013;DC Converters," *IEEE Trans. Power Electron.*, vol. 26, no. 7, pp. 1920–1932, Jul. 2011.
- [39] C. Li, T. Dragicevic, N. L. Diaz, J. C. Vasquez, and J. M. Guerrero, "Voltage scheduling droop control for State-of-Charge balance of distributed energy storage in DC microgrids," in *2014 IEEE International Energy Conference (ENERGYCON)*, 2014, pp. 1310–1314.
- [40] T. Dragičević, J. M. Guerrero, and J. C. Vasquez, "A Distributed Control Strategy for Coordination of an Autonomous LVDC Microgrid Based on Power-Line Signaling," *IEEE Trans. Ind. Electron.*, vol. 61, no. 7, pp. 3313–3326, Jul. 2014.
- [41] Y. Gu, X. Xiang, W. Li, and X. He, "Mode-Adaptive Decentralized Control for Renewable DC Microgrid With Enhanced Reliability and Flexibility," *IEEE Trans. Power Electron.*, vol. 29, no. 9, pp. 5072–5080, Sep. 2014.
- [42] D. Wu, F. Tang, T. Dragicevic, J. M. Guerrero, and J. C. Vasquez, "Coordinated Control Based on Bus-Signaling and Virtual Inertia for Islanded DC Microgrids," *IEEE Trans. Smart Grid*, vol. 6, no. 6, pp. 2627–2638, Nov. 2015.
- [43] R. Scattolini, "Architectures for distributed and hierarchical Model Predictive Control – A review," *J. Process Control*, vol. 19, no. 5, pp. 723–731, May 2009.
- [44] X. Lu, J. M. Guerrero, K. Sun, and J. C. Vasquez, "An Improved Droop Control Method for DC Microgrids Based on Low Bandwidth Communication With DC Bus Voltage Restoration and Enhanced Current Sharing Accuracy," *IEEE Trans. Power Electron.*, vol. 29, no. 4, pp. 1800–1812, Apr. 2014.

-
- [45] S. Anand, B. G. Fernandes, and J. Guerrero, "Distributed Control to Ensure Proportional Load Sharing and Improve Voltage Regulation in Low-Voltage DC Microgrids," *IEEE Trans. Power Electron.*, vol. 28, no. 4, pp. 1900–1913, Apr. 2013.
- [46] V. Nasirian, A. Davoudi, and F. L. Lewis, "Distributed adaptive droop control for DC microgrids," in *2014 IEEE Applied Power Electronics Conference and Exposition - APEC 2014*, 2014, pp. 1147–1152.
- [47] V. Nasirian, S. Moayedi, A. Davoudi, and F. L. Lewis, "Distributed Cooperative Control of DC Microgrids," *IEEE Trans. Power Electron.*, vol. 30, no. 4, pp. 2288–2303, Apr. 2015.
- [48] M. S. Mahmoud, S. Azher Hussain, and M. A. Abido, "Modeling and control of microgrid: An overview," *J. Frankl. Inst.*, vol. 351, no. 5, pp. 2822–2859, May 2014.
- [49] A. S. Dobakhshari, S. Azizi, and A. M. Ranjbar, "Control of microgrids: Aspects and prospects," in *2011 International Conference on Networking, Sensing and Control*, 2011, pp. 38–43.
- [50] G. W. Wester and R. D. Middlebrook, "Low-Frequency Characterization of Switched dc-dc Converters," *IEEE Trans. Aerosp. Electron. Syst.*, vol. AES-9, no. 3, pp. 376–385, May 1973.
- [51] R. D. Middlebrook and S. Cuk, "A general unified approach to modelling switching-converter power stages," in *1976 IEEE Power Electronics Specialists Conference*, 1976, pp. 18–34.
- [52] M. F. N. Tajuddin, N. A. Rahim, I. Daut, B. Ismail, and M. F. Mohammed, "State space averaging technique of power converter with digital PID controller," in *TENCON 2009 - 2009 IEEE Region 10 Conference*, 2009, pp. 1–6.
- [53] W. M. Polivka, P. R. K. Chetty, and R. D. Middlebrook, "State-Space Average modelling of converters with parasitics and storage-time modulation," in *1980 IEEE Power Electronics Specialists Conference*, 1980, pp. 119–143.
- [54] A. Frances, R. Asensi, O. Garcia, R. Prieto, and J. Uceda, "Modeling Electronic Power Converters in Smart DC Microgrids - An Overview," *IEEE Trans. Smart Grid*, pp. 1–1, 2017.
- [55] H. Qin and J. W. Kimball, "Generalized Average Modeling of Dual Active Bridge DC-DC Converter," *IEEE Trans. Power Electron.*, vol. 27, no. 4, pp. 2078–2084, Apr. 2012.

-
-
- [56] T. L. Nguyen, G. Griepentrog, and V. T. Phung, "Modeling and control of dual active bridge converter with two control loops and output filter," in *IECON 2017 - 43rd Annual Conference of the IEEE Industrial Electronics Society*, 2017, pp. 4683–4689.
- [57] V. A. Caliskan, O. C. Verghese, and A. M. Stankovic, "Multifrequency averaging of DC/DC converters," *IEEE Trans. Power Electron.*, vol. 14, no. 1, pp. 124–133, Jan. 1999.
- [58] A. Griffo, J. Wang, and D. Howe, "Large signal stability analysis of DC power systems with constant power loads," in *2008 IEEE Vehicle Power and Propulsion Conference*, 2008, pp. 1–6.
- [59] F. Zhao, N. Li, Z. Yin, and X. Tang, "Small-signal modeling and stability analysis of DC microgrid with multiple type of loads," in *2014 International Conference on Power System Technology*, 2014, pp. 3309–3315.
- [60] S. Anand and B. G. Fernandes, "Reduced-Order Model and Stability Analysis of Low-Voltage DC Microgrid," *IEEE Trans. Ind. Electron.*, vol. 60, no. 11, pp. 5040–5049, Nov. 2013.
- [61] S. Bae and A. Kwasinski, "Dynamic Modeling and Operation Strategy for a Microgrid With Wind and Photovoltaic Resources," *IEEE Trans. Smart Grid*, vol. 3, no. 4, pp. 1867–1876, Dec. 2012.
- [62] D. Marx, P. Magne, B. Nahid-Mobarakeh, S. Pierfederici, and B. Davat, "Large Signal Stability Analysis Tools in DC Power Systems With Constant Power Loads and Variable Power Loads #x2014;A Review," *IEEE Trans. Power Electron.*, vol. 27, no. 4, pp. 1773–1787, Apr. 2012.
- [63] Q. Shafiee, T. Dragicevic, J. C. Vasquez, and J. M. Guerrero, "Modeling, stability analysis and active stabilization of multiple DC-microgrid clusters," in *Energy Conference (ENERGYCON), 2014 IEEE International*, 2014, pp. 1284–1290.
- [64] A. A. A. Radwan and Y. A. R. I. Mohamed, "Linear Active Stabilization of Converter-Dominated DC Microgrids," *IEEE Trans. Smart Grid*, vol. 3, no. 1, pp. 203–216, Mar. 2012.
- [65] T. L. Nguyen and G. Griepentrog, "A self-sustained and flexible decentralized control strategy for DC nanogrids in remote areas/islands," in *2017 IEEE Southern Power Electronics Conference (SPEC)*, 2017, pp. 1–6.

-
- [66] T. L. Nguyen and G. Griepentrog, "Modeling, Control and Stability Analysis for a DC Nanogrid System," in *2018 IEEE 19th Workshop on Control and Modeling for Power Electronics (COMPEL)*, 2018, pp. 1–8.
- [67] T. L. Nguyen, J. M. Guerrero, and G. Griepentrog, "A Self-Sustained and Flexible Control Strategy for Islanded DC Nanogrids without Communication Links," *Has Been Accept. Publ. J. Emerg. Sel. Top. Power Electron.*, 2019.
- [68] S. Bifaretti, S. Cordiner, V. Mulone, V. Rocco, J. L. Rossi, and F. Spagnolo, "Grid-connected Microgrids to Support Renewable Energy Sources Penetration," *Energy Procedia*, vol. 105, pp. 2910–2915, May 2017.
- [69] V. Joseph and P. C. Thomas, "Grid connected mode of microgrid with reactive power compensation," in *2013 International Conference on Advanced Computing and Communication Systems*, 2013, pp. 1–6.
- [70] A. C. Luna, N. L. Diaz, L. Meng, M. Graells, J. C. Vasquez, and J. M. Guerrero, "Generation-side power scheduling in a grid-connected DC microgrid," in *2015 IEEE First International Conference on DC Microgrids (ICDCM)*, 2015, pp. 327–332.
- [71] D. Wu, J. M. Guerrero, J. C. Vasquez, T. Dragicevic, and F. Tang, "Coordinated power control strategy based on primary-frequency-signaling for islanded microgrids," in *2013 IEEE Energy Conversion Congress and Exposition*, 2013, pp. 1033–1038.
- [72] M. Tucci, S. Riveros, J. C. Vasquez, J. M. Guerrero, and G. Ferrari-Trecate, "A Decentralized Scalable Approach to Voltage Control of DC Islanded Microgrids," *IEEE Trans. Control Syst. Technol.*, vol. 24, no. 6, pp. 1965–1979, Nov. 2016.
- [73] Q. Jiang, M. Xue, and G. Geng, "Energy Management of Microgrid in Grid-Connected and Stand-Alone Modes," *IEEE Trans. Power Syst.*, vol. 28, no. 3, pp. 3380–3389, Aug. 2013.
- [74] Z. Yi, W. Dong, and A. H. Etemadi, "A Unified Control and Power Management Scheme for PV-Battery-Based Hybrid Microgrids for Both Grid-Connected and Islanded Modes," *IEEE Trans. Smart Grid*, pp. 1–1, 2017.
- [75] J.-Y. Kim, J. H. Park, and H.-J. Lee, "Coordinated Control Strategy for Microgrid in Grid-Connected and Islanded Operation," *IFAC Proc. Vol.*, vol. 44, no. 1, pp. 14766–14771, Jan. 2011.

-
-
- [76] T. Dragičević, X. Lu, J. C. Vasquez, and J. M. Guerrero, "DC Microgrids #x2014;Part I: A Review of Control Strategies and Stabilization Techniques," *IEEE Trans. Power Electron.*, vol. 31, no. 7, pp. 4876–4891, Jul. 2016.
- [77] F. Katiraei, R. Iravani, N. Hatziargyriou, and A. Dimeas, "Microgrids management," *IEEE Power Energy Mag.*, vol. 6, no. 3, pp. 54–65, May 2008.
- [78] J. Y. Kim *et al.*, "Cooperative Control Strategy of Energy Storage System and Microsources for Stabilizing the Microgrid during Islanded Operation," *IEEE Trans. Power Electron.*, vol. 25, no. 12, pp. 3037–3048, Dec. 2010.
- [79] M. Savaghebi, A. Jalilian, J. C. Vasquez, and J. M. Guerrero, "Secondary Control Scheme for Voltage Unbalance Compensation in an Islanded Droop-Controlled Microgrid," *IEEE Trans. Smart Grid*, vol. 3, no. 2, pp. 797–807, Jun. 2012.
- [80] Q. Shafiee, J. M. Guerrero, and J. C. Vasquez, "Distributed Secondary Control for Islanded Microgrids #x2014;A Novel Approach," *IEEE Trans. Power Electron.*, vol. 29, no. 2, pp. 1018–1031, Feb. 2014.
- [81] J. M. Rey, P. Martí, M. Velasco, J. Miret, and M. Castilla, "Secondary Switched Control With no Communications for Islanded Microgrids," *IEEE Trans. Ind. Electron.*, vol. 64, no. 11, pp. 8534–8545, Nov. 2017.
- [82] H. Lotfi and A. Khodaei, "AC Versus DC Microgrid Planning," *IEEE Trans. Smart Grid*, vol. 8, no. 1, pp. 296–304, Jan. 2017.
- [83] E. Rodriguez-Diaz, F. Chen, J. C. Vasquez, J. M. Guerrero, R. Burgos, and D. Boroyevich, "Voltage-Level Selection of Future Two-Level LVdc Distribution Grids: A Compromise Between Grid Compatibiliy, Safety, and Efficiency," *IEEE Electrification Mag.*, vol. 4, no. 2, pp. 20–28, Jun. 2016.
- [84] J. J. Justo, F. Mwasilu, J. Lee, and J.-W. Jung, "AC-microgrids versus DC-microgrids with distributed energy resources: A review," *Renew. Sustain. Energy Rev.*, vol. 24, pp. 387–405, Aug. 2013.
- [85] J. M. Guerrero and D. F. D. Tan, "Guest Editorial Special Issue on Structured DC Microgrids," *IEEE J. Emerg. Sel. Top. Power Electron.*, vol. 5, no. 3, pp. 925–927, Sep. 2017.
- [86] S. Parhizi, H. Lotfi, A. Khodaei, and S. Bahramirad, "State of the Art in Research on Microgrids: A Review," *IEEE Access*, vol. 3, pp. 890–925, 2015.
-

-
- [87] M. Soshinskaya, W. H. J. Crijns-Graus, J. M. Guerrero, and J. C. Vasquez, "Microgrids: Experiences, barriers and success factors," *Renew. Sustain. Energy Rev.*, vol. 40, no. Supplement C, pp. 659–672, Dec. 2014.
- [88] E. Planas, J. Andreu, J. I. Gárate, I. Martínez de Alegría, and E. Ibarra, "AC and DC technology in microgrids: A review," *Renew. Sustain. Energy Rev.*, vol. 43, pp. 726–749, Mar. 2015.
- [89] S. Sumathi, L. Ashok Kumar, and P. Surekha, *Solar PV and Wind Energy Conversion Systems*. Springer International Publishing Switzerland, 2015.
- [90] M. G. Villalva, J. R. Gazoli, and E. R. Filho, "Comprehensive Approach to Modeling and Simulation of Photovoltaic Arrays," *IEEE Trans. Power Electron.*, vol. 24, no. 5, pp. 1198–1208, May 2009.
- [91] R. Bansal, *Handbook of Distributed Generation*. University of Pretoria, Pretoria, South Africa: Springer International Publishing AG, 2017.
- [92] R. Mandelbaum, "Reap the wild wind [offshore wind farm]," *IEEE Spectr.*, vol. 39, no. 10, pp. 34–39, Oct. 2002.
- [93] O. Anaya-Lara, N. Jenkins, J. Ekanayake, P. Cartwright, and M. Hughes, *Wind Energy Generation: modeling and control*, The first edition. A John Wiley and Sons, Ltd, Publication, 2009.
- [94] G. M. Masters, *Renewable and Efficient Electric Power Systems*. Stanford University: A John Wiley & Sons, Inc., Publication, 2004.
- [95] J. P. Barton and D. G. Infield, "Energy storage and its use with intermittent renewable energy," *IEEE Trans. Energy Convers.*, vol. 19, no. 2, pp. 441–448, Jun. 2004.
- [96] P. F. Ribeiro, B. K. Johnson, M. L. Crow, A. Arsoy, and Y. Liu, "Energy storage systems for advanced power applications," *Proc. IEEE*, vol. 89, no. 12, pp. 1744–1756, Dec. 2001.
- [97] Z. M. Salameh, M. A. Casacca, and W. A. Lynch, "A mathematical model for lead-acid batteries," *IEEE Trans. Energy Convers.*, vol. 7, no. 1, pp. 93–98, Mar. 1992.
- [98] S. M. Mousavi G. and M. Nikdel, "Various battery models for various simulation studies and applications," *Renew. Sustain. Energy Rev.*, vol. 32, pp. 477–485, Apr. 2014.
- [99] A. Rufer, *Energy Storage: System and Components*. Taylor & Francis Group, LLC, 2018.

-
-
- [100] F. Vasca and L. Iannelli, *Dynamics and Control of Switched Electronic Systems*. Springer-Verlag London Limited, 2012.
- [101] X. Wang, J. M. Guerrero, F. Blaabjerg, and Z. Chen, "A Review of Power Electronics Based Microgrids," *J. Power Electron.*, vol. 12, no. 1, pp. 181–192, 2012.
- [102] F. Blaabjerg, F. Iov, R. Teodorescu, and Z. Chen, "Power Electronics in Renewable Energy Systems," in *2006 12th International Power Electronics and Motion Control Conference*, 2006, pp. 1–17.
- [103] M. Rezkallah, A. Chandra, B. Singh, and S. Singh, "Microgrid: Configurations, Control and Applications," *IEEE Trans. Smart Grid*, vol. PP, no. 99, pp. 1–1, 2017.
- [104] S. Saravanan and N. R. Babu, "Non-Isolated DC-DC Converter for Renewable Based Grid Application," *Energy Procedia*, vol. 103, pp. 310–315, Dec. 2016.
- [105] X. Lu, K. Sun, J. M. Guerrero, J. C. Vasquez, L. Huang, and J. Wang, "Stability Enhancement Based on Virtual Impedance for DC Microgrids With Constant Power Loads," *IEEE Trans. Smart Grid*, vol. 6, no. 6, pp. 2770–2783, Nov. 2015.
- [106] U. B. Tayab, M. A. B. Roslan, L. J. Hwai, and M. Kashif, "A review of droop control techniques for microgrid," *Renew. Sustain. Energy Rev.*, vol. 76, pp. 717–727, Sep. 2017.
- [107] P. Karlsson and J. Svensson, "DC bus voltage control for a distributed power system," *IEEE Trans. Power Electron.*, vol. 18, no. 6, pp. 1405–1412, Nov. 2003.
- [108] J.-W. Kim, H.-S. Choi, and B. H. Cho, "A novel droop method for converter parallel operation," *IEEE Trans. Power Electron.*, vol. 17, no. 1, pp. 25–32, Jan. 2002.
- [109] J. M. Guerrero, M. Chandorkar, T. L. Lee, and P. C. Loh, "Advanced Control Architectures for Intelligent Microgrids #x2014;Part I: Decentralized and Hierarchical Control," *IEEE Trans. Ind. Electron.*, vol. 60, no. 4, pp. 1254–1262, Apr. 2013.
- [110] B. Subudhi and R. Pradhan, "A Comparative Study on Maximum Power Point Tracking Techniques for Photovoltaic Power Systems," *IEEE Trans. Sustain. Energy*, vol. 4, no. 1, pp. 89–98, Jan. 2013.
- [111] R. B. Godoy *et al.*, "Procedure to Match the Dynamic Response of MPPT and Droop-Controlled Microinverters," *IEEE Trans. Ind. Appl.*, vol. 53, no. 3, pp. 2358–2368, May 2017.

-
- [112]D. E. Olivares, C. A. Cañizares, and M. Kazerani, "A centralized optimal energy management system for microgrids," in *2011 IEEE Power and Energy Society General Meeting*, 2011, pp. 1–6.
- [113]F. Martin-Martínez, A. Sánchez-Miralles, and M. Rivier, "A literature review of Microgrids: A functional layer based classification," *Renew. Sustain. Energy Rev.*, vol. 62, pp. 1133–1153, Sep. 2016.
- [114]R. Tongia, "Microgrids in India: Myths, misunderstandings, and the need for proper accounting," *Brookings*, Feb-2018. .
- [115]J. Sun and H. Grotstollen, "Symbolic analysis methods for averaged modeling of switching power converters," *IEEE Trans. Power Electron.*, vol. 12, no. 3, pp. 537–546, May 1997.
- [116]J. Sun, D. M. Mitchell, M. F. Greuel, P. T. Krein, and R. M. Bass, "Averaged modeling of PWM converters operating in discontinuous conduction mode," *IEEE Trans. Power Electron.*, vol. 16, no. 4, pp. 482–492, Jul. 2001.
- [117]Y. S. Lee, "A Systematic and Unified Approach to Modeling Switches in Switch-Mode Power Supplies," *IEEE Trans. Ind. Electron.*, vol. IE-32, no. 4, pp. 445–448, Nov. 1985.
- [118]S. R. Sanders and G. C. Verghese, "Synthesis of averaged circuit models for switched power converters," *IEEE Trans. Circuits Syst.*, vol. 38, no. 8, pp. 905–915, Aug. 1991.
- [119]V. Vorperian, R. Tymerski, and F. C. Y. Lee, "Equivalent circuit models for resonant and PWM switches," *IEEE Trans. Power Electron.*, vol. 4, no. 2, pp. 205–214, Apr. 1989.
- [120]A. Reatti and M. K. Kazimierczuk, "Small-signal model of PWM converters for discontinuous conduction mode and its application for boost converter," *IEEE Trans. Circuits Syst. Fundam. Theory Appl.*, vol. 50, no. 1, pp. 65–73, Jan. 2003.
- [121]D. Czarkowski and M. K. Kazimierczuk, "Circuit models of PWM DC-DC converters," in *Proceedings of the IEEE 1992 National Aerospace and Electronics Conference@m_NAECON 1992*, 1992, pp. 407–413 vol.1.
- [122]D. Czarkowski and M. K. Kazimierczuk, "Circuit models of PWM half-bridge DC-DC converter," in *[1992] Proceedings of the 35th Midwest Symposium on Circuits and Systems*, 1992, pp. 469–472 vol.1.
- [123]W. Janke, "Equivalent circuits for averaged description of DC-DC switch-mode power converters based on separation of variables approach," *Bull. Pol. Acad. Sci. Tech. Sci.*, vol. Vol. 61, no. nr 3, 2013.

-
- [124] R. W. Erickson and D. Maksimovic, *Fundamentals of Power Electronics*, Second Edition. University of Colorado: Kluwer Academic Publishers, 2004.
- [125] G. D. Demetriades, "On small-signal analysis and control of the single and the Dual Active Bridge topologies," Ph.D. dissertation, Royal Institute of Technology, Department of Electrical Engineering, Electrical Machines and Power Electronics, KTH, Stockholm, 2005.
- [126] H. Qin, "Dual active bridge converters in solid state transformers," Ph.D. dissertation, Missouri university of science and technology, 2012.
- [127] M. K. Kazimierczuk, *Pulse-width Modulated DC-DC Power Converters*. Wright State University, Ohio, USA: A John Wiley and Sons, Ltd, Publication, 2008.
- [128] A. Yazdani and R. Iravani, *Voltage-sourced converters in power system: Modeling, control and applications*. John Wiley & Sons, Inc., Hoboken, New Jersey, 2010.
- [129] A. Riccobono and E. Santi, "Comprehensive Review of Stability Criteria for DC Power Distribution Systems," *IEEE Trans. Ind. Appl.*, vol. 50, no. 5, pp. 3525–3535, Sep. 2014.
- [130] C. Zhao, S. D. Round, and J. W. Kolar, "Full-order averaging modelling of zero-voltage-switching phase-shift bidirectional DC-DC converters," *IET Power Electron.*, vol. 3, no. 3, pp. 400–410, May 2010.
- [131] H. Bai, C. Mi, C. Wang, and S. Gargies, "The dynamic model and hybrid phase-shift control of a dual-active-bridge converter," in *2008 34th Annual Conference of IEEE Industrial Electronics*, 2008, pp. 2840–2845.
- [132] G. D. Demetriades and H. P. Nee, "Dynamic modeling of the Dual-Active Bridge topology for high-power applications," in *2008 IEEE Power Electronics Specialists Conference*, 2008, pp. 457–464.
- [133] F. Krismer and J. W. Kolar, "Accurate Small-Signal Model for the Digital Control of an Automotive Bidirectional Dual Active Bridge," *IEEE Trans. Power Electron.*, vol. 24, no. 12, pp. 2756–2768, Dec. 2009.
- [134] S. R. Sanders, J. M. Noworolski, X. Z. Liu, and G. C. Verghese, "Generalized averaging method for power conversion circuits," *IEEE Trans. Power Electron.*, vol. 6, no. 2, pp. 251–259, Apr. 1991.

-
- [135] R. W. A. A. D. Doncker, D. M. Divan, and M. H. Kheraluwala, "A three-phase soft-switched high-power-density DC/DC converter for high-power applications," *IEEE Trans. Ind. Appl.*, vol. 27, no. 1, pp. 63–73, Jan. 1991.
- [136] F. Krismer, "Modeling and Optimization of Bidirectional Dual Active Bridge DC–DC Converter Topologies," Ph.D. dissertation, Power Electronic Systems Laboratory (ETH Zürich), 2010.
- [137] J. C. Vasquez, J. M. Guerrero, J. Miret, M. Castilla, and L. G. de Vicuna, "Hierarchical Control of Intelligent Microgrids," *IEEE Ind. Electron. Mag.*, vol. 4, no. 4, pp. 23–29, Dec. 2010.
- [138] J. Schönberger, "Distributed Control of a Nanogrid Using DC Bus Signalling," Ph.D. dissertation, University of Canterbury, Christchurch, New Zealand, 2005.
- [139] M. Coleman, C. K. Lee, C. Zhu, and W. G. Hurley, "State-of-Charge Determination From EMF Voltage Estimation: Using Impedance, Terminal Voltage, and Current for Lead-Acid and Lithium-Ion Batteries," *IEEE Trans. Ind. Electron.*, vol. 54, no. 5, pp. 2550–2557, Oct. 2007.
- [140] Z. Xuhui, X. Wen, G. Qiujian, and Z. Feng, "A new control scheme for DC-DC converter feeding constant power load in electric vehicle," in *2011 International Conference on Electrical Machines and Systems*, 2011, pp. 1–4.
- [141] EPCOS AG, "ETD 49/25/16 Core and accessories." May-2017.
- [142] N. Mohan, T. M. Underland, and R. P. William, *Power Electronics: Converters, Applications, and Design*, Third Edition. John Wiley & Sons, Inc, 2003.
- [143] EPCOS AG, "ETD 39/20/13 Core and accessories." May-2017.
- [144] S. Chander, P. Agarwal, and I. Gupta, "Design, modeling and simulation of DC-DC converter for low voltage applications," in *2010 IEEE International Conference on Sustainable Energy Technologies (ICSET)*, 2010, pp. 1–6.

Publications

IEEE Journal

- [1] **T. L. Nguyen**, J. M. Guerrero, and G. Griepentrog, “A Self-Sustained and Flexible Control Strategy for Islanded DC Nanogrids without Communication Links,” *IEEE Journal of Emerging and Selected Topics in Power Electronics*, 2019, Accepted.

International Conferences

- [1] **T. L. Nguyen** and G. Griepentrog, “Modeling, Control and Stability Analysis for a DC Nanogrid System,” in *2018 IEEE 19th Workshop on Control and Modeling for Power Electronics (COMPEL)*, 2018, pp. 1–8.
- [2] **T. L. Nguyen** and G. Griepentrog, “A self-sustained and flexible decentralized control strategy for DC nanogrids in remote areas/islands,” in *2017 IEEE Southern Power Electronics Conference (SPEC)*, 2017, pp. 1–6.
- [3] **T. L. Nguyen**, V. T. Phung, and G. Griepentrog, “Modeling and control of dual active bridge converter with two control loops and output filter,” in *IECON 2017 - 43rd Annual Conference of the IEEE Industrial Electronics Society*, 2017, pp. 4683–4689.